Development and Characterization of Cryogenic Detectors for the CRESST Experiment

Wolfgang Westphal

May 5, 2008

To the memory of our friend and colleague Wolfgang Westphal. He suffered from a serious traffic accident which occurred on May 13th, 2008 and died on May 21st, 2008. Wolfgang was working with E15 for almost 5 years. He was a brilliant Physicist and contributed significantly to the success of the experiment CRESST (Cryogenic Rare Event Search with Superconducting Thermometers) and to all our EURECA (European Underground Rare Event Calorimeter Array) related activities.

He had almost finished his PhD thesis work and had intended to submit it the same week he died. This file of his thesis dates of May 5th, 2008 and reflects the broad range of activities he was involved in. We lost an outstanding and highly successful scientist and a wonderful friend.

Wolfgang's colleagues
at the Physik-Department E15
Technische Universität München

Abstract

In the standard cosmological model derived from several observations of, e.g., the cosmic microwave background radiation and galaxy movements, the universe consists of $\sim$ 70% dark energy and $\sim$ 30% matter. Most of the matter is non-luminous (i.e. dark matter) and 80% of the matter content in the universe consists of a new kind of non-baryonic particles. In most scenarios these particles are weakly interacting massive particles (WIMPs), as their interaction with normal matter is rare. So far these particles have not been directly observed. A chance to detect them is by elastic scattering off nuclei of normal matter (see chapter 1).

The Cryogenic Rare Event Search with Superconducting Thermometers (CRESST) aims at the direct detection of these non-baryonic dark matter particles in the halo of the milky way by coherent scattering off the nuclei in scintillating $CaWO_4$ crystals (see chapter 2). The detectors are cryogenic detectors, which are sensitive enough for the expected low recoil energies (a few tens of keV). As the WIMPs only interact weakly and the particle density is low (a few particles per litre), the anticipated count rates are well below one count per day and kilogram target mass. Thus, an efficient background suppression is required. For this reason the experiment is located in the Gran Sasso underground laboratory and equipped with a strong shielding against natural radioactivity. Still, the count rate from the internal gamma and beta activity of the setup would by far exceed the count rate from the WIMPs. To veto this background both the scintillation light and the heat originating from an event in the $CaWO_4$ crystal are detected. As the emitted light per deposited energy is significantly more for electron recoils than for nuclear recoils, the gamma and beta background can be rejected effectively. The basic working principles of cryogenic detectors are discussed in chapter 3. The low-temperature cryostat and the new data acquisition system necessary to operate the cryogenic detectors are described in chapter 4. The basic procedures for the fabrication of cryogenic detectors are presented in chapter 5.

The amount of emitted light per energy deposition for nuclear recoils depends also on the recoiling nucleus (O, Ca or W). This opens a possibility to discriminate background from neutron interactions from the anticipated WIMP signal, as WIMPs are expected to mostly interact with tungsten, while most neutron events in the relevant energy window (up to 40 keV) are oxygen recoils. For this discrimination the quenching of the scintillation light, i.e. the reduction of the emitted light (compared to electron recoils) for oxygen, calcium and tungsten recoils has to be measured at millikelvin temperatures. For this purpose a cryogenic neutron scattering experiment

has been set up at the accelerator of the Maier-Leibnitz-Laboratory (MLL) in Garching.

In this work detectors for these calibration measurements were developeded and optimized for the requirements of a neutron scattering experiment performed without much shielding. The measurements are carried out at mK temperatures, the same temperature regime where also the CRESST experiment is being performed. The energy deposition in the absorber is detected with superconducting transition edge sensors (TESs) based on Ir/Au bi-layers with transition temperatures in the range of 30–60 mK. The $CaWO_4$ crystal is smaller than those in the dark matter experiments to avoid multiple neutron scattering events (see chapter 6.2). The design of the cryogenic detector is optimized for the higher count rates (including background) expected in these measurements. A matching cryogenic light detector was also produced in this work (see chapter 6.3). Both detectors were successfully installed in the neutron scattering experiment, and have already been used in several measurement campaigns.

An important component of the transition edge sensors used in this work are phonon collectors made of superconducting aluminum (see chapter 3.2). In these phonon collectors phonons from the absorber break up cooper pairs, thus exciting quasiparticles which then spread diffusively in the collector and may thermalize in the Ir/Au TES. For the design of these collectors the diffusion properties of the quasiparticles in the aluminum have to be known. Those properties depend on the quality of the thin films and have been determined in this work for the aluminum films produced at our institute (see chapter 5.7).

A potentially harmful background for the CRESST dark matter search originates in alpha decays on surfaces close to the target crystal. This background is typically from ^{210}Po, which is a product of ^{222}Rn contamination. The energy deposition of the recoiling ^{206}Pb nuclei (from the ^{210}Po alpha decay) into the $CaWO_4$ crystal is 104 keV or less and can tail down to the relevant energy window, thus limiting the experiment's sensitivity. In this work measurements and simulations investigating this kind of background were performed using a source with enriched ^{210}Po activity (see chapter 7.1).

From the coincident measurement of the heat and scintillation light and from pulse shape analysis of the light detector signals information on the scintillation properties of $CaWO_4$ at mK temperatures could be deduced. The decay time of the scintillation light was extracted for the light detector signals by comparing scintillation light events with events in the light detector from an X-ray calibration source (see chapter 6.3). From the coincident measurements of the heat and light of events using a gamma calibration of the $CaWO_4$ crystal the absolute amount of emitted scintillation light can be

determined (see chapters 7.1 and 7.2).

The summary and outlook of chapter 8 describe future detector developments which appear to be necessary to improve the sensitivity of the CRESST experiment to better than 10^{-8} pb for the WIMP-nucleon cross-section and for the future large-scale dark matter search EURECA (European Underground Rare Event Calorimetric Array) which is planned to use a 1 ton cryogenic target mass.

Contents

1 Introduction **1**
- 1.1 The Dark Matter Problem . . . 1
  - 1.1.1 Evidence for Dark Matter . . . 1
  - 1.1.2 Dark Matter Candidates . . . 4
  - 1.1.3 Halo Model . . . 7
- 1.2 Direct Dark Matter Detection . . . 7
  - 1.2.1 Background Considerations . . . 9
  - 1.2.2 Setting Constraints on Dark Matter . . . 14
  - 1.2.3 CDMS . . . 14
  - 1.2.4 EDELWEISS . . . 17
  - 1.2.5 DAMA/LIBRA . . . 19
  - 1.2.6 Liquid Noble Gases . . . 21
- 1.3 Indirect Dark Matter Detection . . . 23

2 The CRESST Experiment **25**
- 2.1 Detectors With Phonon-Light Discrimination . . . 26
- 2.2 CRESST Setup . . . 28
- 2.3 Background . . . 31
- 2.4 Quenching Factors . . . 33
  - 2.4.1 Time-of-Flight Mass Spectrometer . . . 33
  - 2.4.2 Neutron Scattering Experiment . . . 34
  - 2.4.3 Measurements with Standard Neutron Sources . . . 38
- 2.5 CRESST Results . . . 40
  - 2.5.1 Dark Matter Limits Before Upgrade . . . 40
  - 2.5.2 Dark Matter Limits After Upgrade . . . 41
  - 2.5.3 Rare Alpha Decays . . . 43
- 2.6 Status and Future . . . 44

3 Basics of Cryogenic Detectors **45**
- 3.1 Transition Edge Sensors . . . 45
  - 3.1.1 Calorimeter Model . . . 48

3.1.2 Slow Energy Input . . . 51
3.1.3 Composite Detectors . . . 51
3.1.4 Electrothermal Feedback . . . 54
3.2 Phonon Collectors . . . 56
3.2.1 Quasiparticle Diffusion - Two Sensors . . . 58
3.2.2 Quasiparticle Diffusion - One Sensor . . . 60

4 Low-Temperature Cryostat and New Data Acquisition System 65
4.1 Cryostat . . . 65
4.1.1 Detector Setup and Temperature Control . . . 67
4.1.2 SQUIDs . . . 69
4.2 New Data Acquisition System . . . 72
4.2.1 Custom Trigger Module . . . 72
4.2.2 Cross Talk Checks on the NI-PXI-6115 Module . . . 73
4.3 Measurement Techniques . . . 76
4.3.1 Recording Superconducting Transitions . . . 76
4.3.2 Recording Detector Events . . . 79

5 Fabrication of Cryogenic Detectors 83
5.1 Ir/Au Films . . . 83
5.2 Photolithography . . . 85
5.3 Aluminum Films . . . 87
5.4 Gold Pads . . . 88
5.5 Membrane Etching . . . 88
5.6 Ir/Au Thermometers . . . 89
5.6.1 Film Production Parameters . . . 90
5.6.2 Results and Discussion . . . 91
5.7 Measurement of the Quasiparticle Diffusion in Aluminum Films 96
5.7.1 Detector Design . . . 96
5.7.2 Results . . . 98

6 Detector Development for the CRESST Experiment and for the Neutron Calibration Measurements 107
6.1 Composite Detector Design with $CaWO_4$ Absorbers . . . 107
6.1.1 Experimental Setup . . . 108
6.1.2 Results . . . 110
6.1.3 Discussion and Prospects . . . 113
6.2 A Phonon Detector for Neutron Calibration Measurements . . 114
6.2.1 Requirements . . . 114
6.2.2 Detector Design . . . 115

6.2.3 Performance at Low Energies . . . 119
6.2.4 Performance at High Energies . . . 120
6.2.5 Neutron Measurement . . . 130
6.3 Scintillation Light Detection . . . 132
6.3.1 Detector Design . . . 133
6.3.2 Determination of the Light Collection . . . 133
6.3.3 Discussion of the Energy Threshold . . . 137
6.3.4 Scintillation Time Constants . . . 138

7 Background Suppression and Calibration Measurements for CRESST 145
7.1 Recoiling Nuclei from Surface Alpha Decays . . . 145
7.1.1 Motivation . . . 145
7.1.2 Source Preparation and Installation . . . 146
7.1.3 Results . . . 148
7.1.4 Monte Carlo Simulations . . . 156
7.1.5 Outlook: Radon Activated Reflector . . . 158
7.2 Transport Mechanism for Calibration Sources in CRESST . . 160
7.2.1 Setup . . . 160
7.2.2 First Calibration Measurements . . . 162

8 Summary and Outlook 165

Appendix

A Some Calculations 169
A.1 Quasiparticle Diffusion . . . 169
A.2 Mean Free Path of Neutrons in $CaWO_4$ . . . 172

Bibliography 175

Chapter 1

Introduction

1.1 The Dark Matter Problem

1.1.1 Evidence for Dark Matter

The existence of non-luminous matter exceeding the observable matter in abundance by a factor of at least 6, was first proposed in the 1930s by the Swiss Fritz Zwicky [1]. He introduced this "dark matter" to explain the observed motion of galaxies in the Coma cluster, which could not be described by the luminous component in those galaxies alone.

In more modern times the mass content of galaxy clusters can be determined using the gravitational lensing effect. Light from objects behind a large mass is distorted in its gravitational field. From the strength of this distortion the total mass along the light path can be deduced. From these observations it has been concluded that the visible matter only contributes a small fraction to the total mass of galaxy clusters (e.g. [2]). A new kind, i.e., non-baryonic dark matter is expected to exist.

Recently, the observation of two merging galaxy clusters has delivered a strong evidence for the existence of dark matter [3]. The largest contribution to the visible mass of galaxy clusters is the intracluster plasma. The observed clusters have passed through each other during the merging process. The plasma has been slowed down during this process and is now concentrated between the two subclusters (Fig. 1.1, right). The galactic cores, however, have just moved on undisturbed (Fig. 1.1, left). The shape of the gravitational field now suggests that the greater part of the mass is concentrated at the location of the galactic cores and not where the intracluster plasma is. This means that there has to be much more mass in the cluster, than the stars of galaxies and the plasma make up.

From Newtonian dynamics the rotation velocity of an object orbiting at

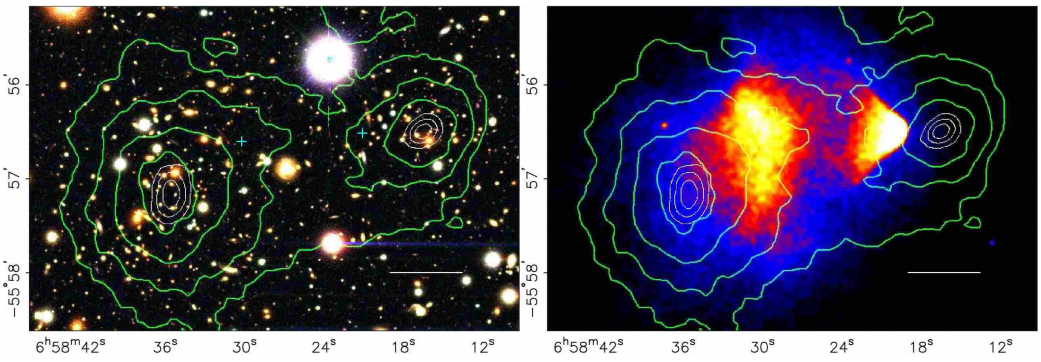

Figure 1.1: Direct evidence for non-baryonic dark matter from observations of two galaxy clusters [3]. Left: Image in the visible wavelengths. Right: X-ray observation of the intracluster plasma. The green lines indicate the gravitational field deduced from gravitational lensing.

a distance r from a galactic core is

$$v(r) = \sqrt{\frac{GM(r)}{r}} \tag{1.1}$$

where $M(r)$ is the total mass within the orbit. Thus at larger distances from the visible disc one would expect a velocity dependence $\propto r^{-1/2}$. Measurements of the rotation curves of galaxies on the other hand show a flat distribution also far away from the galactic core which cannot be explained alone with the mass of the gas orbiting the galaxy (see Fig. 1.2).

For the sake of completeness it should be mentioned, that if the rotation curves were the only observation suggesting a lack of mass, the introduction of a new kind of matter would not be the only solution to this problem. The galactic rotation curves could also be a hint for a deviation of the gravitational potential from the $1/r$ form for small accelerations. This possibility is examined by the MOND theory [5].

On cosmic scales evidence for the existence of non-baryonic dark matter can be found in the cosmic microwave background (CMB). The Wilkinson Microwave Anisotropy Probe (WMAP) [6] has mapped small temperature fluctuations in the CMB over the whole sky with an angular resolution of less than 1°. Fig. 1.3 shows the resulting map of the temperature anisotropy in the CMB. The fluctuations on the average temperature of 2.73 K are smaller than 200 μK.

The temperature anisotropy map is expanded into spherical harmonic functions Y_{lm}, yielding a power spectrum over the multipole moment l. For small l the anisotropy power is small, meaning the CMB is homogeneous over larger scales. The first maximum delivers a measure for the size of the

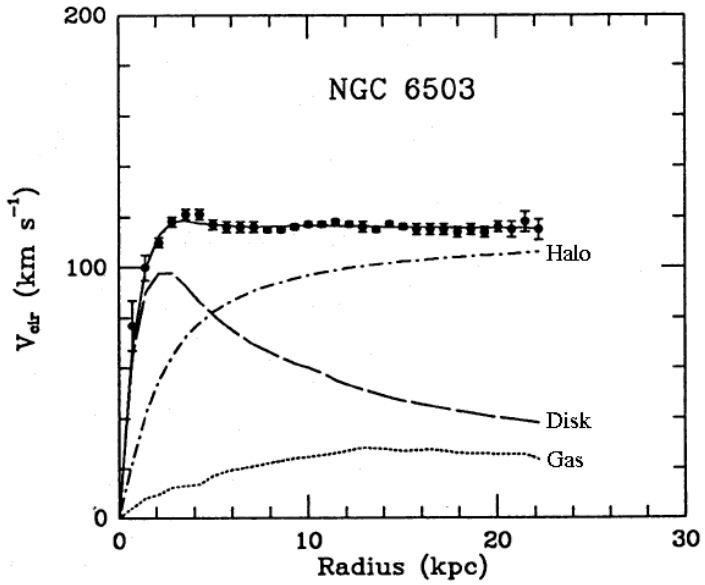

Figure 1.2: Measured rotation curve (points) of the galaxy NGC 6503 and a model fit (solid line) with contributions of the star disk, the galactic gas and a dark matter halo [4].

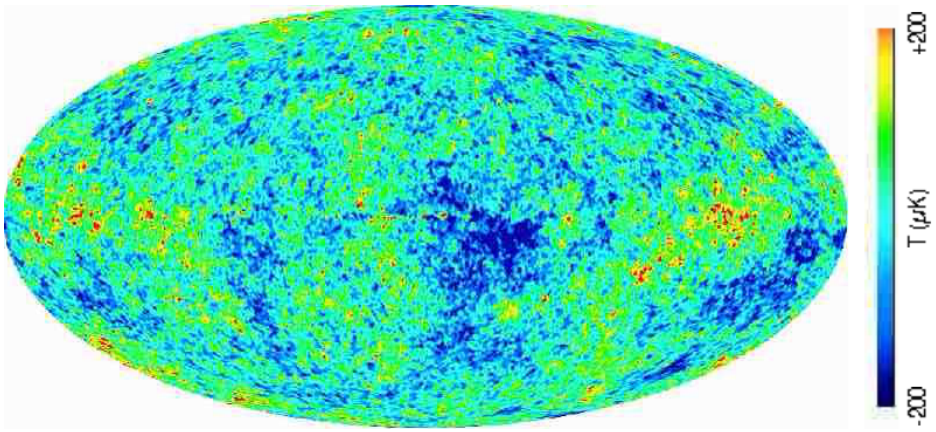

Figure 1.3: Map of the cosmic microwave background as measured by WMAP [6]. The background of the milky way has been subtracted.

temperature fluctuations in Fig. 1.3. The overall structure of the angular power spectrum can be compared with predictions of cosmological models.

The best match is found for a ΛCDM cosmology, where the universe is dominated by the cosmological constant Λ and cold dark matter. The cosmological constant, which is assigned to the unknown dark energy, accounts for more than 70% of the total density of the universe. The density of all matter accounts for $\Omega_m h^2 = 0.128 \pm 0.008$, with the reduced hubble expansion parameter $h = H_0/100 = (0.73 \pm 0.03)\,\mathrm{MPc}^{-1}\,\mathrm{km\,s}^{-1}$. However, the abundance of baryons is only $\Omega_b h^2 = 0.0223 \pm 0.0007$ [7]. The difference between Ω_m and Ω_b consists of non-baryonic particles.

1.1.2 Dark Matter Candidates

The nature of dark matter is still unknown except for the constraints that it has to be non-baryonic and has to clump on small (i.e. galactic) scales. For big bang relic particles this means that they have to be heavy as light particles would be relativistic and thus would smear out the structures found in the universe. Furthermore, the particles have to interact weakly with normal matter, otherwise they would have already been discovered. In general these generic particles are addressed as Weakly Interacting Massive Particles (WIMPs). Some of the most important candidates considered are presented below.

Neutrinos

Since the observation of neutrino oscillations it is proven [8] that neutrinos have mass. It is thus obvious that relic neutrinos contribute to the missing dark matter component of the universe. The relic density of neutrinos can be calculated as [9]:

$$\Omega_\nu h^2 = \sum_{i=1}^{3} \frac{m_i}{93\,\mathrm{eV}} \tag{1.2}$$

From the current experimental limit for neutrino mass $m_{\nu_e} < 2.05\,\mathrm{eV}$ [10] this leads to a limit for the relic density of $\Omega_\nu h^2 < 0.07$. Observations from the CMB anisotropy set an even stronger constraint of $\Omega_\nu h^2 < 0.0067$. Therefore, the three standard neutrinos cannot be the (only) dark matter particles. Due to their small mass relic neutrinos move at relativistic velocities and are thus hot cold, but not dark matter.

A proposed fourth kind of neutrino, which would only participate in mixing, but not in the weak interaction, could also be a dark matter particle. In many scenarios these sterile neutrinos would, however, be warm or hot dark

matter [11]. This would have at first formed larger then smaller structures in contradiction to the observed history of the universe. Under certain circumstances, however, sterile neutrinos could be cold or "cool" dark matter [12].

Axions

Axions are hypothetical particles introduced as solution of the so-called CP problem in theories of strong interaction. Although they are predicted to be very light ($m_A < 10^{-2}\,\mathrm{eV}/c^2$), there are scenarios where axions could be the particles making up for the cold dark matter. The coupling of axions to matter and radiation would be very weak, and due to their small mass they could not be detected in dark matter searches devoted to the search of WIMPs. A possible direct detection of axions would be possible, however, by looking for axion to photon conversion [13].

Supersymmetric Particles

Supersymmetry was introduced as a symmetry between particles and interactions. It is a possible solution to the mass hierarchy problem in particle physics. The supersymmetric model with the smallest possible field content is the miminal supersymmetric extension of the standard model (MSSM) [14].

The MSSM introduces supersymmetric partners (superpartners, sparticles) to all standard model particles and interactions differing by spin 1/2. The superpartners of quarks and leptons, the squarks and sleptons have spin 0. The superpartners of the exchange particles of the standard model interactions, e.g. the gluinos, have spin 1/2. The superpartners are denoted with the symbols of the normal particles marked with a tilde (e.g. $\tilde{g}$ for a gluino).

Standard model particles and superpartners differ by the R-parity. The former have $R = 1$ and the latter $R = -1$. Since R parity is conserved, a sparticle cannot decay into a single particle. As a consequence the lightest supersymmetric particle (LSP) is stable and a possible dark matter candidate.

One of the most likely LSPs is the lightest neutralino. The four neutralinos $\tilde{\chi}_1^0 \ \ldots \ \tilde{\chi}_4^0$ are mixtures of the superpartners of the photon, the Z^0 and the two neutral higgs bosons. The lightest neutralino $\tilde{\chi}_1^0$ is usually simply noted as χ.

Neutralinos would interact with normal matter via weak interaction. They could be detected directly by nuclear scattering, either by coherent (spin-independent) or by spin-dependent interaction. As they would be Ma-

jorana particles they would coannihilate and could thus also be detected indirectly by looking for annihilation products [15].

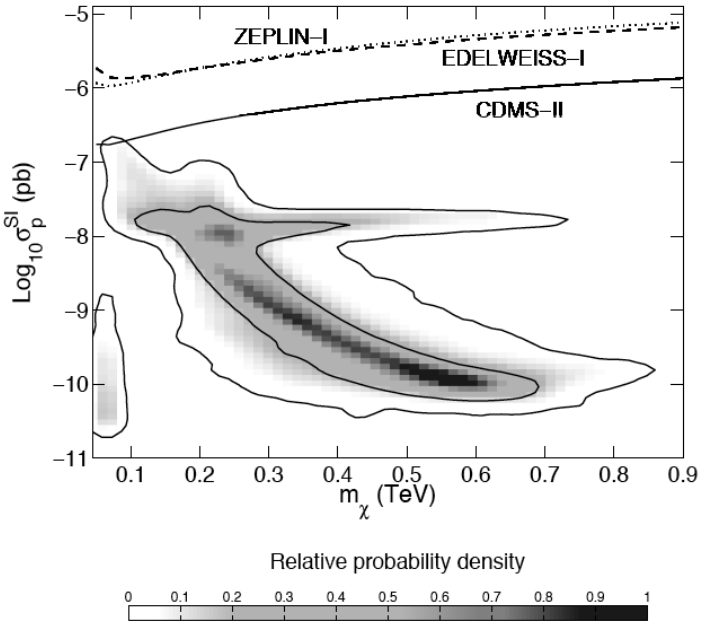

Figure 1.4: Probabilities for the neutralino mass and the spin-independent neutralino-nucleon cross section in the CMSSM [16].

The Constrained MSSM (CMSSM) sets constraints on the supersymmetric parameter space that arise from collider experiments and the predicted cold dark matter abundance. From this the most probable neutralino masses and cross sections for spin-independent neutralino-nucleon scattering can be deduced [16]. Fig. 1.4 depicts the allowed parameter space for the neutralino in CMSSM. The cross sections down to 10^{-8} pb should be reached with the current experiments, while the region down to 10^{-10} pb will be covered by the next generation experiments. If the neutralino is the dark matter particle there is a high discovery potential.

The neutralino is not necessarily the LSP, other sparticles have been considered too. The superpartner of the neutrino, for example, the sneutrino would have the right relic density if its mass is in the range between 550 and 2300 GeV. This, however, is ruled out by direct search experiments [17].

Some supersymmetric scenarios allow the gravitino to be the LSP. This particle as the superpartner of the graviton would only interact by gravitation and thus to be detected in direct searches would be very difficult [18].

Other Candidates

The particles presented above are not the only possible candidates. Examples for other candidates are Kaluza-Klein particles resulting from extra space dimensions or superheavy dark matter like Wimpzillas. For an overview over the variety of these candidates see [14] and references therein.

1.1.3 Halo Model

For the interpretation of the results of particle dark matter searches it is crucial to know how dark matter is distributed within a galaxy, particulary in our milky way. The density profile of dark matter halos is studied with N-body simulations (e.g. [19]). In general the radial dependence of the halo profile is described with functions of the form [20]:

$$\varrho(r) = \frac{1}{\left(\frac{r}{a}\right)^{\gamma}\left[1+\left(\frac{r}{a}\right)^{\alpha}\right]^{\frac{\beta-\gamma}{\alpha}}}, \tag{1.3}$$

with a characteristic radius a. The shape of the halo is determined by the exponents α, β and γ. For an isothermal spherical halo, $\alpha = \beta = 2$ and $\gamma = 0$. In this case the halo follows $\varrho \propto r^{-2}$ at large radii, as naively expected from the flat rotation curves.

The local dark matter density ϱ_D (at the location of the earth) is determined from the rotation curve of the milky way, but the obtained value depends on the assumed halo profile. For the case of an isothermal spherical halo $\varrho_D = (0.3 \pm 0.1)\,\mathrm{GeV}/c^2/\mathrm{cm}^3$ is found. However, the galactic halo may be flattened, leading to a larger spread of allowed values from $0.2\,\mathrm{GeV}/c^2/\mathrm{cm}^3$ to $0.8\,\mathrm{GeV}/c^2/\mathrm{cm}^3$ [20]. Dark matter searches generally use $\varrho_D = 0.3\,\mathrm{GeV}/c^2/\mathrm{cm}^3$ when calculating constraints on the WIMP properties.

The galactic halo does not follow the rotation of the star disk of the galaxy. The dark matter particles are assumed to follow a Maxwellian velocity distribution truncated at the galactic escape velocity.

1.2 Direct Dark Matter Detection

Direct detection of particle dark matter is attempted via observation of the scattering from nuclei of a target material. The spectrum of count rate R over the recoil energy E_R in a uniform target stationary in the galaxy is expected to be of the form [21]

$$\frac{dR}{dE_R} = \frac{R_0}{E_0 r}\mathrm{e}^{-\frac{E_R}{E_0 r}} \tag{1.4}$$

where E_0 is the most probable kinetic energy of a WIMP and r is a kinematic factor depending on the WIMP mass M_D and the mass of the target nucleus M_T:

$$r = 4\frac{M_D M_T}{(M_D + M_T)^2} \tag{1.5}$$

The factor R_0 in (1.4) defines the event rate per unit target mass:

$$R_0 = \frac{2}{\sqrt{\pi}} \frac{N_A}{A} \frac{\varrho_D}{M_D} \sigma_0 v_0 \tag{1.6}$$

where N_A is the Avogadro number $(6.02 \cdot 10^{26}\,\mathrm{kg}^{-1})$[1], A is the mass number of the target nucleus, ϱ_D the local dark matter density, σ_0 the cross section for zero momentum transfer and v_0 the rotation velocity of the galaxy at the location of the detector.

In most cases the wavelength of the momentum transfer $q = \sqrt{2M_T E_R}$ to the target nucleus is not large compared to the nuclear radius, and thus the nucleus cannot be treated as point-like. Therefore, the extension of the nucleus has to be taken into account. The basic cross section σ_0 in (1.6) has to be replaced by a cross section reduced by a nuclear form factor:

$$\sigma(E_R) = \sigma_0 \cdot |F(E_R)|^2 \tag{1.7}$$

Usually, the Helm form factor is used [22]:

$$|F(q)|^2 = \left(\frac{3j_1(qR_1)}{qR_1}\right)^2 \mathrm{e}^{-q^2 s^2} \tag{1.8}$$

with the effective nuclear radius R_1 and a skin thickness s. j_1 is the Bessel function and q the momentum transfer.

In the following spin independent coherent WIMP-nucleus scattering is considered. In this case, the cross section in (1.6) scales with a coherence factor I_c. In the simplest case, which is assumed for most WIMP candidates, this is $I_c = A^2$. σ_0 then denotes the spin independent cross section for zero momentum transfer, which can be calculated from the single WIMP-nucleon cross section σ_{WN} as

$$\sigma_0 = \frac{\mu_A^2}{\mu_1^2} \cdot A^2 \cdot \sigma_{\mathrm{WN}}, \tag{1.9}$$

with $\mu_A = M_D M_T/(M_D + M_T)$ the reduced mass for the target nucleus and μ_1 the reduced mass for $A = 1$.

[1] The Avogadro number would normally be noted as $6.02 \cdot 10^{26}\,\mathrm{kmol}^{-1}$, but in (1.6) N_A is given for $A = 1$, so it is the same per kmol and per kg.

To calculate the expected spectrum for a detector located on the earth, the motion of the detector through the halo has to be accounted for. For this two parameters are introduced in (1.4):

$$\frac{dR}{dE_R} = c_1 \frac{R_0}{E_0 r} \mathrm{e}^{-\frac{c_2 E_R}{E_0 r}} . \tag{1.10}$$

c_1 and c_2 depend on the season, leading to an annual modulation of the count rate. However, this dependence is small. For most experiments it is sufficient to use values averaged over one year of $c_1 = 0.75$ and $c_2 = 0.56$.

In total, the expected count rate per recoil energy for a target material with mass number A is:

$$\frac{dR}{dE_R} = \frac{c_1 N_A}{2\sqrt{\pi}} \frac{\varrho_D}{\mu_1^2} \sigma_{\mathrm{WN}} \left|F(E_R)\right|^2 v_0 \frac{A^2}{E_0} \mathrm{e}^{-\frac{c_2 E_R}{E_0 r}} \tag{1.11}$$

For a compound target the total count rate is calculated from the count rates for each element weighted with the respective mass fraction. For $CaWO_4$ one gets for example:

$$\left.\frac{dR}{dE_R}\right|_{\mathrm{CaWO_4}} = 0.139 \left.\frac{dR}{dE_R}\right|_{\mathrm{Ca}} + 0.638 \left.\frac{dR}{dE_R}\right|_{\mathrm{W}} + 0.222 \left.\frac{dR}{dE_R}\right|_{\mathrm{O}} \tag{1.12}$$

Fig. 1.5 shows calculated WIMP recoil spectra for materials that are used in direct dark matter search experiments. For the calculation a WIMP mass of 60 GeV is assumed, which is a typical mass for a supersymmetric neutralino. For the WIMP-nucleon cross section σ_{WN} a value of 10^{-8} pb was chosen, as this is the level of sensitivity most present experiments are aiming for. For this cross section a total count rate of $1.06\,\mathrm{kg}^{-1}\,\mathrm{a}^{-1}$ between 10 and 100 keV for germanium and $0.59\,\mathrm{kg}^{-1}\,\mathrm{a}^{-1}$ between 12 and 40 keV for $CaWO_4$ is expected.

1.2.1 Background Considerations

To reach this level of sensitivity large absorber masses, long measurement times and an ultra low background environment are essential. As these challenges are the same for all direct dark matter searches, the issue of background suppression is discussed in general before the most important dark matter experiments are briefly presented.

An important background source is cosmic radiation. Highly energetic particles (e.g. nucleons) interact in the upper atmosphere producing showers of hadrons and leptons. To reduce the exposure to this radiation, dark matter searches are set up in deep underground facilities. The shielding capability

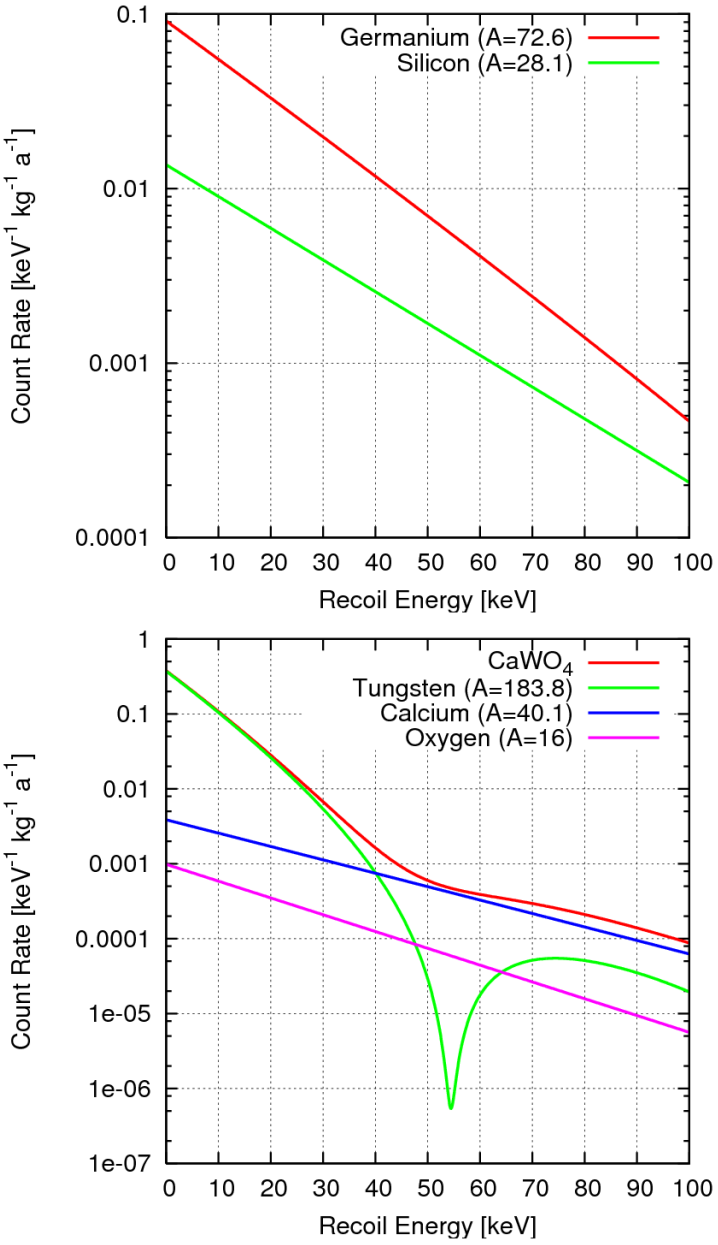

Figure 1.5: Expected WIMP recoil spectra for target materials germanium and silicon (top) (as used by CDMS and EDELWEISS) and $CaWO_4$ (bottom) (used by CRESST) for a WIMP mass of 60 GeV and a WIMP-nucleon cross section of 10^{-8} pb. For $CaWO_4$ also the contributions of the constituent elements are depicted. The strong suppression of events for tungsten around 55 keV is an effect of the Helm form factor.

of an underground site is characterized in meters water equivalent (m.w.e.). For example one meter of "standard" rock shields as much as three meters of water, accounting for 3 m.w.e. The hadrons from atmospheric showers are shielded by a few m.w.e., for an efficient reduction of cosmic muons much deeper sites are needed. The reduction of the muon flux at larger depths $h \gtrsim 1\,\text{km.w.e.}$ can be described by a simple empirical formula [23]:

$$I_\mu(h) = I_1 \mathrm{e}^{-\lambda_1 h} + I_2 \mathrm{e}^{-\lambda_2 h} + I_\mu^\nu \tag{1.13}$$

with the parameters $I_1 = 1.34{\cdot}10^{-5}\,\text{cm}^{-2}\text{s}^{-1}\text{sr}^{-1}$, $I_2 = 7.52{\cdot}10^{-7}\,\text{cm}^{-2}\text{s}^{-1}\text{sr}^{-1}$, $\lambda_1 = 2.62\,\text{km.w.e.}^{-1}$ and $\lambda_2 = 1.21\,\text{km.w.e.}^{-1}$. $I_\mu^\nu = 2.17 \cdot 10^{-13}\,\text{cm}^{-2}\text{s}^{-1}\text{sr}^{-1}$ is a constant contribution of ν_μ-induced muons, causing a saturation of the muon background at depths of $\gtrsim 11\,\text{km.w.e.}$ For obtaining the total flux at an underground site $I_\mu(h)$ has to be integrated over all directions using the amount $h = h(\phi, \theta)$ of overburden in each direction.

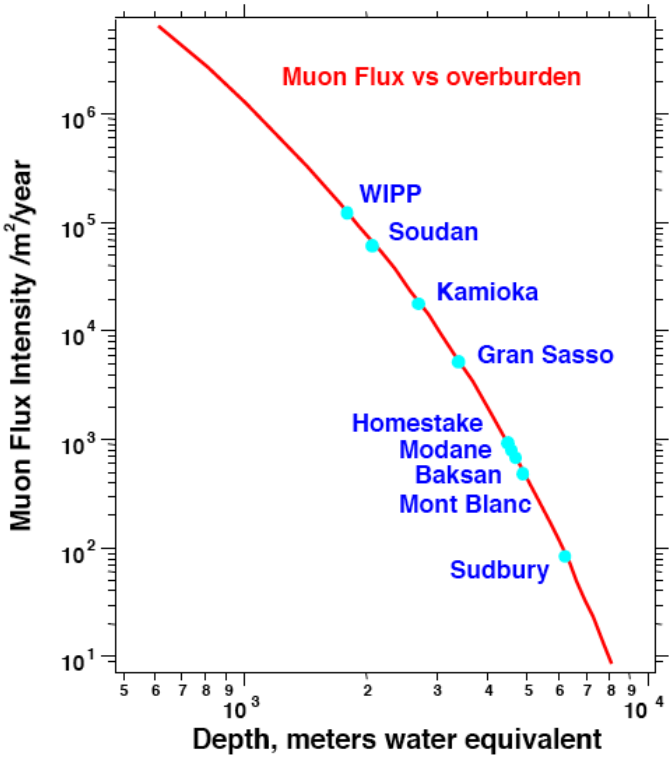

Figure 1.6: Flux of cosmic muons in dependence of overburden in meter water equivalent [24]. Some important deep underground laboratories are marked in the plot.

Fig. 1.6 shows the measured total muon flux for several important deep underground laboratories in dependence of their depth. The direct dark

matter searches discussed below are (or were) located in Soudan (CDMS), Modane (EDELWEISS) and Gran Sasso (XENON, CRESST). For the latter a total muon flux of about $1\,\mathrm{m}^{-2}\mathrm{h}^{-1}$ has been determined, a reduction by six orders of magnitude compared to the surface.

Apart from the cosmic radiation the natural radioactivity of materials in the proximity of the detector has to be kept under control. Experiments for direct dark matter search are typically equipped with a large lead shield against gamma radioactivity. Often archeological lead is used, for example from roman water pipes. This lead was cut off from the radon activity in the atmosphere for several hundred years and has thus a very low ^{210}Pb content.

All materials close to the detectors have to be carefully selected and monitored regarding their radioactive content. Parts of the experimental setup, where a certain amount of contamination cannot be avoided are usually separated from the detector volume. For example in experiments with cryogenic detectors, the cryostats needed to cool the detectors are typically set up outside the shield.

Shielding and careful selection of materials can reduce background only to a certain degree. For this reason many experiments employ techniques for identifying the kind of interaction. The most relevant count rate from background radiation is due to gammas and betas, which deposit their energy into the electron system of the absorber, while WIMPs are expected to interact with the nuclei. A discrimination of these two classes of events is possible, when two different signals are recorded, to which the energy deposited in the absorber is distributed differently for different event types.

Fig. 1.7 shows the discrimination of electron and nuclear recoils using the scintillation light from a $CaWO_4$ crystal like it is employed in the CRESST experiment (see chapter 2). The primary signal from which the information on the recoil energy is gained is the heat generated by an event. The secondary signal used for the discrimination is the scintillation light. The left plot in Fig. 1.7 shows the amplitudes of both signals for events recorded with a gamma and a neutron source. Two bands are observed, the light output for electron recoils is clearly higher than that for nuclear recoils. It is common to plot the ratio of the secondary and the primary signal versus the recoil energy (Fig. 1.7, right). This ratio or "yield" is, in first approximation, energy independent and can thus be used as a discrimination criterion. Besides light and heat the two signals can also be charge and heat (for semiconductor absorbers) or charge and light (for liquid noble gases).

Background candidates inducing nuclear recoils can not be rejected so easily. An important example for this class of events are neutron interactions. Neutrons can be classified by their energy which is connected to the production process and the location of the production within or outside of

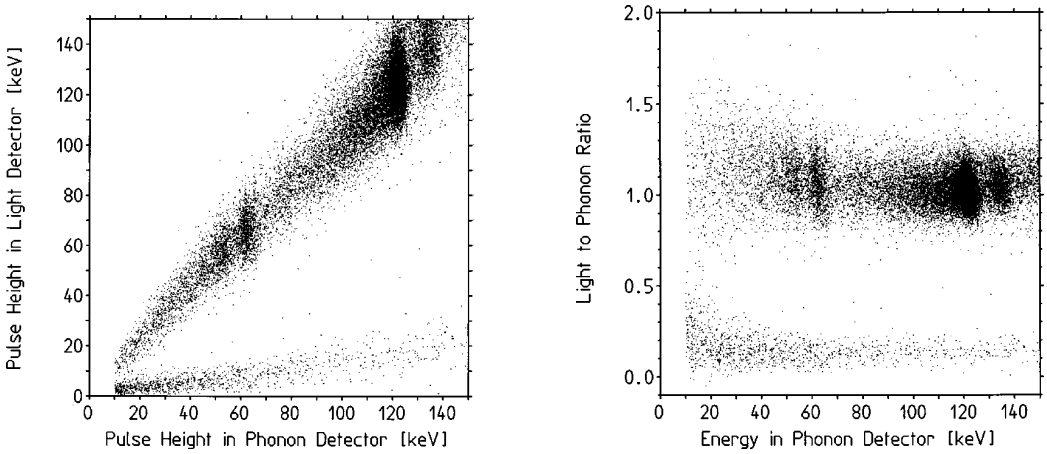

Figure 1.7: Example for the discrimination of electron recoil events caused by beta/gamma interactions from nuclear recoil events caused by neutron or WIMP interactions. Here the simultaneous measurement of the heat and scintillation light from a $CaWO_4$ crystal is used [25]. Left: Amplitudes of the signals in both detectors. Right: Ratio of light/heat versus energy (see text).

the experimental setup.

- *Low energy neutrons produced by radioactive decays in the rock or in the walls of the experimental site.* Those neutrons are produced by spontaneous fission of ^{238}U or (α, n) reactions in the rock, like $^{17}\mathrm{O}(\alpha, \mathrm{n})^{20}\mathrm{Ne}$. Their energy is below 10 MeV and thus they can be effectively moderated below the detection threshold by several centimeters of proton rich materials, e.g. polyethylene.

- *Fission neutrons in the experiment.* Fission neutrons can also originate from a ^{238}U contamination in a lead shield. This contamination is typically in the order of a few ppb. If the lead shield of an experiment is within the neutron shield, neutrons produced in it cannot be moderated before they hit the detector. In this case the ^{238}U content of the lead shield can be a limiting factor for the experiment's sensitivity.

- *Muon induced neutrons.* Neutrons of higher energies can be induced by the interactions of muons in the material. Direct production is possible via inelastic scattering of muons from nuclei:

$$\mu + \mathrm{Nucleus} \longrightarrow \mu + \mathrm{Nucleus}^* + \mathrm{n}$$

  Indirect production is possible from muon induced hadronic showers (pion-nucleus or nucleon-nucleus reactions) or from gammas (photonuclear reactions). The energy of such neutrons is up to 100 MeV. For

those high energy neutrons a neutron moderator is less efficient in reducing the event rate. However, events from muon induced neutrons produced in the inner shield can be rejected via a coincidence in a muon veto.

1.2.2 Setting Constraints on Dark Matter

In order to set constraints on the WIMP properties from observed data, an experiment for direct dark matter detection will select a window for the recoil energy where the best signal/background ratio is expected. The total count rate expected in this energy window then depends on the WIMP mass and cross section (see equation (1.11)). Therefore, an experiment that observes no or only few counts can set a limit on the cross section for a given WIMP mass. In the simplest case for each investigated WIMP mass the cross section is investigated where the probability to see more than the observed events is higher than 90%. This would exclude all higher cross sections at a confidence level of at least 90%.

However, this simple approach underestimates the sensitivity of the experiment as it neglects the shape of the spectrum. More sophisticated methods are used to set stronger constraints on the cross section. The standard method used by direct dark matter searches is the "optimum interval method" [26]. Here, not the complete energy window is used to set the limit on the cross section, but for each investigated WIMP mass the interval within the energy window is selected that sets the strongest constraint on the expected count rate.

The plots in Fig. 1.8 for the CDMS (section 1.2.3), EDELWEISS (section 1.2.4) and XENON (section 1.2.6) experiments are produced using this method. The cross sections above the plotted line are excluded at a 90% confidence level, while lower cross sections are still allowed.

1.2.3 CDMS

Presently, the leading dark matter experiment with cryogenic detectors is the Cryogenic Dark Matter Search (CDMS) [27], which is currently located in the Soudan Underground Laboratory in Minnesota (USA).

CDMS uses the simultaneous measurement of the heat and the ionisation signals induced by an event in a semiconductor absorber. As absorber materials silicon and germanium are used. A CDMS detector consists of a cylindrical crystal of 7.6 cm diameter and 1 cm thickness. On one side of the cylinder tungsten transition edge sensors (TESs) with aluminum phonon

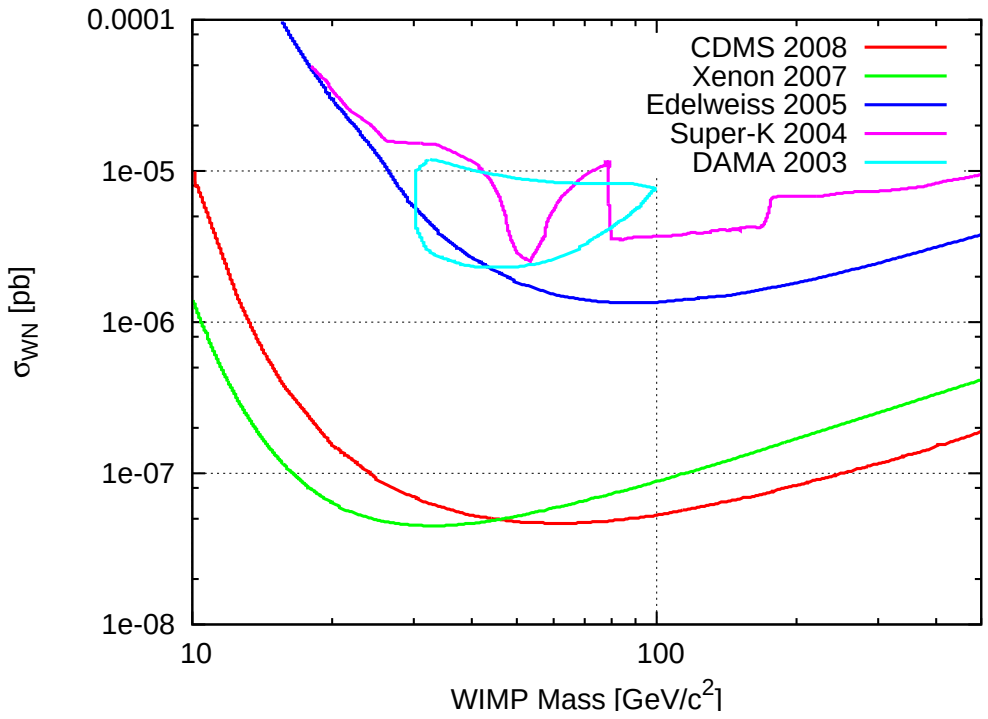

Figure 1.8: Exclusion plots for spin-independent interacting WIMPs from the experiments described in Section 1.2. The limits of CDMS, XENON and EDELWEISS are calculated by the method described in section 1.2.2. DAMA has published a positive claim. Super-K attempts to detect WIMPs indirectly.

collectors (see chapter 3) are superimposed with which the heat signal is detected. For the ionisation signal there are electrodes on the other side of the crystal.

The discrimination between electron and nuclear recoils can be achieved by calculating the ratio $Y = E_{\text{Ionisation}}/E_{\text{Heat}}$ of the measured signal in the heat and the ionisation channel. This ratio is approximately a factor of 3 lower for nuclear recoils than for electron recoils.

The experiment is set up in the Soudan Underground Laboratory in a depth of 780 m thus providing a shielding of 2090 meters water equivalent (m.w.e.) against cosmic radiation. This reduces the flux of cosmic muons by a factor of $5 \cdot 10^4$. For a further reduction of the background the detectors are surrounded by several layers of passive and active shielding (see Fig. 1.9).

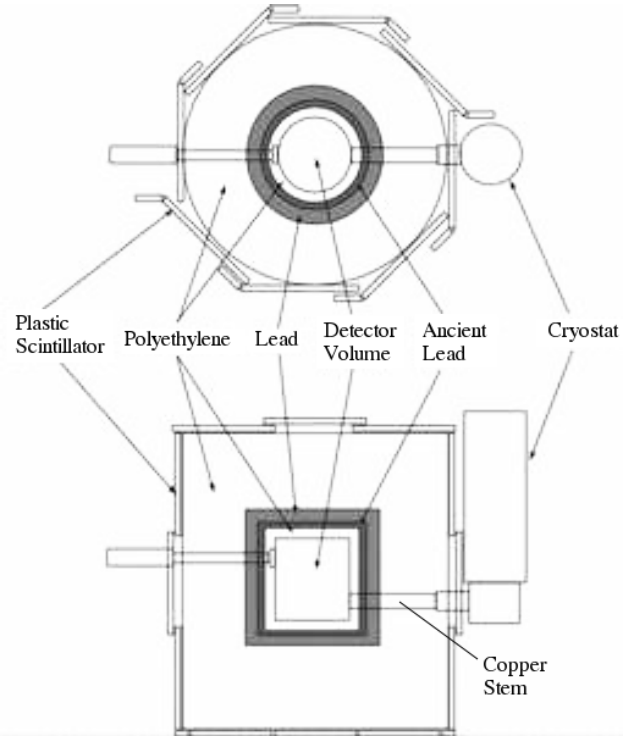

Figure 1.9: Schematic view of the CDMS-II shielding and veto [27]. The detector volume (the "icebox") is connected to the cooling stages of the cryostat via a copper stem (the "cold stem"). The components of the shielding are (from outside to inside): Muon-veto (plastic scintillator), neutron moderator (polyethylene), gamma shield (lead) and more neutron moderator for neutrons produced in the shield.

The detectors are located in an "icebox" inside this shielding. This icebox consists of several copper shields which are coupled via a "cold stem" to the

various temperature stages of a ^{3}He/^{4}He dilution refrigerator. The copper is ultra pure copper and acts as an additional shield against radiation. The icebox contains a holder structure for 7 "towers" of 6 detectors each coupled to the mixing chamber of the cryostat where the detectors are cooled to their operation temperature of 50 mK. As a typical germanium detector has a mass of 250 g and a silicon detector a mass of 100 g the experiment can have up to 10.5 kg of germanium as target (or 4.2 kg of silicon). In practice there are always detectors of both materials installed, as this provides a means to identify neutron background events.

The CDMS detector design allows a three-dimensional reconstruction of the event location and thus the rejection of surface events [28]. This results in a reduced fiducial mass for the dark matter analysis.

In mid-2004 CDMS performed a dark matter run with six germanium and six silicon detectors distributed over two towers [29]. Later the experiment was upgraded and operated with five detector towers [30]. From the combined data of these runs a 90% C.L. limit for the WIMP-nucleon cross section of $\sigma_0 < 4.6 \cdot 10^{-8}$ pb for a WIMP mass of 60 GeV could be set (see Fig. 1.8).

With the current setup CDMS aims for a sensitivity of σ_0 down to a level of 10^{-8} pb. Further improvement is planned for the future version of the experiment, SuperCDMS [31], which is supposed to reach a level below 10^{-10} pb. This ton-scale experiment is planned to be set up at SNOLab which is located at greater depth than the Soudan Underground Laboratory and thus providing an even better shielding against cosmic radiation. The increase in mass from about 10 kg today up to several hundred kg is to be achieved by increasing the number as well as the size of the detectors. Improved shielding, enhanced veto methods and improved discrimination techniques should help to remove almost all background and thus to increase the sensitivity into the desired region.

1.2.4 EDELWEISS

The French-German EDELWEISS (=Expérience pour Détecter les WIMPs en Site Souterrain) experiment [32] also uses the simultaneous measurement of heat and ionization in a semiconductor target to discriminate between electron and nuclear recoils.

An EDELWEISS detector [33] consists of a 320 g germanium crystal shaped as a beveled cylinder of 70 mm diameter and 20 mm height. For the charge collection two aluminum electrodes are sputtered onto the two sides of the crystal. The heat signal of an event is measured with a Neutron Transmutation Doped germanium crystal ("NTD") glued onto the absorber crystal.

The completed phase I of the experiment was set up in the Laboratoire Souterrain de Modane in the Fréjus tunnel in the French-Italian alps. This site provides 4800 m.w.e. shielding against cosmic radiation.

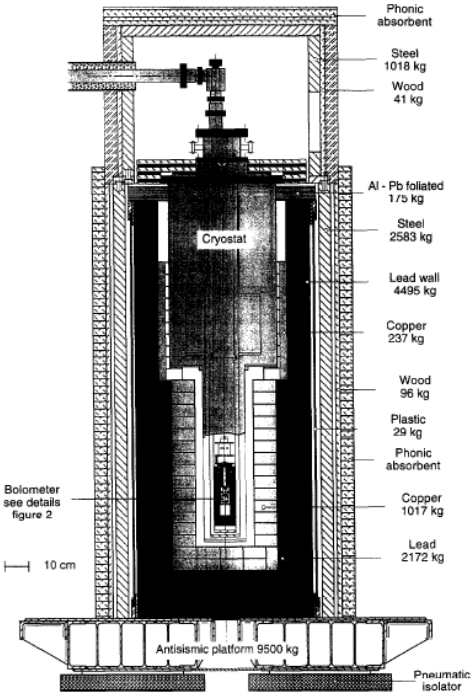

Figure 1.10: Set up of the EDELWEISS-I experiment [34].

Up to three detectors were mounted in a low-background dilution refrigerator [34] where they were cooled to their operation temperature below 30 mK. The cryostat was shielded against gamma background by 10 cm of copper and 15 cm of lead (see Fig. 1.10). 30 cm of paraffin served as neutron moderator. The volume between shielding and cryostat was flushed with pure nitrogen to reduce radon contamination.

With this setup several data taking runs with intermediate change of detectors were performed between the years 2000 and 2003, collecting a total net exposure of 62 kg d. The 90% C.L. upper limit for the WIMP-nucleon cross section from this data was set at about $1.5 \cdot 10^{-6}$ pb for WIMP masses around 80 GeV (see Fig. 1.8). This result was limited by the background of the experiment, so that an increase of exposure could not improve the sensitivity.

After the completion of EDELWEISS-I the experiment was upgraded to its present stage EDELWEISS-II [35]. A new cryostat with a larger experimental space was set up in the Modane laboratory providing room for more

than 100 detector modules and thus an overall target mass of more than 30 kg. Neutrons are now moderated by 50 cm of polyethylene and a muon veto has been installed. With this setup a first phase with 28 detectors was started in 2006. Eventually, EDELWEISS-II aims for a sensitivity in the range of 10^{-8} pb.

Gamma events close to the detector surface are a potentially harmful background also for the EDELWEISS experiment. Two approaches to address this issue are being investigated, one is to improve the charge collection by using layers of amorphous silicon underneath the electrodes or thicker electrodes. The other approach is to replace the NTD thermistors with NbSi sensors evaporated directly onto the absorber crystal [36]. Those sensors provide the potential to identify events close to the surface by pulse shape analysis.

To reach a sensitivity level of 10^{-10} pb the members of the EDELWEISS collaboration are working together with the CRESST collaboration and other European groups to plan EURECA [37], a ton-scale cryogenic dark matter search in Europe (see also section 2.6).

1.2.5 DAMA/LIBRA

The DAMA experiment plays a special role within the direct matter searches. It has realized several setups, namely DAMA/NaI with 100 kg of highly radiopure NaI, DAMA/LXe with liquid xenon and DAMA/LIBRA with 250 kg of highly radiopure NaI [38].

A DAMA/NaI detector module consists of a 10 kg NaI scintillating crystal coupled to two photomultipliers. In total 10 of those detector modules have been operated in the Gran Sasso underground laboratory in Italy.

The signal, the experiment is looking for, is an annual modulation of the count rate in the detector which would be caused by the motion of the earth around the sun. The expected count rate depends on the velocity of the detector with respect to the WIMP halo. This velocity formed by rotation of the galaxy is superimposed with the motion of the earth around the sun. In June the velocities of galaxy and earth are summed up resulting in a higher expected count rate, in December the total velocity is minimal as is the count rate. As this modulation effect is small compared to the total expected count rate, a large mass and exposure time is needed in order to observe this effect.

Over a period of seven years DAMA/NaI has collected a total exposure of 107.8 t d. For the analysis all counts in energy windows from 2 to 4, and 6 keV recoil energy are considered. In all these windows a modulation of the signal with a period of 365.36 days has been observed [39] (see Fig. 1.11). This is claimed to be a positive signal for the existence of the dark matter

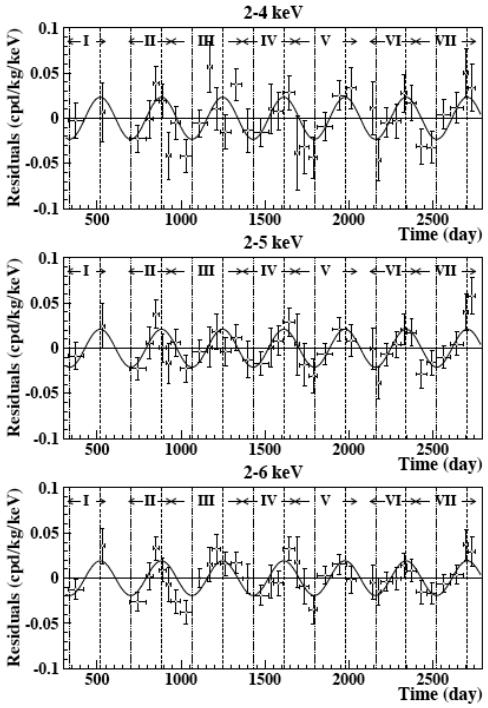

Figure 1.11: Annual modulation as observerd by DAMA/NaI [39].

halo.

The interpretation of this observation depends on the model for the halo and the WIMP that is considered. For example for a purely spin-independent interacting WIMP forming a triaxial halo with the earth on the major axis [40], maximal ϱ_D and $v_0 = 170\,\mathrm{km/s}$, the result is in agreement with a WIMP mass of $m_W = 74^{+17}_{-12}\,\mathrm{GeV}/c^2$ and a cross section $\sigma_{\mathrm{SI}} = (2.6 \pm 0.4) \cdot 10^{-6}\,\mathrm{pb}$. Using the standard assumptions for the galactic halo the annual modulation suggests a WIMP mass of $m_W = 74^{+17}_{-12}\,\mathrm{GeV}/c^2$ and a WIMP-nucleon cross section of $\sigma_{\mathrm{SI}} = (7.2^{+0.4}_{-0.9}) \cdot 10^{-6}\,\mathrm{pb}$ [41]. Although this result has been excluded meanwhile by results of other direct searches like CDMS, EDELWEISS or XENON, it is still used as a landmark for WIMP search experiments (see Fig. 1.8).

DAMA has upgraded its NaI-setup to 25 modules and thus a total mass of 250 kg. Data taking is ongoing and results are expected to be published soon.

1.2.6 Liquid Noble Gases

A different approach for direct detection of dark matter is the use of liquid noble gases as target instead of solid state detectors. Examples for this type of experiments are WARP [42] with liquid argon or ZEPLIN [43] and XENON [44] with liquid xenon as target material. The discrimination of electron and nuclear recoils is realized by the simultaneous measurement of the scintillation light and the charge produced by an event in the liquid noble gas absorber. Again, as for cryogenic detectors, the ionisation yield for nuclear recoils is reduced compared to electron recoils.

Compared to cryogenic detectors, liquid noble gas setups are simpler as for cooling the gas only a liquid nitrogen stage is necessary. For this reason, large scale setups are expected to be realised in relatively short time at comparably low costs. However, the discrimination of electron and nuclear recoils from the ratio Ionization/Scintillation is less efficient than from the ratio Ionization/Heat or Scintillation/Heat. In the relevant energy region for dark matter search there is an overlap of the electron and the nuclear recoil band in liquid noble gas experiments so that not all nuclear recoil events can be identified unambiguously (see Fig. 1.12, right).

The most successful liquid noble gas experiment so far is the XENON experiment. The XENON detector (see Fig. 1.12, left) is realised as a two phase time projection chamber (TPC) with liquid xenon as the target and a volume of xenon gas on top of it for detecting the ionization signal. An event in the liquid phase produces a flash of scintillation light and free charge carriers. The latter are drifted through a high-voltage field through the liquid phase into the gas phase where they induce a second light pulse [45]. The light signals are detected by arrays of photomultiplier tubes on top and bottom of the xenon chamber.

The photomultiplier arrays enable the reconstruction of the lateral position of the event from the primary scintillation signal (S_1), the vertical position can be deduced from the time delay between primary and secondary signal (S_2). This way a three dimensional reconstruction of the event location in the LXe volume is possible and thus a cut on an inner fudicial volume can be set thus reducing the background originating from external gammas.

A prototype detector with 15 kg of xenon (XENON10 [46]) was set up and operated in the Gran Sasso underground laboratory. For the detection of the primary scintillation light 41 PMTs were installed at the bottom of the LXe volume, for the secondary light 48 PMTs were positioned above the gas phase. The charge was drifted by a field of 0.73 kV/cm applied through the liquid. The position reconstruction was possible on a millimeter scale. The detector was shielded with 10 cm of PE and 10 cm of lead against neutrons

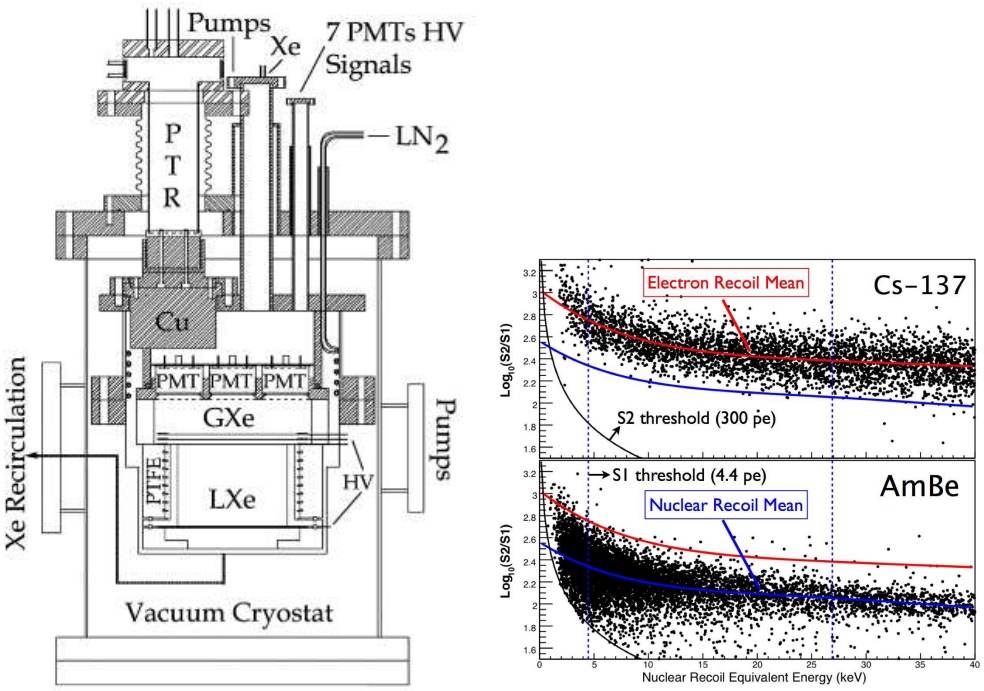

Figure 1.12: Left: Schematic of the XENON10 prototype dectector [44] (without shielding). Right: Ratio of secondary/primary scintillation light for a measurement with a gamma source (top) and a neutron source (bottom).

and gammas from outside. No muon veto was installed.

During the winter 2006/2007 XENON10 collected data with a total life time of 58.6 days. After volume cuts a fiducial mass of 5.4 kg is considered for dark matter analysis. For discrimination of electron and nuclear recoils the ratio S_2/S_1 of the two scintillation light signals is used. As the two bands overlap over the whole analysis window from 4.5 to 26.9 keV nuclear recoil energy (see Fig. 1.12, right), only the lower half of the nuclear recoil window is considered. This reduces the detector efficiency to 50%.

In the analysis window 10 events remain, 5 of those are considered to be statistical leakage from the electron recoil band (7 leaked events were expected for this exposure time). Also the other 5 events are explained either as noise fluctuations or detector artefacts. However, for the calculation of the dark matter limit all 10 events were treated as WIMP candidates. The sensitivity the experiment achieved this way is at $4.5 \cdot 10^{-6}$ pb for a WIMP mass of $30\,\mathrm{GeV}/c^2$ which is presently the best value (see Fig. 1.8).

XENON now plans to increase the detector mass up to the ton scale. This should be achieved by constructing 10 detector modules of ~ 100 kg active mass each. With this mass the experiment is expected to reach a sensitivity in the range of 10^{-10} pb.

1.3 Indirect Dark Matter Detection

Apart from direct detection, WIMPs could also be detected indirectly by looking for products from WIMP coannihilations. These coannihilations would occur in regions of increased WIMP density, for instance where WIMPs are captured by massive objects.

When a massive object moves through the galactic halo, there is a small probability for a WIMP to scatter off nuclei in the object. They can then lose enough energy to be bound in the object's gravitational field, subsequent scattering processes will then lead to an aggregation of WIMPs in the object's center. With rising WIMP density the coannihilation rate will rise to the point where capture and annihilation are in equilibrium.

The only annihilation products that can leave a large massive object are neutrinos, which in turn could eventually be detected in a neutrino detector. For an earth bound detector sources leading to a reasonable flux are the earth itself [47], the sun [48] and possibly our galactic center. However, for the latter the capture processes are highly uncertain due to the unsufficient knowledge of the halo profile in the galactic center.

The Super-Kamiokande experiment in Japan [49] is a 50 kt water Cherenkŏv detector for neutrino detection. Neutrinos are detected by the obser-

vation of the Cherenkŏv light from charged particles produced in neutrino interactions. The angular resultion of the detector is about 1° [50]. With this resolution it is possible to look for an excess of neutrino induced muons from the direction of possible WIMP annihilation centers above the dominant background from atmospheric neutrinos.

Such an excess was looked for in the Super-Kamiokande data collected between April 1996 and July 2001 for the directions of the center of the earth, the sun, as well as the galactic center. No significant signal above the background was observed for any of these potential WIMP annihilation centers. From the lack of a positive signal from the earth and the sun a limit for the spin-independent WIMP-nucleon cross section could be deduced [51], which is comparable to the last results of EDELWEISS and CRESST (see Fig. 1.8 and Fig. 2.12).

Chapter 2

The CRESST Experiment

The CRESST (=Cryogenic Rare Event Search with Superconducting Thermometers) experiment aims at the direct detection of WIMPs with cryogenic detectors consisting of large absorber crystals equipped with tungsten transition edge sensors (TESs). In the original configuration (CRESST-I) sapphire crystals with a mass of 262 g were used as absorbers. Four of these crystals could be installed and operated in the CRESST cryostat located in the Gran Sasso underground laboratory. Thanks to the low energy threshold of the detectors of about 500 eV and the low mass of the target nuclei the experiment offered an especially good sensitivity for low WIMP masses. In 2001 a data set of 138 h was used to set then the best constraints for the WIMP-nucleon cross section for WIMP masses below 5 GeV [52].

As the single channel sapphire detectors provided no discrimination possibility between electron and nuclear recoils, the sensitivity of CRESST-I was limited by the dominant background from betas and gammas. In the experiment's second phase the sapphire detectors were replaced by two-channel detectors with scintillating absorbers and a separate light detector. With this concept it was possible to reject the beta/gamma background. The new detector design was successfully tested in several prototype runs in 2003/2004 [53].

From 2004 until 2006 the CRESST setup was undergoing a major upgrade phase after which the cryostat can accommodate a larger number of detectors and therefore a higher total target mass (up to 10 kg). Furthermore, the shielding of the experiment was improved by adding 45 cm of PE and an active muon-veto. Since autumn 2006 the new setup is cold and taking data. With the current setup CRESST aims to reach a sensitivity for the spin-independent WIMP-nucleon cross section in the range of 10^{-8} pb.

2.1 Detectors With Phonon-Light Discrimination

For the second phase of CRESST detectors with simultaneous measurement of the heat and the scintillation light induced by an event in an absorber crystal have been developed [25]. As scintillating absorber $CaWO_4$ was chosen. It contains a heavy nucleus (tungsten), which makes it a good target for spin-independent coherent WIMP interactions.

The crystals employed in the experiment are cylindrical $CaWO_4$ single crystals of 40 mm diameter and 40 mm height with a mass of ~ 300 g equipped with tungsten transition edge sensors (TESs) directly evaporated onto them. With the TES the heat signal induced by an event is detected, delivering the primary information about the deposited energy. This part of the detector module is referred to as the "phonon detector".

For the detection of the scintillation light cryogenic light detectors also with tungsten TESs are used. The absorber crystals for the light detectors are either $30 \times 30 \times 0.4\,\mathrm{mm}^3$ silicon wafers or sapphire discs of 40 mm diameter coated with silicon on one side ("SOS": silicon on sapphire).

Phonon and light detector are mounted together in a copper housing. The inner surfaces are covered with a highly reflective scintillating polymeric foil for efficient light collection. Fig. 2.1 depicts a schematic drawing of the detector setup.

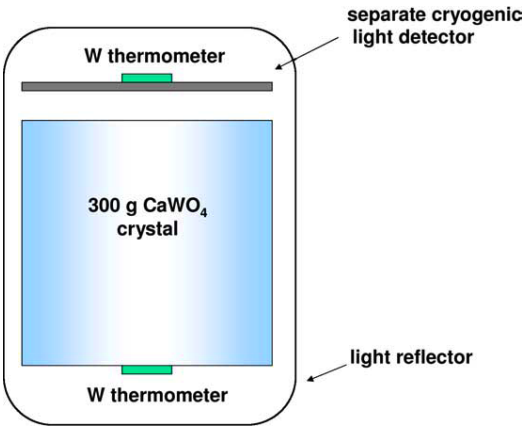

Figure 2.1: Schematic drawing of a CRESST-II detector [53]. The phonon detector, consisting of a $CaWO_4$ crystal with W TES, is mounted together with a cryogenic light detector in a reflectiv housing.

It is common to characterize the light output of an event by its "light

yield" Y defined as

$$Y = \frac{\text{Signal Amplitude in Light Detector}}{\text{Signal Amplitude in Phonon Detector}}. \tag{2.1}$$

Y is usually normalized to 1 for electron recoil events. For other event classes, like alphas or nuclear recoils from neutron or WIMP interactions, the light yield is reduced. The reduction of the light yield is expressed by the quenching factor $Q = 1/Y$.[1]

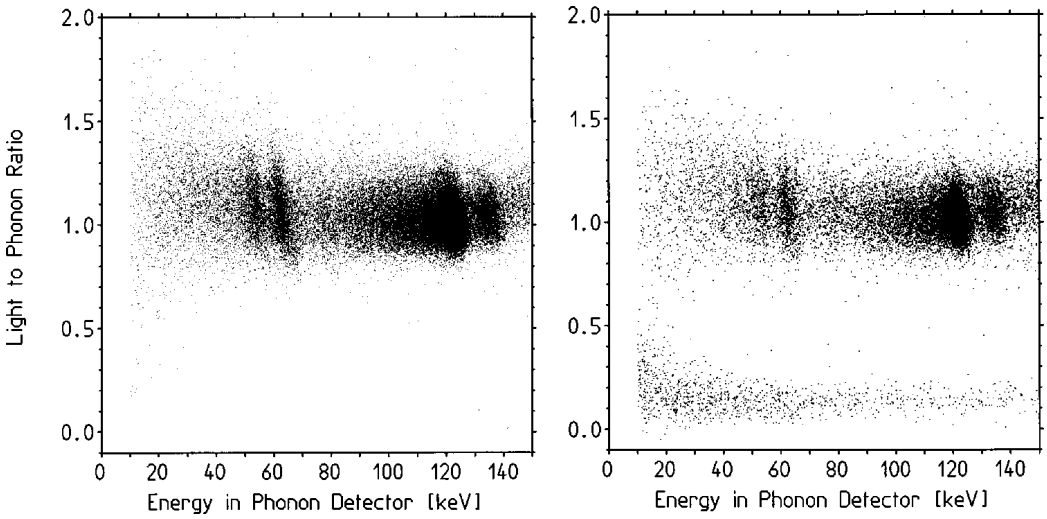

Figure 2.2: Light yield versus phonon energy from measurements with a ^{57}Co gamma source (left) and additionally a neutron source (right) performed with one of the first 6 g phonon-light test detectors [25].

Fig. 2.2 shows an early measurement with a 6 g prototype $CaWO_4$ detector demonstrating the different response to gamma and neutron sources. The scintillation light for neutron induced nuclear recoil events in this case was quenched by a factor of 7.4 compared to electron recoils of the same energy [25]. This allows an effective suppression of background from gamma and beta events down to low energies.

No degradation of the scintillation light for events close to the surface has been observed yet, contrary to the ionization yield of CDMS or EDELWEISS detectors. Thus, surface beta or gamma events can be rejected with the same efficiency as bulk events.

[1]This is the definition of the quenching factor that is common within the CRESST collaboration and will be used throughout this thesis. In other places the definition of the quenching factor is identical with the definition of Y given in the text.

2.2 CRESST Setup

The Gran Sasso underground laboratory where the CRESST experiment is set up provides a shielding of 3600 m.w.e. against cosmic rays. The detectors are cooled by a 1 mW ^{3}He/^{4}He dilution refrigerator to their operating temperature at $\sim$ 10 mK (See Fig. 2.3). To avoid exposing the detector to the natural radioactivity originating from the cryostat materials they are installed in a separate volume made of radiopure copper, the "cold box", where they are thermally coupled via a copper rod, the "cold finger", to the mixing chamber. The cold box itself consists of several copper shields thermally coupled to the various temperature stages of the cryostat to minimize the heat load on the detectors. The cryostat is capable of carrying a payload of 100 kg.

Until 2004 the cryostat was equipped with SQUIDs and electronics for the operation of four single detectors, or two two-channel detectors. Thereafter the system was replaced by a new setup with 66 SQUID channels with custom electronics [54] thus enabling to read out of up to 33 phonon-light detector modules. A new detector holder for 33 detector modules was designed and installed successfully in the cold box. CRESST can now be run with $\sim$ 10 kg of $CaWO_4$.

The original shielding of the experiment consists of a two layer shield against gamma radiation. It is made of copper and lead with a total mass of about 30 t enclosing the cold box. An internal lead shield in the line of sight of the detectors from the top of the refrigerator ensures shielding against the unavoidable internal radioactivity of the cryostat's components. The lead and copper shields are surrounded by an air-tight stainless steel box, the so-called radon box, flushed with cold nitrogen (boiled off from the liquid) and kept under a slight overpressure to keep radon activity away from the proximity of the detectors. As the electronics for the operation and read out of the detectors is very sensitive to electromagnetic interference the whole setup is placed in a Faraday cage.

During the upgrade process also the shielding of the experiment was improved (see Fig. 2.4). The outer layer now consists of a 45 cm thick polyethylene neutron moderator against neutron activity from the surrounding rock. In addition, plastic scintillator panels acting as muon veto have been installed, enclosing the whole radon box except for the area, where the cryostat feedthrough is located. Myons going through this hole should be seen in the bottom panels though.

The energy calibration of the detectors is performed with a ^{57}Co source. This has to be brought inside the lead shielding close to the cold box without opening the radon box. For that purpose a new transport mechanism for

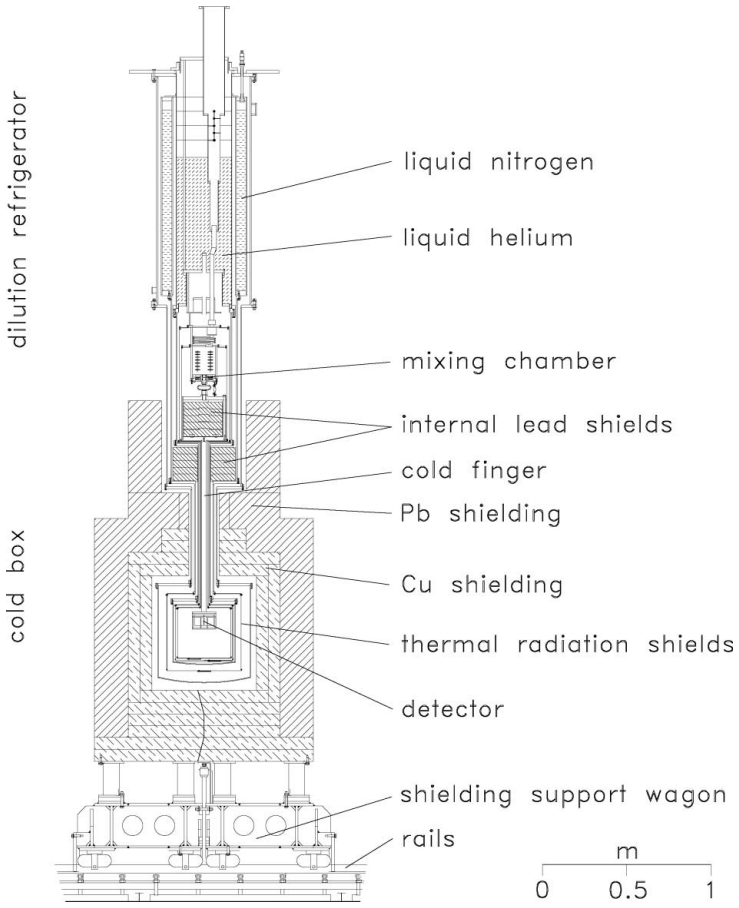

Figure 2.3: Drawing of the CRESST cryostat with the shielding status before the upgrade [52]. The cryostat and the first-stage read-out electronics (not shown) are installed together in a Faraday cage (see Fig. 2.4).

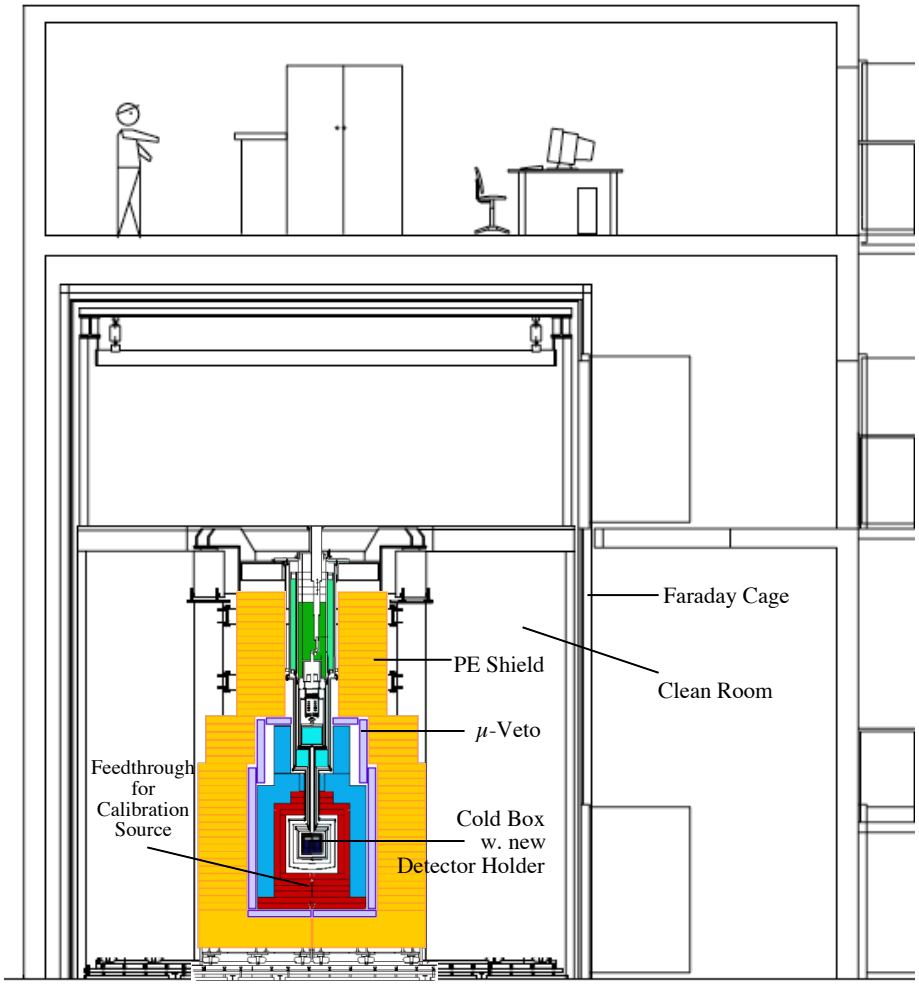

Figure 2.4: Cut through the CRESST building at the LNGS with the upgraded cryostat's shielding. The Faraday cage housing the cryostat is accessible at two floors. The lower floor, where the detectors and the shielding are located, is a class 100 clean room [52]. In the upper floor of the cage the electronics for the detectors is located. Refilling of cryoliquids is also performed from the upper floor, without the need to enter the clean room. The computers for the data aquisition are located in the top floor of the building.

calibration sources was developed and installed (see chapter 7.2).

2.3 Background

As oxygen and calcium represent light nuclei in comparison to tungsten, the dominant contribution to the WIMP signal is expected to arise from tungsten according to the A^2-scaling of the cross section (see Fig. 1.5). In more than 95% of the events the energy transfer will be less than 40 keV. Thus it is reasonable to set an upper energy threshold for the WIMP search at this energy. CRESST is expected to be able to detect WIMPs with a cross section σ_{WN} of 10^{-8} pb, which means a count rate of less than one count per kg and year. As a consequence the background of the experiment has to be known very well and rejected as efficiently as possible. For a general discussion of background issues see section 1.2.1. In the following the special case of the CRESST experiment is discussed.

- *Beta/Gamma background.* The background originating from betas or gammas, can be well discriminated from nuclear recoils, via the light yield. The discrimination is limited by the resolution of the light output of the crystals. Typical detector modules show a good separation with an effiency of more than 99.7% down to 12 keV recoil energy. This sets the lower boundary of the energy window used for dark matter search.

- *Neutron background.* The neutron background in CRESST has been studied with Monte Carlo simulations [55]. Fig. 2.5 shows the simulated recoil spectra expected in the $CaWO_4$ detectors for neutrons from different origins. The largest flux is from low energy neutrons produced by radioactive decays in the rock or in the concrete walls around the experimental hall of the Gran Sasso laboratory. Those neutrons can be moderated below the detection threshold with the experiment's PE shielding (See lines (a) and (b) in Fig. 2.5). The flux of these neutrons depends on the water content of the hall's concrete as wet concrete acts as a neutron moderator to a certain degree. Calculations for the worst case of dry concrete predict an event rate of 69 counts per kg and year between 15 and 25 keV recoil energy without PE shielding. The shielding would reduce this to $6 \cdot 10^{-3}$ counts per kg and year [56].

  The fission neutrons originating from a ^{238}U contamination in the lead shield cannot be moderated before they reach the detector as unfortunately there is no moderator between the lead shield and the cold box. Thus, the ^{238}U content of the lead shield can be a limiting factor for

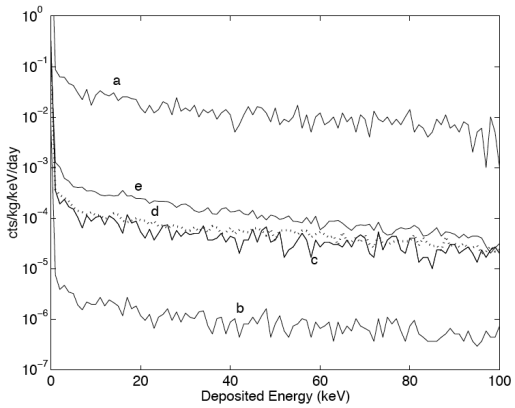

Figure 2.5: Simulated neutron spectra in a $CaWO_4$ detector for neutrons from different origins: (a) Low energy neutrons from the rock and concrete surrounding the experimental hall without neutron moderator around the experiment, (b) the same after adding 50 cm PE, (c) low energy neutrons from ^{238}U contamination in the Pb shield, and high energy neutrons induced by muons in the rock (d) or in the experimental setup (e) [56].

the experiment's sensitivity. Line (c) in Fig. 2.5 depicts the expected recoil spectrum for the optimistic case of 0.1 ppb ^{238}U concentration.

Due to their high energies muon induced neutrons from the rock are less efficiently moderated by the PE shield. According to the Monte Carlo simulations a 50 cm PE moderator only reduces the event rate in the detectors by one order of magnitude [55, Fig. 4.9]. However, events from muon induced neutrons produced in the inner shield can be rejected via a coincident event in the muon veto.

- *Surface alpha decays.* A potentially harmful background is due to recoiling nuclei from surface alpha decays, mainly from surface ^{210}Po contamination, which is a radon daughter. In half of the alpha decays on surfaces facing the $CaWO_4$ crystal or on the crystal surface itself the alpha particle moves away from the crystal and so the daughter nucleus receives a momentum towards the crystal. Depending on the decay location these events can induce nuclear recoil-like events also with energies less than 40 keV, thus limiting the experiment's sensitivity. For a detailed discussion of this background along with calibration measurements performed in the scope of this thesis see chapter 7.1.

- *Phonon only events.* Due to the different thermal contraction of the absorber crystal and the materials of the holder the crystal can suffer under mechanical stress when cooled down. This stress can lead to

micro-fractures of the crystal leading to phonon signals in the TES similar to pulses from particle interactions but without scintillation light. In early runs of CRESST I with sapphire detectors these fracture processes were the limiting factor of the experiment [57]. In order to reduce the mechanical stress of the crystals and thus the background of these "phonon only" events the originally very stiff suspensions of the crystals have been replaced by $CuSn_2$ clamps, which adjust to the thermal contractions and still sufficiently fix the crystal at its position.

2.4 Quenching Factors

Most neutron events in the relevant energy window between 10 and 40 keV are due to scattering off oxygen. On the other hand, the WIMP events in this energy window are expected to be mainly scatterings off tungsten nuclei in the $CaWO_4$ crystals (see Fig. 1.5). Thus, the identification of the recoiling nucleus would help to discriminate the neutron background from a possible WIMP signal. This can be achieved by measuring the quenching of the scintillation light, which depends on the nucleus. There are several approaches to measure the quenching factors for the elements in $CaWO_4$.

2.4.1 Time-of-Flight Mass Spectrometer

Assuming that there is no difference in the light yield for surface and bulk events with the same energy, the crystal's response to ions coming from outside with a given energy should be the same as to recoils in the bulk induced by neutrons or WIMPs. Thus, the measurement of the scintillation light of a crystal that is bombarded with ions of a fixed energy should make it possible to deduce the quenching factors for the elements in the crystal, and – as one is not restricted to the constituents of the scintillator – for any other element. Such a measurement is realized with a time-of-flight mass spectrometer (TOF-MS) set up at the Max-Planck Institut für Physik in Munich [58].

Fig. 2.6 shows a schematic drawing of the experimental setup of the TOF-MS. The ions are produced in a Laser Desorption/Ionisation (LDI) ion source. In the LDI a target of the desired material is irradiated with a pulsed laser, producing a number of ions small enough that, on average, less than one per pulse reaches the target $CaWO_4$ crystal. The ions are accelerated by a high voltage of up to 18 kV. In the main chamber of the TOF-MS ions of the desired mass and energy are selected. After passing the TOF chamber the ions hit the target $CaWO_4$ crystal, which is optically coupled

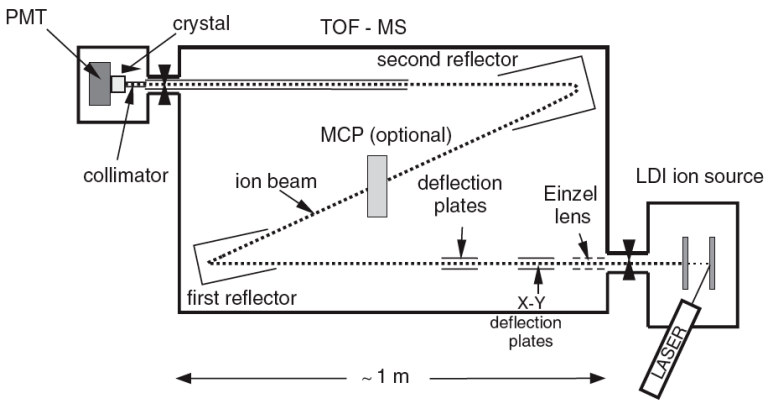

Figure 2.6: Setup for the quenching factor measurement with a time-of-flight mass spectrometer [58]. Ions are produced and accelerated in the LDI ion source. In the time of flight mass spectrometer (TOF-MS) ions of the desired mass and energy are selected and finally shot into the target $CaWO_4$ crystal. The resulting scintillation light is then detected in a PMT.

to a photomultiplier tube (PMT).

The light output is determined by counting the photons of an event and then comparing the result with a reference measurement performed with an ^{55}Fe source. From the distribution of the arrival time of the photons of all events for a given ion the shape of the scintillation curve of $CaWO_4$ can be determined. Two decay times of $\tau_1 = 1.08\,\mu$s and $\tau_2 = 7.96\,\mu$s have been found.

Measurements with the TOF-MS have been performed with targets in the mass range from hydrogen ($A = 1$) up to gold ($A = 197$). The results for the quenching factors obtained are depicted in Fig. 2.7. They can be summarized by the following rule: The higher the atomic mass the lower the light output. For the CRESST experiment, of course, the values for oxygen ($Q = 14.3 \pm 0.5$), calcium ($Q = 27.4 \pm 1$) and tungsten ($Q = 41 \pm 3$) are the most important ones.

Those values are obtained at room temperature for events at the crystal's surface. They have to be verified for the bulk as well as for temperatures in the mK range. This can be accomplished by using neutrons as probes.

2.4.2 Neutron Scattering Experiment

For a good determination of the quenching factors in a neutron scattering experiment it is desirable, that the signals for the three different elements form distinct populations in the data. This can be achieved by performing

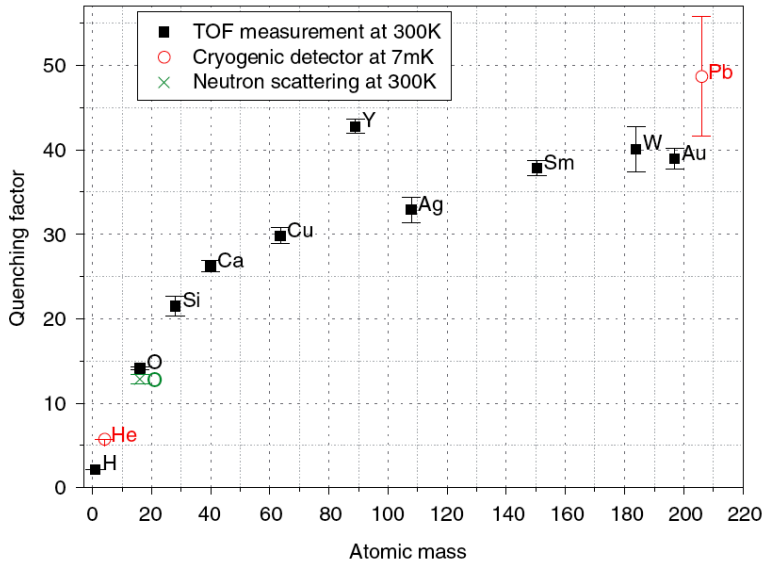

Figure 2.7: Results of the quenching factor measurements performed with the TOF-MS (■). For comparison also the results from neutron scattering measurements (see section 2.4.2) and from dark matter data are shown [58]. The value found for Y is probably a measurement error, as it could not be reproduced in later experiments [59].

the scattering with monoenergetic neutrons and selecting a single scattering angle. This way the nuclei can be discriminated via the recoil energy.

A neutron scattering experiment for scintillator quenching factor measurements is set up at the tandem accelerator in the Maier-Leibnitz-Laboratory in Garching. Neutrons are produced via the reaction $^{1}\mathrm{H}(^{11}\mathrm{B},\mathrm{n})^{11}\mathrm{C}$. Boron ions with a kinetic energy of 60 MeV from the accelerator are shot onto a hydrogen gas target, producing neutrons with an energy of 11 MeV [61]. The pulsing of the boron beam defines the reference time for the time of flight measurement of the neutrons.

The further setup (see Fig. 2.8) consists of a central detector unit containing the scintillator/crystal to be investigated and a set of 40 neutron detectors placed at a fixed angle with respect to the beam and the central detector, thus defining the scattering geometry. The neutron detectors consist of chambers with NE213 liquid scintillator read out by PMTs. NE213 allows an excellent discrimination between neutron and gamma events via pulse shape discrimination. PE shielding in the line of sight between the neutron detectors and the neutron source suppresses the background from direct neutrons.

The scintillators investigated in this setup are NaI(Tl), NE213 [62] and

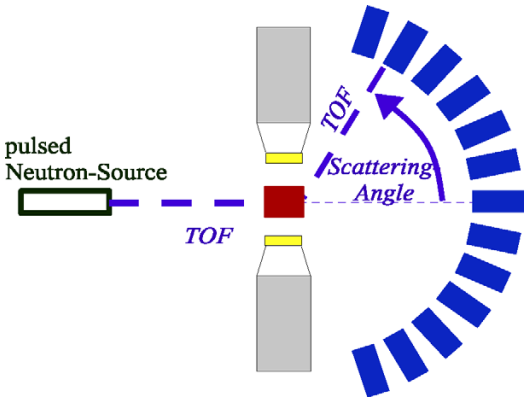

Figure 2.8: Principle setup for a scattering experiment with a monoenergetic pulsed neutron source [60]. Neutrons from a monoenergetic pulsed neutron source scatter off the investigated scintillator (red) and are detected in neutron detectors (blue) positioned at a fixed scattering angle. In the room temperature setup the scintillation light is measured with two PMTs.

$CaWO_4$ [60]. For the latter cylindrical crystals of 20 mm diameter and 10 mm height were coupled to two PMTs by an optical compound providing a good light collection.

A scattered neutron is first seen in the neutron detectors, as $CaWO_4$ is a slow scintillator. A neutron event in one of the 40 detectors starts the time of flight measurement, which is in fact deduced from the time until the next beam pulse arrives. Furthermore a time window for the central detector is opened and when a signal is seen in this window, the event is recorded. Only events where the time of flight is within certain constraints are taken into account, so that for example inelastic scattering events with high excitation energies can be filtered out.

Several measurements with scattering angles between 80° and 140° have been performed. The PMTs of the central detector deliver a differentiated and an integrated signal, the latter being used to determine the light energy. The differentiated signal gives information on the time distribution of the incoming photons. Combining this for all events allows for a calculation of the scintillation decay time τ of $CaWO_4$. A value $\tau = (12.3 \pm 0.3)\mu$s was found.

For calibrating the light output of electron recoils ^{55}Fe, ^{241}Am and ^{57}Co sources were used, providing data points from 6 to 136 keV. No nonlinear behaviour of the light output within this energy range was found. The top plot in Fig. 2.9 shows the light output determined for oxygen and calcium in dependence of the scattering angle. The fits give the respective quench-

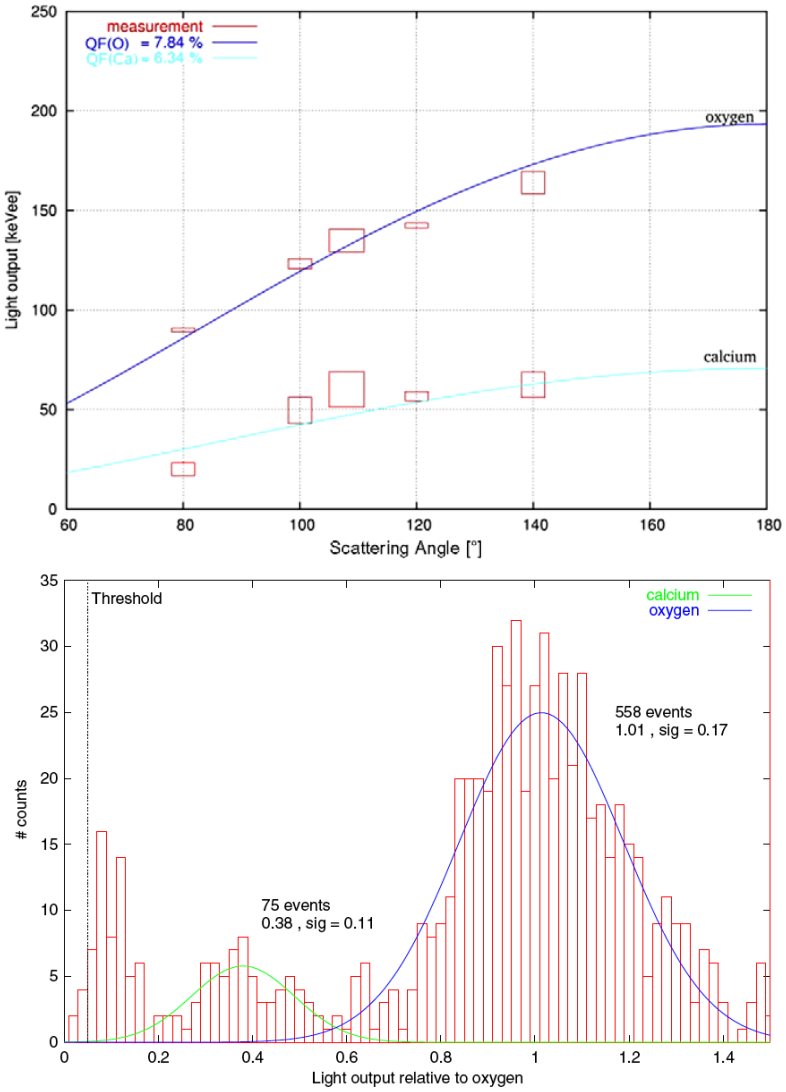

Figure 2.9: Results of quenching factor measurements performed at room temperature with $CaWO_4$. Top: Light output in keV_{ee} in dependence of the scattering angle for calcium and oxygen with the best fits for their respective quenching factors. Note that the quenching factor actually is the light yield as defined by equation (2.1). Bottom: Light spectrum for all neutron events measured at scattering angles of 100° and 140° normalized to one for oxygen events. Two distinct Gaussian distributions representing oxygen and calcium are observed. The tungsten events are close to or below the threshold [60].

ing factor under the assumption that it is energy independent. The values obtained are $Q = 12.8 \pm 0.5$ for oxygen and $Q = 16 \pm 4$ for calcium.

The bottom plot in Fig. 2.9 shows the light output for neutron events in the $CaWO_4$ crystal for scattering angles of 100° and 140° normalized to one for oxygen events. Two separate populations are assigned to oxygen and calcium recoils. The calcium recoils have a significantly lower light output due to the lower recoil energy at a given scatttering angle. The tungsten population would then be expected at even lower energies, but they are obscured by the noise level. Thus only a lower limit for tungsten of $Q > 33$ could be obtained.

The neutron scattering experiments so far were performed at room temperature. However, the goal is to measure the quenching factors at low temperatures, i.e. in the mK range. For that purpose the central detector will be replaced with a cryogenic detector installed in a dilution refrigerator that is presently being set up [63]. The measurement at low temperatures brings additional challenges to the already complex experiment. The cryostat for example introduces much more material into the beam than the old central detector and thus possibly a larger background level due to neutron interactions in that material. The timing of the experiment has to account for the even slower scintillation of $CaWO_4$ at low temperatures (see chapter 6.3).

On the upside the low temperature measurements will benefit from the use of detectors with the phonon-light technique. This solves some problems of the room temperature experiments. In the light-only data, for example, the tungsten events could not be observed, as they were below the threshold. The recoil energy of tungsten for 11 MeV neutrons is in the range of 100–200 keV which should deliver a clear signal in the phonon channel of the cryogenic detector. The phonon-light measurement also allows to discriminate inelastic tungsten $(n, \gamma n)$ events with γ energies of 46 keV or 100–123 keV which in the past contaminated the calcium and oxygen data.

An optimized cryogenic detector for the requirements of a cryogenic neutron scattering experiment with large count rates was developed in this work and is described in chapter 6.2.

2.4.3 Measurements with Standard Neutron Sources

In measurements using cryogenic phonon-light detectors exposed to standard neutron sources like ^{241}Am-Be or ^{252}Cf the total nuclear recoil band is an overlap of the recoil bands of the three elements of the $CaWO_4$ crystal. Provided a good resolution of the light channel is achieved one can then attempt to extract the quenching factors from the structure of the band without the need of a complex scattering setup.

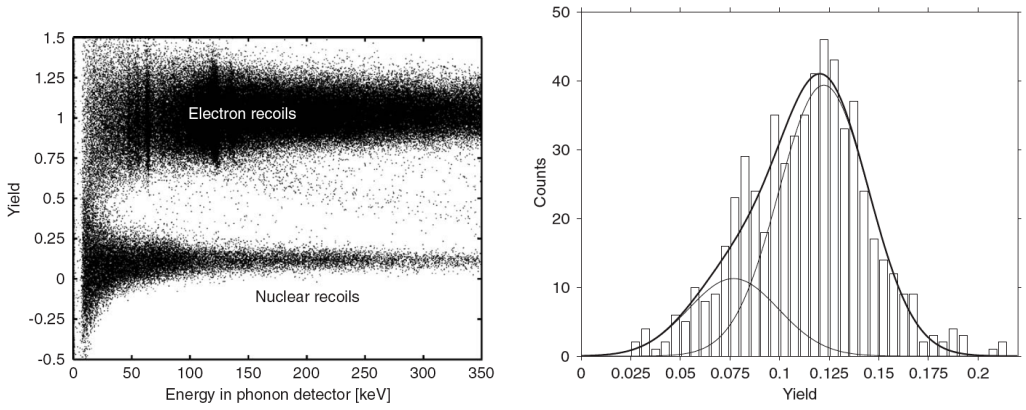

Figure 2.10: Results of measurements with a cryogenic phonon-light detector irradiated with an Am-Be neutron source and a ^{57}Co calibration source. Left: Phonon-Yield plot of the data. Right: Histogram of the yield of nuclear recoil events between 280 and 340 keV [64].

Fig. 2.10 shows the results of a measurement with an Am-Be neutron source. The detector used here consisted of a cylindrical $CaWO_4$ crystal of 20 mm diameter and 20 mm height together with a $20 \times 20 \times 0.5\,\mathrm{mm}^3$ silicon light detector. The histogram of the light yield for nuclear recoil events with energies between 280 and 340 keV (Fig. 2.10, right) shows a clear asymmetry towards lower yields. In this energy range a strong contribution of calcium is expected, while tungsten recoils should not be present.

This asymmetry is attributed to the mixture of oxygen and calcium recoil events. A fit with two Gaussians, where the ratio of the amplitudes is fixed to the expected value from theoretical calculations, reveals the quenching factors $Q = 8.2 \pm 0.2$ for oxygen and $Q = 13.0 \pm 1.7$ for calcium [65].

Especially the value for calcium obtained with this procedure has to be taken with care as a crystal of the size used for this measurement still has some contribution of double scattering. If a neutron scatters twice it is very likely that one of the partners is oxygen. Scatter events with two different nuclei lead to a population in the light yield between the bands of the individual elements. In the fitting procedure described above this leads to a quenching factor for calcium that is systematically too low.

Recently this experiment has been repeated [63] with a new phonon detector developed in this work for the scattering experiment. In the new measurement the separation of the oxygen and calcium bands is improved (see chapter 6.2).

While this method yields reasonable results for calcium and oxygen it is unlikely that it can be used to obtain the quenching factor for tungsten, as the

tungsten recoils are concentrated at very low energies where the resolution of the light channel is not good enough to resolve the structure of the nuclear recoil band.

2.5 CRESST Results

In spring 2004, before the upgrade, during a data taking period of two months two prototype detector modules with $CaWO_4$ single crystals of a total mass of $\sim 600\,\mathrm{g}$ were used. With these two detectors we achieved an exposure of about $20\,\mathrm{kg\,d}$. No muon veto or neutron shield was present for these measurements. After the upgrade a commissioning run was started in autumn 2006 for testing the new electronics and shielding. In this run a total exposure of $50\,\mathrm{kg\,d}$ has been achieved so far. In the following, the results of the dark matter runs before and after the upgrade are presented and compared.

2.5.1 Dark Matter Limits Before Upgrade

For a conservative dark matter limit all nuclear recoils from 12 to 40 keV are considered without any assumption on the origin of the events (WIMP interaction or background). In this region a total of 16 events were observed, resulting in a count rate of 0.87 ± 0.22 per kg d. From this result an upper limit for the WIMP nucleon cross section σ_{WN} as shown in Fig. 2.12 (topmost solid red line) is derived using the standard assumptions about the WIMP distribution in the halo (see section 1.1.3). The obtained count rate, however, is in agreement with the expected neutron background rate for a measurement without neutron shield as calculated in Monte Carlo simulations (see section 2.3).

One of the detector modules, the module "Daisy", showed a sufficient resolution in the light channel to allow for a reasonable separation between O and W recoils. In Fig. 2.11 (left) the dashed red lines indicate the region, where oxygen recoils are expected at a 90% confidence level, while tungsten recoils are expected below the black line, assuming a quenching factor of 40. In this module with an exposure of about $10\,\mathrm{kg\,d}$ all nuclear recoils are then in the assumed oxygen band, suggesting that they are indeed neutron interactions. From the absence of events in the tungsten window a considerably stronger limit for the WIMP-nucleon cross section can be deduced, which is shown in figure Fig. 2.12 as green solid line.

This demonstrates that the identification of the recoiling nucleus is a powerful tool for suppressing the neutron background. The limit obtained here is relatively robust against variation of the quenching factor of tungsten

and of the analysis threshold. When the quenching factor for W recoils is assumed to be in the range from 23.4 to 35.8 a single event falls into the signal region, changing the limit by about 50%. A reduction of the threshold to 10 keV gives 2 events in the analysis region, but no significant change in the limit [66].

2.5.2 Dark Matter Limits After Upgrade

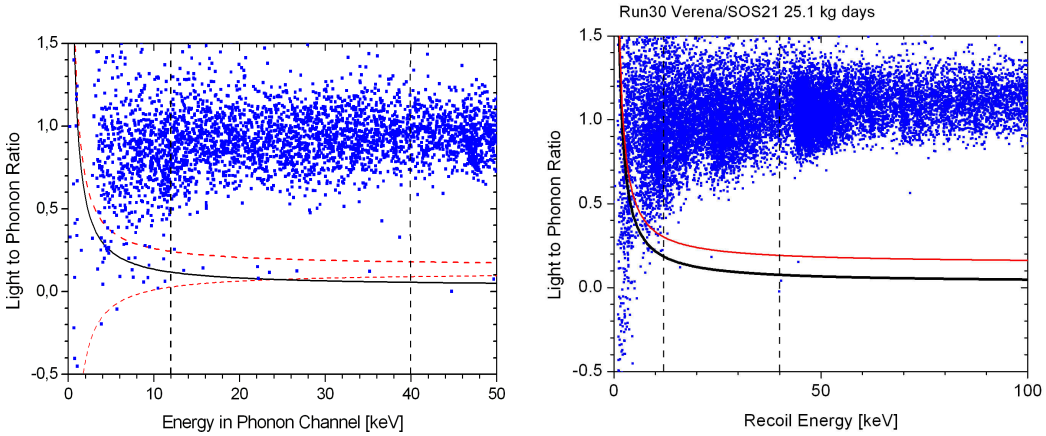

Figure 2.11: Yield plots of events observed in CRESST detector modules during run 28 before the upgrade (left) in the module "Daisy" [53] and during run 30 after the upgrade of the shielding (right) in the module "Verena" [67]. The exposure of "Daisy" was $\sim$ 10 kg d, while that of "Verena" was $\sim$ 25 kg d. Note the reduced count rate in the nuclear recoil band after the introduction of the PE shielding. For an explanation of the various lines, see the main text.

After the upgrade a commissioning run was started in autumn 2006 with nine detector modules and one phonon detector without light detector. For two of the nine complete modules – "Verena" and "Zora" – both the phonon and the light channel show a performance good enough for dark matter data taking. With these two modules a total exposure of $\sim$ 50 kg d has been collected and analysed so far [67].

Within these 50 kg d in total 4 events in the nuclear recoil band (below the red line in Fig. 2.11 for the module "Verena") in the relevant energy window are observed. This corresponds to a count rate of 0.08 $\mathrm{kg^{-1}\,d^{-1}}$, a reduction by one order of magnitude compared to the count rate before the upgrade. However, two of those events are compatible with tungsten recoils, thus limiting the sensitivity. The limit for the WIMP-nucleon cross section resulting from those events is plotted in Fig. 2.12 as solid blue line.

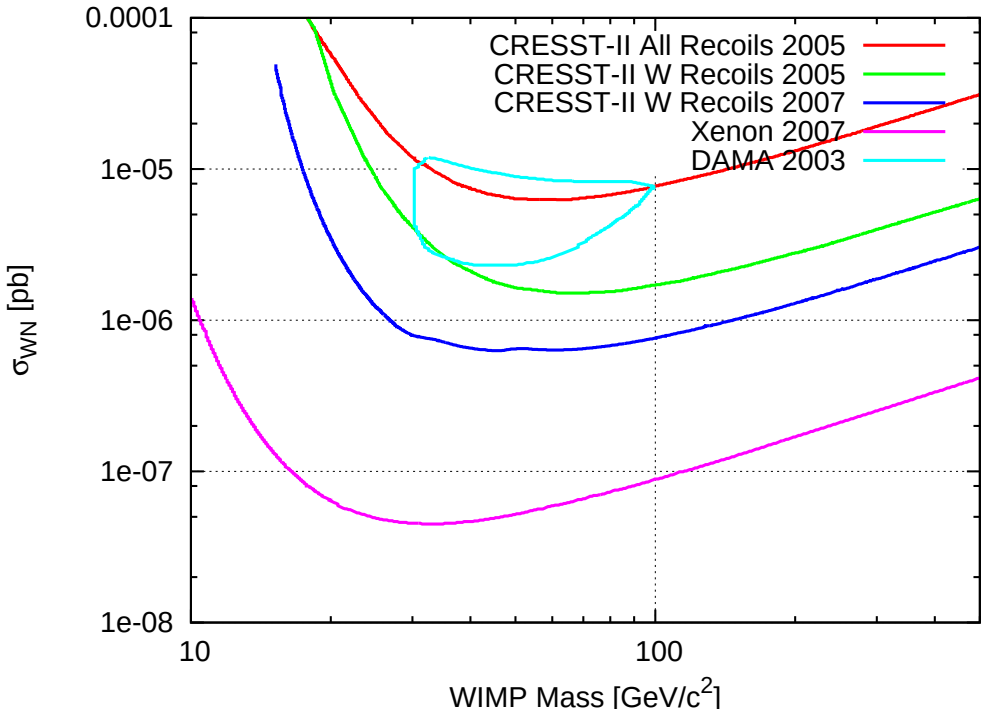

Figure 2.12: Limits for the spin indepedent WIMP-nucleon cross section obtained for CRESST II. For comparison also the currently best limit from XENON and the positive claim of DAMA are shown.

2.5.3 Rare Alpha Decays

The alpha events form a population in the data sets that can easily be separated from all other event types (see Fig. 2.13). It is thus possible to measure alpha decays basically free of background. For all stable tungsten isotopes alpha decay is energetically allowed, but long half lifes in the region of 10^{18} years (^{180}W) or 10^{32} years (^{182}W, ^{183}W, ^{184}W and ^{186}W, respectively) are expected. The $CaWO_4$ detectors of CRESST are thus ideal for the expected low count rates of these decays.

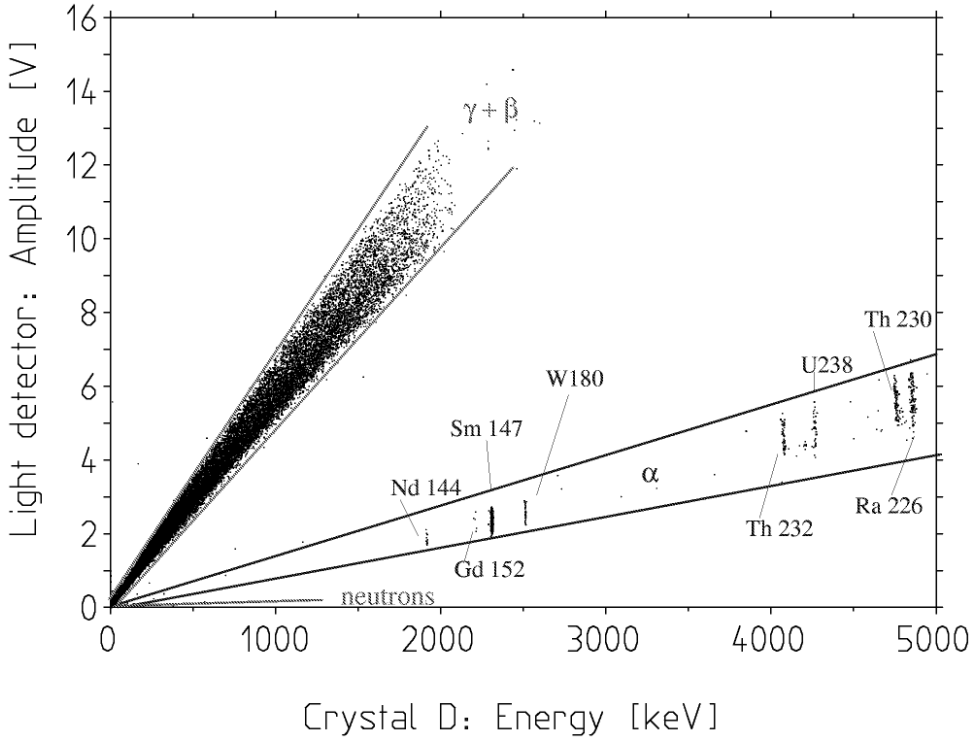

Figure 2.13: Phonon-light plot with alpha lines observed in the dark matter run 28 (spring 2004) of CRESST [68]. The alpha events can be separated clearly from beta and gamma events and neutron events.

All lines in the alpha spectrum except one could be identified and assigned to known contaminations in our crystals or the detector housing. This one line at 2516 keV fits the Q-value for the alpha decay of ^{180}W. From the abundance of the isotope in the crystals and the count rate of the line taken from four CRESST runs (22, 23, 27 and 28) a half-life of $(1.8 \pm 0.2) \cdot 10^{18}$ years was determined. While indications for this decay have been reported earlier [69], this is the first unambiguous detection of the natural alpha decay of ^{180}W.

No signal has been seen for the potential alpha decays of the other four stable isotopes of tungsten. Thus new limits for the half-lifes of these isotopes could be set, which improved the previous decay limits by a factor of about 50 [68].

2.6 Status and Future

The commissioning run 30 was continued until the needed neutron calibration of the detectors was performed. The origin of the observed nuclear recoil events is partly assigned to neutron events due to a leakage in the neutron moderator, which has been fixed meanwhile. Other candidates are recoiling nuclei from surface alpha decays or electronic artefacts. For the next run the upgrade-related problems revealed in the current run are addressed, non-functional detectors are replaced. Troublesome electronic channels, for example those with non-working SQUIDs, are repaired before the detectors are reinstalled.

Once fully equipped with 10 kg of $CaWO_4$ target mass, the CRESST experiment should be able to reach a sensitivity at the 10^{-8} pb level. For a higher sensitivity a more massive target and a better background suppression both in terms of shielding and discrimination are needed. This is the objective of the proposed EURECA experiment, initiated by collaborators from the CRESST and EDELWEISS experiments and other groups [37]. EURECA is at the moment in an early design phase. The intention is to build an array of cryogenic detectors with a total mass in the ton scale. The present experiments CRESST and EDELWEISS can be considered as R&D projects for EURECA as the latter will benefit from the experience gathered in the former. The use of several different target materials will allow to discriminate a possible WIMP signal from neutron background.

Chapter 3

Basics of Cryogenic Detectors

3.1 Transition Edge Sensors

The heat deposited into an absorber crystal by an event can in principle be detected by measuring the resulting temperature rise. To get a reasonable sensitivity in doing so, it is best to go to very low temperatures (mK range), where the heat capacities are small. Still, the changes in temperatures caused by events in the keV range are small (a few or few tens of μK). Thus sensors are needed that convert a small temperature signal into a larger signal.

One possibility is the use of transition edge sensors (TESs), where a superconductor is operated within its transition from the normal conducting to the superconducting state. As this transition is very steep small variations of the temperature lead to a large variation of the resistance (see Fig. 3.1). The steepness of the transition is crucial for the sensitivity of the TES, this is expressed with the parameter α defined as the logarithmic derivation of the sensor resistance R_T over the temperature T:

$$\alpha = \frac{d \ln R_T}{d \ln T} = \frac{T}{R_T} \frac{dR_T}{dT} \tag{3.1}$$

Fig. 3.2 depicts the basic idea of the realization of a detector with transition edge sensor. A film of the superconducting material is produced on the absorber crystal. As the dimensions of the absorber crystal (several mm to cm) are large compared to the typical dimensions of the TES film (sub-mm), this kind of detector is also addressed as "macrocalorimeter" in contrast to "microcalorimeters" with absorbers in the μm regime.

In order to measure the resistance changes of the TES the sensor is typically installed in a circuit as shown in Fig. 3.3. The sensor is parallel to a reference resistance R_S, which is similar to the TES resistance R_T. A bias current I_0 will then split according to the ratio $I_S/I_T = R_T/R_S$ with I_S and

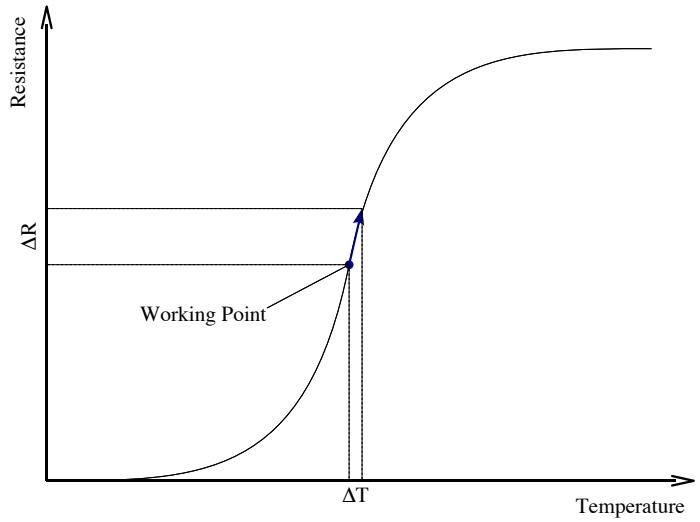

Figure 3.1: Basic principle of transition edge sensors: The temperature of a superconductor is stabilized within its transition. A small change of temperature, for example due to an energy input into the system, will then lead to a large change of resistance.

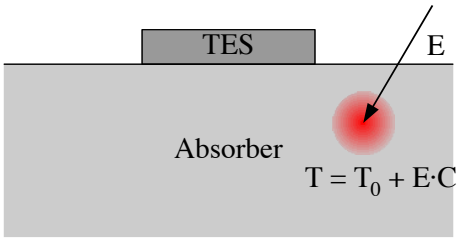

Figure 3.2: Macrocalorimeter: Energy E deposited in an absorber crystal causes an increase of temperature which is then sensed by a transition edge sensor on the crystal. The change in temperature $(T - T_0)$ is determined by the energy E and the heat capacity C of the absorber crystal.

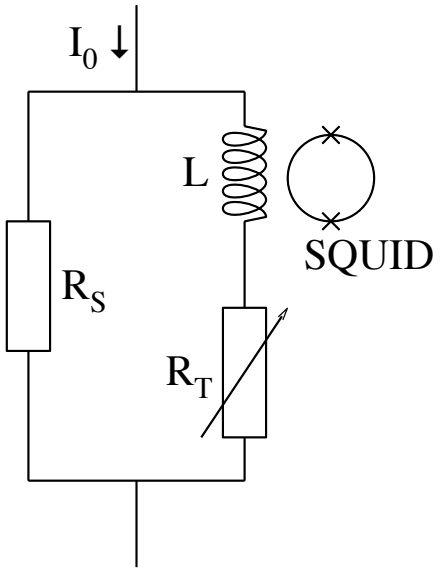

Figure 3.3: Typical readout circuit for transition edge sensors. The TES R_T is in parallel with a reference resistance R_S. The whole cuircuit is biased with a constant current I_0. A change of R_T causes a change of the current in the superconducting coil L. The resulting change of the magnetic field in the coil is then sensed in a Superconducting Quantum Interference Device ("SQUID").

I_T denoting the currents in the two branches of the circuit, and $I_S + I_T = I_0$. In the branch of the TES a superconducting coil L accompanied with a Superconducting Quantum Interference Device (SQUID) is installed. A SQUID is an extremely sensitive detector for changes in magnetic fields. Small variations in I_T will lead to variations in the magnetic field of the coil, which are detected by the SQUID. The output signal of the SQUID is then proportional to dI_T/dt, which is usually integrated to get $I_T(t)$.

3.1.1 Calorimeter Model

For transition edge sensors (TESs) on relatively large absorber crystals, operated with negligible heating power from the detector bias, the signal can be described by a simple model [70]. Fig. 3.4 shows a scheme of the components and thermal couplings involved in the model. Pulses from particle events in the absorber are described by two components: a fast non-thermal part arising from initial high-frequency phonons and a slower thermal part.

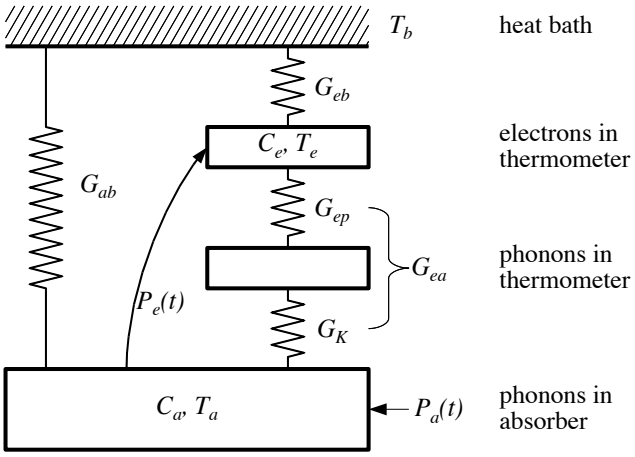

Figure 3.4: Coupling scheme for a simple TES directly connected to an absorber crystal [70]. For the discussion of the various phonon contributions see the main text.

In Fig. 3.4 the boxes indicate the heat capacities in the system: C_a is the heat capacity of the absorber at temperature T_a, C_e is the heat capacity of the electrons of the TES, T_e is their temperature. Absorber and sensor are weakly coupled to a heat bath at temperature T_b. The thermal couplings involved are: G_{ab} absorber to bath, G_{eb} TES electrons to bath, G_{ep} electron–phonon coupling in the sensor, G_K phononic coupling absorber to sensor.

The last two are combined in G_{ea}:

$$\frac{1}{G_{ea}} = \frac{1}{G_K} + \frac{1}{G_{ep}} \tag{3.2}$$

A particle interaction in the absorber initially produces high-energy optical phonons which immediately decay into acoustic phonons with frequencies in the THz regime. The frequency of thermal phonons for temperatures in the mK range is typically of some GHz. However, it takes several milliseconds for the acoustic phonons to decay down to these frequencies. A typical crystal with dimensions in the order of centimeters is filled after a few microseconds with high-frequency non-thermal phonons. When those phonons hit the transition edge sensor they can be absorbed by its electron system, where they quickly thermalize. This input of non-thermal phonons into the sensor is expressed as power $P_e(t)$ in Fig. 3.4.

The power input $P_e(t)$ increases the temperature T_e of the electrons in the sensor. The heat in the sensor can dissipate to the heat bath via the thermal coupling G_{eb} of the sensor to the bath or back to the absorber via G_{ea}. Due to the very weak electron phonon coupling G_{ep} at low temperatures G_{eb} will be the dominant path. The non-thermal phonons in the absorber can also thermalize for example on the crystal surfaces leading to a power input $P_a(t)$ to the thermal phonon population in the crystal.

In this simple picture the time evolution of the temperature of the absorber T_a and of the electrons in the sensor T_e can be described by two coupled differential equations:

$$C_e \frac{dT_e}{dt} + (T_e - T_a)G_{ea} + (T_e - T_b)G_{eb} = P_e(t) \tag{3.3}$$

$$C_a \frac{dT_a}{dt} + (T_a - T_e)G_{ea} + (T_a - T_b)G_{ab} = P_a(t) \tag{3.4}$$

The solution for the temperature development of the sensor for the initial condition $T_a(0) = T_e(0) = T_b$ is then a function of the form

$$\Delta T_e(t) = \theta(t) \left[A_\mathrm{n} \left(\mathrm{e}^{-\frac{t}{\tau_\mathrm{n}}} - \mathrm{e}^{-\frac{t}{\tau_\mathrm{in}}} \right) + A_\mathrm{t} \left(\mathrm{e}^{-\frac{t}{\tau_\mathrm{t}}} - \mathrm{e}^{-\frac{t}{\tau_\mathrm{n}}} \right) \right], \tag{3.5}$$

with the signal rise time τ_in, the non-thermal decay time τ_n and the thermal decay time τ_t. A_n and A_t are the amplitudes of the non-thermal and the thermal component of the signal, respectively. The rise time of the thermal signal is the decay time of the non-thermal, as the thermal phonons in the crystal are populated when the non-thermal decay.

The rise time τ_{in} and the thermal decay time τ_{t} can be expressed by the heat capacities and thermal couplings in the system as

$$\tau_{\mathrm{in}} = \frac{2}{a + \sqrt{a^2 - 4b}} \tag{3.6}$$

$$\tau_{\mathrm{t}} = \frac{2}{a - \sqrt{a^2 - 4b}} \tag{3.7}$$

with the constants

$$a = \frac{G_{ea} + G_{eb}}{C_e} + \frac{G_{ea} + G_{ab}}{C_a} \tag{3.8}$$

$$b = \frac{G_{ea}G_{eb} + G_{ea}G_{eb} + G_{eb}G_{ab}}{C_e C_a} \tag{3.9}$$

τ_{n} is the lifetime of the non-thermal phonons in the absorber. They are diminished by their thermalization in the crystal with the lifetime τ_{crystal} or by their absorption in the TES film with the time constant τ_{film}. Thus, τ_{n} is a combination of those two time constants:

$$\frac{1}{\tau_{\mathrm{n}}} = \frac{1}{\tau_{\mathrm{crystal}}} + \frac{1}{\tau_{\mathrm{film}}} \tag{3.10}$$

The phonon collection time τ_{film} of the sensor can be calculated as

$$\tau_{\mathrm{film}} = \frac{2V_a}{A\bar{\eta}\,\langle v_\perp \alpha \rangle}, \tag{3.11}$$

where V_a is the volume of the absorber, A is the area of the interface between absorber and film and $\bar{\eta}$ the effective absorption probability for the high-frequency phonons in the film. The $\langle \ldots \rangle$ expression denotes the average of the group velocity $v_\perp$ perpendicular to the interface, weighed with the transmission probability α through the interface. The fraction ε of non-thermal phonons detected in the sensor is then

$$\varepsilon = \frac{\tau_{\mathrm{crystal}}}{\tau_{\mathrm{crystal}} + \tau_{\mathrm{film}}} \tag{3.12}$$

The amplitudes in equation (3.5) are

$$A_{\mathrm{n}} = \frac{E\left(\frac{1}{\tau_{\mathrm{in}}} - \frac{G_{ab}}{C_a}\right)}{\tau_{\mathrm{n}}\left(\frac{1}{\tau_{\mathrm{in}}} - \frac{1}{\tau_{\mathrm{t}}}\right)\left(\frac{1}{\tau_{\mathrm{in}}} - \frac{1}{\tau_{\mathrm{n}}}\right)} \cdot \left[\frac{\frac{1}{\tau_{\mathrm{t}}} - \frac{G_{ab}}{C_a}}{G_{eb} - \frac{C_e}{C_a}G_{ab}} - \frac{\varepsilon}{C_e}\right] \tag{3.13}$$

$$A_{\mathrm{t}} = \frac{E\left(\frac{1}{\tau_{\mathrm{t}}} - \frac{G_{ab}}{C_a}\right)}{\tau_{\mathrm{n}}\left(\frac{1}{\tau_{\mathrm{t}}} - \frac{1}{\tau_{\mathrm{in}}}\right)\left(\frac{1}{\tau_{\mathrm{t}}} - \frac{1}{\tau_{\mathrm{n}}}\right)} \cdot \left[\frac{\frac{1}{\tau_{\mathrm{in}}} - \frac{G_{ab}}{C_a}}{G_{eb} - \frac{C_e}{C_a}G_{ab}} - \frac{\varepsilon}{C_e}\right], \tag{3.14}$$

where E is the energy deposited in the absorber.

3.1.2 Slow Energy Input

The function (3.5) describes the signal for an event, where the initial energy input occurs within a very short time scale, e.g. by scattering of a particle or absorption of a photon. However, in some cases the energy is deposited in the absorber over a timescale that is not small compared to the detector time constants.

In a detector for measuring the light emitted by a scintillator for example, the energy is deposited during the decay time of the scintillator (e.g. for $CaWO_4$ $\tau \approx 400\,\mu$s, see section 6.3.4). Each absorbed single photon should give rise to a signal of the form (3.5). This then defines the normalized detector response function f_{Detector}:

$$f_{\mathrm{Detector}}(t) = \theta(t)\left[a_{\mathrm{n}}\left(\mathrm{e}^{-\frac{t}{\tau_{\mathrm{n}}}} - \mathrm{e}^{-\frac{t}{\tau_{\mathrm{in}}}}\right) + a_{\mathrm{t}}\left(\mathrm{e}^{-\frac{t}{\tau_{\mathrm{t}}}} - \mathrm{e}^{-\frac{t}{\tau_{\mathrm{n}}}}\right)\right], \tag{3.15}$$

with the amplitudes a_{n} and a_{t}, which are equal to the amplitudes given in (3.13) and (3.14), only normalized to the energy input:

$$a_{\mathrm{n}} = A_{\mathrm{n}}/E, \qquad a_{\mathrm{t}} = A_{\mathrm{t}}/E. \tag{3.16}$$

A continuous stream of light, which is a good approximation for high energetic events, or averaged pulses, introduces the power $P_{\mathrm{Light}}(t)$ into the absorber, the signal $\Delta T(t)$ of the detector is then a convolution of the two functions [71]:

$$\Delta T(t) = (P_{\mathrm{Light}} * f_{\mathrm{Detector}})(t) \tag{3.17}$$

If the intrinsic detector response function is known, the function P_{Light} can be extracted from the measured signal (3.17) by deconvolution. This method is used in section 6.3.4 to determine the scintillation time constants for $CaWO_4$ at cryogenic temperatures.

3.1.3 Composite Detectors

For some applications composite detectors where the TES is evaporated onto a small individual substrate which later is glued onto the actual absorber are used (see section 6.1). For the development of a detector model the additional component of the glued interface has to be taken into account.

Fig. 3.5 shows the coupling scheme for a composite detector. Here the substrate carrying the TES takes the role of the absorber in Fig. 3.4. The substrate is thermally coupled via the glue spot to the absorber. The absorber is thermally coupled to the heat bath via the detector holder, the TES

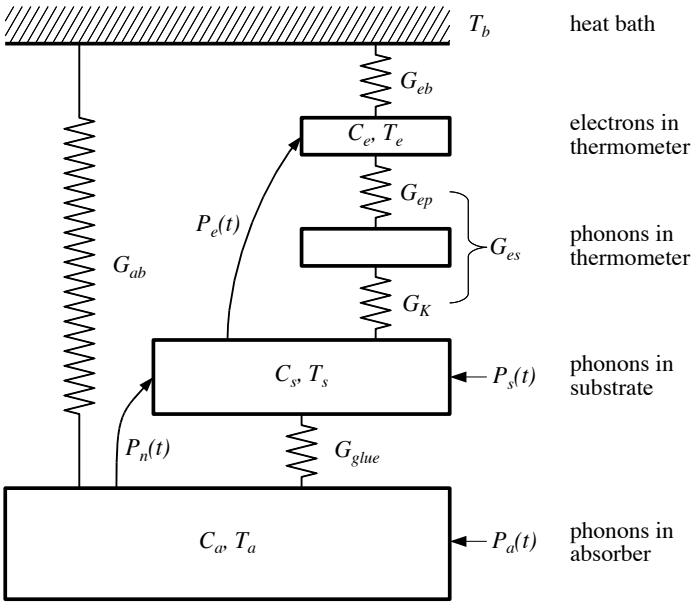

Figure 3.5: Coupling scheme for composite detectors. For a detailed description see the main text.

substrate usually has no contact to the holder and thus is not coupled to the heat bath.

The processes for the generation of the signal can be described in analogy to the processes for the simple detector model presented above. The model now has to be extended by the TES substrate with heat capacity C_s and temperature T_s. This substrate is thermally coupled to the absorber (heat capacity C_a and temperature T_a) via the glue with thermal conductance G_{glue}. A possible contribution of the heat capacity of the glue is not discussed here. The thermal coupling G_{es} of the electron system of the TES to the TES substrate is again the combination of the electron-phonon coupling G_{ep} in the TES and the Kapitza coupling G_K of the film to the substrate.

A particle event in the absorber creates a population of non-thermal phonons, which can either pass through the glue into the sensor substrate (power input $P_n(t)$) or decay in the absorber leading to the heating power $P_a(t)$. The non-thermal phonons in the substrate can then be absorbed in the thermometer film heating it with $P_e(t)$ or thermalize in the substrate leading to the power input $P_s(t)$ which contributes to the thermal part of the signal via G_{es}.

The heat in the absorber from the decaying non-thermal phonons can ei-

ther dissipate over the thermal coupling G_{ab} directly to the heat bath (in this case the energy is lost for the detector signal), or over the thermal coupling of the glue G_{glue} into the thermometer substrate, where it contributes to the thermal part of the signal.

A complete quantitative description of this system is complex, so only two extreme cases are discussed below [72].

Non-Thermal Case

In the first case it is assumed that the thermal coupling G_{glue} of the glue is negligibly small compared to the coupling G_{ab} of the absorber to the heat bath. However, the glue is considered to be transparent for non-thermal phonons. In this case, only the non-thermal power input $P_n(t)$ contributes to the detector signal. As the sensor is thermally decoupled from the absorber this case can be treated like the case for the simple detector of the previous section with slow external energy input.

An instantaneous energy input into the TES substrate would generate a signal described by the function (3.5). Since now there are two non-thermal decay times, the one of the sensor is written as τ_{ns} and the one of the absorber as τ_{na}. Thus the elementary sensor response function is described by the known model with the thermal and non-thermal component:

$$f_s(t) = \theta(t)\left[a_{\mathrm{n}}\left(\mathrm{e}^{-\frac{t}{\tau_{\mathrm{ns}}}} - \mathrm{e}^{-\frac{t}{\tau_{\mathrm{in}}}}\right) + a_{\mathrm{t}}\left(\mathrm{e}^{-\frac{t}{\tau_{\mathrm{t}}}} - \mathrm{e}^{-\frac{t}{\tau_{\mathrm{ns}}}}\right)\right], \tag{3.18}$$

while the power input $P_n(t)$ from the absorber should only have the decay time τ_{na}, the rise of the signal is considered to be infinitely fast on the time scale of the detector:

$$P_n(t) = \theta(t) P_0 \mathrm{e}^{-\frac{t}{\tau_{\mathrm{na}}}} \tag{3.19}$$

The signal for an event in the absorber seen in the detector is then a convolution of $P_n(t)$ and $f_s(t)$:

$$\Delta T(t) = \theta(t)\left[c_{\mathrm{ns}}\left(\mathrm{e}^{-\frac{t}{\tau_{\mathrm{ns}}}} - \mathrm{e}^{-\frac{t}{\tau_{\mathrm{na}}}}\right) + c_{\mathrm{in}}\left(\mathrm{e}^{-\frac{t}{\tau_{\mathrm{in}}}} - \mathrm{e}^{-\frac{t}{\tau_{\mathrm{na}}}}\right) + c_{\mathrm{t}}\left(\mathrm{e}^{-\frac{t}{\tau_{\mathrm{t}}}} - \mathrm{e}^{-\frac{t}{\tau_{\mathrm{na}}}}\right)\right], \tag{3.20}$$

with the amplitudes

$$c_{\mathrm{ns}} = P_0 \frac{\tau_{\mathrm{ns}}\tau_{\mathrm{na}}}{\tau_{\mathrm{ns}} - \tau_{\mathrm{na}}}(a_{\mathrm{n}} - a_{\mathrm{t}}) \tag{3.21}$$

$$c_{\mathrm{in}} = P_0 a_{\mathrm{n}} \frac{\tau_{\mathrm{in}}\tau_{\mathrm{na}}}{\tau_{\mathrm{na}} - \tau_{\mathrm{in}}} \tag{3.22}$$

$$c_{\mathrm{t}} = P_0 a_{\mathrm{t}} \frac{\tau_{\mathrm{t}}\tau_{\mathrm{na}}}{\tau_{\mathrm{t}} - \tau_{\mathrm{na}}} \tag{3.23}$$

Thermal Case

The second scenario considers the glue to be opaque for non-thermal phonons. As a consquence, the phonons have to thermalize in the absorber before the energy can reach the sensor via the thermal couplings G_{glue} and G_{es} of the system. The signal is then purely determined by the thermal components and should rise with the decay of the non-thermal phonons in the absorber.

In practice neither the first nor the second case will be present in pure form, there will also be contributions of the thermal and the non-thermal signal component. Recent studies, however, indicate that for small area glue spots the non-thermal component is dominant, while for larger areas of glue the thermal component makes a significant contribution [73].

3.1.4 Electrothermal Feedback

So far the heating power from the detector bias has been neglected. In general the TES is installed in a read-out circuit as shown in Fig. 3.3 which is biased with a current I_0. The current I_T in the TES is then depending on the reference resistance R_S and the resistance of the sensor R_T:

$$I_T = I_0 \frac{R_S}{R_T + R_S} \tag{3.24}$$

This current dissipates the heating power $P_T = I_T^2 R_T$ in the sensor. This has to be accounted for in equation (3.3) for the power input into the sensor. Thus we have:

$$C_e \frac{dT_e}{dt} + (T_e - T_a)G_{ea} + (T_e - T_b)G_{eb} = P_e(t) + P_T(t) \tag{3.25}$$

As a consequence in thermal equilibrium (i.e. $dT_e/dt = 0$ and $P_e(t) = 0$) and if G_{ea} is small, the temperature of the sensor is higher than the temperature of the heat bath. For a non-negligible coupling of the absorber to the heat bath G_{ab} and a sufficiently high heating power P_T it can be assumed that $(T_e - T_a) \gg (T_a - T_b)$ and thus $(T_e - T_a) \approx (T_e - T_b)$ in equation (3.25). Considering the thermal dependence of the thermal couplings the stationary solution for the sensor then is [74]:

$$K(T_e^n - T_b^n) = I_T^2 R_T \tag{3.26}$$

with a material and geometry dependent parameter K. The exponent n depends on the type of the dominant thermal coupling, for electron-phonon coupling $n = 5 \ldots 6$ and for Kapitza coupling $n = 4$.

The heating power depends on the sensor resistance and thus on its temperature. The dependency can be expressed with the parameter α given in equation (3.1):

$$\frac{\partial P_T}{\partial T_e} = \alpha \frac{P_T}{T_e} \left(\frac{R_S - R_T}{R_S + R_T} \right) = -\alpha_{\text{eff}} \frac{P_T}{T_e} \tag{3.27}$$

The parameter α_{eff} accounts for the finite reference resistance R_S:

$$\alpha_{\text{eff}} = \alpha \left(\frac{R_T - R_S}{R_T + R_S} \right) \tag{3.28}$$

For $R_S < R_T$: $\alpha > 0$ and $\partial P_T / \partial T_e < 0$. This means for rising temperature the heating power decreases and vise versa. As a consequence the self heating of the sensor compensates temperature fluctuations. This negative feedback has been called "electrothermal feedback" and acts as a self-stabilizing effect for the working point of the sensor.

For small temperature fluctuations ΔT_e around the thermal equilibrium the changes of the heating power can be treated as linear. Thus the response of the sensor for events with small amplitude is described by two differential equations, which can be derived from the equations (3.25) and (3.4) after eliminating the stationary case:

$$C_e \frac{dT_e}{dt} + (\Delta T_e - \Delta T_a) G_{ea} + \Delta T_e G_{eb} + \alpha_{\text{eff}} \frac{P_{T,0}}{T_{e,0}} \Delta T_e = P_e(t) \tag{3.29}$$

$$C_a \frac{dT_a}{dt} + (\Delta T_a - \Delta T_e) G_{ea} + \Delta T_a G_{ab} = P_a(t), \tag{3.30}$$

where ΔT_a and ΔT_e are, respectively, the deviations of the absorber and sensor temperature from equilibrium. $P_{T,0}$ and $T_{e,0}$ are the heating power and temperature of the sensor at its (undisturbed) working point. In equation (3.29) the electrothermal feedback acts as additional thermal coupling G_{etf} of the sensor to the heat bath [75]:

$$G_{\text{etf}} = \alpha_{\text{eff}} \frac{P_{T,0}}{T_{e,0}} \tag{3.31}$$

The solution of the two equations (3.29) and (3.30) follows from the formalism presented in section 3.1.1. In the results for the decay times τ_{in} and τ_{t} and amplitudes A_{n} and A_{t}, G_{eb} has to be replaced by $(G_{eb} + G_{\text{etf}})$. For the common case $C_e \ll C_a$, the expressions (3.6) and (3.7) for the decay times τ_{in} and τ_{t} can be simplified:

$$\tau_{\text{in}} \approx \frac{C_e}{G_{ea} + G_{eb} + G_{\text{etf}}} \tag{3.32}$$

$$\tau_{\text{t}} \approx \frac{C_a}{\frac{(G_{eb}+G_{\text{etf}})G_{ea}}{G_{ea}+G_{eb}+G_{\text{etf}}} + G_{ab}} \tag{3.33}$$

As the steepness α can be very large for normal to superconducting transitions, G_{etf} is the dominant thermal coupling for TES sensors operated in strong electrothermal feedback. While the feedback can make the signal rise time τ_{in} very short, τ_{t} is limited by the effective coupling G_{ea} of the TES electrons to the absorber. As the non-thermal decay time τ_{n} is only determined by the decay of the non-thermal phonons in the absorber, this time constant is not influenced by the feedback.

Electrothermal Oscillations

The readout circuit contains the inductivity L of the SQUID input coil. L and the total resistance define the characteristic time constant of the circuit:

$$\tau_{\mathrm{el}} = \frac{L}{R_S + R_T} \tag{3.34}$$

If τ_{in} becomes less than $5.8\tau_{\mathrm{el}}$ the system gets into a state where it oscillates due to the inductivity L and the heat capacity of the sensor C_e [76, 75]. These "electrothermal oscillations" set the limit for the stabilization of the detector by electrothermal feedback. The best performance in terms of stability and signal to noise ratio, however, has been found if the feedback ist just entering the oscillation regime [75].

3.2 Phonon Collectors

For fast and efficient sensors it is important that the non-thermal phonons of the absorber are collected as effectively as possible. According to equations (3.11) and (3.12) this could be achieved by maximizing the area covered by the TES film. However, this would also increase the heat capacity of the sensor and thus decrease the signal amplitude. A solution to this problem is the use of phonon collectors, which are superconducting at the operating temperature of the TES. This way the phonon collecting area can be increased without increasing the heat capacity of the sensor [77].

Fig. 3.6 depicts the working principle of a phonon collector. The collector is an area of a superconductor with a higher transition temperature than that of the TES to which it is connected. Energy deposited into the collector, for example by absorption of high energy phonons from the substrate, or absorption of X-rays, breaks up cooper pairs in the superconductor, and thus excites quasiparticles (QP) above the energy gap. The QP spread diffusively over the whole area of the collector. At the interface to the TES, which is stabilized in its transition, the energy gap becomes zero. QP reaching this point can thermalise and thus deposit heat into the TES.

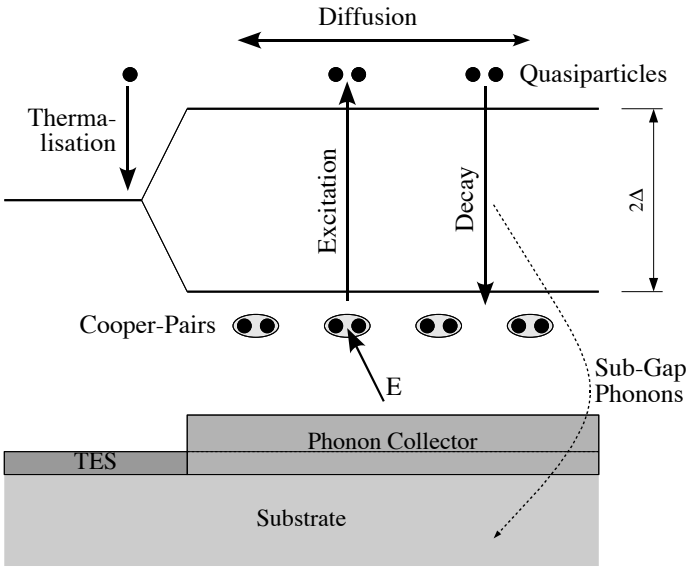

Figure 3.6: Principle of phonon collectors. Bottom: Cut through a typical sensor structure with a phonon collector. A TES is connected to a strip of material (phonon collector) with higher transition temperature than that of the TES. Top: Energy scheme of the sensor structure. Energy (E) absorbed in the collector (e.g. high-energy phonons from the substrate) breaks up cooper pairs and excites quasiparticles (QP). The QP diffuse through the collector strip to the TES, where they can thermalize. QP can also decay in the collector under emission of sub-gap phonons, which end up in the substrate.

The QP which do not thermalise in the sensor can recombine (decay) to cooper pairs in the collector under emission of phonons. Those phonons carry not enough energy to break up cooper pairs again ("sub-gap phonons") and are thus lost for the phonon collector.

In the model presented in section 3.1.1 the phonon collector provides an additional contribution to the decay of the non-thermal phonons in the absorber. The lifetime of the non-thermal phonons is then given as

$$\frac{1}{\tau_{\mathrm{n}}} = \frac{1}{\tau_{\mathrm{film}}} + \frac{1}{\tau_{\mathrm{coll}}} + \frac{1}{\tau_{\mathrm{crystal}}}, \tag{3.35}$$

with τ_{film} being the collection time of phonons in the TES film given by equation (3.11), τ_{coll} the collection time of the phonon collector and τ_{crystal} the decay time of the phonons in the absorber crystal.

The decay time observed in the TES can deviate from τ_{n} due to the time the quasiparticles need to reach the sensor. The non-thermal power input into the sensor is a combination of the directly absorbed non-thermal phonons $P_e(t) \propto \mathrm{e}^{-t/\tau_{\mathrm{n}}}$ in Fig. 3.4 and the power input from the thermalised QP, $P_{qp}(t)$. The time dependence of the latter is discussed in section 3.2.2.

An ideal phonon collector would cover as much surface of the absorber crystal as possible and transport the energy of the absorbed non-thermal phonons in form of quasiparticles to the TES, where they completely thermalise. In reality the efficiency of the collector is limited by the quasiparticle decay, the larger the collector, the larger are the losses therefrom. The critical parameter is the lifetime τ_{qp} of the quasiparticles in the collector film. Imperfections in the film, for example grain boundaries, are decay centers for QP. A characterization of the produced films with respect to their QP diffusion properties is thus needed to allow an optimized collector design.

3.2.1 Quasiparticle Diffusion - Two Sensors

In experiments for the determination of the quasiparticle diffusion properties in a superconducting film typically a setup as depicted in Fig. 3.7 is used. A strip of length L of the investigated superconductor (the "diffusion strip") is connected to two thermal sensors, one on each end. Here the diffusion strip itself acts as absorber for localized events of known energy, for example from an X-ray calibration source. The axis from sensor to sensor defines the x axis in the calculations below.

An event at position x_0 along the strip generates an initial distribution of quasiparticles which spreads diffusively over the whole volume of the strip. Symmetry considerations lead to the conclusion that only the dependence on the x coordinate is significant [78]. The diffusion and decay of the QP

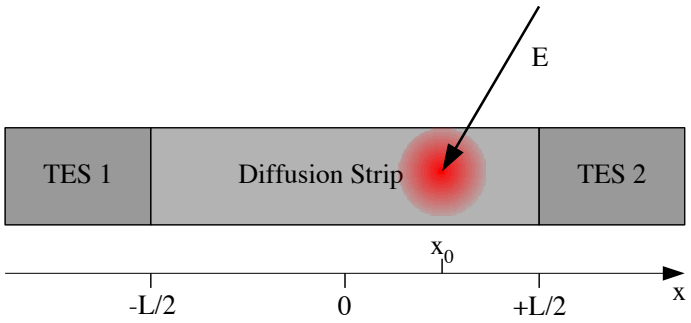

Figure 3.7: Typical setup for the measurement of quasiparticle diffusion parameters. A diffusion strip of length L is connected at both ends to transitions edge sensors. An event with energy E (e.g. an X-ray being absorbed) at position x_0 generates quasiparticles which diffuse in the strip and thermalise in the sensors. From the position dependence of the two signals the diffusion constant D and the quasiparticle lifetime τ_{qp} can be deduced.

in the strip can then be described with a one-dimensional time-dependent differential equation [79]:

$$\frac{\partial n}{\partial t} - D\frac{\partial^2 n}{\partial x^2} + \gamma_D n = 0, \tag{3.36}$$

where $n = n(x,t)$ is the one-dimensional quasiparticle density in particles per unit length at position x and time t. $\gamma_D = \tau_{\mathrm{qp}}^{-1}$ is the decay rate of the QP, and D is the diffusion constant of the film in m^2/s.

The number N_1 of QP collected in sensor 1 at position $-L/2$ and the number N_2 of QP collected in sensor 2 at position $+L/2$ is the integral over all times of the number of QP crossing the interface and thermalising in the sensor:

$$N_{1,2} = D\int_0^\infty \frac{\partial n}{\partial x}(x = \mp L/2, t)dt. \tag{3.37}$$

In the simplest case it is assumed that all QP crossing the interface to the sensor thermalise therein. This sets the boundary conditions for solving equation (3.36):

$$n(x = \pm L/2, t) = 0. \tag{3.38}$$

The initial quasiparticle distribution for a point-like event at position x_0 can be expressed as:

$$n(x, t = 0) = N_0\delta(x - x_0), \tag{3.39}$$

where N_0 is the number of QP excited by the absorbed energy E.

Solving equation (3.36) for this initial distribution and boundary condition (3.38) leads to the following expression for the number of particles collected in the sensors:

$$N_{1,2} = N_0 \frac{\sinh\alpha\left(\frac{1}{2} \mp \frac{x_0}{L}\right)}{\sinh\alpha}, \tag{3.40}$$

with the diffusion parameter $\alpha = L\sqrt{D\tau_{\mathrm{qp}}}$.

If the timescale within the quasiparticle thermalise in the sensor is not small in comparison to the timescale of the diffusion, there is non-disappearing probability that quasiparticles diffuse back into the strip instead of depositing their energy in the TES. The boundary condition for the quasiparticle density at the coordinate of the interface then changes from (3.38) to [80]:

$$n(x = \pm L/2, t) = \sqrt{D\tau_{\mathrm{tr}}}\frac{\partial}{\partial x} n(x = \pm L/2, t), \tag{3.41}$$

with the quasiparticle trapping time τ_{tr}, defining the timescale of the thermalisation.

With these boundary conditions the solution of (3.36) with the initial QP distribution (3.39) leads to the number of particles collected in the sensors [80]:

$$N_{1,2} = N_0 \frac{\sinh\alpha\left(\frac{1}{2} \mp \frac{x_0}{L}\right) + \beta\cosh\alpha\left(\frac{1}{2} \mp \frac{x_0}{L}\right)}{(1+\beta^2)\sinh\alpha + 2\beta\cosh\alpha}, \tag{3.42}$$

with the new parameter $\beta = \sqrt{\tau_{\mathrm{tr}}/\tau_{\mathrm{qp}}}$. In the limit of $\beta = 0$ this equation becomes (3.40).

Fig. 3.8 shows a comparison for the signal amplitude in both sensors of events of fixed energy distributed over the hole strips for the case of perfect collection ($\beta = 0$) and finite collection time ($\beta > 0$). In the second case even for events directly at the interface to one sensor, a non-zero amplitude is seen in the other. The total amount of energy absorbed in the sensors is reduced, however.

3.2.2 Quasiparticle Diffusion - One Sensor

In the case of phonon collectors there is only a sensor on one end of the diffusion strip (see Fig. 3.9). This changes the boundary conditions for the description of the diffusion in the strip.

Assuming perfect collection, the condition for the quasiparticle density at the interface to the sensor is similar to that of equation (3.38). At the end

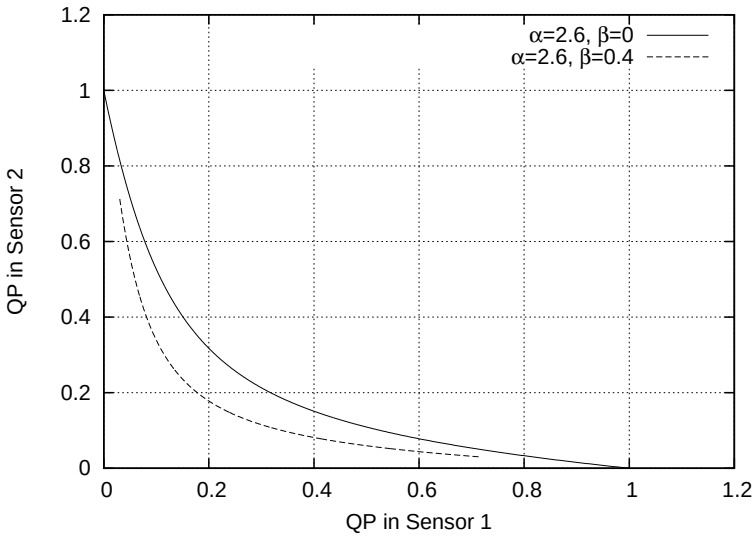

Figure 3.8: Fraction of quasiparticle detected in the two sensors for perfect collection ($\beta = 0$) and for finite trapping time (here $\beta = 0.4$). Both lines are for the same initial energy and events over the hole length of the strip.

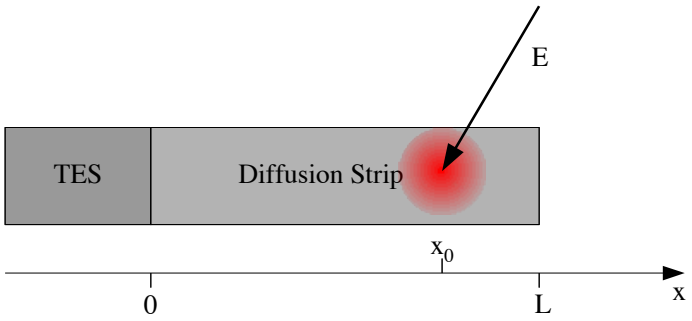

Figure 3.9: Configuration of a quasiparticle diffusion strip contacted to one transition edge sensor. This configuration applies to phonon collectors.

without sensor no QP may cross the boundary of the strip. This leads to the two boundary conditions under which equation (3.36) has to be solved:

$$n(x = 0, t) = 0 \tag{3.43}$$

$$\frac{\partial}{\partial x} n(x = L, t) = 0. \tag{3.44}$$

With these conditions and a point like initial quasiparticle distribution (3.39) at position x_0 in the strip, the number N of QP collected in the sensor calculated from the solution of (3.36) is (for the derivation of this equation see appendix A.1)

$$N = N_0 \frac{\cosh\left(\alpha\left(1 - \frac{x_0}{L}\right)\right)}{\cosh \alpha}. \tag{3.45}$$

If the diffusion strip serves as a phonon collector the energy of an event is not deposited all in a single spot, but evenly distributed over the whole strip due to the absorption of a large number of phonons from the absorber. Assuming at first that the whole energy is deposited at the same time $t = 0$, this leads to an initial quasiparticle distribution of the form

$$n(x, t = 0) = \frac{N_0}{L} \theta(x)\theta(L - x) \tag{3.46}$$

With this initial distribution the current of quasiparticles crossing the interface to the sensor is (see appendix A.1)

$$D \frac{\partial n}{\partial x}(x = 0, t) = D \sum_{k=0}^{\infty} \frac{2N_0}{L^2} \mathrm{e}^{-\left(D(2k+1)^2 \frac{\pi^2}{4l^2} + \gamma_D\right)t}. \tag{3.47}$$

This is for an instantaneous energy input into the collector. In order to obtain the contribution of the collector to the time structure of the pulses observed in the TES, equation (3.47) has to be convoluted with the decay function of the non-thermal phonons in the absorber $f \propto \mathrm{e}^{-t/\tau_{\mathrm{n}}}$.

Efficiency of the Phonon Collector

Integrating (3.47) over all times yields the fraction of the quasiparticles collected in the sensor (see appendix A.1):

$$\frac{N}{N_0} = \frac{l_D}{\sqrt{2}L} \tanh\left(\frac{\sqrt{2}L}{l_D}\right), \tag{3.48}$$

with $l_D = \sqrt{2D\tau_{\mathrm{qp}}}$ as the characteristic length for the QP diffusion. This characterizes the efficiency of a phonon collector. In Fig. 3.10 this efficiency is plotted in dependence of the collector length.

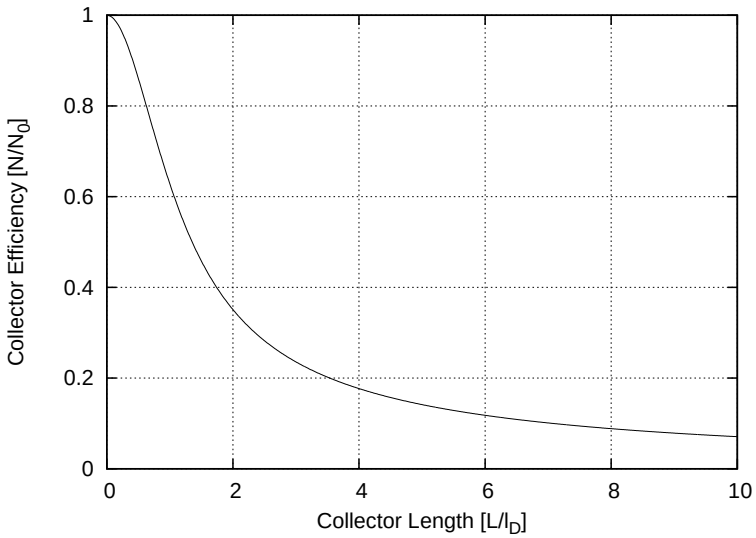

Figure 3.10: The efficiency of a phonon collector in terms of quasiparticle collection in dependence of the length L normalized to the characteristic length l_D of the QP diffusion.

Equation (3.48) describes the fraction of the collected energy that eventually reaches the TES. For the design of a phonon collector also the total amount of absorbed phonons from the crystal has to be considered. This number scales up with the total surface area covered by the collector and thus also with the collector length. The dependency of the collected energy from the collector area has been studied with Monte Carlo simulations in [65].

To summarize, the following points have to be considered for designing a TES structure with phonon collectors:

- The total area of the structure has to be as large as possible for best possible phonon collection. The scaling of the total amount of collected energy depends on the geometry of the absorber. Also the absorber material has an influence as only phonons with energies larger than twice the energy gap of the superconductor used as phonon collector contribute to the collected energy.

- The length of the collector strips is limited by the efficiency given by equation (3.48).

- The total area covered by the actual TES should be kept small to avoid a too large heat capacity and thus a reduced sensitivity of the detector.

The best results so far have been obtained with "distributed TES" structures as described in [65]. Here several individual TES structures each with several phonon collector strips are electrical connected to form a large scale detector structure (see also chapter 6.2).

Chapter 4

Low-Temperature Cryostat and New Data Acquisition System

4.1 Cryostat

The cryostat used for the measurements in this work is a ^{3}He/^{4}He dilution refrigerator of the Oxford 200 TLE type. It provides a cooling power of 200 μW at 100 mK. The specified base temperature is 7 mK, with the present customization (wiring, detector holder structure) a base temperature of 10-12 mK is reached typically.

Fig. 4.1 shows a drawing of the cooling unit of the cryostat. During operation this unit (the inner vacuum chamber = IVC) is evacuated and placed in a liquid helium dewar. The cooling effect of the dilution refrigerator makes use of the fact that below 0.87 K ^{3}He has only a limited solubility in ^{4}He (6.6% at 0 K). Mixtures with a ^{3}He content exceeding this limit form two liquid phases at very low temperatures – one with almost pure ^{3}He and one which consists of a ^{4}He rich phase with a few percent of ^{3}He. The continuous cooling effect is achieved by removing ^{3}He from the ^{4}He phase in the mixing chamber. This loss is compensated by ^{3}He from the other phase. As the specific heat capacity of ^{3}He in the ^{4}He phase is larger than in the ^{3}He phase, for this phase transition the mixing chamber has to absorb heat from the environment, thus cooling it. For further details see e.g. [81, chapter 7].

The most important steps of the cooldown procedure for the cryostat are as follows:

- Evacuate the IVC down to 10^{-6} mbar and fill it with 5 mbar of He gas. This He gas acts as exchange gas providing a thermal coupling between the components of the insert and the liquid helium bath during the first steps of the cooldown until ~ 5 K.

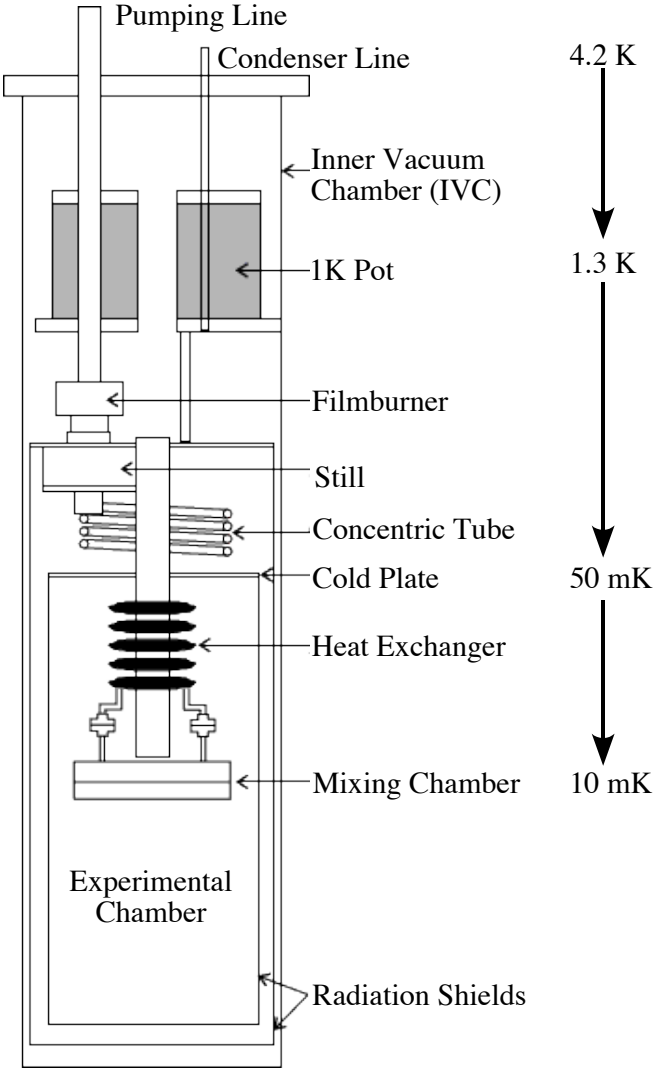

Figure 4.1: Schematic drawing of the inner vacuum chamber (IVC) with the cooling unit of the cryostat used in this work (drawing from [75]).

- Fill the dewar with liquid nitrogen until the insert is below 100 K. Afterwards remove the liquid nitrogen from the dewar and flush the dewar and 1 K pot with He gas.
- Cool the dewar and insert below 10 K with cold He gas boiled off from the liquid He storage tank.
- Remove the He exchange gas by evacuating the IVC. A pressure well below 10^{-6} mbar should be reached.
- Fill the dewar and 1 K pot with liquid helium and pump on the 1 K pot to reduce its temperature.
- As soon as the 1 K pot reaches its operating temperature of about 1.5 K the mixture can be condensed in. At first "offer" mixture to the cryostat by opening the dumps and slowly letting mixture pass through the nitrogen cold traps into the condensor line and the still (see Fig. 4.1). A favorable condensor pressure for this step is about 50–100 mbar.
- When the pressure in the dumps no longer decreases, slowly start circulating. The pressure at the condensor should not exceed 300 mbar.

4.1.1 Detector Setup and Temperature Control

The detector crystals in the cryostat are mounted in specially designed copper holders. The holders serve as heat sink for the detectors. Since only a weak thermal coupling from the detector to the holder is desired, the contact area between holder and detector is minimized, e.g. by placing the substrate on small sapphire spheres. Larger detectors, like the phonon detectors of the CRESST detector modules, are placed on teflon or CuBe clamps to avoid mechanical stress on the crystal while still maintaining thermal decoupling. A defined thermal coupling between holder and detector is eventually realized by a thin gold wire bonded on the crystal and the copper holder. Fig. 4.2 shows a schematic drawing of a typical mounting of a cryogenic detector.

The detector holder itself is also only weakly coupled to the mixing chamber of the cryostat to allow temperature stabilization of the detector at temperatures above the cryostat's base temperature without too much heating of the mixing chamber. The mechanical connection is decoupled by Sintimid, a material with small thermal conductance. The weak coupling is realized with a 1.5 mm^2 cross section copper wire connecting the holder with the mixing chamber.

For controlling the holder temperature a thermometer and heater are mounted on the detector holder. As thermometers, resistors of the type

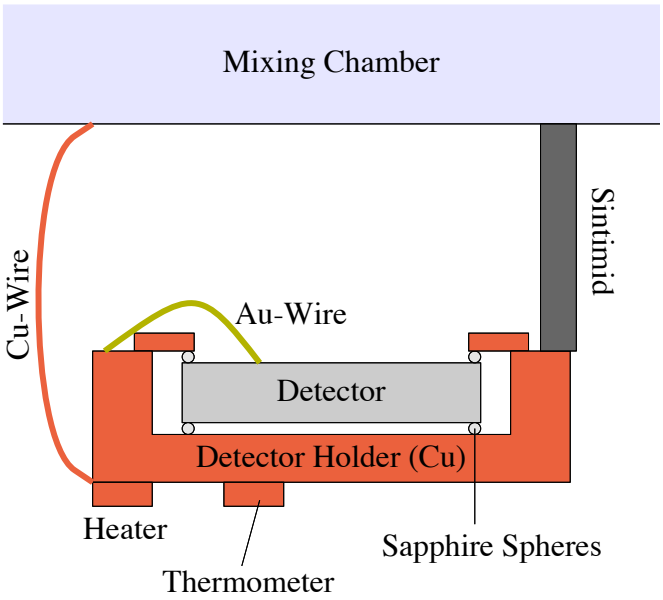

Figure 4.2: Schematic drawing of a typical mounting of a cryogenic detector in the ^{3}He/^{4}He refrigerator. The detector crystal is mounted in a copper holder. Detector and holder are thermally decoupled by placing the crystal on small sapphire spheres (1–2 mm in diameter). A defined weak thermal coupling from the crystal to the holder is provided by a 25 μm thin gold wire. The holder itself is weakly coupled to the cryostat's mixing chamber via a 1.5 mm^2 cross section copper wire. The mechanical connection to the mixing chamber is realised by a rod made of Sintimid, an insulator material with small thermal cunductance. A heater and thermometer are mounted on the detector holder for temperature monitoring and stabilization (see Fig. 4.3).

Speer or ruthenium oxide (RuO_2)[1] are used, both with very steep resistance-temperature characteristics at temperatures below 100 mK. Typical thermometers have a resistance of about 5 kΩ at 100 mK, which rises to 30–50 kΩ at base temperature. The thermometer resistance is measured with a resistance bridge of the Picowatt AVS-47 type. The holder temperature is regulated with a Picowatt TS-580A temperature controller. The resistance bridge and temperature controller are connected by an analogue link, where a voltage corresponding to the measured resistance is passed from the bridge to the controller. The deviation of this voltage from a given set point is converted into a heater output by the TS-580As PID controller (see Fig. 4.3).

Due to the weak thermal coupling of the detector holder to the mixing chamber, the holder can be heated up to more than 100 mK without seriously affecting the base temperature of the cryostat. This way, up to five detectors with different transition temperatures can be operated simultaneously, provided that enough resistance bridges and temperature control units are accessible. In this work up to two channels were used simultaneously. The required heating power and thus the head load on the refrigerator is typically less than 1 μW per channel. As heater resistors, strain gages by Vishay Micro-Measurements glued onto a copper plate are used. These gages have a resistance of 120 Ω at room temperature, which is close to the 100 Ω heater resistance expected by the Picowatt temperature controller.

Previously the wiring between the 1 K stage and the mixing chamber was realised with the same co-axially shielded twisted pair NbTi wires as they are used below the mixing chamber to the experimental set-up. However, this wiring needed too much space and blocked the feedthroughs through the thermal shields of the cryostat. Therefore, this wiring was replaced with unshielded twisted pair NbTi wires which need significantly less space. This way, capacities for future extensions of the set-up became available, e.g. for the wiring needed for Neganov-Luke amplified detectors [82].

4.1.2 SQUIDs

As already mentioned in the previous chapter, the detector signal is read out using Superconducting Quantum Interference Devices (SQUIDs), which are very sensitive to small changes of magnetic fields. The current through the detector is converted into a flux in the input coil of the read out circuit (see Fig. 3.3 and Fig. 4.4). Changes in the flux cause corresponding changes of the voltage in the SQUID. The SQUID response is periodic with one flux

[1] For an overview on thermometers at very low temperatures see e.g. [81, chapter 12]

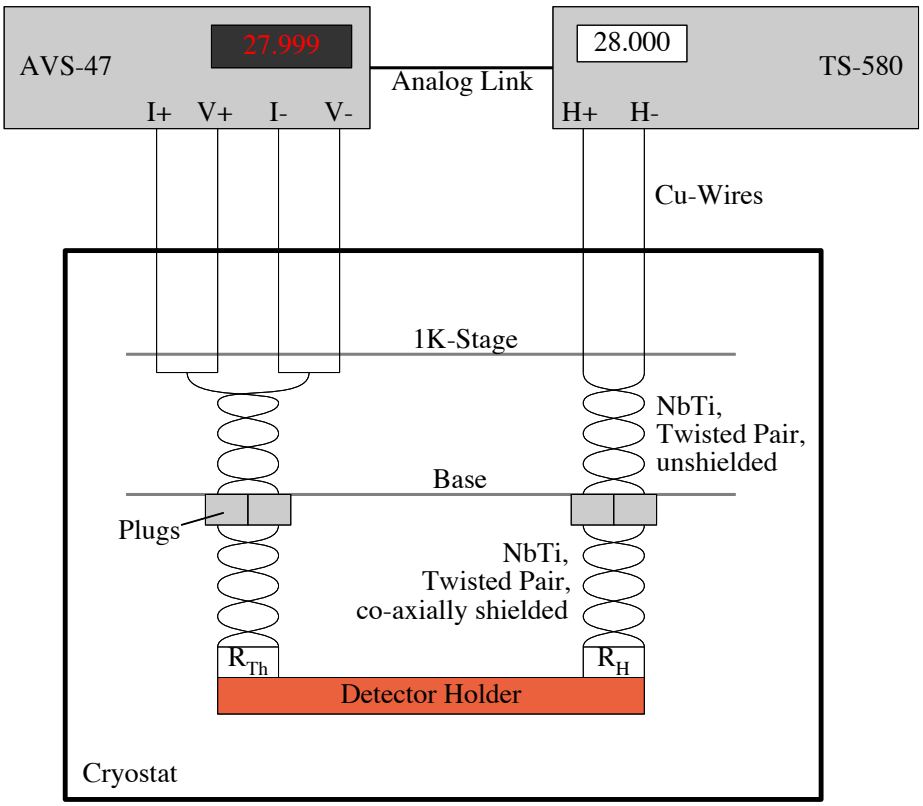

Figure 4.3: Wiring for the temperature stabilization/control of the detectors. The resistance R_{Th} of the thermometer on the detector holder is read out by a resistance bridge of the Picowatt AVS-47 type. The measured resistance value is fed as an analogue signal into a PID temperature controller of the Picowatt TS-580A type which regulates the power applied to the heater resistance R_{H} on the detector holder. The wiring in the cryostat down to the 1 K stage is copper wiring provided by the cryostat manufacturer. For the lower stages superconducting NbTi twisted pair wires are used. Plugs on the mixing chamber allow the easy removal of unused wires from the experimental chamber.

quantum (Φ_0) which would limit the dynamic range of the measurement. To overcome this problem the SQUIDs are operated in Flux-Locked-Loop (FLL) mode, where the field in the input coil is compensated by a field in a second coil, the feedback coil. Thus, the SQUID is kept at one working point. Fig. 4.4 shows the FLL unit of one of the employed SQUIDs.

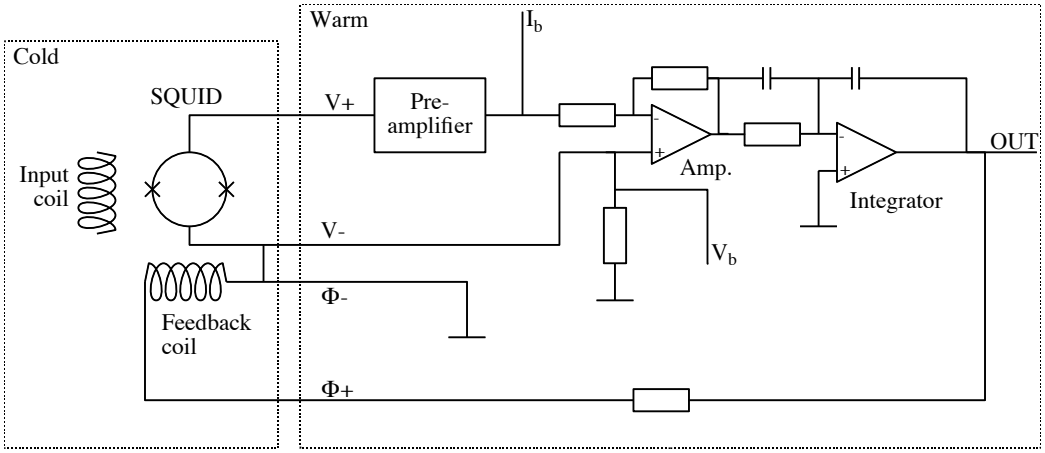

Figure 4.4: Diagram of the Flux-Locked-Loop (FLL) of the Jena SQUID (IPHT, Jena). The employed FLL unit is equipped with an additional custom made pre-amplifier. The input coil is part of the readout circuit shown in Fig. 3.3. The SQUID is biased by a current I_b, a flux change in the input coil causes a voltage change in the SQUID. This deviation from the equilibrium voltage V_b is amplified and integrated. The output of the integrator is sent into the feedback coil to compensate the flux variations in the input coil. The integrator output is also the recorded detector signal (OUT).

The cryostat is equipped with four individual SQUID systems: Two Applied Physics (labeled "AP1" & "AP2"), one from Biomagnetic Technologies (BTI) and one from IPHT Jena. All SQUIDs except that from BTI are installed on the 1 K stage of the cryostat. The BTI SQUID has to be operated in liquid helium and is thus installed in the helium bath. Each SQUID has its own read out circuit with an individual reference (shunt) resistor. Table 4.1 lists the employed SQUIDs together with the shunt resistance values R_S and the amplification factors. The amplification factor is defined the ratio between the amplitude of the output voltage of the SQUID electronics (OUT in Fig. 4.4) to the amplitude of the current in the SQUID input coil.

The Applied Physics and BTI SQUIDs have several selectable pre-amplifications allowing total amplifications as listed in Table 4.1. The electronics of the Jena SQUID, however, is only delivered with a fixed amplification of 10^5 V/A. Often, a larger factor is desired. For this reason the FLL-unit of the

SQUID	$R_S[\mathrm{m}\Omega]$	**Amplifications** [V/A]
AP1	21.7	$4.5 \cdot 10^4$, $4.5 \cdot 10^5$, $4.5 \cdot 10^6$, $4.5 \cdot 10^7$
AP2	30	$4.5 \cdot 10^4$, $4.5 \cdot 10^5$, $4.5 \cdot 10^6$, $4.5 \cdot 10^7$
Jena	56.7	$1 \cdot 10^5$, $10.1 \cdot 10^5$, $20.1 \cdot 10^5$, $49.7 \cdot 10^5$
BTI	6.7	$5 \cdot 10^4$, $5 \cdot 10^5$, $5 \cdot 10^6$, $5 \cdot 10^7$

Table 4.1: SQUIDs used in the Oxford TLE200 cryostat, their shunt resistor values and amplification factors.

Jena SQUID was equipped with an additional pre-amplifier with selectable amplification factors of 10, 20 and 50.

4.2 New Data Acquisition System

For recording the detector data, a new data acquisition was set up as part of this work, replacing the old CAMAC-based system described in [75] and [65]. The new system is based on a PXI-Bus system with a controller type 8186 from National Instruments. The PXI system is based on standard PC technology, the bus is an extension of the PCI bus with a different slot format optimized for data acquisition systems. The controller is a fully functional individual Windows XP computer with a 40 GB hard disc, so that no additional computer for data storage is required.

The system is equipped with two National Instruments ADC (analogue to digital converter) cards. One is the 16 bit and 16 channel multiplexed (i.e. one ADC for all channels) PXI-6250 card with 1 MS/s (= 1 million samples per second) sampling rate. This card is mainly used as a digital volt meter, e.g. for recording the analogue output signal of the resistance bridge along with the detector pulses. The pulses are recorded with the second card, a 12 bit and 10 MS/s card of the PXI-6115 type with 4 simultaneously sampled channels, i.e. each channel has its own ADC.

4.2.1 Custom Trigger Module

The recording of an event in the detector should be triggered whenever the signal amplitude rises beyond a given threshold above the baseline. The PXI-6115 module can trigger the recording of a pulse either internally on one of the recorded channels or on a signal of a special trigger-input channel. However, for the latter the signals from the cryodetectors are too small. Therefore, if the internal trigger of the module is to be used, the digitizer channel which is being recorded has to be the trigger source. In this case

the baseline of the signal constitutes a problem: the baseline has to be at 0 V for the trigger to work properly, thus the signal for the trigger has to be AC coupled. However, the DC output of the SQUID signal is an important information for the stability of the detector and should thus be recorded with each pulse. As the coupling of the trigger and the ADC of a channel are not independent, it is not possible to maintain the baseline information in the recorded data *and* to have a working trigger.

To overcome these problems a PXI module providing an external trigger for the ADC module was developed together with N. Halder (Halder Elektronik, Seehausen). The module is based on a PXI prototyping board of the PX2000-107 type from PXIT (no longer available). The board provides a basic interface to the PXI bus and has room for custom circuits. The custom circuit is a simple trigger logic with two input channels for the signals and two output channels for the trigger signal – one with an AND gate and one with an OR gate. Each input channel can be activated for the logical operation of either output channel.

Fig. 4.5 shows a simplified circuit diagram of the trigger module. The coupling (AC or DC) of an input channel I_i from the detector can be selected with a relais switch (Rel_i). The signal level of I_i is compared with the user-defined trigger threshold T_i. If I_i is higher, the trigger line S_i for this channel is set to high. The trigger lines S_i for all four channels are fed into the logic circuits for the AND and the OR logic. To enable channel i for the AND or OR gate, line A_i is set low or line O_i is set high. The output of the AND logic is high, when all active channels are above the threshold. The output of the OR logic is high, as soon as one of the active channels has triggered. The outputs of the logic units are then finally passed through a TTL pulse shaper, generating a short ($\sim 1\,\mu$s) TTL pulse that starts at the time when the output of the logic switches to high. This TTL pulse can then be used as the input for the designated trigger channel of the PXI-6115 ADC module.

All settings of the module are performed via the on-board computer interface. The trigger level is set using four 12-bit DAC (digital-to-analogue converter), one per channel. The input voltage range is ± 10 V, which is the dynamic range of the utilized SQUID electronics, and thus also the selected range in the ADC module for event recording. For controlling the trigger board a LabView program (`trigger_config`) was written.

4.2.2 Cross Talk Checks on the NI-PXI-6115 Module

The most common situation where more than one channel of the ADC card is used, is the recording of coincident phonon and light events in a double detector as described in chapter 2. Especially for nuclear recoil events the

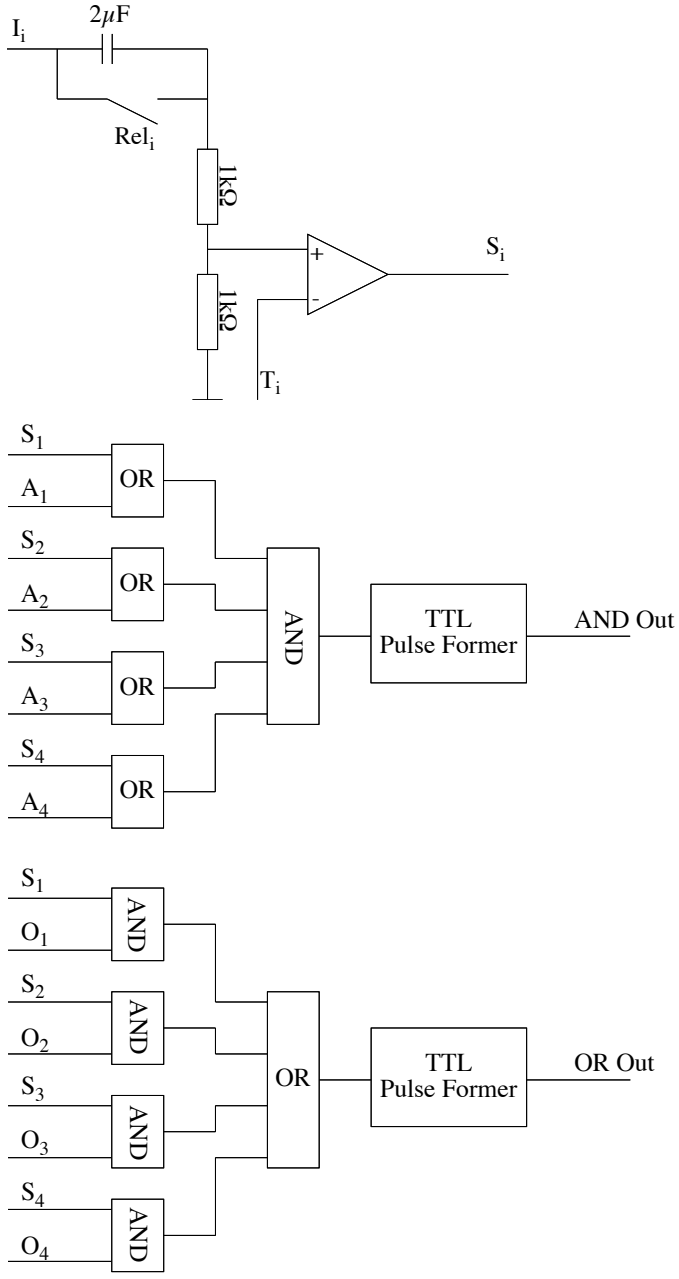

Figure 4.5: Simplified circuit diagram of the trigger module provided by Halder Elektronik. The components for the computer interface are omitted. Top: Comparator circuit for one input channel. I_i is the signal from the detector. With the relais switch Rel_i the coupling AC or DC can be selected. The output S_i is high if the input voltage is above the threshold voltage T_i. The two diagrams below show the logical connection for the four channels for AND and OR output respectively. To enable channel i for the AND or OR gate, line A_i is set low or line O_i is set high respectively. The trigger signal on the output lines is a short ($\sim 1\,\mu$s) TTL pulse.

signal in the light channel is small compared to the one in the phonon channel. Thus, a potential electronic cross talk from the large phonon signal into the light channel is to be considered as part of the systematic error of the measurement.

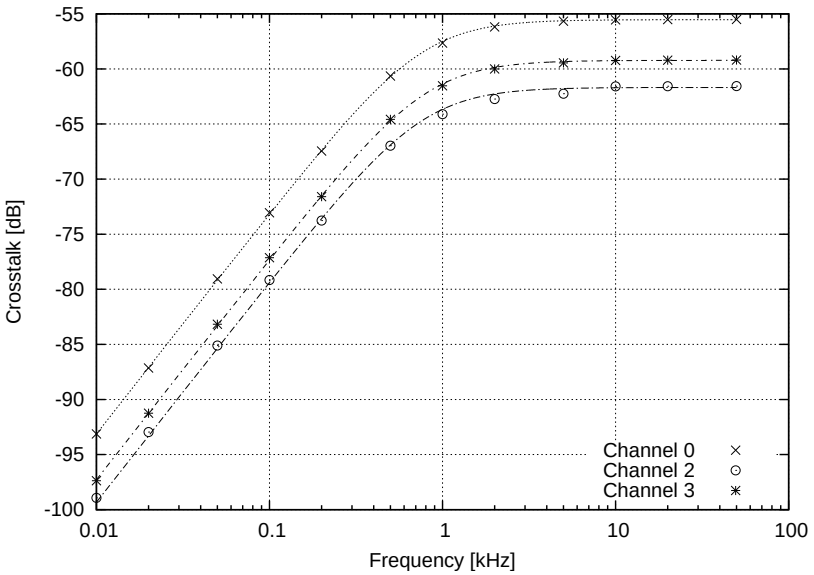

Figure 4.6: Frequency dependent cross talk in terms of power (amplitude squared) on channels 0, 2 and 3 when applying a sinusoidal signal of 10 V amplitude to channel 1. The dotted lines are fits to the data with a first order high pass characteristic (see equation (4.1)).

The cross talk between all four channels was measured for frequencies from 10 Hz to 50 kHz. For each frequency a sine wave with an amplitude of 10 V from a wave-form generator was applied to the investigated input channel of the PXI-6115. The other three channels are left open, i.e. are freely floating. The corresponding power (amplitude squared) on the open channels for the particular input frequency is then determined. Fig. 4.6 shows the results of these measurements for the cross talk power from channel 1 to the channels 0, 2 and 3.

The dependency of the measured cross talk on the frequency ν can be well fitted with a first-order high-pass characteristic combined with a frequency independent attenuation:

$$T(\nu) = \frac{\frac{\nu}{\nu_0}}{T_0\sqrt{1+\left(\frac{\nu}{\nu_0}\right)^2}}, \tag{4.1}$$

where T_0 is the frequency independent attenuation and ν_0 is the characteristic frequency of the high pass. The attenuation between channel 1 and the other three read-out channels is at least 55 dB. From a 1 V signal amplitude on channel 1, at most 1.7 mV are observed in the other channels. Similar results are obtained for signals on the other channels. Table 4.2 summarizes the results for the cross talk measurements between all channels. Listed are the values obtained for T_0 as this is the minimum attenuation for high frequencies (up to 50 kHz), at low frequencies the attenuation is stronger and less cross talk is observed (see Fig. 4.6).

		From Channel			
		0	1	2	3
To Channel	0	×	55.5	72.1	90.1
	1	55.2	×	60.8	59.3
	2	72.3	61.7	×	52.2
	3	90.5	59.2	51.8	×

Table 4.2: The frequency independent attenuation T_0 in dB as derived from the measured cross talk between all channels of the PXI-6115 module.

4.3 Measurement Techniques

The two major demands on the data acquisition system are the recording of the transition curves of the TESs and the recording of detector events. The required software for those tasks is programmed in LabView. Below, the set up and programs for recording transitions and events are briefly presented.

4.3.1 Recording Superconducting Transitions

For recording the transition from the normal to the superconducting state of a TES, the method of applying stepwise changes of the detector-bias current as described in [75] is used. In this method the detector is alternately biased with a current $+I_0$ and $-I_0$. The corresponding change ΔI_T in the TES branch of the read-out circuit (see Fig. 3.3) is recorded. The TES resistance R_T can be calculated as:

$$R_T = R_S \left(\frac{2I_0}{\Delta I_T} - 1 \right), \tag{4.2}$$

where R_S is the reference resistance in the read-out circuit. By varying the temperature of the detector holder, the transition curve of the sensor can be recorded.

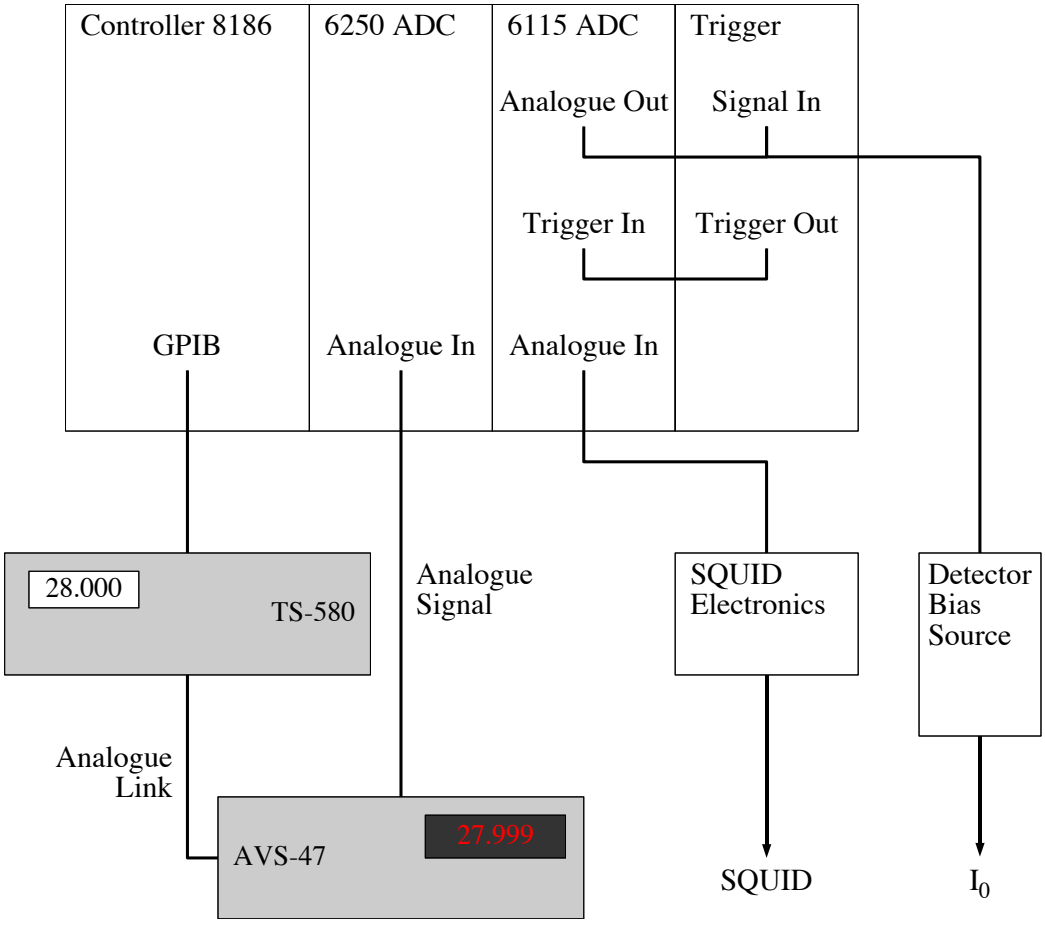

Figure 4.7: Connection scheme of the new data acquisition system for recording transition curves. Details are given in the text.

Fig. 4.7 shows how the components of the new DAQ system have to be connected for the recording of detector transition curves. Via an analogue-output channel of the PXI-6115 voltage step functions from $-V_0$ to $+V_0$ (V_0 being typically 1 V) are generated and fed into the external voltage input of the detector bias current source, where they are converted into current steps. The resulting current steps should not be too large, as the heating power generated in the sensor might otherwise shift the transition. Typically, $I_0 = \pm 1\,\mu$A is chosen.

The voltage steps are also fed into a signal input of the trigger board in order to obtain a trigger signal on the rising edge of the voltage steps. Following this trigger signal, the detector response to the step in the bias current is recorded via the PXI-6115 board. Pretrigger and record length are chosen in such a way that the switch from negative to positive current is in the center of the recorded time window. From the signal amplitudes at the beginning and at the end of the window ΔI_T can then be derived.

The holder temperature is monitored by recording the analogue output voltage of the resistance bridge AVS-47, which corresponds to the displayed value. The temperature can be varied by the computer by connecting the computer interface of the Picowatt TS-580 temperature controller to the GPIB interface of the controller 8186 of the PXI system.

On the software side three LabView programs are needed for recording transition curves:

- `transition_analogue` is the central tool performing the actual data recording. It generates the bias steps, records the detector response and the holder temperature. The program contains the parameters for the employed SQUID systems and calibration curves of the thermometers. Thus, an online conversion of the measured voltage steps to TES resistance and thermometer resistance to temperature is possible. The data is written to the disc as a text file, containing the raw data (SQUID voltage and thermometer resistance) as well as the corresponding converted values.

- `trigger_config` for configuring the trigger module.

- `sweep_pid` performs sweeps on the set point of the temperature controller and thus allows the variation of the holder temperature. It comes in two forms: `sweep_pid` sweeps from a given start to an end point and stops, `sweep_pid2` sweeps back and forth between start and end point until it is stopped by the user.

4.3.2 Recording Detector Events

When recording events from the detector both the holder temperature and the detector bias have to be constant. Thus, they are not set by the computer but manually on the temperature controller and the detector bias source. Fig. 4.8 shows the set up of the data acquisition system for recording detector events. Since triggering is performed on the detector pulses, the SQUID output is fed into one input channel (e.g. signal 1) of the trigger module and in parallel into one of the ADC channels of the PXI-6115 module. The trigger is operated in AC mode, while the ADC module runs in DC mode, maintaining the base line information of the recorded pulses. To reduce the noise on the signal the SQUID output can be cleaned a low-pass filter with a typical cut-off frequency of 10 kHz.

To determine the detector threshold noise samples without pulses are needed. Those can be recorded together with the normal events by triggering at arbitrary times. To achieve this, a second trigger input consisting of a low frequency TTL signal ($\sim$ 0.5 Hz) from a waveform generator is fed into a second input channel (signal 2) of the trigger module. Using the OR logic, a baseline sample of the SQUID signal is then recorded every two seconds, while the triggering on the event pulses is still maintained.

For monitoring the stability of the system the holder temperature can be recorded along with the detector pulses. To do this the analogue output signal of the AVS resistance bridge is connected to an input channel of the 16 bit ADC module PXI-6250.

On the software side again several LabView programs are involved to perform this task:

- `main_panel` is the main program, where the settings for the ADC module PXI-6115 are made. It allows the simultaneous recording of up to four input channels. For each channel the parameters (e.g. dynamic range, the type of coupling) can be set individually. As trigger source usually the trigger input channel (Trigger In) of the ADC module is selected, but if required, the trigger can also be set on one of the data channels (Analogue In).

- `trigger_config` is again used to perform the settings for the trigger module.

- `saver_new` is actually a family of programs for saving pulses. The pulses are saved in the "rop data" (rdt) format, which is also used by the CRESST experiment. Thus the same tools as used in CRESST can be employed for data analysis. The versions of the saver tool are:

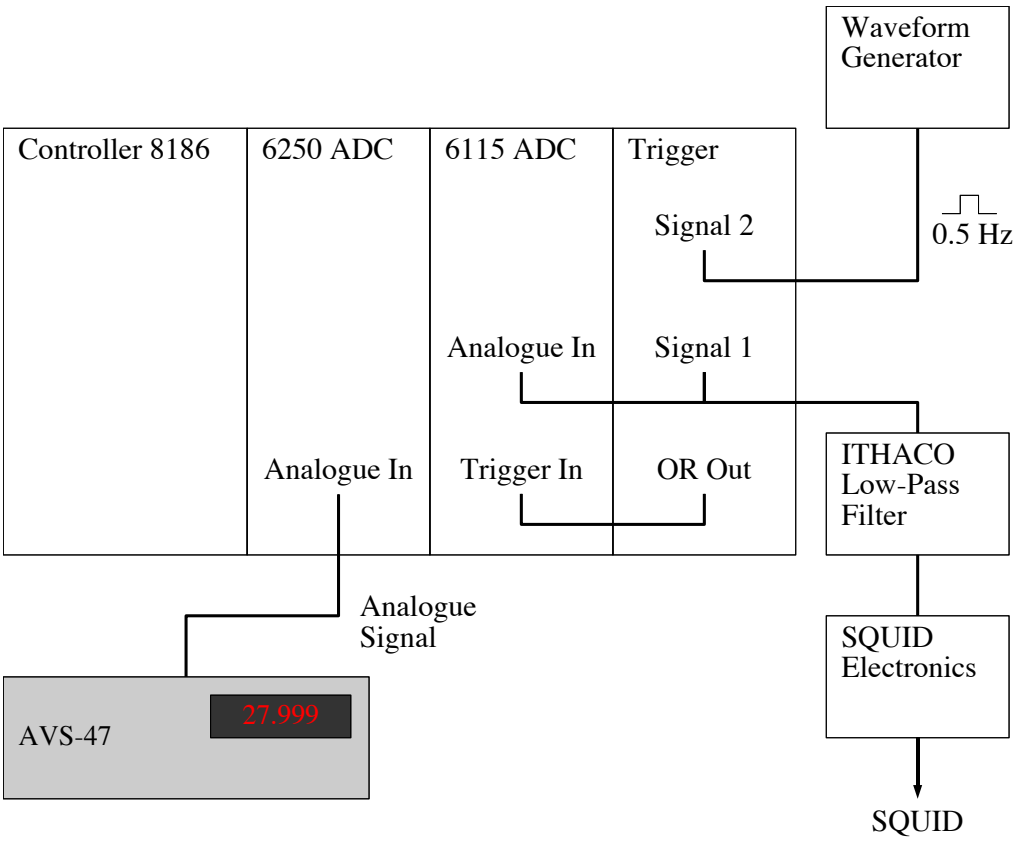

Figure 4.8: Connection scheme of the new data acquisition system for recording detector events.

  - `saver_new`, which is the basic version. It saves a given number of events and stops once the selected number is reached.
  - `saver_new_dvm` records four voltage values along with each event. The voltage values are measured by the PXI-6250 module using the `monitor_voltages` program. This saver is used, whenever the holder temperature is to be monitored.
  - `saver_multi` saves multiple files. This way huge statistics can be collected without running into the 2 GB size limit of the file system. Whenever a given number of events is written, a new file is started. The filenames consist of a user defined prefix and a number which is incremented with each new file.

- `mca` provides an online spectrum. It performs online a basic pulse height determination and plots a spectrum. It can be used to quickly find the best working point of the detector. As it is very CPU consuming, it should not be active while data is actually recorded, as it would limit the possible count rate.

Chapter 5

Fabrication of Cryogenic Detectors

5.1 Ir/Au Films

The Ir/Au films are produced by electron beam evaporation performed in a dedicated ultra high vacuum system [83]. Fig. 5.1 shows a photograph of the Ir/Au system with its two vacuum chambers. The residual pressure in the main chamber in idle state is in the 10^{-8} mbar range. During film deposition, the walls are cooled by liquid nitrogen to freeze out the residual gas. This improves the pressure by another two orders of magnitude, i.e. $\sim 10^{-10}$ mbar. In order to introduce the substrates into the system without having to vent and open the main chamber, a second, smaller vacuum chamber (the load lock) is connected to it. The load lock can be vented and pumped independently of the main chamber. After loading the substrates into the load lock, the latter can be pumped and the substrates can be transferred into the main chamber without breaking the vacuum.

As substrate materials, silicon, germanium, $CaWO_4$ and sapphire (in the form of silicon-on-sapphire, see section 6.3) were used in this work. Before being introduced into the evaporation system the substrate surfaces are cleaned in a class 10000 clean room. The surface to be covered with the film has to be free of any dust particles and other contaminations. For cleaning the substrates, they are put into baths of aceton (or isopropanol) and deionized water and then flushed with nitrogen gas. If the substrate materials are suitable for it, the cleaning with aceton can be supported by putting them into an ultra-sonic bath. This, however, is not advisable for germanium and $CaWO_4$, as these materials have a tendency of cleavage, and often break when exposed to ultra-sonic vibrations. In order to minimize the exposure

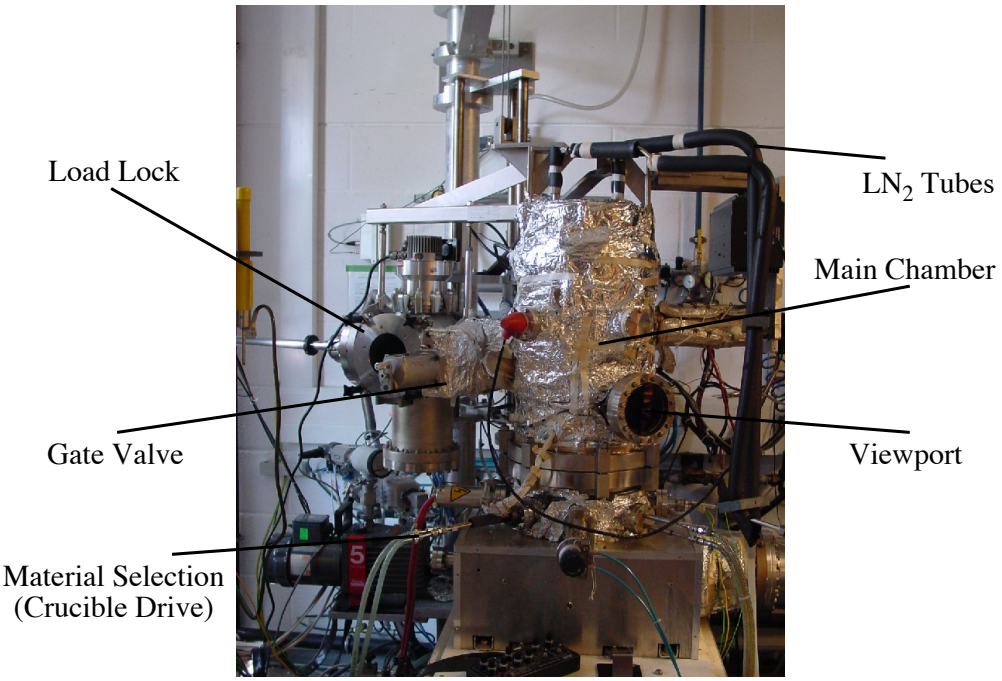

Figure 5.1: Photograph of the Ir/Au UHV evaporation system with its two vaccum chambers. The larger one, the "main chamber", houses the electron gun for the evaporation of the materials. The smaller chamber, the "load lock" is used to introduce the substrates into the system. The two chambers are separated by a gate valve, so that the load lock can be vented independently of the main chamber. During film deposition the walls of the main chamber are cooled by liquid nitrogen to obtain a better pressure ($\sim 10^{-10}$ mbar).

of the cleaned substrates to normal air outside the clean room, they are put into a pumped exsiccator for the transport to the evaporation system.

In the evaporation system the substrates are maintained in tantalum holders with shadow masks limiting the size of the film to the area needed for the later detector structure. Fig. 5.2 shows an overview of shadow masks that were used for Ir/Au film production. The sizes of the masks range from circles with 1.5 mm diameter (mask "E", used for the TES substrates employed in composite detectors) up to areas that almost completely cover $20 \times 10\,\mathrm{mm}^2$ substrates (mask "C"). The evaporation system is equipped with a boron nitride substrate heater allowing to heat the substrates during deposition up to $\sim 500°\mathrm{C}$.

For the Ir/Au films the best results are obtained, when the iridium film is evaporated on top of the gold film [84]. However, for many substrate materials the gold film does not stick very well to the substrate surface. For this reason the Ir/Au films are realized as a three-layer structure: a thin (50 Å) Ir layer as "sticking layer", then the gold layer and finally the actual superconducting Ir layer. The thicknesses of the two latter layers depend on the desired transition temperature.

5.2 Photolithography

Two kinds of photolithographic processes are involved in the fabrication of the detector structures presented in this work: A positive process for structurizing films after evaporation and a negative process for creating lift-off masks before film deposition. The photoresists for both processes are obtained from *micro resist*, Berlin [85].

The positive process is used to create the TES structure from the iridium gold films. It involves the following steps:

- Cover the substrate with photoresist of type ma-P 215 and spin it at 1000 rpm.
- Bake the resist. Thin substrates are put on the hot plate at 95°C for 5 min. $CaWO_4$ crystals are baked in the oven at 100°C for 20 min.
- Align the mask in the mask aligner and expose the photoresist for 20 s to the light of a 300 W mercury-vapor lamp.
- Develop in developer of type ma-D 332S for about 1 min.
- Rinse the substrate with ultrapure water and flush it with nitrogen to dry it.

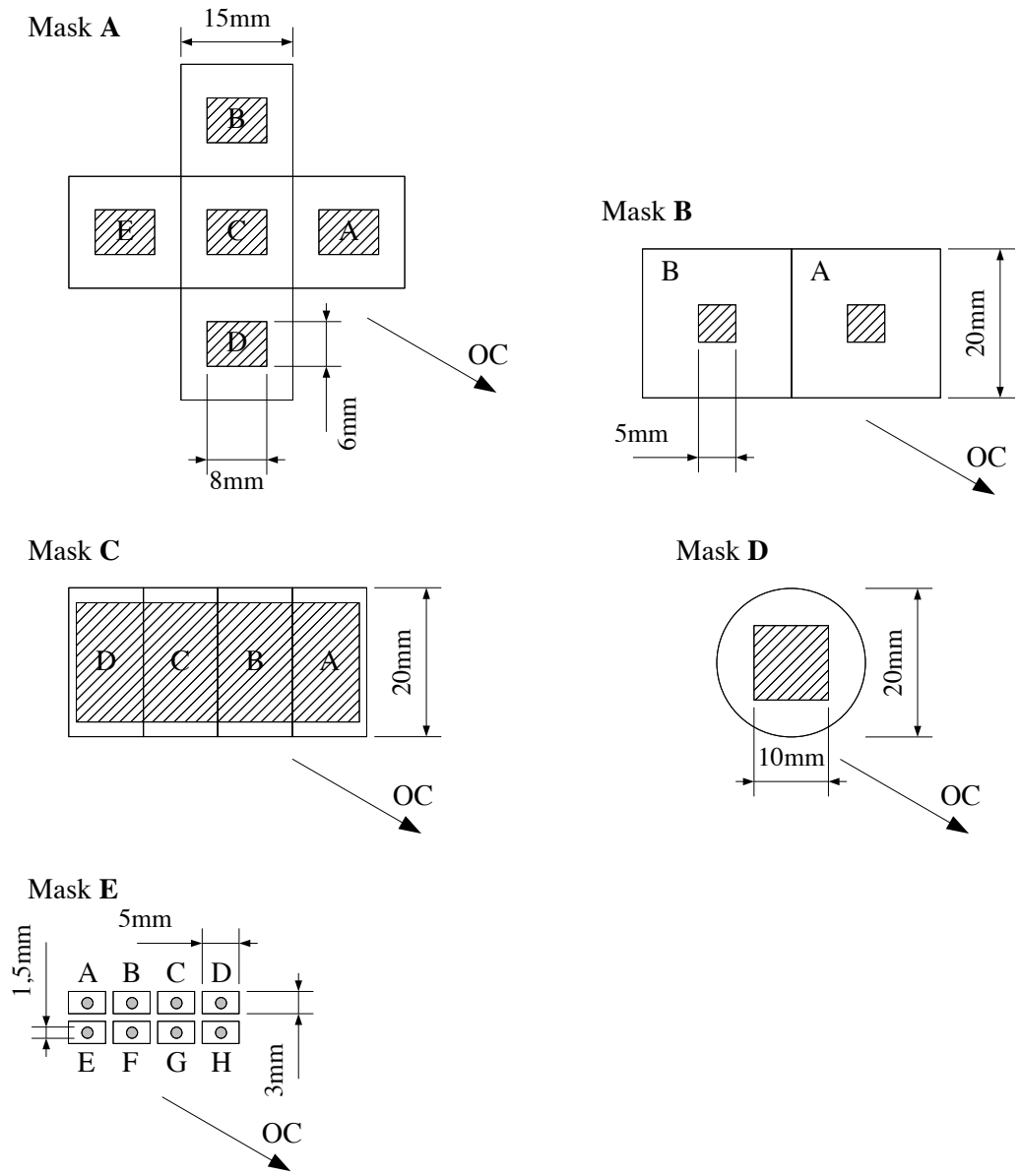

Figure 5.2: Shadow masks used for Ir/Au film production. The shaded areas are exposed to the evaporating Au or Ir. Masks A,B,C and E are designed to carry more than one substrate. The letters indicate the respective positions of the substrates relative to the oscillating crystal. The arrow labeled "OC" indicates the direction, where the oscillating crystal of the deposition monitor is located in the evaporation system. In the drawings the masks are viewed from the top, i.e. the film is deposited from below.

The Ir/Au films are structurized by ion etching in an argon sputtering system. Afterwards the remaining photoresist is removed in acetone.

For the aluminum structures and gold bond pads lift-off masks are produced before the film deposition with the following photolithographic process:

- Cover the substrate with photoresist of type ma-N 420 and spin it at 3000 rpm.
- Bake the resist. Thin substrates are put on the hot plate at 100°C for 5 min. $CaWO_4$ crystals are baked in the oven at 100°C for 20 min.
- Align the mask in the mask aligner and expose the photoresist for 120 s to the light of a 300 W mercury-vapor lamp.
- Develop in developer of type ma-D 330 for about 1 min.
- Rinse the substrate with ultrapure water and flush it with nitrogen to dry it. For very fine structures, like the phonon collectors of a distributed thermometer structure, the strong flow from the nitrogen bottle may destroy the structure. In this case the substrate can be dried using the spinner at 1000 rpm.

The aluminum or gold films are then deposited (see the sections below) on top of the lift-off mask, which covers the whole surface except the desired structure. After the film deposition the photoresist along with the excess deposited material is removed in acetone.

5.3 Aluminum Films

The aluminum films for the phonon collectors (see section 3.2) are produced using electron beam evaporation in a dedicated ultra high vacuum system. The system consists of several connected vacuum chambers. The load lock, where the substrates are brought into the system, can be vented independently from the other chambers. The "argon chamber" contains an argon sputtering cathode which can be used for precleaning of the substrates. The films are produced in the "evaporation chamber" with the electron gun for the aluminum deposition. The evaporation chamber contains a refill system for the crucible with a storage for several refills. This way the chamber can stay evacuated for long periods of time.

A heater installed above the substrate holder in the evaporation chamber can be used to heat the substrate via radiation during deposition. As there is no temperature control or even monitoring installed, the applied heating

power can only be characterized by the current through the heater resistance. For the aluminum films for detector structures this heater current is typically set to 10 A, at higher currents the photoresist of the lift off mask may be destroyed.

For the film production the following process is used:

- Insert the substrate into the load lock and pump it to the 10^{-6} mbar range.
- Transfer the substrate into the argon chamber and clean it for 90 s in the argon beam to remove adsorbates from the surface.
- Transfer the substrate into the evaporation chamber. Turn on the substrate heater and wait until the heating current stays stable. Start evaporating at a low deposition rate (~ 0.5 Å/s). After 200 Å increase the electron beam current, so that an average deposition rate of about 10 Å/s is reached. This setting is kept until the final film thickness of 8 kÅ is reached.
- Transfer the substrate into the load lock and vent it with nitrogen. Remove the substrate from the load lock.

5.4 Gold Pads

The gold films for the gold bond pads are produced using argon sputtering in a multipurpose sputtering system. The system is not dedicated to one target material, but is used for the deposition of a variety of materials. This may effect the purity of the produced gold films, but as for those no special requirements are needed, this is not an issue.

The sputtered gold films have shown a tendency to lift off the substrate when directly deposited onto the crystal. For this reason a thin Ir film is also deposited, before the gold bond pad is mode, similar to the sticking layer of the Ir/Au films.

5.5 Membrane Etching

For some applications the sensors are not produced on a solid substrate but on a thin membrane. This membrane consists of a thin ($\sim$ 400 nm) silicon nitride (Si_3N_4) layer on a silicon substrate. At the place of the sensor structure the silicon substrate has a hole, leaving only the membrane. The thin membrane suppresses phonon propagation and thus detectors on it are

phononically decoupled from the substrate. A typical application for these membrane substrates are microcalorimeters with small metallic absorbers [86]. In this work they are used for the detectors for the determination of the quasiparticle diffusion properties of aluminum (see chapter 5.7).

As the thin membrane is extremely sensitive and can easily be destroyed, the substrates are delivered with a few microns of silicon underneath the membranes for protection. This silicon is left there during the sensor fabrication and has to be removed as a final step. This is performed by etching the silicon in a solution of KOH and isopropanol in water.

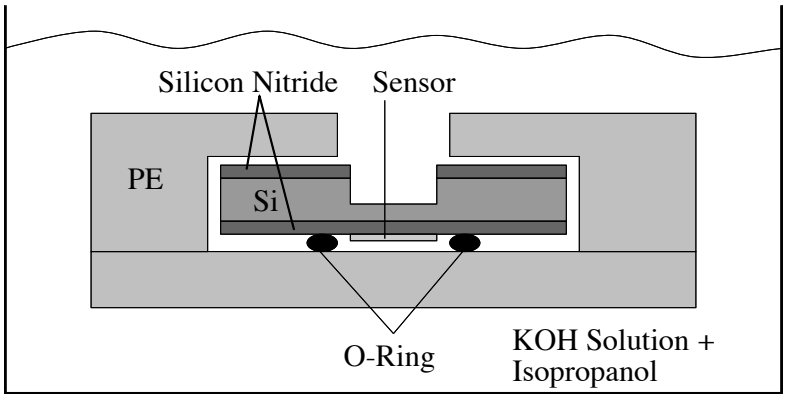

Figure 5.3: Set up for etching of membrane substrates. The substrates are tightly held in PE holders. To protect the sensor it is kept in a O-ring sealed volume. The etching of the silicon is performed in a KOH solution together with isopropanol.

Fig. 5.3 shows a schematic view of the set-up for the etching of the silicon underneath the membrane. The substrate is kept in a polyethylen (PE) holder, which leaves access to the parts that have to be exposed to the etching solution. As the detector films, particulary the aluminum films, would be destroyed after a contact to the KOH, the sensor is sealed in the holder by an O-ring. For etching the silicon the beaker containing the PE holder with the substrate and the KOH solution is carefully heated in a water bath (the solution must not boil). After a few hours the etching is completed. Before dismounting the holder it has to be rinsed with ultrapure water, so that all remaining KOH is removed. After that the seal to the detector can be opened.

5.6 Ir/Au Thermometers

The detectors presented in this work are all based on transition edge sensors consisting of superconducting Ir/Au bi-layer thin films. Due to the proximity

effect (see e.g. [87]) such bi-layers show a transition from the normal to the superconducting state at lower temperatures as compared to pure Ir films ($T_c = 112.5\,\mathrm{mK}$ for bulk material [88]).

For bi-layers of two materials with different transition temperatures, the combined transition temperature of the proximity film is mainly influenced by the thicknesses of the films of the two materials and the electronic coherence lengths [89]. If these parameters vary over the area of the film, this will result in a broadened and non-uniform transition curve. The coherence length is strongly influenced by the grain sizes of the deposited films.

5.6.1 Film Production Parameters

The three layers are deposited at different substrate temperatures:

- The first iridium layer is evaporated at 300°C for all substrate materials except $CaWO_4$. For this crystal a higher temperature of 450°C is used.
- The gold layer initially was deposited at 100°C. For later films this was changed to 150°C, as this showed better results (see below).
- The final iridium layer is deposited at room temperature. At first this meant to let the substrate cool down as far as possible. Due to the cooling of the liquid nitrogen shield, the starting temperature was even below room temperature. At the start of the evaporation the substrate was at 5–10°C. However, due to the heating power of the electron gun the temperature rose to 30°C and more during the process. Thus, in order to provide more stable conditions during the film deposition, in later films the temperature was stabilized at 30°C.

In the first films produced a large variation of the deposition rate was tolerated, as long as the films were deposited within reasonable time. For films produced later on in this work, it was attempted to keep the rates at the same values for all produced films, in order to keep stable and reproducible conditions concerning the film production. The chosen rates were $0.3\,\text{Å/s}$ for iridium and $1.4\,\text{Å/s}$ for gold.

One of the factors influencing the transition curve of the film is the effective electronic coherence length ξ. Measurements of the Ir/Au films with transmission electron microscopy showed a granular structure of the gold layer [65]. As mentioned above, the size of the grains influences the coherence length. Thus, for the best possible transitions it is necessary, that the grains are as large as possible, and – even more important – that the grain size is homogeneous over the whole film area. Smaller grains in thin films can

be "healed out" by annealing the film after deposition [90]. For this reason an annealing step was introduced at the end of the production process of our Ir/Au films. After deposition they are heated to 200°C for two hours in the vacuum of the evaporation system. For $CaWO_4$ crystals, however, this step is omitted, as heating the crystals in vacuum can lower their light output [91], thus, the time at high temperatures for the crystal has to be minimized.

5.6.2 Results and Discussion

A list of Ir/Au films produced and investigated in this thesis is given in Table 5.1 and Table 5.2. Table 5.1 lists the production parameters of the films, such as substrate temperature, thickness, and deposition rates for the three layers. Between the films 471 and 489 the electron gun of the Ir/Au system was undergoing major maintenance. From film 501 on, the deposition rates and the substrate temperature for the final iridium layer were stabilized.

In Table 5.2 the transition temperatures T_c and transition widths ΔT_c of the investigated films are listed. For the determination of T_c and ΔT_c the measured resistance $R_{\mathrm{meas}}(T)$ is corrected by subtracting the measured residual resistance $R_{\mathrm{meas,min}}$ for the film in the superconducting regime:

$$R(T) = R_{\mathrm{meas}}(T) - R_{\mathrm{meas,min}}. \tag{5.1}$$

T_c and ΔT_c are then defined with respect to the normal conducting resistance R_{normal}:

$$T_c = T(R = 0.5R_{\mathrm{normal}}) \tag{5.2}$$

$$\Delta T_c = T(R = 0.9R_{\mathrm{normal}}) - T(R = 0.1R_{\mathrm{normal}}). \tag{5.3}$$

$R_{\mathrm{meas,min}}$ can be non-zero due to possibly present extra resistances in the circuit or due to the uncertainties of the SQUID amplification factors used (the factors are taken from [75]). The latter can even lead to apparent negative resistances.

In comparison with the untreated films, the films that went through photolithographic processing show a lower transition temperature in most cases. This can be an effect of the treatment of the films, which includes annealing in air while baking the photoresist. However, the shift to lower temperatures can also be due to inhomogeneities in the films. An untreated film covers a larger area than a structurized one, thus it is more likely to find a connected superconducting path already at a higher temperature.

Evidence for inhomogeneities of the deposited layers can be observed on large scales, when comparing the T_c of the films of the same batch, at different positions in the shadow masks. In the orientation of Fig. 5.2 the trend is a

		Ir			Au			Ir			
Film	**Mask**	**d [Å]**	**T_{sub} [°C]**	**R [Å/s]**	**d [Å]**	**T_{sub} [°C]**	**R [Å/s]**	**d [Å]**	**T_{sub} [°C]**	**R [Å/s]**	**Annealed**
D465	A	50	300	0.45	800	103 – 101	0.5	300	5 – 13	0.44 – 0.4	
D471	A	50	300	0.42 – 0.41	800	100	0.9 – 1.7	300	5 – 11	0.39 – 0.33	
Si489	B	50	300	0.18 – 0.20	800	200	0.2 – 0.7	300	200	0.08 – 0.17	
Si491	C	50	300	0.1	800	100	0.53 – 1.65	450	9 – 37	0.16 – 0.23	√
Si492	B	50	300	0.11	800	100	0.58 – 1.7	300	6 – 29	0.2 – 0.17	√
Si493		50	300	0.15 – 0.10	900	100	0.7 – 1.6	250	5 – 27	0.11 – 0.18	
Ge495	B	50	300	0.16 – 0.13	900	150	0.22 – 1.2	250	9 – 34	0.14 – 0.17	
Si501	B	50	300	0.3	800	150	1.4	300	30 – 32	0.29 – 0.30	√
Ge505	B	50	300	0.3	800	150	1.4 – 1.5	300	30 – 31	0.3	√
Si509	B	50	300	0.3	850	150	1.37 – 1.43	300	30 – 31	0.3	√
Cw512	D	50	450	0.3	1000	150	1.4	380	30 – 33	0.3	
Cw516	D	50	450	0.3	1000	150	1.4	450	30 – 38	0.3	
SOS517	B	50	300	0.3	800	150	1.4	300	30 – 33	0.3	
Si519	E	50	300	0.3	800	150	1.4	300	30 – 31	0.3	√
Cw520	D	50	450	0.3	800	150	1.4	500	30 – 41	0.3	

Table 5.1: Deposition parameters of the Ir/Au films investigated in this work. The first column denotes the film number, the letters indicate the substrates used: **D**: SiNi membrane substrates (used for diffusion measurements), **Si**: Silicon, **Ge**: Germanium, **Cw**: $CaWO_4$ and **SOS**: Silicon on sapphire (the Ir/Au film is deposited onto the sapphire side). The mask refers to the shadow mask used (Fig. 5.2). In the three groups "Ir", "Au", "Ir", d denotes the layer's thickness, T_{sub} the substrate temperature during deposition and R the deposition rate. Films with a check mark in the last column are annealed for two hours at 200°C after deposition.

	Without Photolithography		After Photolithography	
Film	$\mathbf{T_c}$ **[mK]**	$\mathbf{\Delta T_c}$ **[mK]**	$\mathbf{T_c}$ **[mK]**	$\mathbf{\Delta T_c}$ **[mK]**
D465B			60.8/−	1.6/−
D471A			52.0/39.1	6.1/13.2
D471B			36.8	4.9
D471C			41.4/ > 44	1.2/−
D471D			50.0/45.6	1.0/2.1
D471E			46.7/44.1	2.1/2.6
Si489B	38.6	41.2	< 12	
Si491B	45.4	0.21		
Si491C	61.1	0.31		
Si492A	53.0	4.4		
Si493	50.6	3.0		
Ge495B	41.9	3.4	32.2	3.8
Si501A			37.5	0.88
Si501B	32.1	2.9		
Ge505A			29.5	4.6
Ge505B	34.9	1.4	27.3	0.81
Si509B	40.7	7.1		
Cw512	16.7	14.2	< 12	
Cw516	43.5	13.1		
SOS517B	< 20			
Si519A	< 12			
Si519B	25.1	3.8		
Si519C	48.3	2.7		
Si519G	41.3	3.1		
Cw520	61.8	4.1	61.5	2.8

Table 5.2: The transition temperatures and transition widths of the investigated films. The transition temperature T_c is the temperature where $R = 0.5R_{\text{normal}}$. The transition width ΔT_c is the difference $T(R = 0.9R_{\text{normal}}) - T(R = 0.1R_{\text{normal}})$. The first two columns denote the values for films without further treatment after evaporation, while the last two columns denote the values after photolithographic processing and structurizing. The letter appended to the film number denotes the position of the substrate in the shadow mask as shown in Fig. 5.2. The uncertainties in the temperature values are typically $\sim 5\%$.

rising T_c for substrate positions from left to right. This indicates a different variation of the layer thicknesses for iridium and gold, which can be explained by different evaporation profiles of the materials.

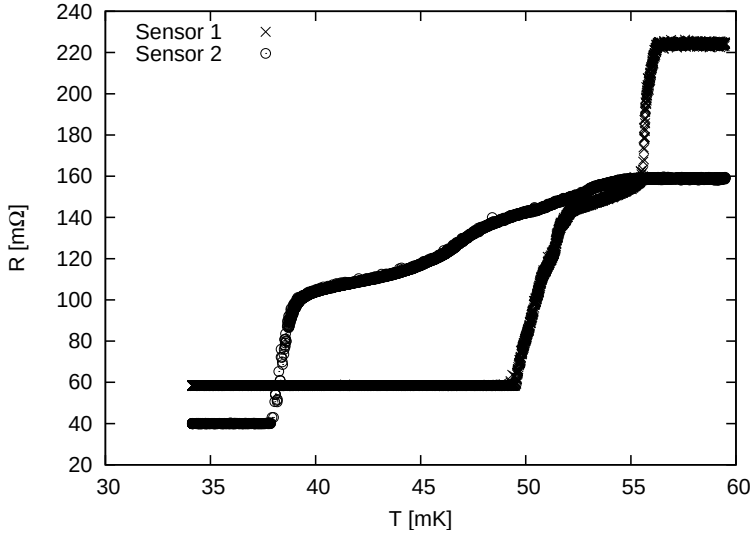

Figure 5.4: Transition curves of the two sensors of the diffusion detector D471A. The sensors are two pixels structurized from one Ir/Au film on a silicon substrate with a silicon nitride membrane layer. The distance between the pixels is 1.5 mm. The residual resistances at low temperatures are due to extra resistances present in the TES branch of the readout circuit.

A variation of T_c can also be observed on small scales, within the dimensions of a sensor structure. Fig. 5.4 shows the transitions curves of a detector for measuring the diffusion properties of aluminum films (see chapter 5.7). Here, two Ir/Au pixels are structurized on the substrate at a distance of 1.5 mm. Despite the small distance, the T_c of the two sensors differs by ~ 13 mK. The transition curves also show a steplike structure as it would be observed for several superconductors with different transition temperatures connected in series.

A possible explanation for this behavior can be found in the grain structure of the films. Suppose the film is composed of grains, where, for example, the grain centers have a higher transition temperature than the grain boundaries. In this case, when starting at high temperatures and going to low temperatures, the inner parts of the grains will become superconducting first, causing a lower total resistance of the film. A current through the film would, however, always also have to pass the grain boundaries, which are still normal conducting. Only when the boundaries become also superconducting the measured film resistance disappears.

Annealing films after deposition can lead to a growth of the existing grains leading to larger and better connected grains. This should reduce the observed steplike structure (Fig. 5.4) in the transitions of films treated this way. This was indeed observed with the films in this work that underwent post-deposition annealing, which more often showed a smoother transition than the unannealed films. An example of such a transition curve is shown in Fig. 5.5. In this case the film had an extremely sharp transition with a ΔT_c of 0.2 mK.

While annealing can improve the shape of the transitions, inhomogeneities on larger scales remain, also within one substrate. From the substrate of the film Si491B two smaller pieces were used for composite detectors used in the cryoGNO project [92]. The transition temperatures of the TES films on the two pieces differed by 11 mK. As a conclusion, the annealing heals inhomogeneities on small scales, for example by reducing the suppression of the transition in grain boundaries, but the variation of the T_c on larger scales, which is due to differences in the layer thickness, remains.

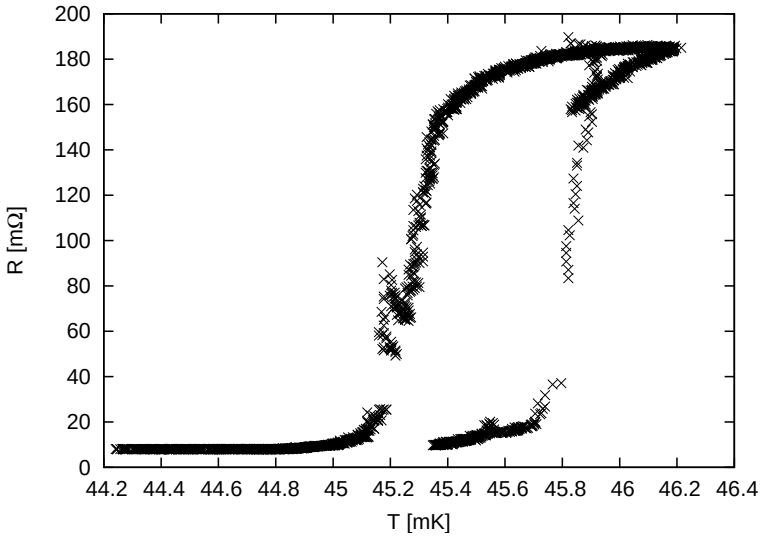

Figure 5.5: Transition curve of the Ir/Au film Si491B. The film was annealed for two hours at 200°C in high vacuum directly after evaporation. The transition is very sharp. The two transition curves were obtained for rising and falling temperatures and are an effect of the stronger thermal coupling of the film (compared to that of the thermometer) to the holder (see also section 4.1.1).

Both the stabilization of the deposition rates and the post-deposition annealing of the films are new steps. The parameters have more or less been chosen arbitarily and kept, as they yielded good results. It is, however, possi-

ble, that tuning the parameters will lead to even better and more reproducible transitions.

5.7 Measurement of the Quasiparticle Diffusion in Aluminum Films

As discussed in chapter 3, a crucial parameter that has to be considered in the design of phonon collectors is the diffusion length $l_D = \sqrt{2D\tau_{\mathrm{qp}}}$ of the quasiparticles (QPs) in the aluminum film of the collector. Regions with reduced energy gap, caused by impurities, lattice defects or grain boundaries in the film are decay centers for quasiparticles, and thus a limiting factor for the quasiparticle life time τ_{qp} [93, 94]. Therefore, the quasiparticle diffusion length is highly dependend on the quality of the films. As a consequence, l_D has to be measured for such films which have been produced under comparable conditions as those films for the phonon collectors.

A common method for the determination of the diffusion parameters for quasiparticles in a superconductor is the observation of the signals at two ends of a strip of the material to be investigated. The signals can, e.g., be caused by X-rays (from a calibration source) absorbed in the strip. The expected signal is discussed in section 3.2.1. Measurements of this kind have been performed in the past with superconducting tunnel junctions [80, 78] or with transition edge sensors [95].

5.7.1 Detector Design

For the phonon collectors of the detectors in this work, the aluminum film is deposited not directly onto the substrate, but on top of the Ir/Au film used as a TES. Since the aluminum film (8 kÅ) is significantly thicker than the Ir/Au film ($\sim$ 1 kÅ) the proximity effect between Ir, Au and Al will lead to a transition temperature for the collector that is close to that of pure aluminum. The goal of the measurements is the determination of the quasiparticle diffusion parameters for this type of aluminum films which are produced in the same evaporation systems as the other detectors.

Fig. 5.6 shows a schematic drawing of the detector used for the measurements of the quasiparticle diffusion parameters. In order to avoid background from substrate events, the films are deposited on a thin silicon nitride membrane. The strip spans over the full width (1.5 mm) of the membrane. The TES sensors at both ends are thus located on the silicon substrate.

To allow an easier position reconstruction of the events in the strip an aperture made of stainless steel is glued onto the substrate. The slits in the

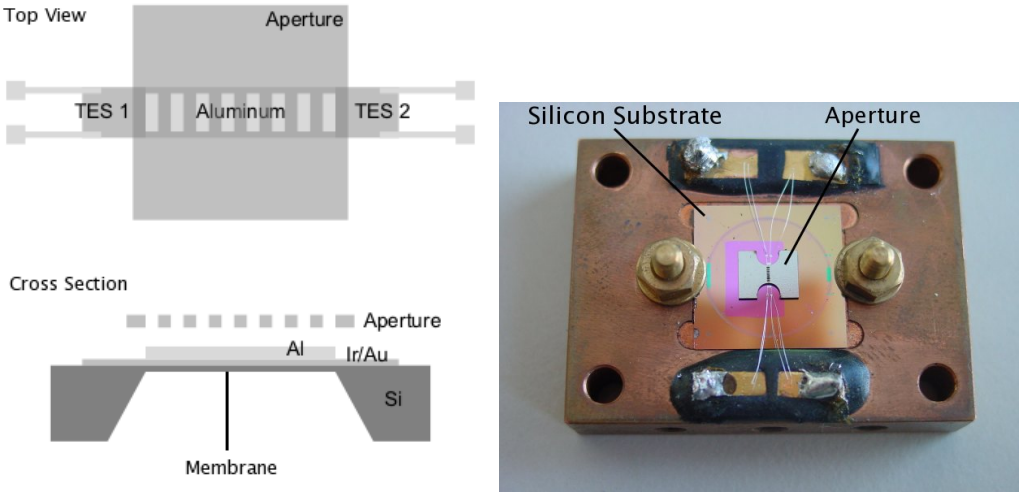

Figure 5.6: Schematics and photograph of the detector used for quasiparticle diffusion measurements. The aluminum diffusion strip is produced on a silicon nitride membrane and is connected to a transition edge sensor on either end. An aperture with eight slits of 100 μm length and distance exposes discrete sections of the strip to the X-rays from a ^{55}Fe source, which helps the position reconstruction in the data analysis. The photograph shows the silicon substrate with the diffusion strip mounted in the holder. The strip itself is obscured by the aperture. For the final installation the larger part of the substrate is shielded from the X-rays with a copper plate attached to the two screws seen in the picture.

aperture expose eight segments, each of 100 μm length and 100 μm separation, to the X-rays from a ^{55}Fe source. To reduce the background from events in the silicon substrate around the membrane, a further aperture covers the holder, leaving only a hole in the center, where the diffusion strip resides.

5.7.2 Results

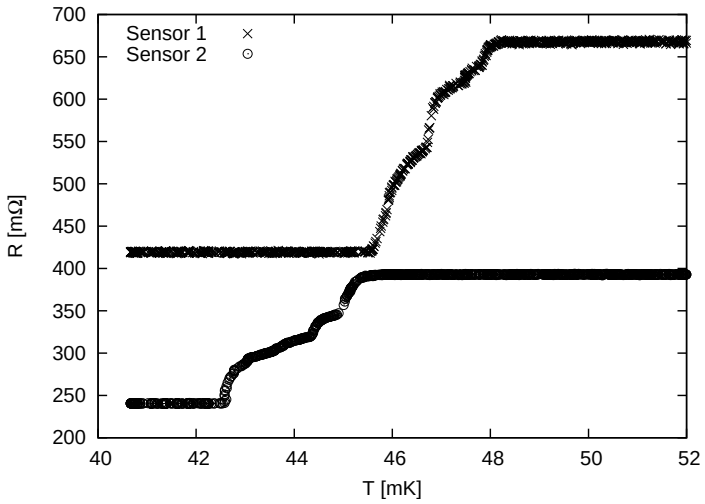

Figure 5.7: Transition curves of the two sensors of the diffusion detector D471e. Both curves were measured simultaneously. No significant cross talk between the channels was observed. The steps in the transitions originate from inhomogenities in the films (see chapter 5.6).

Fig. 5.7 shows the transition curves obtained for both sensors of the diffusion detector D471e. The transitions of both sensors were measured simultaneously, i. e. the current steps (see section 4.3.1) were applied to both sensors at the same time, the temperature indicates the holder temperature. The two curves are very distinct, no sign of cross talk between the channels is observed.

Initially the signals from the TESs were too fast and too high in amplitude for the employed SQUIDs leading to unusable data. For this reason extra resistors consisting of manganin-alloy wires with a resistance of 200-400 mΩ were introduced in the detector branch of the readout circuit. In this way the ratio of TES resistance to shunt resistance could be adjusted leading to a better detector performance.

Identification of Aluminum Events

Most of the recorded events are expected to originate from the substrate, as still a significant area around the TESs is exposed to the X-ray source. The expected ratio of the count rates from the diffusion strip and the substrate can be estimated considering the exposed areas and absorption efficiencies. For the diffusion strip a total absorption efficiency of 13% for 5.9 keV photons is calculated from the attenuations in the layers involved: 0.8 μm of aluminum, 0.115 μm of Ir/Au and the 0.4 μm thick Si_3N_4 membrane. The area of the strip exposed to the X-ray source is defined by the eight slits of the aperture, this is in total $8 \cdot 0.1\,\mathrm{mm} \cdot 0.3\,\mathrm{mm} = 0.24\,\mathrm{mm}^2$. The exposed area of the substrate is about ten times larger with an absorption efficiency of 100%. Thus, the count rate from the substrate should be two orders of magnitude larger than from the diffusion strip.

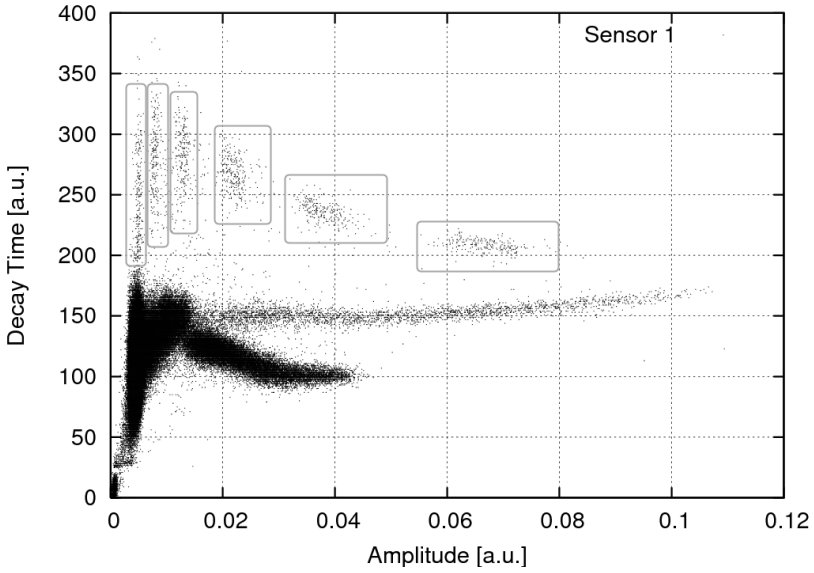

Figure 5.8: Decay times of the events recorded in TES 1 in dependence of the pulse amplitude. In the group of the slowest pulses several distinct populations are observed, corresponding to the six of the eight slits in the aperture and thus different positions on the diffusion strip. The events below the slits closest to the TESs are not seen as they are beyond the dynamic range. The double band of faster events originates from the silicon substrate, where the events with decay time ~ 100 show almost no signal in TES 2 and are thus close to TES 1. The band with decay time shows a similar pulse height in both TESs as it is expected for events at greater distance from the two TESs.

Fig. 5.8 shows the decay times of the pulses recorded in TES 1 in de-

pendence of the pulse height. Several event classes can be discriminated via the duration of the pulses. The faster pulses are assigned to events in the substrate. The slowest class of events shows several individual groups with different pulse heights, which are identified as events from the diffusion strip. Each of the six observed groups can then be assigned to one of the slits of the aperture. Two slits are missing in the data, presumably those closest to the TESs, causing events still too fast and too high in amplitude, despite the use of the extra resistors. The strip events can thus easily be discriminated from the background of the substrate by selecting the class of slowest events. This event class contains about 1500 of the total 240000 events, thus accounting for 0.6% of the total count rate, which is consistent with the estimation given above.

Pulse Height Determination

The currents $j_{1,2}$ of quasiparticles into the sensors is calculated from the quasiparticle density n at the location of the interface (for a detailed discussion of the theory on quasiparticle diffusion see section 3.2):

$$j_{1,2}(t) = -\frac{\partial}{\partial x} n\left(x = \pm\frac{L}{2}, t\right). \tag{5.4}$$

The time dependence of the current is related to the location x_a of the event in the strip, where the initial δ-like distribution of the quasiparticles is produced. For an event close to the sensor the quasiparticle distribution is still very sharp when the first QPs reach the interface, and thus the derivation of n is large, resulting in a fast and high rising signal. For an event further away from the sensor, the distribution is already more smeared out, when the QPs reach the interface, thus the signal will rise more slowly.

This dependence of the signal rise time on the event location is clearly observed in the measured pulses. Fig. 5.9 shows averaged pulses for events in the strip under the aperture slit closest to the sensor and under the slit which is most distant. The events at the largest distance to the sensor are significantly slower than those close to it. As a consequence, the simple pulse height, i.e. the distance of the pulse maximum to the baseline, cannot be used as a measure for the energy, as this would underestimate the slower pulses. Instead the integral of the pulses has to be calculated. As the record window does not contain the full decay back to the baseline of the pulses, a simple numerical integration would again underestimate the slower pulses, as for those more of the decay is missing. For this reason, the pulses identified as strip events are fitted with the model given by equation (3.5) (section

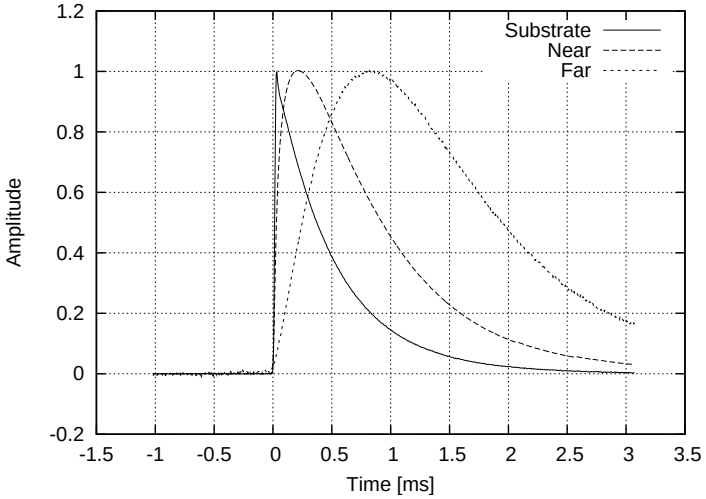

Figure 5.9: Averaged pulse shapes for strip events near to and far away from a sensor in comparison with the averaged pulse shape of substrate events in the same sensor. For better comparison the amplitudes of the pulses are normalised to 1.

3.1.1). The integral A_i of the pulses in TES i is then calculated according to the following equation:

$$A_i = A_\mathrm{n}(\tau_\mathrm{n} - \tau_\mathrm{in}) + A_\mathrm{t}(\tau_\mathrm{t} - \tau_\mathrm{n}) \qquad i = 1, 2. \tag{5.5}$$

This fit is performed for the strip events in both sensors. The respective amplitude $A_{1,2}$ for the two channels is calculated from equation (5.5)[1]. Fig. 5.10 shows the resulting amplitudes for the well fitted diffusion strip events. The six populations originating from the six observed aperture slits are well separated.

Calibration of the Relative Amplitude

The pulse integrals A_1 and A_2 are proportional to the respective numbers N_1 and N_2 of the collected quasiparticles. The individual scaling factors would normally be derived from the end points of the curve shown in Fig. 5.10, i.e. from events close to or in the sensors. These, however, are beyond the dynamic range of the detector and thus missing in the data. An alternative method to calibrate the relative amplitudes of the two sensors uses the onset

[1]The detector model used for fitting does not include quasiparticle diffusion and collection, the result for the fit parameters A_n, A_t, τ_in, τ_n and τ_t have thus no physical meaning. However, the function describes the observed pulse shapes well enough to use it as an extrapolation beyond the recorded time window.

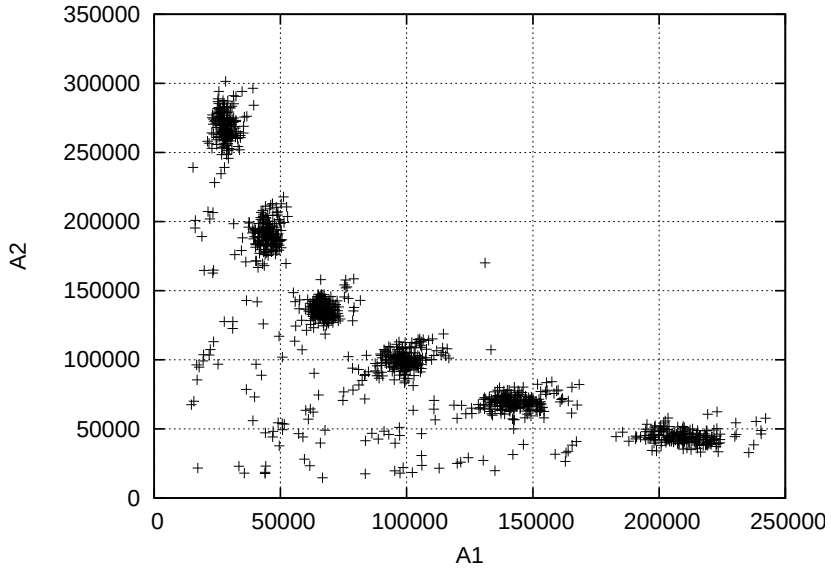

Figure 5.10: The pulse integrals A_1 and A_2 of the two sensors for aluminum events. The six distinct populations are assiged to six of the eight slits of the aperture.

of the signals, i.e. the time when the first QPs reach the sensor. For events at the center of the strip ($x_a = 0$) both signals should have the same amplitude and start at the same time. These events can be used to calibrate the scaling of the amplitudes in the two channels.

To develop a model for the onset difference of the two channels the current of quasiparticles into the sensors is examined. The number of quasiparticles collected in the sensors up to the time t for an event at time $t = 0$ and the location x_a in the strip can be written as [95] (again, for a detailled discussion of the theory on quasiparticle diffusion see section 3.2):

$$N_{1,2}(x_a, t) \propto \frac{N_0}{\pi} \sum_{k=1}^{\infty} \frac{1}{k} \left(1 - \mathrm{e}^{-(k\pi)^2 Dt/L^2}\right) \cdot \left[\sin k\pi \left(\mp\frac{1}{2} - \frac{x_a}{L}\right) - (-1)^k \sin k\pi \left(\mp\frac{1}{2} + \frac{x_a}{L}\right)\right], \quad (5.6)$$

with the diffusion constant D, the number of initially excited quasiparticles N_0 and the length of the strip L. The lifetime τ_{qp} and the trapping time τ_{tr} of the quasiparticles are neglected here, as they do not have much influence on the time dependence of the pulse.

The onset time $t_{0,i}$ of an event in channel i is then defined as the point where the tangent with the steepest slope to the curve $N_i(t)$ defined by (5.6) crosses the $N_i = 0$ axis. In a measurement the absolute onsets with respect

to the event time $t = 0$ cannot be determined. Instead the onset difference $\Delta t_0 = t_{0,1} - t_{0,2}$ between the two channels is used. In [95] this has been calculated numerically from equation (5.6) with the result only given as a plot. The solution for the onset difference can, however, also be described using the empirical function:

$$\Delta t_0 = \frac{L^2}{2\pi^2 D} \sin\left(\frac{\pi x_a}{L}\right), \tag{5.7}$$

with the length L of the diffusion strip, the diffusion constant D and the position x_a of the event. The latter is not a priori known, but can be substituted by the ratio N_1/N_2 of the numbers of collected QPs using equation (3.42) in section 3.2. This ratio can then be expressed by the measured pulse integrals using a scaling factor for the relative calibration: $N_1/N_2 = C \cdot A_1/A_2$. Equation (5.7) then becomes:

$$\Delta t_0 = B \sin\left[\frac{\pi}{2\alpha} \ln\left(\frac{C\frac{A_1}{A_2}(1-\beta)\mathrm{e}^{-\alpha/2} + (1+\beta)\mathrm{e}^{\alpha/2}}{C\frac{A_1}{A_2}(1+\beta)\mathrm{e}^{\alpha/2} + (1-\beta)\mathrm{e}^{-\alpha/2}}\right)\right], \tag{5.8}$$

with the parameter

$$B = \frac{L^2}{2\pi^2 D} \tag{5.9}$$

and the diffusion parameters α and β as defined in section 3.2.1. The model function (5.8) can then be fitted to the measured onset difference with α, β, B and C as free parameters.

Fig. 5.11 depicts the measured onset difference and the model fit in dependence of the ratio A_1/A_2 of the pulse integrals in the two channels. The experimental onset is determined from the pulses as the last sample before the pulse maximum that is within the baseline noise. The scaling factor C is well defined by the zero-crossing of the onset curve and is fitted as $C = 0.791^{+0.043}_{-0.033}$ (95% C.L.). The other parameters are not well constrained by the data and thus the fit does not yield meaningful results. With the parameter C the values for N_1 and N_2 can be calibrated with $N_1 = C \cdot A_1$ and $N_2 = A_2$. Note, that these values for N_1 and N_2 are proportional to but not equal to the number of collected quasiparticles.

Obtaining the Diffusion Parameters

With the number of quasiparticles N_1 and N_2 the total number of quasiparticles initially created can be calculated in dependence of α and β as (derived

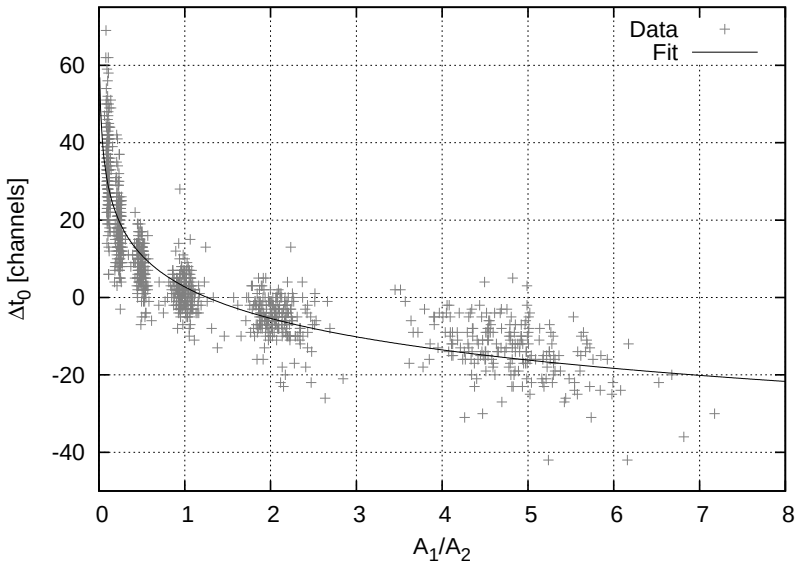

Figure 5.11: Time difference of the pulse onsets of the two sensors in dependence of the ratio A_1/A_2 of the pulse integrals. The scaling factor for the pulse integrals is obtained from the fit.

from equation (3.42) in section 3.2.1):

$$N_0 = \sqrt{\left[N_1(1-\beta)\mathrm{e}^{-\alpha/2} + N_2(1+\beta)\mathrm{e}^{\alpha/2}\right]\left[N_1(1+\beta)\mathrm{e}^{\alpha/2} + N_2(1-\beta)\mathrm{e}^{-\alpha/2}\right]} \tag{5.10}$$

For the observed separation of the integrals in Fig. 5.10 the ^{55}Fe source can be considered to be monoenergetic, as no separation of the K_α and K_β line is observed. Thus N_0 should be constant within the detector resolution for all events, and represent the average X-ray energy of the ^{55}Fe source. Thus for obtaining the diffusion parameters α and β it is sufficient to minimize the relative standard deviation s_{N_0} of N_0 with α and β as free parameters:

$$s_{N_0}(\alpha,\beta) = \frac{\sigma_{N_0}(\alpha,\beta)}{\overline{N_0(\alpha,\beta)}}, \tag{5.11}$$

where σ_{N_0} is the standard deviation and $\overline{N_0}$ is the mean value of N_0.

Fig. 5.12 shows the results for N_0 and the event location x_a for such a minimization performed for all strip events. The obtained values for the diffusion parameters are $\alpha = 3.1$ and $\beta = 0.17$. The calculated distance for the aperture slits is about 170 μm which is reasonably close to the nominal slit distance of 200 μm. From α the diffusion length l_D can be calculated as

$$l_D = \sqrt{2}\frac{L}{\alpha} = 0.68\,\mathrm{mm}. \tag{5.12}$$

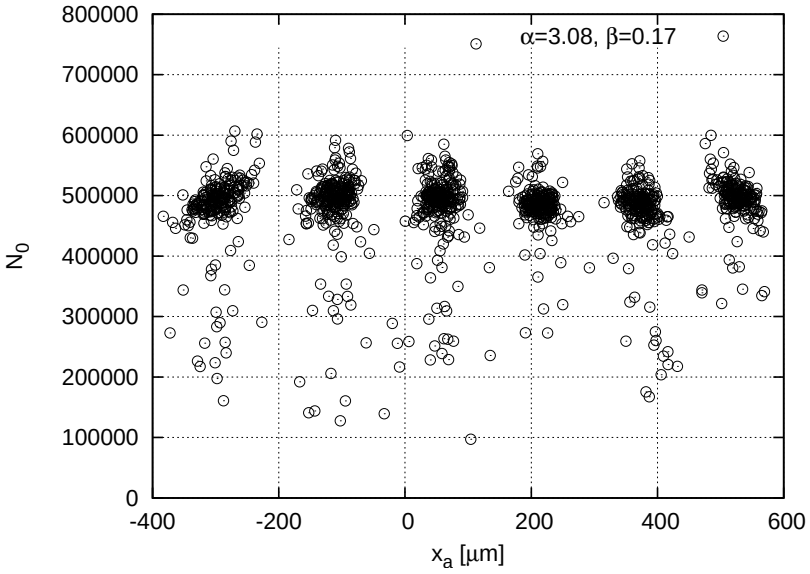

Figure 5.12: Reconstructed deposited energy and event position calculated with the diffusion parameters α and β obtained for the minimal s_{N_0}.

The energy spectrum obtained by calibrating the values of N_0 to the energies emitted by the ^{55}Fe source is shown in Fig. 5.13. The resolution of the 5.9 keV line, which is of course linked to the minimized s_{N_0}, is 510 eV full width half maximum.

The measured diffusion properties are comparable to those obtained in [95] for Al films on Ir/Au. The diffusion length is very long, which indicates a high quality of the aluminum films. As typical phonon collectors used for the detectors in this work are 0.25 mm long, the losses due to quasiparticle decay should be small and thus the collectors very efficient (see also Fig. 3.10).

Error Estimation

Finally it should be discussed, how well the diffusion parameters α and β are constrained by the data. The impact of the uncertainty of the calibration factor C obtain in section 5.7.2 can by investigated by retriefing the values for α and β for the minimal and maximal C. For $C = 0.76$, this results in $\alpha = 3.19$ and $\beta = 0.14$, and for $C = 0.82$ in $\alpha = 3.22$ and $\beta = 0.07$.

For a well fitted parameter pair (α, β) the lines of constant initial energy in the plots of the pulse height in one channel versus the other (see Fig. 5.10) reflect the curvature of the measured data. However, as the end points of the 5.9 keV line are missing, the data lacks an important constraint on the

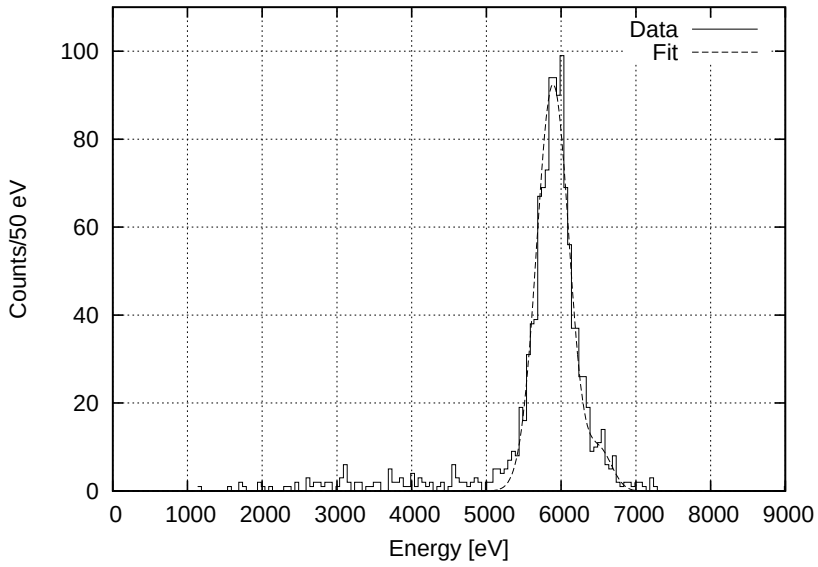

Figure 5.13: Reconstructed energy spectrum of the strip events calculated with the diffusion parameters α and β obtained for the minimal s_{N_0}. The resolution is here 510 eV FWHM at 5.9 keV.

parameters. Without the end points a large number of α and β combinations are possible to generate similar curvature. A smaller α, which would end up in a smaller curvature, can be compensated with a larger β and vice versa (see also Fig. 3.8 in section 3.2). The two parameters are thus heavily correlated.

The calculated distance of the six populations provides an alternative measure for the uncertainty of the obtained (α, β) pairs, as this distance should reflect the real distance of the slits in the aperture. Due to the strong correlation of the two parameters they are not investigated independently. Instead the parameter α is varied and a matching value for β is obtained by minimizing equation (5.11) until the calculated distance of the six populations is more than 20% off the value for the best fitted α and β. This results in $\alpha = 4.1$ and $\beta = 0$ at the lower boundary for the distance and $\alpha = 2.6$ and $\beta = 0.4$ at the upper boundary.

Chapter 6

Detector Development for the CRESST Experiment and for the Neutron Calibration Measurements

6.1 Composite Detector Design with $CaWO_4$ Absorbers

The light yield of $CaWO_4$ crystals depend on their oxygen content. During the detector fabrication process the crystals have to be processed in several high vacuum systems, where they are heated to temperatures up to 450°C (e.g. during evaporation of the first iridium layer). During this procedure the crystal may outgas some of its oxygen, resulting in a reduction of the light yield. This can be reverted by annealing the crystal in an oxygen atmosphere. However this thermal treatment destroys the superconducting film the sensor is made of.

A possible solution to this problem is the use of composite detectors, where the TES is produced individually on a small substrate which is then glued onto the large absorber. Within the "cryoGNO" project this concept was successfully tested [96, 92, 72]. In those experiments Ir/Au TES of $1 \times 3\,\mathrm{mm}^2$ were produced on 0.25 mm thin silicon substrates, which were afterwards cut into pieces of $5 \times 7\,\mathrm{mm}^2$. Those pieces were glued onto sapphire crystals of $20 \times 10 \times 1\,\mathrm{mm}^3$. With this configuration a threshold of 100 eV and a resolution of 187 eV for 5.9 keV events in the sapphire absorber were achieved. With larger crystals the glueing technique is applied for example in the EDELWEISS experiment, where the NTDs for the heat channels are

glued onto 320 g Ge crystals.

Applying this technique to $CaWO_4$ would result in several benefits:

- The crystals are no longer exposed to the sensor fabrication process, and thus should not suffer from degraded light output.

- The production of TESs on smaller substrates is easier and can be performed in larger numbers. The sensors can be tested first, and then the best ones are selected for being glued on a crystal.

- At the TUM a new Czochralski facility for growing $CaWO_4$ crystals is being set up [97]. For optimizing the production process the crystals should be characterized regarding their optical properties, as well as for their performance as phonon detectors, without causing great changes to them.

6.1.1 Experimental Setup

For a first test measurement of a composite $CaWO_4$ detector, a crystal produced in the existing Czochralski facility at the TUM was used. The crystal "Little Boy" was the first crystal grown there, big enough to cut a cylinder of the dimensions 20 mm diameter and 20 mm height out of it [97].

The TES consisted of a round 2 mm Ir/Au spot evaporated on $3 \times 5 \times 0.5\,\mathrm{mm}^3$ small silicon substrate using a shadow mask. The shadow mask used allows the production of eight such sensors at once, i.e. in one evaporation process. Those can then be used without any further processing, i.e. where no photolithography of the film or cutting of the substrate is necessary [82]. With this concept a large number of sensors can be produced in a short time.

The TES substrate was then glued onto the $CaWO_4$ crystal using EPO-TEK 301-2, a special cryo-resin. For the small $20 \times 10 \times 1\,\mathrm{mm}^3$ absorbers the best results were obtained with small glue spots [92], thus this was also aimed for using the larger crystal "Little Boy". The glue spot of the composite detector shown in Fig. 6.1 was less than 1 mm in diameter.

The transition of the Ir/Au sensor was at a temperature of about 48 mK (half normal resistance) with a width of about 3 mK (see Fig. 6.2). For recording a spectrum the temperature of the detector holder was stabilized at 43.6 mK and the sensor was heated into its transition with a bias current of 63 μA. A ^{60}Co source placed outside the cryostat should have provided a gamma energy calibration.

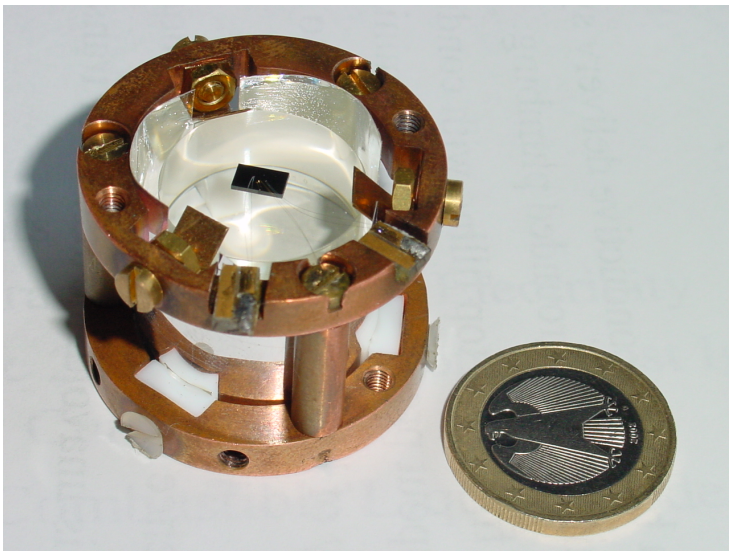

Figure 6.1: Photograph of the first macro composite detector made from the 38 g $CaWO_4$ crystal "Little Boy" with a $3 \times 5 \times 0.5\,\mathrm{mm}^3$ silicon substrate carrying an Ir/Au TES glued on it.

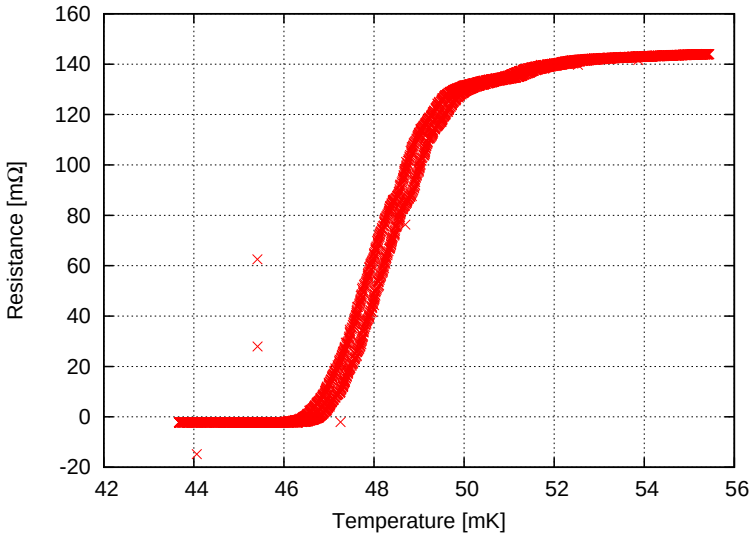

Figure 6.2: Transition of the TES Si519c, which was glued onto the crystal "Little Boy".

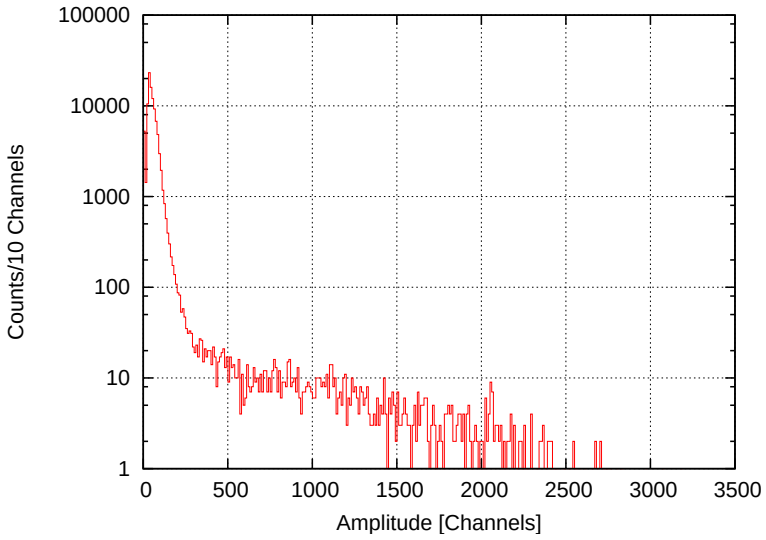

Figure 6.3: Pulse height spectrum obtained with the composite $CaWO_4$-detector. The crystal was irradiated with a ^{60}Co gamma source, yet neither the characteristic lines nor a compton edge are observed.

6.1.2 Results

In the pulse height spectrum (Fig. 6.3) obtained with this configuration no line and not even a compton edge is observed. Thus no energy calibration and no information about the sensitivity of the sensor could be deduced.

However from the characteristical pulse shape of the detector some basic information about the properties of such a composite detector can be extracted. Fig. 6.4 shows a template pulse for events from the $CaWO_4$ absorber. The template was fitted with the model function given in equation (3.5), revealing a rise time $\tau_{\mathrm{in}} = (85.5 \pm 0.7)\,\mu$s, a fast decay time $\tau_{\mathrm{n}} = (500 \pm 3)\,\mu$s and a slow decay time $\tau_{\mathrm{t}} = (22.9 \pm 0.6)$ ms.

The pulses exhibit two very different decay times. If the signal is purely due to the phonons from the $CaWO_4$ crystal, this leads to the following interpretation:

The slow decay time τ_{t} from the fit is due to the heat transport through the thermal coupling from the crystal to the TES substrate, indicating a weak thermal coupling of the glue. The fast component τ_{n} originates from the transport of non-thermal phonons through the glue spot into the sensor substrate. This time constant is very short compared to τ_t. According to equation (3.10) this would either mean that the phonon collection through the small glue spot is very efficient (τ_{film} being small) or that the non-thermal phonons decay very rapidly in the crystal (small τ_{crystal}).

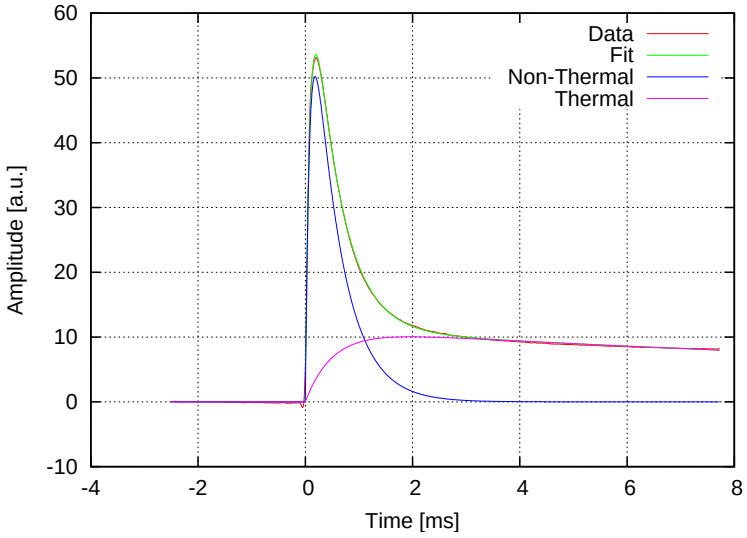

Figure 6.4: Pulse template of events from the absorber crystal "Little Boy" with slow decay time $\tau_t = 22.9\,\text{ms}$. This very slow component is due to the slow phonon collection through the small glue spot.

In later experiments performed in the scope of the diploma thesis of S. Roth [73], the silicon substrate was replaced by a sapphire substrate of the same size. The TES on the sapphire is a rf-sputtered tungsten film produced by using the same shadow mask technique as for the Ir/Au-TES. The sapphire substrate was not glued onto the $CaWO_4$ with a small spot of glue, but the whole contact area was covered with a thin film of EPO-TEK 301-2. For the pulses obtained with this configuration also two decay times were observed. The time constants here being $\tau_n = 5\,\text{ms}$ and $\tau_t = 12\,\text{ms}$, also being interpreted as a non-thermal and thermal component of the signal from the absorber.

Assuming that the phonon collection time for non-thermal phonons collected through a glue interface follows the same law as the phonon collection time of a film directly evaporated onto the absorber as given in equation (3.11), the non-thermal time constant should scale reciprocally with the area of the glue spot. As a large-area interface of $15\,\text{mm}^2$ exhibits a decay time of 5 ms, an even longer non-thermal decay time for a small spot of glue would be expected.

These considerations lead to a different interpretation of the pulse shape shown in Fig. 6.4: The slow component of 22.9 ms is indeed the phonon signal from the crystal. Whether this is thermal or non-thermal or a mixture of both cannot be decided from the existing data. For the case that it is

the non-thermal decay time this would imply a very long life time τ_{crystal} of high-frequency phonons in the crystal.

When assuming that the 5 ms decay time for the large glue area as well as the 23 ms for the small glue spot are both non-thermal signal components, it is possible to estimate the phonon collection times for the large glue area τ_{la} and the spot τ_{sa}. The two time constants should scale reciprocally with the glue area, for the spot 0.8 mm^2 are estimated. Solving the three simple equations

$$\frac{\tau_{\text{la}}}{\tau_{\text{sa}}} = \frac{0.8\,\text{mm}^2}{15\,\text{mm}^2} \tag{6.1}$$

$$\left(\frac{1}{\tau_{\text{la}}} + \frac{1}{\tau_{\text{crystal}}}\right)^{-1} = 5\,\text{ms} \tag{6.2}$$

$$\left(\frac{1}{\tau_{\text{sa}}} + \frac{1}{\tau_{\text{crystal}}}\right)^{-1} = 22.9\,\text{ms}, \tag{6.3}$$

yields $\tau_{\text{la}} = 6\,\text{ms}$, $\tau_{\text{sa}} = 113\,\text{ms}$ and $\tau_{\text{crystal}} = 29\,\text{ms}$. The phonon collection efficiencies (3.12) calculated from these time constants are $\varepsilon_{\text{la}} = 0.83$ and $\varepsilon_{\text{sa}} = 0.20$ for the large area and the spot respectively.

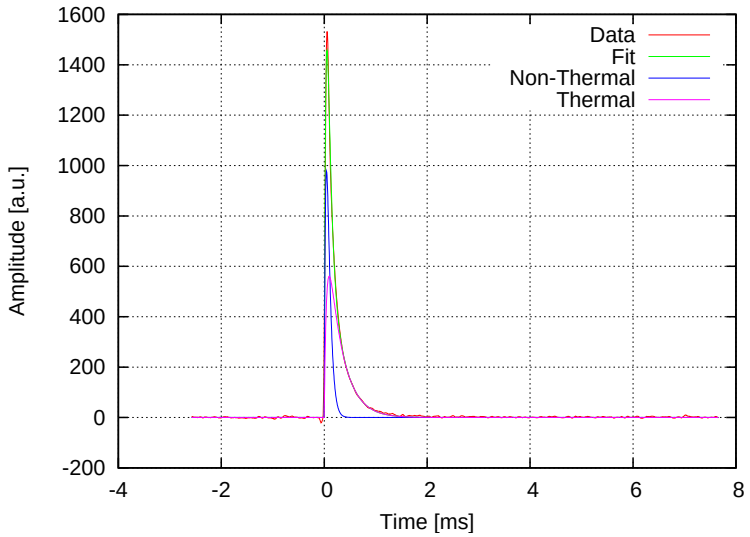

Figure 6.5: Pulse template of fast events. Those pulses are assigned to events occurring directly in the small Si thermometer substrate.

To understand the fast decay time of the pulse shown in Fig. 6.4 a comparison with the pulse shapes of events originating from interactions directly in the silicon substrate is helpful. Fig. 6.5 shows a template averaged

from three high energetic direct hit candidates together with a fit using the model (3.5). The fit yields time constants of $\tau_{\mathrm{in}} = (44 \pm 140)\,\mu$s, $\tau_{\mathrm{n}} = (45 \pm 144)\,\mu$s and $\tau_{\mathrm{t}} = (273 \pm 10)\,\mu$s. The errors for the non-thermal decay times are larger than the fit value, suggesting that the only real decay time present in the pulse is τ_{t}.

For a light detector with this intrinsic decay time, pulses similar to the fast component in Fig. 6.4 would be expected for the scintillation light from a $CaWO_4$ crystal (see section 6.3.4). When the detector was designed a possible contribution of the scintillation light to the signal was considered, but it was expected to be small for two reasons: First, the silicon substrate is small and thus the light collection should not be very efficient. Second, only a small fraction of the deposited energy is converted into light, so that for an efficient and fast phonon detection the signal should be dominated by the phonon component.

However, as estimated above the phonon collection efficiency $\varepsilon_{\mathrm{sa}}$ for the given setup is rather low and the energy signal is slow, resulting in phonon pulses with small amplitudes. The light collection on the other hand is probably better than expected, as the glue acts as an optical coupling between the $CaWO_4$ and the silicon crystal. In fact the glue spot is very likely the point where a large portion of the emitted light leaves the crystal, as it is polished on all sides, usually leading to trapped light.

6.1.3 Discussion and Prospects

In summary there are strong indications that with this type of a composite detector of a $CaWO_4$ crystal and a silicon substrate with a TES, both the phonon and the light signal were measured simultaneously in one pulse. A distinction between light and phonon signal would still be possible using the different decay times of the pulse components, where the fast component represents the light, and the slow component the phonons. The amplitudes of the phonon and the light channel could be obtained by first extracting the decay times from a fit of (3.5) to a template pulse and then fitting all events to the same function with fixed decay times and the amplitudes (apart from onset and baseline) as the only free parameters.

If the presented interpretation of the observed pulse shapes proves to be correct, this detector concept would allow to record two signals simultaneously with only one SQUID circuit. This reduces the number of needed readout channels by a factor of two, which would be a significant benefit for large scale experiments. The presented detector did not show a reasonable resolution or threshold, however, an optimization of the phonon collection should be possible, for example by increasing the extent of the glue spot. The chal-

lenge is to improve the phonon collection without making the phonon pulses too fast, in order to maintain the discrimination possibility between phonon and light signals.

An increased phonon collection efficiency will increase the amplitude of the phonon component in the pulses, while the light amplitude would remain the same. This could result in the relative amplitude of the light signal being too small for a good discrimination. In this case the application of the Neganov-Luke effect [98, 82] could help by "readjusting" the ratio of the two amplitudes, so that a clear separation of the two signals is achieved. Applying a voltage to a semiconductor equipped with a phonon sensor (e.g. a TES) amplifies the signal in this sensor by accelerating the charge carriers produced by a photon interaction in the semiconductor, thus leading to a phonon amplification.

Photons originating from the scintillating $CaWO_4$ crystal produce free charge carriers in the silicon, which is not the case for phonons passing through the glue spot. Applying a voltage to the silicon substrate of the presented composite detector should then only amplify the light component of the signal.

6.2 A Phonon Detector for Neutron Calibration Measurements

6.2.1 Requirements

In section 2.4 several methods for the determination of the quenching factors for nuclear recoils in $CaWO_4$ are discussed. The neutron calibration measurements, particularly the neutron scattering experiment, are of special interest here. These experiments are performed at low temperatures with cryogenic detectors similar to the CRESST detectors described in section 2.1. However, the special requirements regarding the detector design for the calibration measurements are different in comparison to the dark matter experiment. Two major aspects have to be considered in the designing the detectors for the calibration measurements:

- For the neutron scattering experiment the scattering kinematics is used to identify the recoiling nucleus. Thus it is important that only one nucleus scatters in the crystal. As a consequence the size of the crystal has to be chosen such that one gets as few multiple scattering events as possible, while still having a reasonable event yield for a given neutron flux.

- The calibration experiments are performed above ground with little shielding against background. This leads to a higher count rate in the detectors both from the background and from the calibration sources. This count rate is in the order of a few tens per seconds compared to less than one per second in the dark matter experiment. Therefore the detectors have to be designed such that thay can cope with this increased count rate.

6.2.2 Detector Design

The issue of multiple scattering is a problem related to the crystal size, while the count rate affects the design of the TES. Both aspects are discussed below.

Crystal Size

The scattering experiment is performed at a neutron energy of 11 MeV. In this energy range the mean free path of neutrons in $CaWO_4$ is about 6 cm (see appendix A.2). Using this mean free path the expected fraction of multiple scattering events for given crystal dimensions can be estimated in a Monte Carlo calculation. Such calculations have been performed for cylindrical crystals with different radii and heights with parallel neutron beams coming from the side and from the top, respectively.

To keep the calculations simple, several strong simplifications are made. As the maximum energy transfer for 11 MeV neutrons is about 2 MeV for elastic scattering off oxygen and the mean free path does not vary much in this energy range, the energy transfer during a scattering event is simply neglected and the mean free path is considered to be constant.

For each simulated neutron an initial trajectory with random coordinates evenly distributed over the crystal's cross section area normal to the desired direction is generated. Then the intersection of this trajectory with the crystal is calculated. Starting from the entry point into the crystal a random point on the trajectory, in accordance with a distribution determined by the mean free path, is selected as possible scattering center. If this point is within the crystal the neutron counts as a scattered event and a new trajectory with a random direction starting at the scattering center is generated. Then a random point on this new trajectory is selected and if this is again within the crystal the neutron counts as multiple scattered. This procedure is repeated until the randomly selected point on the trajectory is outside the crystal bounds.

40×40 crystal			
	Scatter Prob.	**Mult. Scatters**	**Fraction**
From Side	$(40.1 \pm 0.3)\%$	$(9.2 \pm 0.2)\%$	$(22.9 \pm 0.5)\%$
From Top	$(48.7 \pm 0.3)\%$	$(11.2 \pm 0.2)\%$	$(23.0 \pm 0.5)\%$
20×20 crystal			
From Side	$(22.8 \pm 0.3)\%$	$(2.88 \pm 0.11)\%$	$(12.6 \pm 0.5)\%$
From Top	$(28.4 \pm 0.3)\%$	$(3.59 \pm 0.12)\%$	$(12.6 \pm 0.5)\%$
20×5 crystal			
From Side	$(22.8 \pm 0.3)\%$	$(1.65 \pm 0.08)\%$	$(7.2 \pm 0.4)\%$
From Top	$(8.0 \pm 0.2)\%$	$(0.58 \pm 0.05)\%$	$(7.3 \pm 0.7)\%$

Table 6.1: Results for the overall scattering probability and multiple scattering probability for the simple Monte Carlo calculations described in the text. Three cylindrical crystals were used as target for 10^5 simulated neutrons coming in from the side and from the top. The crystal dimensions are noted as *diameter*×*height* in mm. The first column ("Scatter Prob.") denotes the probality for neutrons entering the crystal to scatter at least once. The second column ("Mult. Scatters") denotes the probality for the neutrons to scatter more than once. "Fraction" finally is the fraction of multiple scatter events with respect to the corresponding scatter probability. The errors are the statistical errors at 2σ.

The results of the Monte Carlo simulations performed with three different $CaWO_4$ crystal geometries are summarized in Table 6.1. As reference a crystal with 40 mm diameter and height, which is the size of the target crystal in the CRESST experiment, is given. For a crystal of this size about one of four neutron events is a multiple scatter event. In [65] a detector for calibration measurements was presented, which uses a crystal of 20 mm × 20 mm height and diameter as absorber. This smaller crystal size reduces the contribution of multiple scatter events by a factor of two compared to the larger crystal.

The detector presented in this section uses an even smaller crystal as absorber: a cylinder with 20 mm diameter and 5 mm height. This reduces the contribution of the multiple scatter events by more than 40% compared to the 20 mm × 20 mm crystal. The multiple scatter probability is the same for neutrons coming from the side and from the top (or bottom) of the cylinder. As the height of the crystal is considerably smaller than its diameter, the overall scattering probality is much smaller for neutrons entering perpendicularly through the top surface. However, as in the experiment at the accelerator the neutron beam covers a much larger area than the target crystal, for a comparison of the expected event rate for the crystal's orientation in the beam the solid angle has to be taken into account. Thus the expected

rate from the top has to be scaled by the ratio of the cross section areas, i.e. a factor of 314/100, accounting for the larger number of neutrons entering through the top surface. This way the orientation of the crystal with respect to the neutron beam does not matter – neither concerning the multiple scattering contribution nor concerning the overall event rate.

These simple calculations give a rough estimate of the expected double scattering rate for a given crystal geometry. For a deeper understanding of the processes in a neutron scattering experiment more sophisticated simulations are required. Simulations of that kind involving the neutron scattering experiments are performed at the Universität Tübingen using the GEANT4 simulation tools [99].

TES Design

For the choice of the TES design to be employed several aspects have to be taken into account. First of all, the detector has to be fast enough for the expected count rates in the experiment. This can be achieved by collecting the non-thermal phonons in the crystal before they thermalize. The sensor design will thus use phonon collectors covering a large area of the crystal's top surface. However, the size of a single phonon collector is limited by the quasiparticle diffusion (see sections 3.2 and 5.7). For larger structures an array of several TESs each with its own phonon collectors has been proven to be of advantage [100, 65]. In [65] Monte Carlo simulations of the phonon propagation in a 40 mm × 40 mm $CaWO_4$ crystal were performed, including a phonon collecting area on the top of the cylindrical crystal, in order to find the phonon collection efficiency for non-thermal phonons in dependence of the collector area.

For small signals the measured amplitude at the SQUID output is proportional to the temperature change in the TES. Thus the amplitude for a given energy absorbed in the TES scales with the reciprocal heat capacity C_e^{-1} of the TES. The contribution of the intrinsic TES noise scales with $\sqrt{C_e}$ [74]. While a larger sensor area increases the amount of energy collected in the TES, the signal amplitude per energy diminishes. As the TES area scales linearly with the total phonon collecting area, the scaling of the signal per energy can be combined with the phonon collection efficiency from the Monte Carlo simulations to find the sensor area with the minimal energy threshold, i.e. the energy where the signal can be discriminated from the noise. The scaling of the detector threshold with the sensor area S then depends on the dominant noise contribution. If the TES noise is dominant, the threshold scales with $\sqrt{S^{-1}}$, because it is a statistical fluctuation. If the read-out electronics is dominant, the scaling is proportional to S^{-1}, because in this case

the signal scales with the TES area.

Another possible trade off of a sensor area covering a large portion of one crystal surface is the light loss due to the absorption of the scintillation light in the sensor structure. It is unknown how big these losses really are as the reflectivity and absorption of the sensor structure was never determined. However, for the quenching factor measurements a high light yield is crucial. It is thus desirable to keep the sensor as small as possible to reduce the risk of too large a light loss.

These considerations led to the decision to use a relatively small sensor structure similar to those used for the light detectors in [65]. The sensor structure consists of a parallel connection of 28 individual Ir/Au TESs, each connected to 10 aluminum phonon collector fins. Each fin has a size of $50 \times 250\,\mu\mathrm{m}^2$, so that the total phonon collection area is $3.5\,\mathrm{mm}^2$. This structure should provide a good compromise between the fast phonon collection of a large sensor and a good threshold and small light loss of a small sensor. Fig. 6.6 shows a photograph of the completed detector (Cw520) mounted in its holder.

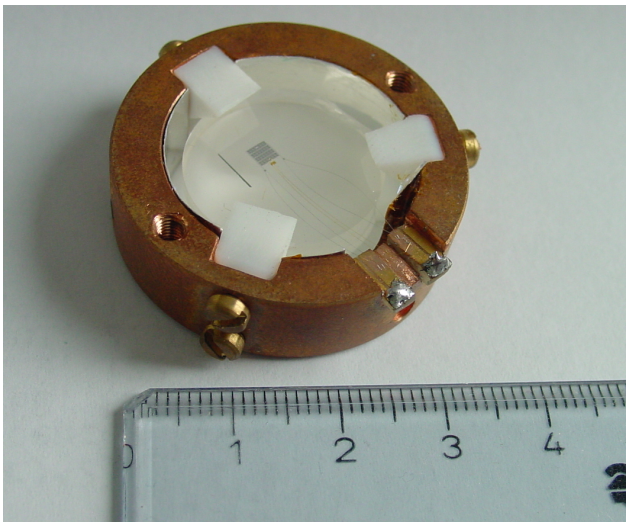

Figure 6.6: Photograph of the detector Cw520 in its holder. The inner surfaces of the copper holder are covered with the reflective foil also used in the CRESST experiment. The crystal is fixed by pieces of highly reflective teflon. For the final mounting a copper cap also equipped with a reflective foil is attached on the top of the holder, the light detector module is then mounted on the bottom side.

Fig. 6.7 shows the normal-to-superconduction transition curve of the sensor. For the fabrication parameters of the Ir/Au film see Table 5.1. The transition temperature is at about 60 mK, which allows an operation in all

relevant cryostats at our institute. Additionally, the small transition width of less than 3 mK and the high linearity of the lower part of the transition are ideal prerequisites for a sensitive detector.

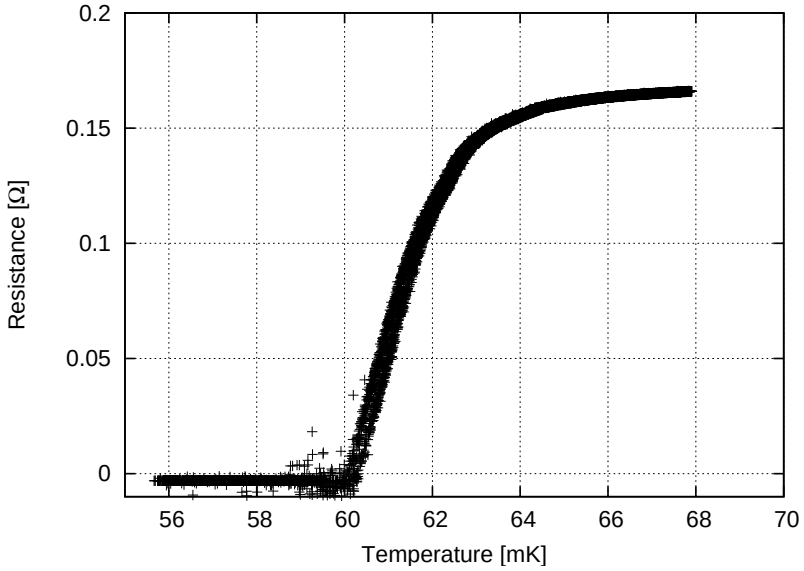

Figure 6.7: Recorded transition curve of detector Cw520. The apparent negative resistance in the superconducting state is a systematic deviation due to the uncertainty of the SQUID-amplification factor and the actual height of the current steps.

6.2.3 Performance at Low Energies

The detector was installed in the cryostat without light detector. The crystal was irradiated from the side opposite to the sensor structure with an ^{55}Fe source through an aperture.

The amplitude of the events is determined in off-line analysis from the recorded pulses by generating a template pulse averaged from good events and then fitting the pulses with this template. Fig. 6.8 shows a histogram of the fit amplitudes for the Mn K_α and K_β lines from the ^{55}Fe source. The resolution is obtained from a fit of this histogram with two gaussian functions. The full width at half maximum (FWHM) of the 5.9 keV line is 340 eV.

To obtain the detector's energy threshold noise samples are recorded every two seconds using a second trigger independent of the SQUID signal (see section 4.3.2). Fig. 6.9 depicts the amplitude histogram of the template fit to these noise samples. The width of this noise peak is 120 eV FWHM corresponding to a 5σ threshold of 250 eV. This threshold defines the minimal

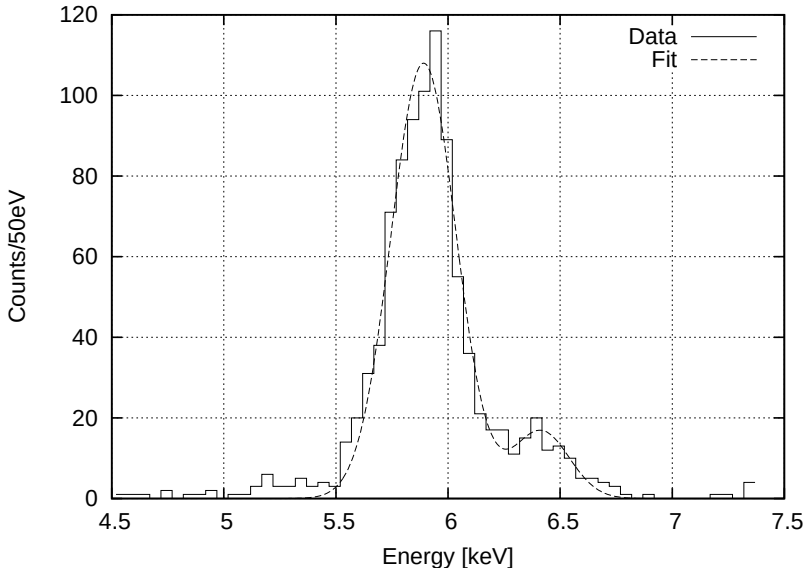

Figure 6.8: Histogram of the Mn K_α (5.9 keV) and K_β (6.4 keV) line obtained with a ^{55}Fe X-ray source.

energy, where a signal can be discriminated from noise in an off-line analysis using the template fit. For the data acquisition, however, the minimal possible signal amplitude for the hardware trigger is important, i.e. the amplitude where only real signals and no noise is triggered. This threshold can be obtained from the distribution of the baseline noise of the sampled signal. The standard deviation of this distribution is 100 eV corresponding to a 5σ threshold of 500 eV.

The pulse template used for fitting the events is shown in Fig. 6.10. The pulse was fitted with the theoretical model defined in equation (3.5). In the plot the individual contributions of the non-thermal and thermal component of the model are shown together with the pulse and the total fit. From the fit an intrisinsic decay time τ_{in} of 0.1 ms, a non-thermal decay time τ_{n} of 0.7 ms and a thermal decay time τ_{t} of 1.7 ms are obtained. The slowest decay time is the limiting factor for the possible count rate. τ_{t} corresponds to a frequency of 590 Hz, thus for count rates well below 100 counts per second the measurement should not suffer from too much pile-up events.

6.2.4 Performance at High Energies

The energy range relevant for the performed and planned neutron calibration measurements extends to a few hundred keV. The main goal is the measurement of the quenching factor of tungsten. With typical neutron energies of

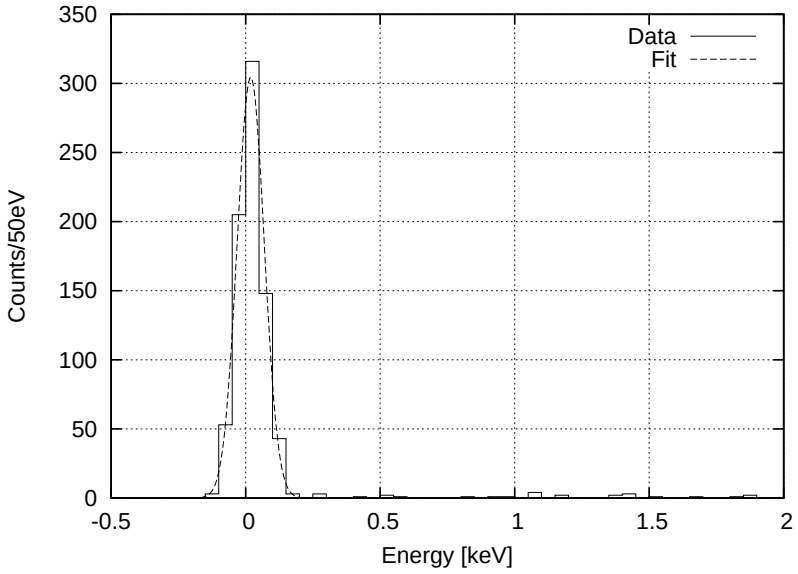

Figure 6.9: Histogram of fit amplitudes for the recorded noise samples.

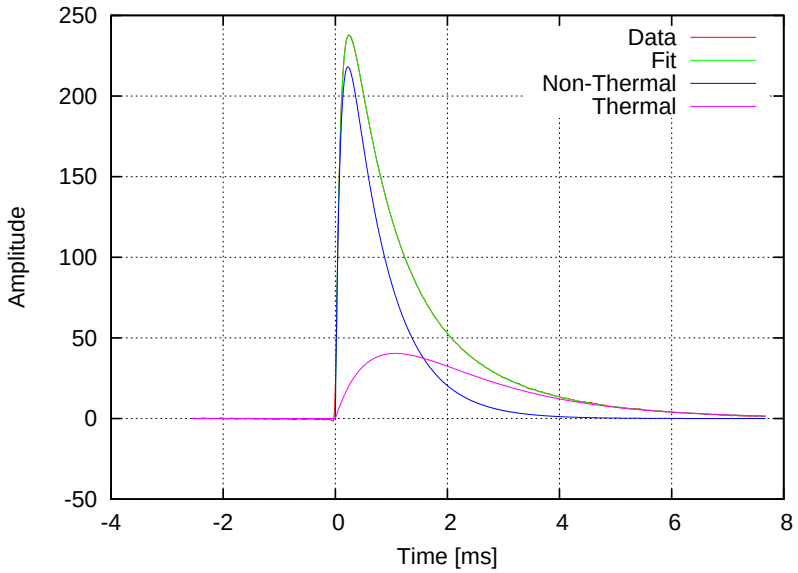

Figure 6.10: Averaged pulse shape for 6 keV events. The pulse is fitted with two decay times ($\tau_n = 0.7\,\text{ms}$ and $\tau_t = 1.7\,\text{ms}$) and one rise time ($\tau_{in} = 0.1\,\text{ms}$).

11 MeV (the beam energy of the neutron scattering facility) the tungsten recoils reach up to 240 keV. In addition to the neutron experiments at the Maier-Leibnitz-Labor (MLL) we also performed neutron measurements with a ^{241}AmBe and a ^{252}Cf neutron source. For these experiments a gamma calibration of the detector is necessary. The gamma calibration data was taken in between the data taking with the neutron sources, such that the neutron sources were replaced by the gamma sources. Before resumption of the recording of the neutron data the gamma sources were again removed. The goal of the γ calibration procedure described below is to provide an energy calibration for the neutron data, which is also to a certain degree robust against fluctuations of the working point of the detector.

The measurements covered a period of two days, with regular γ calibration runs of two hours after the daily liquid helium refill and in between switching the neutron sources (e.g. after removal of the AmBe source, before the measurement with the Cf source). For a quick glance at the results of the neutron data see the next section, a detailed description of these experiments will be given in [63]. The calibration was performed with a ^{57}Co (relevant gamma energies 122 and 136 keV) and a ^{133}Ba source (relevant gamma energies 276, 303, 356 and 384 keV) covering the important energy range for the experiment.

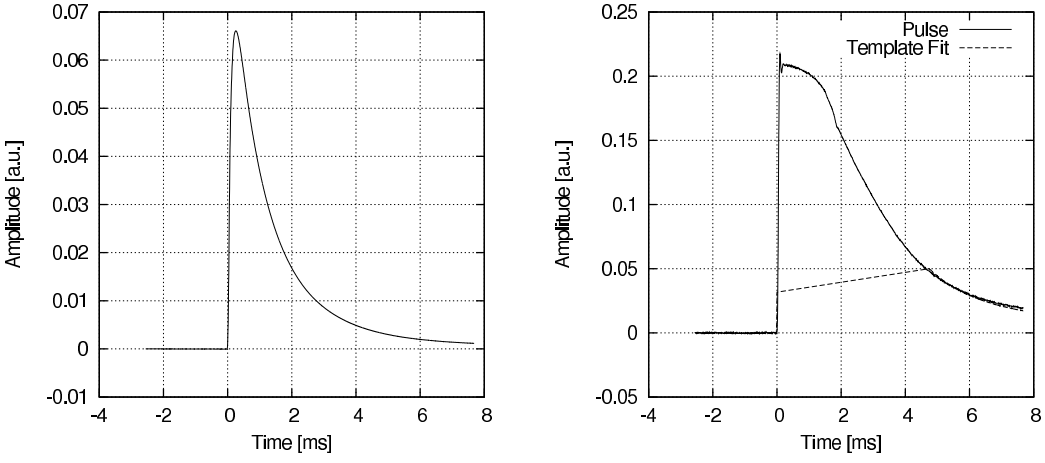

Figure 6.11: Left: Template pulse generated from good events around 60 keV. Right: High energy event (about 1 MeV). The detector goes into full saturation, the amplitude is extrapolated by only fitting the lower part of the pulse (below amplitudes of 0.05).

For the determination of the pulse amplitudes again a template fit is used. However, as the detector is very sensitive, the pulses reach saturation already at relative moderate energies. Saturation occurs when the deposited energy

heats the TES completely into its normal conducting state. At this point the resistance does not change any more with temperature and the measured pulse is flattened at the top until the sensor is cooled into its transition region again. In the data presented here this was the case at energies above about 200 keV. In the left image of Fig. 6.11 the template pulse used for fitting the data is shown. The template is generated from events around the 60 keV energy, where the pulse shape is unaffected from saturation. The right image of Fig. 6.11 depicts a recorded pulse shape of a high energy event, where the detector is in full saturation. A simple template fit would underestimate the amplitude of such events.

In order to reconstruct the amplitude of saturated pulses, a "cut off" template fit is used. The same method is also used in the CRESST experiment to reconstruct high energy events (see for example [68], method "A" therein). For fitting, a maximal amplitude is chosen, up to which the signals are considered to be unaffected from saturation or strong non-linearities of the upper part of the transition. Only the part of the pulses below this threshold is then included in the fit. The fit in the right plot of Fig. 6.11 illustrates this method, here the pulses are only fitted up to an amplitude of 0.05. The fit amplitude is calculated from the data points below the threshold as:

$$A = \frac{\sum_i p_i t_i}{\sum_i t_i t_i}, \tag{6.4}$$

where A is the calculated amplitude. p_i are the data points of the pulse to be fitted, t_i are the data points of the normalized template pulse (i.e. the amplitude of the template is 1). The index i iterates over all data points p_i below the cut-off threshold. In the example in Fig. 6.11 the fit then assigns a reconstructed amplitude of 0.96 to the pulse, while a simple maximum determination would yield too small an amplitude of 0.21. With this method saturated high energy events can be reconstructed, as long as the pulses relax below the cut-off threshold within the recorded time window.

Fluctuations of the holder temperature are reflected by resistance changes in the TES. This leads to fluctuations of the bias current in the detector branch of the read-out circuit on a time-scale that is long compared to the pulses. In a measurement this manifests itself as a change of the DC baseline of the signals. Depending on the non-linearity of the transition this goes along with a correlated change of the measured pulse height.

Fig. 6.12 shows the pulse amplitude and the baseline, i.e. the working point of the sensor, for the gamma calibration data taken over the two days measurement period. The lines from the γ calibration sources can be identified, and the dependence of the pulse height from the baseline manifests

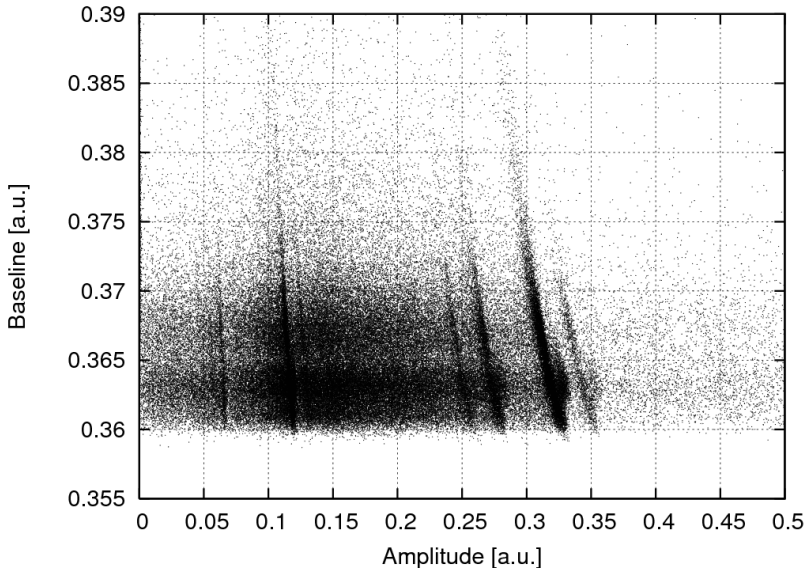

Figure 6.12: Dependence of the fit amplitude on the signal baseline. The four lines above amplitude 0.25 originate from the ^{133}Ba gamma source (276, 303, 356 and 383 keV), the lines between 0.10 and 0.15 correspond to the ^{57}Co gamma source (122 and 136 keV). The structure at amplitude 0.05–0.07 originates from the W escape peak caused by escaping W X-rays after absorption of an 122 keV gamma leading to lines at $\sim$ 55 and $\sim$ 63 keV.

itself in the tilt of the lines in the plot. Without compensation of this effect, i.e. by only using the pulse height, one would obtain a spectrum with poor resolution. However, it is possible to extract a better resolved energy information from the events by using the baseline as well as the amplitude. In order to find a calibration function, the data is split into bins according to the baseline. The chosen bins are 0.001 units wide and cover the range from 0.36 to 0.37. For each baseline bin a calibration factor for the 356 keV gamma line is obtained, that converts pulse height to energy. This calibration factor can be expressed as a linear function of the baseline. This leads to a first calibration function, which calculates the energy of an event from the baseline and amplitude of a pulse:

$$E^{(\mathrm{n.l.})} = (c_1 \cdot B + c_2) \cdot A. \tag{6.5}$$

Here, A is the pulse amplitude, as obtained from the template fit, B is the baseline level. c_1 and c_2 are parameters describing the dependence of the calibration factor from the baseline. For the given data these were fitted as $c_1 = 7855$ and $c_2 = -1739$ $E^{(\mathrm{n.l.})}$ is the calculated energy, which is calibrated at 356 keV. The positions of the other lines are not yet correct, hence the superscript "(n.l.)" for "not linearized".

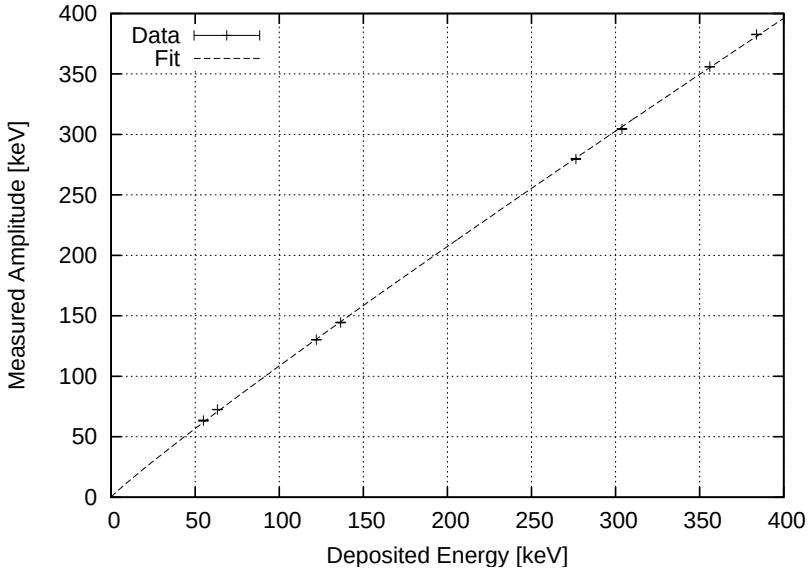

Figure 6.13: Measured pulse height versus the real energy taken from the γ lines of the calibration sources. The data is fitted with a power law.

In the next step a linearisation function for the remaining energy spectrum up to 384 keV is generated. Fig. 6.13 shows the pulse height (amplitude) after

calibrating with function (6.5) versus the real energy absorbed in the crystal. The curve shows the typical non-linearity of the cryodetector, where higher energies are underestimated. This originates from the shape of the transition which flattens in the upper part. The "cut off" fit procedure described above cannot fully compensate this. As the spectrum is calibrated to 356 keV, lower energies are now overestimated, the 122 keV line for example is shifted to an energy of ∼130 keV.

For the given data a very good description for the dependence of the fit amplitude from the real energy was found in a simple power law:

$$E^{(\mathrm{n.l.})} = aE^b \tag{6.6}$$

This power law is fitted to the curve in Fig. 6.13 with the two free parameters a and b. Using the fit parameters (in this case $a = 1.47 \pm 0.12$ and $b = 0.934 \pm 0.014$) the linearisation function for detector response at energies below 400 keV can be defined as:

$$E = \left(\frac{E^{(\mathrm{n.l.})}}{a}\right)^{\frac{1}{b}}, \tag{6.7}$$

with the parameters a and b, obtained from the power law fit. $E^{(\mathrm{n.l.})}$ is the non-linearized energy calculated with function (6.5) and E is then the linearized energy. The functions (6.5) and (6.7) provide a calibration for the detector signal, where the energy of the calibration lines is accurate within an energy window of 2 keV.

Fig. 6.14 depicts the energy spectrum of the calibration data after compensating the baseline drift with the function (6.5) and linearisation with the function (6.7). The resolution obtained from Gaussian fits to the peaks is 3.1 keV FWHM at 122 keV and 20 keV at 356 keV. Only the high energy lines of the ^{133}Ba source are observed. The line with the highest intensity emitted by the source is at 80 keV. However, as the calibration sources are placed outside the cryostat this energy is strongly suppressed by photoabsorption in the material of the cryostat shields.

The two lines around 60 keV do not directly originate from the calibration sources but from the $CaWO_4$ crystal itself. The dominant process for the absorption of the 122 keV gammas is the photoelectric effect on the inner shell of tungsten. The refilling of the resulting vacancy in the K-shell goes along with the emission of X-rays. Their energies are 58 and 59 keV for K_α and 67 to 69 keV for K_β. Those X-rays can leave ("escape") the crystal, in which case their energy is missing for the event resulting in the escape peaks at 55 keV (122 keV with 67 keV escaped, i.e. $K_{\beta 1}$ and $K_{\beta 3}$) and 63 keV (the

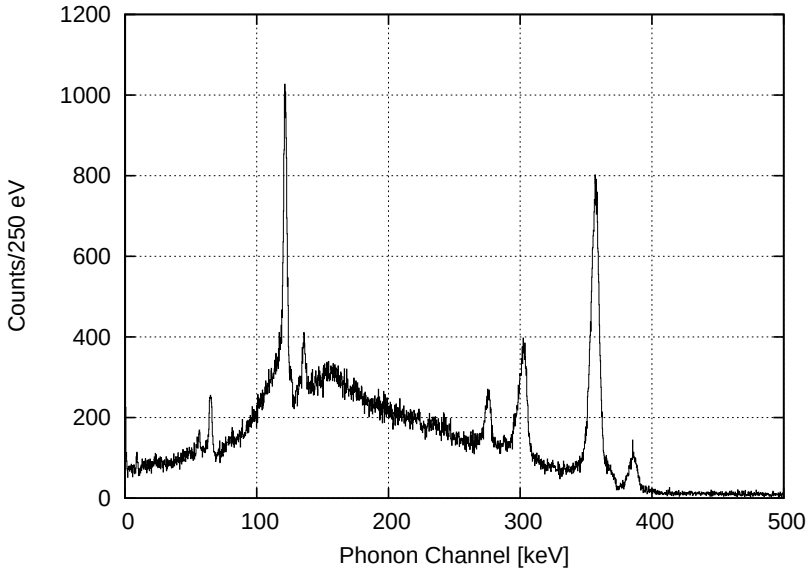

Figure 6.14: Gamma spectrum with linearized energy recorded with a ^{133}Ba and a ^{57}Co source. The observed lines are at 276, 303, 356 and 384 keV from the ^{133}Ba source, at 122 and 136 keV from the ^{57}Co source and the tungsten escape peaks at 55 and 63 keV caused by escaping K_α and K_β X-rays after photoabsorption of a 122 keV gamma by tungsten.

two K_α escapes combined, as they cannot be resolved). In measurements with higher statistics similar peaks appear for the 136 keV photoabsorption.

The 122 keV peak has a strong tailing down to lower energies. This is connected to the fact, that the source is located outside the cryostat and thus a significant amount of material is present between the source and the detector, e.g. the steel and copper of the shields. In those materials the gammas of the source are likely to undergo compton scattering. The compton spectrum for 122 keV photon energy goes up to ∼40 keV. This energy is lost for the scattered photon, leading to the tail of the 122 keV peak reaching down to about 80 keV. The same effect can be observed for the 136 keV line. At higher energies, e.g. at the ^{133}Ba lines, however, the compton spectrum spreads over a wider energy range along with a higher probabilty of multiple compton scattering. The integrated intensity of the compton tail compared to the photopeak is about the same for 120 keV and 350 keV, so that the tailing effect is less prominent for the ^{133}Ba lines due to the broader spreading of the tail.

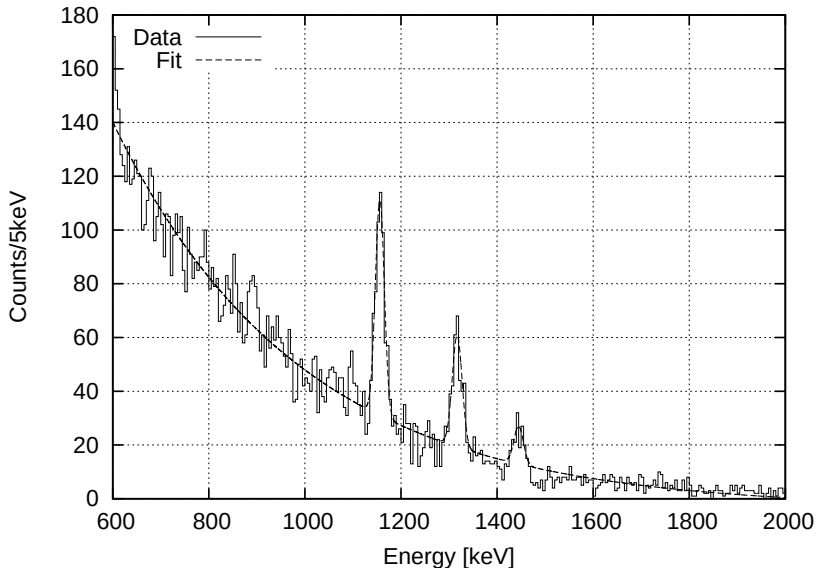

Figure 6.15: Observed photopeaks originating from the ^{60}Co content of the ^{57}Co source and from ^{40}K contamination in the cryostat.

The ^{57}Co source contains also a certain amount of ^{60}Co as an impurity. The decay of ^{60}Co is accompanied by the emission of two gammas with energies of 1173 keV and 1333 keV. The corresponding section of the spectrum is plotted in Fig. 6.15. Note, that for this part of the spectrum the non-linearized energy as calculated with the function (6.5) is used since the lin-

earisation function (6.7) is only applicable for energies below 400 keV. Above this energy the result of the template fit is sufficiently linear.

The spectrum in Fig. 6.15 is fitted with Gaussians for the peaks sitting on an exponential background. The positions for the ^{60}Co are fitted at 1156 and 1317 keV, which is less than 2% deviation from their real energies. A third line is observed at 1445 keV, which can be attributed to ^{40}K decays (gamma energy 1460 keV). ^{40}K is a typical contamination originating from biological sources, e.g. the bodies of the experimentalists. It is thus present in any measurement setup, unless special procedures are applied to keep the setup clean.

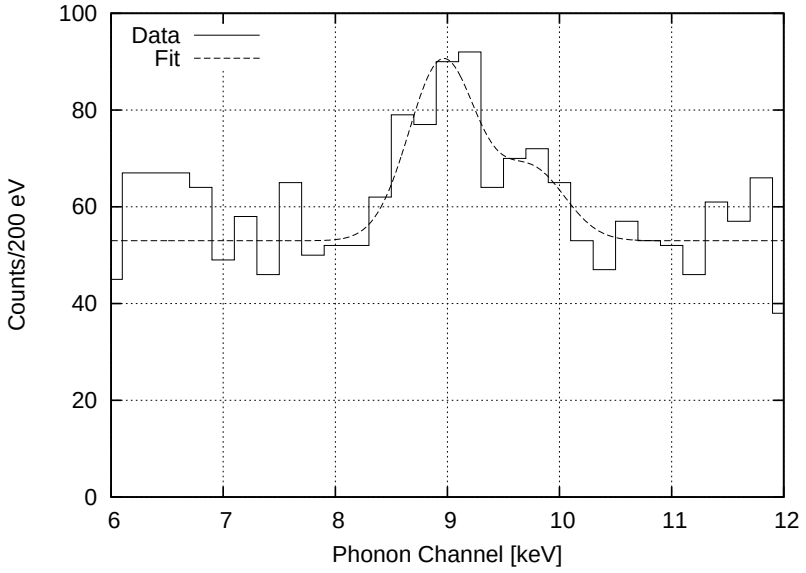

Figure 6.16: Copper fluorescence induced by cosmic muons. The fit is a double Gaussian curve corresponding to the K_α and K_β (8.0 and 8.9 keV) line sitting on a constant background.

In the spectrum shown in Fig. 6.14 a small peak can be seen below 10 keV. This peak is depicted at larger scale in Fig. 6.16. Its origin is copper fluorscence caused by cosmic muons in the holder material surrounding the detector. Despite the high background level and the low statistics the indication for a K_α and K_β separation can be observed. The positions of the lines obtained from a fit with two Gaussians is 9.0 and 9.8 keV, which is about 1 keV off the real energies (8.0 and 8.9 keV). This demonstrates the quality of the linearisation function, which is still accurate at a 10% level for very low energies, although the smallest energy used for generating the function is 55 keV. The resolution obtained from the Gaussian fit is ∼500 eV FWHM,

which is comparable to the resolution for the Mn peaks from the low energy calibration presented in the previous section.

6.2.5 Neutron Measurement

In this section the first results of data obtained with an AmBe neutron source using this detector will be briefly discussed. This measurement is part of the PhD thesis of C. Coppi, where a detailed description of the experiment will be given [63]. Neutrons are produced using the alphas from the decay of ^{241}Am in an (α, n) reaction on Be. This results in a broad neutron spectrum with energies up to 10 MeV with an average neutron energy of 5 MeV. For this measurement the detector was operated together with the silicon light detector presented in [65].

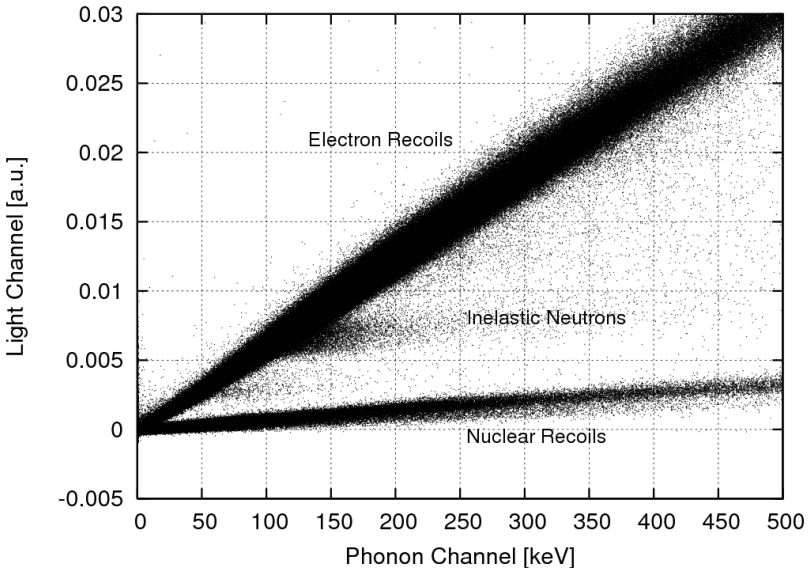

Figure 6.17: Phonon and light signal for the data acquired with an AmBe neutron source. Between the electron recoil band and the nuclear recoil band also mixed neutron and gamma event are observed originating from inelastic neutron scatterings.

Fig. 6.17 shows the signals in the phonon and light detectors obtained with the AmBe neutron source for the energy range up to 500 keV in the phonon channel. The phonon channel is calibrated with functions (6.5) and (6.7) derived from the calibration data presented in the previous section.

To obtain the amplitude of the light channel the events are fitted with a "coincident standard event fit". For such a fit two template pulses for the

phonon and light channels are generated and fitted together to a recorded event with a common onset. This way also very small light signals can be found in the noise, as long as a sufficient phonon signal is present to pinpoint the signal onset. The light signal in the plot is the amplitude of this fit without further calibration. As the light signal is small compared to the phonon signal it is considered to be linear.

The electron recoil and nuclear recoil events are well separated from about 20 keV upwards. In addition to the two main bands from electron and nuclear recoils there are several bands starting in the electron recoil band which are then nearly parallel to the nuclear recoil band. Those bands start at 46 keV and at around 100 keV originating from $(\mathrm{n}, \mathrm{n}\gamma)$ reactions on tungsten nuclei. The emitted gammas from these inelastic scatterings are reabsorbed in the crystal leading to an electron recoil event, while the recoiling nucleus produces a nuclear recoil event at the same time. The resulting event is then a mixture of the two event classes. Furthermore there are a number of events outside those bands between the two main bands which have the same origin but no fixed electron recoil energy. These are due to inelastic scatterings at higher γ energies, where the γ performs compton scattering in the crystal leading to a continuous spectrum, again mixed with the coincindent nuclear recoil event.

Especially at higher energies the nuclear recoil band shows a clear substructure suggesting that it indeed consists of two bands with different scintillation light quenching. These two bands would correspond to oxygen and calcium recoils. Tungsten recoils cannot be separated here, as they contribute only to energies up to $\sim$100 keV where the light signal is still too close to the noise level to be able to resolve the structure of the nuclear recoil band. However, the splitting of the band at higher energies can be used to obtain the quenching factors for oxygen and calcium.

Fig. 6.18 depicts a histogram of the light yield, i.e. the light to phonon ratio, for nuclear recoils in the energy range between 280 and 340 keV. The yield is normalized to 1 for electron recoils at 122 keV. Compared to a similar measurement using a 20 mm $\times$ 20 mm $CaWO_4$ crystal as presented in [65] (see also section 2.4.3) a much clearer separation of the two sub-bands is observed. This is likely to be due to the smaller contribution of multiple scatterings, which lead to mixed oxygen and calcium events, filling the range between the "pure" event classes.

The yield histogram is fitted with two Gaussians representing oxygen and calcium recoils. For the fit no constraints were set. Each Gaussian has three free parameters: position, width and amplitude. From the positions of the gaussians the quenching factors of oxygen and calcium are obtained as 8.66 ± 0.06 (oxygen) and 14.3 ± 0.8 (calcium). The errors originate from

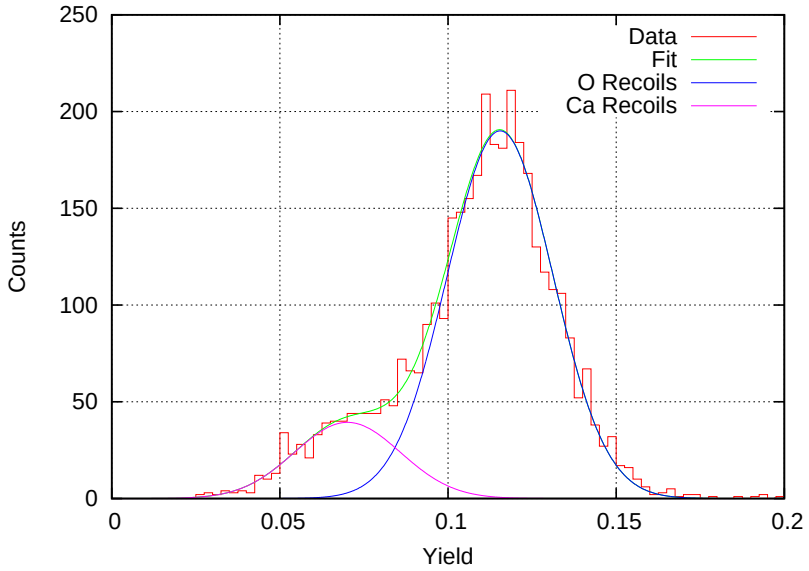

Figure 6.18: Histogram of the light yield for nuclear recoils between 280 keV and 340 keV. The data is fitted with two Gaussians for oxygen and calcium recoils. Compared to earlier measurements with a larger crystal (see Fig. 2.10), the two bands are significantly better resolved.

statistical errors from the fit at a 95% confidence level. The systematic errors, for example the effect of a possible non-linearity of the light detector, are being investigated and will be discussed in [63].

6.3 Scintillation Light Detection

A light detector designed for the calibration experiments, for example the neutron calibration measurements discussed in section 6.2, has to be, like the phonon detector, capable of the count rate that is expected for such a measurement in a non-low-background environment. Furthermore, as the light output for the relevant low energy nuclear recoils is in the order of a few to a few tens of photons, the light detector needs to have a low energy threshold to be able to detect these small amounts of light. Finally, the light collection of the detector module, i.e. the fraction of the emitted light actually detected, has to be maximized. An important factor for this is, of course, the reflective housing, but also the chosen material for the light detector can have an effect, for example due to the reflectivity of the material. In this section detector modules with silicon, germanium and silicon-on-sapphire (SOS) light detectors are investigated concerning the light collection.

6.3.1 Detector Design

The light detectors presented in this section share all the same basic design, regardless of the absorber material. The absorber crystals are formatted to squares of $20 \times 20\,\mathrm{mm}^2$, with a thickness ranging from $375\,\mu$m (SOS) to $525\,\mu$m (silicon). The TES is based on Ir/Au thin films, the transition temperatures are listed in Table 5.2 (see section 5.6). The employed sensor structure is the distributed thermometer structure with aluminum phonon collectors which was also used for light detectors in [65] and for the phonon detector in section 6.2.

6.3.2 Determination of the Light Collection

In order to obtain the absolute light energy absorbed in the light detector, the detector has to be calibrated. This is achieved by installing a low energy calibration source in sight of the light detector (see Fig. 6.19), for this purpose a ^{55}Fe source is used. By comparing the pulses of events originating from the calibration source with pulses from scintillation light events with known energy deposited the $CaWO_4$ crystal, it is possible to calculate the fraction of the energy that is detected as scintillation light in the light detector. The reference energy in the crystal is obtained from a higher energetic calibration source located outside the cryostat, typically a ^{57}Co or ^{137}Cs gamma source.

The energy input of an X-ray in the light detector is instantaneous, while the scintillation light arrives over a larger time scale. This results in different pulse shapes for these event classes. This can be observed in the pulse rise time τ_{rise}, defined as the time span between the pulse onset and the maximum. Fig. 6.20 illustrates this for the light detector Si501A. Here, the scintillation light events show a significantly longer rise time ($\tau_{\mathrm{rise}} \sim 0.6\,\mathrm{ms}$) than the X-ray events ($\tau_{\mathrm{rise}} \sim 0.3\,\mathrm{ms}$). In the X-ray band the 6 keV Mn peak can be clearly identified. The $CaWO_4$ crystal was calibrated with a ^{57}Co source leading to a peak around pulse amplitude 50 in the class of slow events.

For comparing the energy content of the pulses of the two event classes, the pulse height is not a good quantity, as it would underestimate the slower light pulses. The integral of the pulse, however, is always proportional to the total energy, as long as non-linearities of the transition can be neglected. As the recorded time window does not cover the full pulse decays, a model fit is used to extrapolate the pulses beyond the record length, similar to the procedure described for the quasiparticle diffusion measurement in section 5.7. However, instead of fitting each pulse individually, template pulses are generated from X-ray events with fixed energy and from scintillation-light events with fixed energy deposition in the $CaWO_4$ crystal.

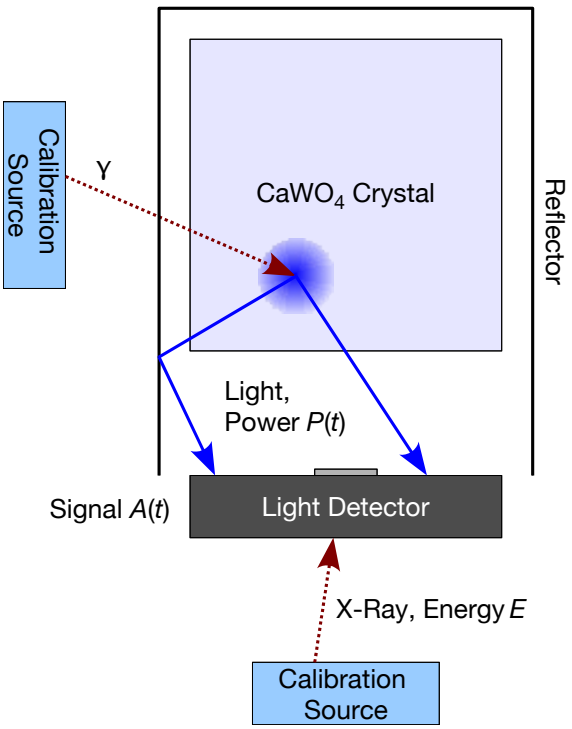

Figure 6.19: Setup for the determination of the light collection of a detector module. The light detector is irradiated with X-rays from a ^{55}Fe calibration source and the scintillation light from a calcium tungstate crystal. The light detector and crystal are mounted together in the usual reflective housing ("Reflector"). To obtain the scintillation light for a known event energy in the crystal, a gamma source (e.g. ^{57}Co or ^{137}Cs) is placed outside the cryostate. As the time characteristics for X-rays and light input in the light detector are different, the two event types can be identified by the shape of the detector signal $A(t)$ (see also Fig. 6.21).

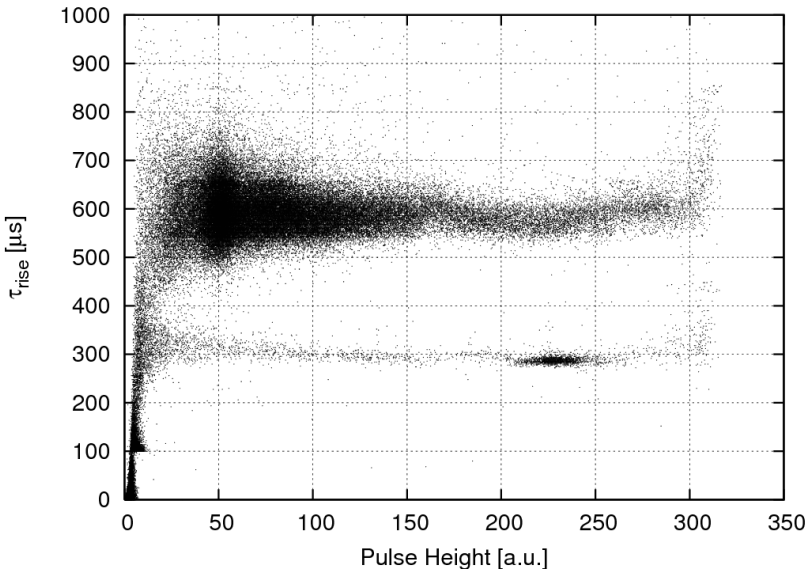

Figure 6.20: Signal rise time τ_{rise} versus the pulse height for data obtained with a light detector irradiated with X-rays from a ^{55}Fe source and the scintillation light from a $CaWO_4$ crystal. Two bands in the rise time characterize the two event classes: The band with fast rise time are events with instaneous energy input (e.g. X-rays), while the scintillation-light events are considerably slower.

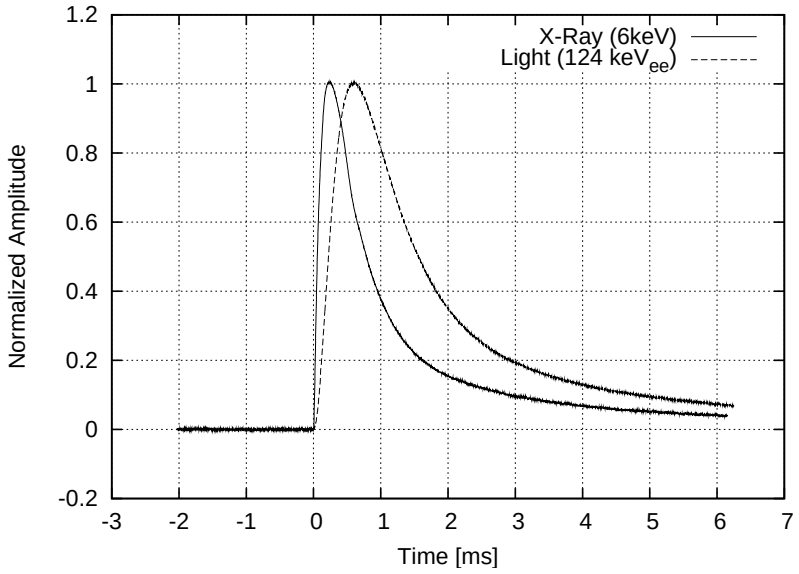

Figure 6.21: Template pulses formed from X-ray pulses around 6 keV and from scintillation light pulses around 124 $\mathrm{keV_{ee}}$. The pulses are normalized to amplitude 1 for better comparison. The scintillation light pulse is significantly slower due to the slow energy input of the light.

Fig. 6.21 shows the normalized template pulses for X-rays and scintillation light for the light detector Si501A in a measurement with the $CaWO_4$ crystal "Cosima". The X-ray template is fitted with the pulse model defined in equation (3.5). For the scintillation light an additional decay time for the light emission is introduced, leading to a model function as defined in equation (3.20), which is used to fit the corresponding pulse template. The fit parameters for the X-ray template provide an energy calibration for the pulse integral. This way the absolute amount of energy E_{light} deposited by the scintillation light in the light detector can be determined. The light collection is then defined as the fraction $E_{\mathrm{light}}/E_{\mathrm{CaWO_4}}$, where $E_{\mathrm{CaWO_4}}$ is the amount of energy absorbed in the $CaWO_4$ crystal.

Table 6.2 lists the light collection measured for various crystals and light detectors. The value for the light collection characterizes the amount of light energy seen in the light detector for electron recoil events in the crystal of the listed gamma energy. This is influenced by the light yield of the crystal, the effiency of the reflective housing and the absorption in the light detector. Most of the crystals are of the dimensions 20×20 (*diameter* $\times$ *height* in mm), which were installed in identical reflective housings, so that for these crystals this factor should make not much difference. The "$\mathrm{Babsi}_{1,2}$" crystals, however, are smaller crystals of the dimension 20×5, which were cut from the

Light Det.	Threshold	Crystal	γ-Line	Light Coll.
Si479A	450 eV	Little Boy	662 keV	0.7%
Si479A	180 eV	Babsi_1 (Cw516)	662 keV	1.6%
Si479A	530 eV	Babsi_2 (Cw520)	356 keV	1.9%
Si501A	185 eV	Cosima (Cw506)	124 keV	1.7%
Ge505B	150 eV	Cosima (Cw506)	124 keV	0.8%
Ge505B	150 eV	Cosima (Cw506)	1170 keV	1.0%
SOS517(∗)	2.7 keV	Babsi_1 (Cw516)	662 keV	1.2%

Table 6.2: Light collection obtained for various light detectors and $CaWO_4$ crystals. Crystals labeled with an Ir/Au film number ("CwXXX") underwent the procedure of evaporating an Ir/Au film onto the crystal and may thus have suffered in the annealing process resulting in a lower light yield. The light detector marked with "(∗)" was measured as unstructurized Ir/Au film and is thus less sensitive than complete detectors. For a detailed discussion of the results see the main text.

20×20 crystal "Babsi". For these smaller crystals the housing is different, particularly the ratio of light detector area to reflector area is larger. In this case the light is less often reflected before reaching the light detector, leading to a possibly higher light collection.

Despite the low statistics some conclusions can be drawn from the results listed in Table 6.2:

- The best light collection was achieved with silicon light detectors. The silicon-on-sapphire absorber showed a slightly lower value than the reference measurement with a pure silicon absorber. For the germanium only half of the light energy seen in the silicon was determined.

- The crystal "Little Boy", which was grown in the old Czochralski facility at the TUM showed a significantly lower light output than the commercially purchased ones. Still it was one of the first crystals produced in that facility with the conditions not being optimal. An improvement can be expected from the newly installed crystal growth facility [97].

6.3.3 Discussion of the Energy Threshold

Each pulse is recorded with a baseline sample before the actual pulse onset. For each event the standard deviation σ of the data points of the baseline is calculated. The energy threshold listed in Table 6.2 is the averaged 5σ value for all events, with the amplitude calibrated to the pulse height of the 5.9 keV events from the ^{55}Fe source. This threshold defines the limit, down

to which a hardware trigger can be set without triggering into the electronic noise.

For the determination of the threshold the detector is assumed to be linear below the 5.9 keV calibration line. However, a typical transition edge sensor shows a non-linearity in a way, that higher pulses are underestimated. As a consquence, after the calibration to the 5.9 keV line, pulses close to the threshold are then assigned higher energy values than they actually represent. This means that the real energy threshold would be lower than the listed value, which is then an extremely conversative estimation of the threshold. How strong this effect is, depends on the strength of the non-linearity and how close to the threshold the calibration line is. Typically the non-linearities are within 10%.

When the light detector is operated together with a phonon detector, the primary signal, i.e. the signal which provides the trigger, is the phonon channel. The light channel is then merely recorded together with the phonon signal. The pulse heights are determined off-line in a coincident template fit, where phonon and light signal channel are fitted together with their respective templates with a common onset. In this case the recorded signal is filtered with the detector's pulse shape, allowing to discriminate also very small signals from pure noise. The energy threshold is then effectively smaller than the trigger threshold defined by the baseline noise.

6.3.4 Scintillation Time Constants

As shown above the observed pulse shapes for X-ray and scintillation light events in a light detector differ in a way that the scintillation light pulses are slower. This is due to the different time characteristics of the two event classes: the X-ray arrives within a short time interval, while the light arrives over a longer time scale with an own characteristic function $f_{\text{light}}(t)$. Assuming that the pulse shape of the detector is energy independent, a single scintillation light photon would lead to a similar pulse shape as the X-ray, only scaled down to its energy. A continuous stream of photons then will end in a pulse shape that is a convolution of the pulse shape of an almost instantaneous event, defined by the X-ray pulses, and the light function f_{light} (see also section 3.1.2).

In a measurement were both event classes are present, it is thus possible to obtain information on the time characteristics of the scintillation light by comparing the pulse shape f_{direct} for X-ray and f_{lp} for scintillation light events, where f_{lp} is the convolution of f_{direct} and f_{light}. In [71] this basic idea was used to obtain two time constants for the decay of the scintillation light. The approach there was to fit the X-ray pulse with the usual model

function defined in equation (3.5) and the scintillation pulse with the same pulse shape convoluted with a bi-exponential decay. In this section, however, a more model independent method is used to extract f_{light}. No a priori assumptions for a parametrisation of the functions are made, except that f_{lp} is the convolution of f_{direct} and f_{light}.

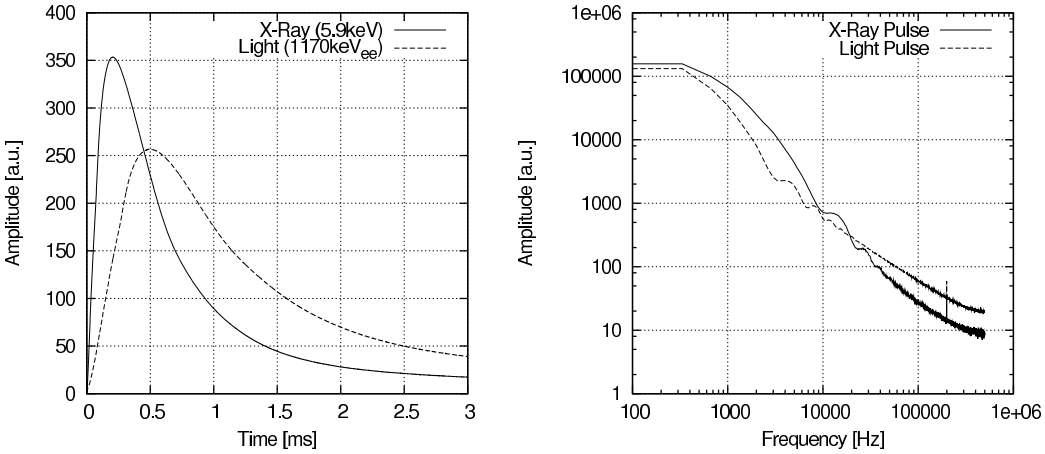

Figure 6.22: Left: Pulse templates for X-ray events (f_{direct}) around 5.9 keV and scintillation light events (f_{lp}) for 1170 keV gamma energy deposition in the $CaWO_4$ crystal. Right: Fast fourier spectra of the template pulses for X-ray and scintillation light events.

For obtaining the pulse shape f_{light} of the original scintillation light signal a numerical deconvolution of the pulse shapes of the light pulse f_{lp} and the direct signal f_{direct} is performed using fast Fourier transformation. In order for this to work pulses with low noise content and equal length (measured from the onset) are required. For this reason pulse templates of the two event classes are formed by summing the recorded pulses starting at their onset, thus omitting the pretrigger part. The left plot in Fig. 6.22 shows the pulse template generated this way for the 5.9 keV X-ray and 1170 keV_{ee} scintillation light events obtained with the light detector Ge505B together with the $CaWO_4$ crystal "Cosima". The frequency spectra of the pulses obtained by fast Fourier transformation are depicted in the right plot of the figure.

The deconvolution is then performed by dividing the Fourier spectrum of the light pulse by the Fourier spectrum of the X-ray pulse. The light curve $f_{\text{light}}(t)$ is then the real part of the inverse Fourier transformation of the resulting Fourier spectrum. Fig. 6.23 shows the light curve obtained in this way from the pulse templates in Fig. 6.22. The curve is very noisy, but the decay of the light emission is observable. A fit with a single decay time τ

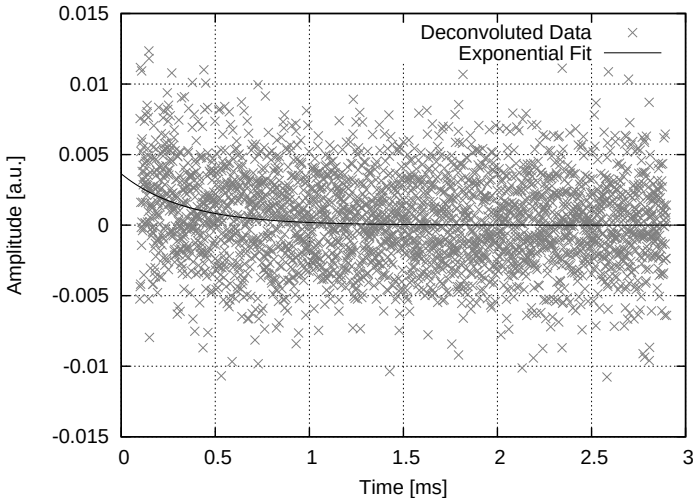

Figure 6.23: Light curve $f_{\text{light}}(t)$ of the crystal "Cosima" obtained via numerical deconvolution of the pulses shown in Fig. 6.22. The data is fitted with a single exponentional decay with decay time $\tau = 340\,\mu$s.

yields $\tau = 340^{+190}_{-90}\,\mu$s. The noise in the scintillation light curve is dominated by the high-frequency noise which is effectively amplified in the deconvolution process. This high-frequency noise can be eliminated by post-processing the deconvoluted data with a digital low pass filter.

After applying a running average filter with a window width of 300 channels, i.e. 10% of the record length, the light decay curve shown in Fig. 6.24 is obtained. The first running average window is neglected here, as it contains an artefact of the sharp rise at the start of the curve. Fitting this filtered curve with a single decay time yields $\tau = (402 \pm 5)\,\mu$s, compatible with the result of the unfiltered curve. However, a better fit is obtained with a bi-exponential decay:

$$f_{\text{light}}(t) = C \cdot \left[\frac{\alpha}{\tau_1} \mathrm{e}^{-t/\tau_1} + \frac{1-\alpha}{\tau_2} \mathrm{e}^{-t/\tau_2} \right] \tag{6.8}$$

with the parameters $\alpha = 0.78 \pm 0.04$, $\tau_1 = (293 \pm 9)\,\mu$s and $\tau_2 = 1.8^{+0.4}_{-0.3}\,$ms. This means that about 80% of the light is emitted with the faster time constant. The values are in agreement with the results given in [71], the faster decay time also agrees with the value reported in [101]. This is not the case with measurements at higher temperatures, where faster decay times were determined (see section 2.4 or ref. [101, 102]). In [101] another, very fast ($\sim 1\,\mu$s) decay time was observed at mK temperatures in addition to the 0.3 ms component. This cannot be seen here, as it would be too fast for

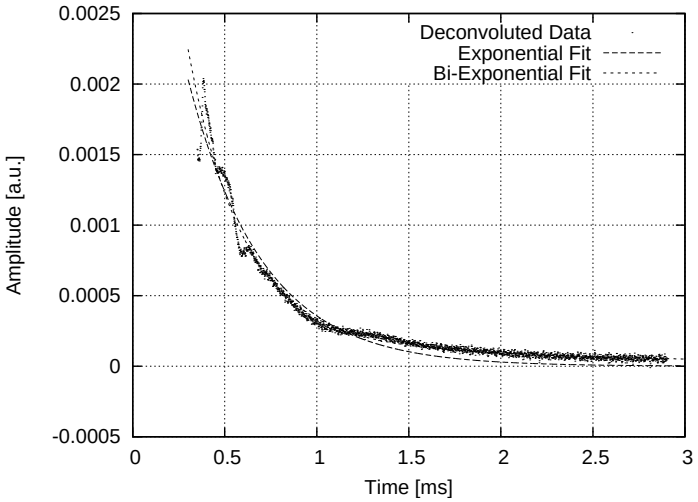

Figure 6.24: Light curve $f_{\text{light}}(t)$ of the crystal "Cosima" obtained via numerical deconvolution of the pulses shown in Fig. 6.22 after applying a running average filter. The data is fitted with a single exponentional decay with decay time $\tau = 402\,\mu$s. A better fit is obtained with two decay times $\tau_1 = 293\,\mu$s and $\tau_2 = 1.84\,$ms.

the given time resolution. However, this fast decay time, if present, cannot contain a large fraction of the light energy, as in this case the light pulses would be faster, similar to the X-ray pulses.

The errors of the fitted decay parameters given above are only the statistical errors of the fit procedure at a 95% confidence level. Further error sources can be in the choice of the running-average interval, the subset of pulses picked for forming the templates, the energy range where the pulses are taken from and in the assumption that pulses for single photons with 3 eV are of the same shape as those for 6 keV X-rays. In the following the impact of these error sources on the results for the decay times is briefly discussed.

- Filtering the light curve with a running average of 350 instead of 300 channels width shifts the results for a single decay time to $\tau = (411 \pm 5)\,\mu$s. Fitting with two decay times yields $\tau_1 = (291 \pm 8)\,\mu$s and $\tau_2 = 1.8^{+0.3}_{-0.2}\,$ms. Using a window of 250 channels ends up in $\tau = (390 \pm 5)\,\mu$s for the single exponential fit and $\tau_1 = (285 \pm 8)\,\mu$s and $\tau_2 = 1.8^{+0.3}_{-0.2}\,$ms for the bi-exponential fit. Thus the impact of the running average window size is small, yet still at least for the single exponential fit larger than the statistical error of the fit.

- The templates used for the deconvolution process were generated from about 3000 individual light and X-ray pulses, respectively. Taking only

a subset of 2000 pulses for each event class leads to pulse templates with a higher residual noise level. The fits yielded here the same results as for the templates from the full set of pulses for the single as well as for the bi-exponential decay function.

- To check the depedence on the light energy a light template for the 1333 keV ^{60}Co peak was generated and deconvoluted with the X-ray template. The decay time obtained here were $\tau = (401 \pm 5)\,\mu$s for the single exponential and $\tau_1 = (292 \pm 9)\,\mu$s and $\tau_2 = (1.7 \pm 0.3)$ ms for the bi-exponential fit. The results are thus also robust in this respect.

- The impact of the energy range, where the X-ray template is generated, and thus the linearity of the light detector, could be checked by generating templates for lower energies. However, there is typically not enough statistics in this event class outside the Mn peaks to form a good enough template. Instead, the influence of the detector is checked by comparing the results with decay times obtained with a different light detector. Fig. 6.26 shows the light curve for electron recoils measured with the light detector Si479A. The decay time obtained here were $\tau = 0.62^{+0.11}_{-0.08}$ ms for the single exponential and $\tau_1 = 0.38^{+0.24}_{-0.10}$ ms and $\tau_2 > 0.9$ ms for the bi-exponential fit. These values are systematically higher than for the measurement with light detector Ge505B, indicating the effect of the light detector on the obtained time constants.

Electron and Nuclear Recoils

In measurements with neutron sources, like the one discussed in section 6.2.5, different pulse shapes in the light detector for electron and nuclear recoil events are observed, where the electron recoils have a slower decay time (see Fig. 6.25). In this measurement also a ^{55}Fe calibration source for the light detector was present, so that the same method as described above can be applied to investigate the scintillation time constants for electron and nuclear recoils.

The obtained light curves for the crystal "Babsi" are shown in Fig. 6.26 (electron recoils) and Fig. 6.27 (nuclear recoils). The plots depict the light curves after the deconvolution and filtering with a running average filter of 150 channels (again 10% of the record length), with the first running average window omitted.

However, the quality of the curves is considerably lower than the light curve in Fig. 6.24. The reason for this is the presence of high-frequency noise (247 kHz) in the signal causing a 47 kHz noise by aliasing. This is a characteristic frequency of the SQUID electronics (Applied Physics SQUID

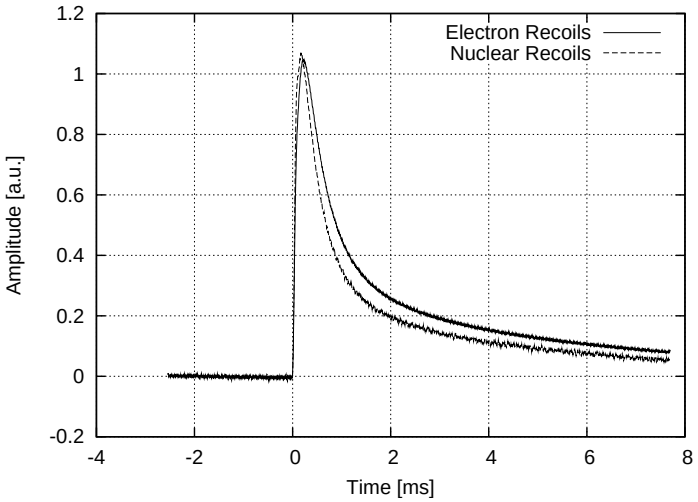

Figure 6.25: Templates of light detector pulses for electron and nuclear recoil events. Both templates were taken from events with the same light energies.

system) used to record the data. While the white noise is efficiently reduced when generating the template pulse, this artefact, which is a clean sine wave, survives the process in a larger fraction, due to two effects:

- The hardware trigger fires as soon as the signal rises over the chosen trigger level. This is more likely the case in the maximum of the 247 kHz sine wave than in the minimum.
- The algorithm used to determine the onset for removing the pre-trigger looks for the last point within the baseline noise before the pulse maximum. This point is more likely to be close to the minimum of the sine wave than close to the maximum.

As a consequence of both effects, the determination of the onset is in phase with this part of the noise and thus this sine wave remains on the pulse templates and finally also on the deconvoluted light curve. Another, although less important, issue is the low sampling rate the data was recorded with (5 μs per time bin), leading to the omission of the first millisecond by cutting the first running-average window.

Nevertheless, the obtained curves can be fitted to the bi-exponential light curve model function (6.8). For the electron recoils (Fig. 6.26) a value for the faster decay time is obtained as $\tau_1 = 0.38^{+0.24}_{-0.10}$ ms. The slower decay time is fitted with $\tau_2 = 2.1$ ms, for the error only a lower boundary $\tau_2 > 0.9$ ms can be set. The data is thus also compatible with a complete absense of a second decay time. To the light curve for the nuclear recoils (Fig. 6.27) only

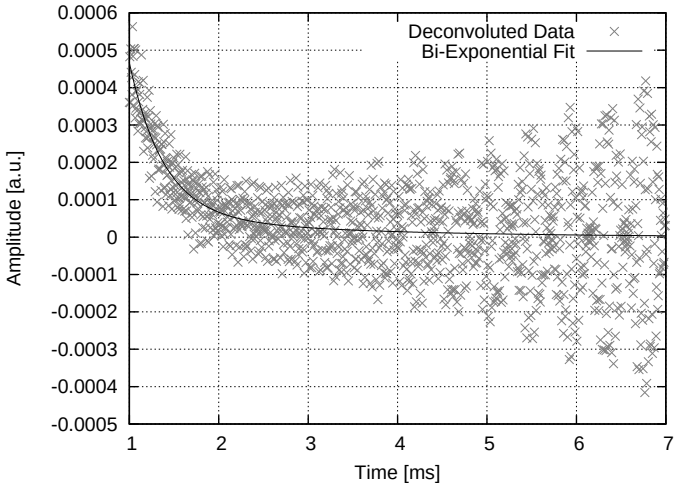

Figure 6.26: Light curve of crystal "Babsi" for electron recoil events.

one decay time could be fitted: $\tau_1 = 0.38^{+0.06}_{-0.05}$, the second component is not observed here.

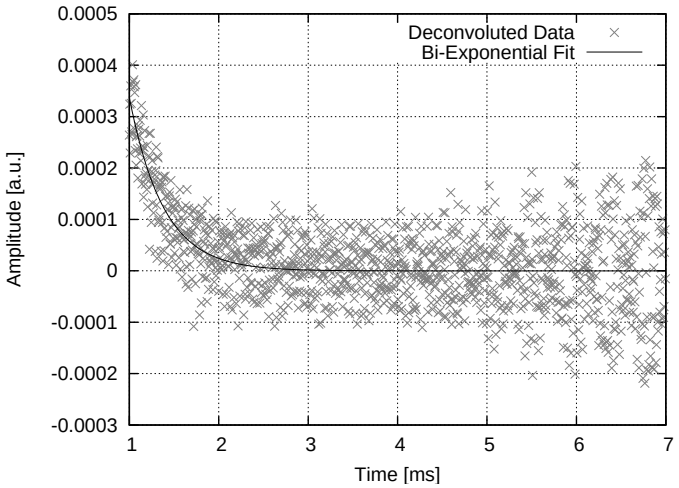

Figure 6.27: Light curve of crystal "Babsi" for nuclear recoil events.

Due to the large errors both fit results are compatible and thus no unambiguous statement about the origin of the slower decay of electron recoil light pulses can be made. However, the fit values can be interpreted as indication, that the fast component is present with the same decay time in both electron and nuclear recoils. For the electron recoils a second, slower, component of the scintillation light lead to longer pulses. For nuclear recoils this second component is strongly suppressed, if not completely absent.

Chapter 7

Background Suppression and Calibration Measurements for CRESST

7.1 Recoiling Nuclei from Surface Alpha Decays

7.1.1 Motivation

The region of interest for dark matter search in CRESST are nuclear recoils up to 40 keV. A background that can be very harmful in this region are recoiling nuclei from surface alpha decays, originating mainly from surface ^{210}Po contamination, which is a radon daughter. ^{222}Rn is a radioactive gas in the ^{238}U chain and as such present in every environment, especially in the air of underground facilities, where it is emanated by the surrounding rock. The decay product of ^{222}Rn, ^{218}Po, is adsorbed at surfaces. The ^{218}Po decay chain is characterized by several alpha decays. In each of the alpha decays, the respective daughter nucleus may also be implanted. The next long lived isotope in the chain is ^{210}Pb, with a half-life of 22.3 years. ^{210}Pb decays via beta decay to ^{210}Bi, which in turn decays with a half-life of 5 days to ^{210}Po. ^{210}Po has a half-life of 138.3 days. Thus, even materials that are kept clear from radon for a long time will exhibit a ^{210}Po activity on and close to the surface that diminishes with the half-life of ^{210}Pb, when the two isotopes are in equilibrium.

In half of the alpha decays on surfaces facing the $CaWO_4$ crystal or on the crystal surface itself the alpha particle moves away from the crystal whereas the daughter nucleus receives a momentum towards the crystal. In 99.99%

of all cases the ^{210}Po decays to the ground state of the daughter nucleus ^{206}Pb. The total energy of the decay (5407.5 keV) is then fully converted into the kinetic energy of the alpha particle (5304.4 keV) and the recoiling ^{206}Pb nucleus (103.1 keV). This energy is deposited in the absorber. For such a heavy nucleus this leads to an event with highly quenched scintillation light.

For decays underneath the surfaces facing the crystal the produced ^{206}Pb nucleus loses some energy on its way to the $CaWO_4$ crystal. Thus this class of events may leak into the relevant detection region below 40 keV and therefore limit the sensitivity of the experiment.

However, these events can be vetoed by making the surfaces facing the crystal scintillating. In this way the escaping alpha particle induces an additional flash of light that is detected in the light detector and adds to the small light signal from the nucleus hitting the $CaWO_4$. The efficiency of this veto was demonstrated in the CRESST run of spring 2004, where a scintillating polymeric foil was used as reflector. The vetoed events could be identified in the light channel, as the scintillation light from the foil produces a different pulse shape than the light from the crystal [53].

In order to characterize this background, calibration experiments were performed as part of this work, where sources with surface activity enriched in ^{210}Po were placed inside the detector housing. The goal of these experiments was the characterization of the energy distribution and light yield of those recoils. These experiments were also a preparation for future measurements aiming at the determination of the efficiency of the veto using the scintillating reflector foil and the characterization of the scintillation properties of the foil at low temperatures.

7.1.2 Source Preparation and Installation

For the first experiments a chemically produced source was used. ^{210}Po from a radium solution is autodeposited onto a polished silver disc [103]. The radium is dissolved in hydrochloric acid, into which the silver disc is immersed. When the solution is heated to 90°C its polonium content (from the radium decays) is deposited onto the silver disc with an efficiency of $\sim 80\%$. After the decay of the short-lived ^{218}Po and ^{214}Po only ^{210}Po is left on the disc. No significant background originating from other decays in the radium chain was observed in the data shown below, so the contribution of possibly deposited radium or ^{210}Pb on the silver disc is negligible.[1]

The silver disc is glued onto the tip of a screw using "IMI" varnish (for-

[1] I would like to thank Dr. Michael Stark for the preparation of the source, which was one of his last tasks before leaving the group.

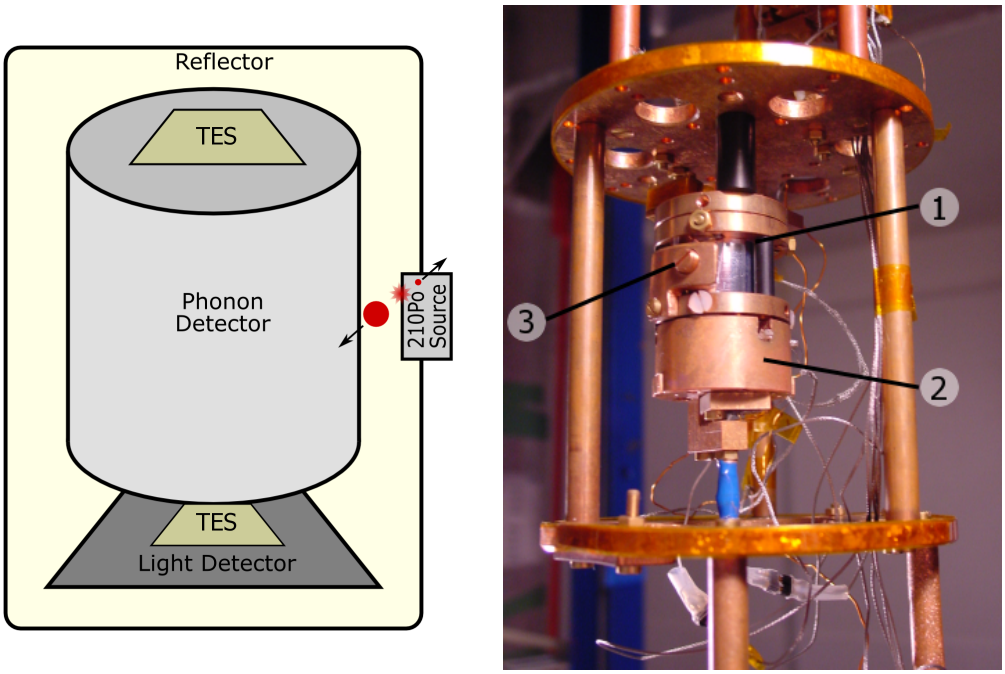

Figure 7.1: Installation of the ^{210}Po source in the detector housing. The schematics (left) show how the source is placed with respect to the $CaWO_4$ crystal. The photograph (right) shows the detector module mounted in the cryostat. The labeled components are: (1) the reflective housing around the crystal, (2) the light detector (holder) and (3) the source holder going through the reflector. The holder parts for phonon and light detector are thermally decoupled to allow for an individual temperature stabilization.

merly "GE" varnish). Using this screw and a matching copper piece on the detector holder, the source is introduced into the reflective housing through a hole in the reflective foil (see Fig. 7.1). The phonon detector used for these measurements is the 20 mm × 20 mm cylindrical $CaWO_4$ crystal "Doreen" (detector Cw466 [65]). A $20 \times 20 \times 0.5\,mm^3$ silicon light detector was used.

7.1.3 Results

As the light signal for nuclear recoils is close to (or even below) the noise level of the light detector, a simple maximum search in the light pulses would overestimate the pulse height and produce wrong result. Instead, a coincident template fit for both phonon and light channel is performed, where the onset of an event is defined by the phonon signal and the amplitude of the light signal is matched at the same position.

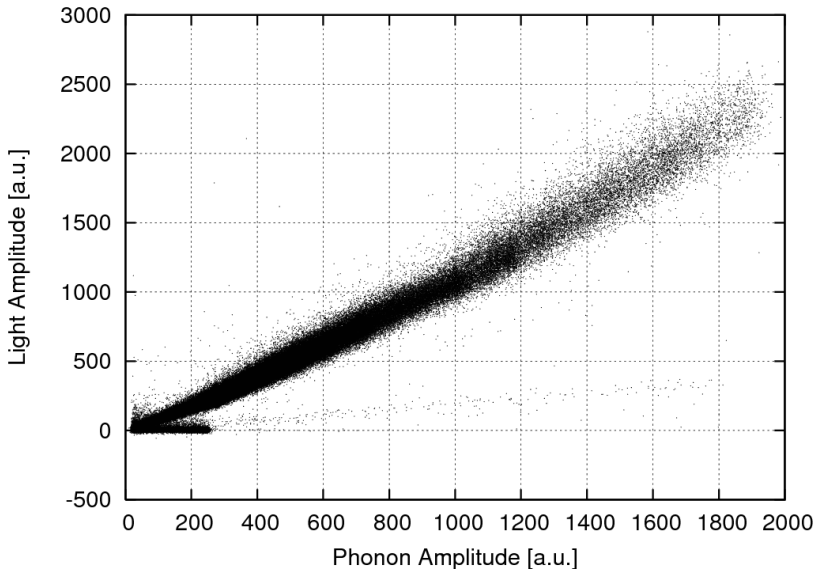

Figure 7.2: Plot of the light amplitude versus the phonon amplitude as obtained from the coincident template fit.

Fig. 7.2 shows the obtained fit amplitudes for phonon and light channels of a 10 hour measurement after cuts on stability and well fitted pulses. Additionally to the electron recoil band with the highest light output and the band caused by the recoiling nuclei with almost no light, a thin band between the two event classes covering the whole dynamic range can be observed. These events can be assigned to alphas from the source which have lost some energy on their way out of the source. The end point of the alpha

band (5.3 MeV), however, is beyond the dynamic range of the measurement, as the detector settings were optimized for low-energetic recoiling nuclei.

Linearisation

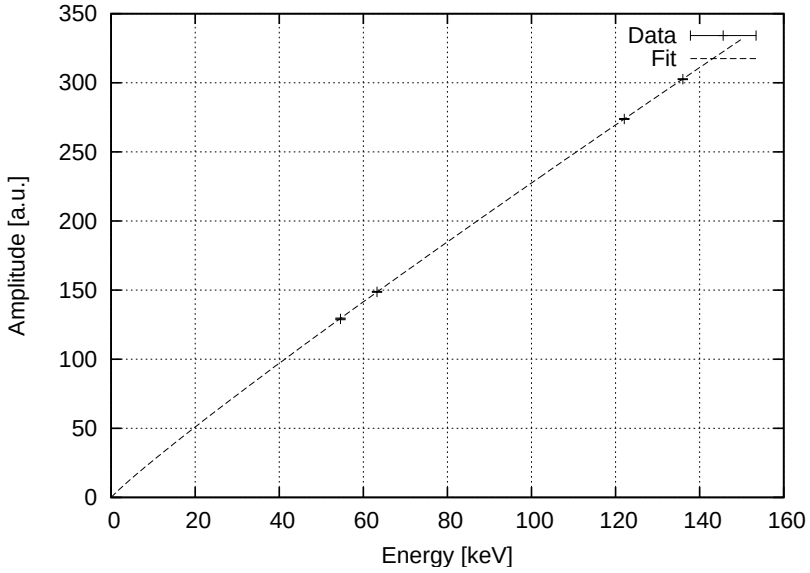

Figure 7.3: Measured pulse height versus expected energy. The data is fitted with a power law $A = aE^b$ (A being the measured amplitude, a and b the fit parameters), the inverse function is then used to convert amplitude to energy.

For the energy calibration a ^{57}Co source is used, providing gamma lines at 122 and 136 keV. The W escape peaks at 55 keV (K_β) and 63 keV (K_α) corresponding to the 122 keV line provide two additional lines for the energy calibration. The escape peaks of the 136 keV absorption are too weak to be used. Fig. 7.3 shows the measured pulse heights for the four calibration lines in the phonon channel. Analogously to section 6.2, a power law is used to convert the pulse height into energy.

Fig. 7.4 shows the spectrum of the electron recoil events in the phonon channel after applying the calibration function. For separating the electron and nuclear recoil band, the ratio of the amplitude in the light channel and the phonon energy is calculated. The separation level is then set at 50% of the average ratio of electron recoils. Everything with a light-to-phonon ratio above this level is considered to be an electron recoil, everything below is a nuclear recoil. The resolution in the phonon channel as obtained from a Gaussian fit to the line in the spectrum is 4.3 keV at 122 keV electron recoil

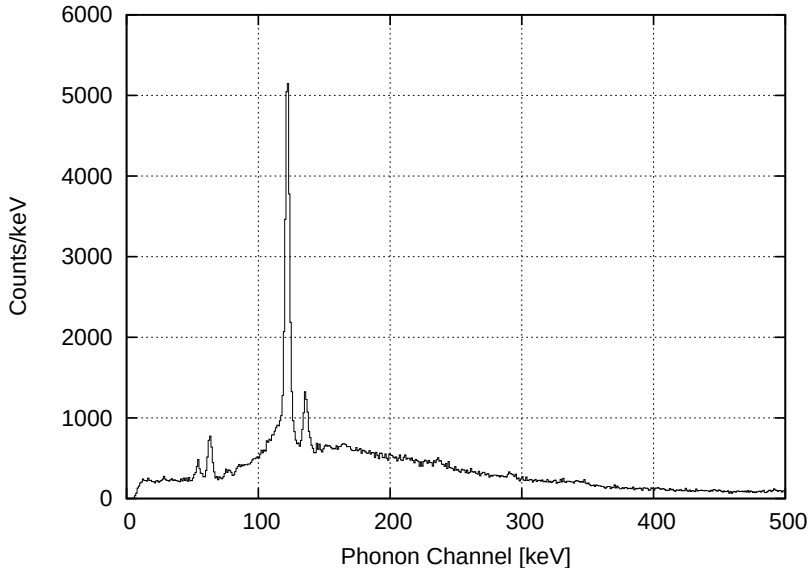

Figure 7.4: Spectrum of the electron recoils as seen in the phonon detector after applying the conversion from pulse height to energy. The lines originating from the ^{57}Co source at 122 and 136 keV, as well as the W escape lines at 55 and 63 keV are observed.

energy. The trigger threshold is at about 5 keV. A full separation of electron and nuclear recoil events is possible from 40 keV on.

Absolute Light Yield and Phonon Quenching

The pulse height in the phonon channel is usually assumed to represent the whole energy of an event for all event classes, as the light output is considered to be negligibly small. In reality the energy deposited in the absorber is split into phonon and light signal (assuming that no other channel with a significant contribution exists):

$$E = C_p A_p + C_l A_l. \tag{7.1}$$

Here, E is the total energy, A_p and A_l are the measured amplitudes in the phonon and light channel and C_p and C_l are calibration factors for the two channels, for the case that they are linear. A calibration of the phonon energy using electron recoil events (like gamma lines) leads then to an overestimation of the energy of events with reduced light output (like nuclear recoils), as for those a higher fraction of the energy is converted into phonons. Thus, in a strict way, the phonon axis of the typical phonon-yield or phonon-light plots

would also have to be labeled as "keV$_{ee}$" like the light axis as also the phonon energy represents the "electron equivalent".

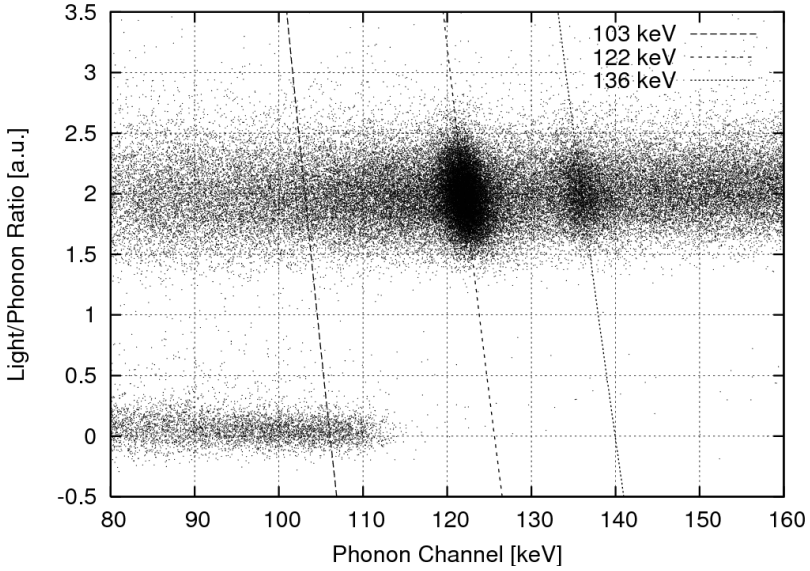

Figure 7.5: The ratio of the light amplitude to the phonon amplitude versus the phonon amplitude for the energy range around the gamma lines of the ^{57}Co source. The tilt of the lines in the gamma band is clearly visible. Also shown are lines of constant energies for the positions of the ^{57}Co gamma energies (122 and 136 keV) and for the expected endpoint of the nuclear recoil band (103 keV).

For an accurate energy calibration of all event classes the different contributions of the scintillation light to the total energy have to be taken into account. This leads to a scaling factor for the phonon channel depending on the event class analogous to the quenching factor in the scintillation light. In Fig. 7.5 this phonon quenching can be observed in two ways: in one case, the band of the ^{206}Pb nuclei exceeds the end point of 103 keV more than it is expected, even if the detector resolution is taken into account. For the other, the gamma lines in the electron recoil band are tilted, so that the events at higher light yields have a lower phonon signal and vice versa.

The calibration factors for the phonon and light channels can be obtained from the tilt of the 122 keV gamma line. For this purpose the electron recoil band is stripped into several bins with constant light-to-phonon ratio, $Y = A_l/A_p$. Where A_p is the linearised phonon amplitude as obtained from the gamma calibration discussed in the previous section. A_l is the raw template fit amplitude in the light channel, the light signal is considered to be sufficiently linear at the given low light energies. For each bin of Y the

position of the 122 keV line in A_p is determined by a Gaussian fit. The dependence of A_p of the yield can be described by the model function:

$$A_p = \frac{E}{C_l Y + C_p}, \tag{7.2}$$

with $E = 122\,\text{keV}$ as the gamma energy of the line. The calibration factors C_l and C_p can then be obtained by fitting this model to the obtained Y and A_p data points.

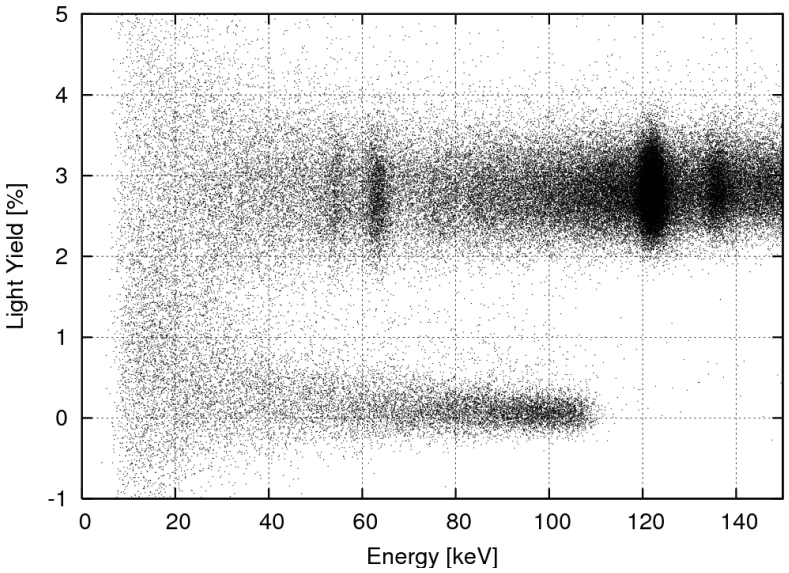

Figure 7.6: Reconstructed relative light output versus deposited energy.

Using the parameters C_l and C_p for each event the total energy E, as well as the phonon energy $E_p = C_p A_p$ and the light energy $E_l = C_l A_l$ can be determined. Fig. 7.6 depicts the fraction E_l/E of the total energy that is emitted as scintillation light for the events up to 150 keV. For electron recoils an average energy fraction of (2.8±0.3)% is converted into scintillation light. Note that this is actually the amount of light *emitted* by the crystal in contrast to the amount of light finally detected in the light detector as it was determined in section 6.3.2. The light collection of this phonon/light detector pair was determined to be 0.7–0.8% [65], thus only about 25–30% of the emitted light is eventually detected in the light detector.

Fig. 7.7 shows a comparison of the spectrum of the nuclear recoils for the cases with and without phonon quenching. For comparing the end point of the spectrum the bin of the histogram is taken, where the count rate is half of the maximum count rate. This point should be not further away from

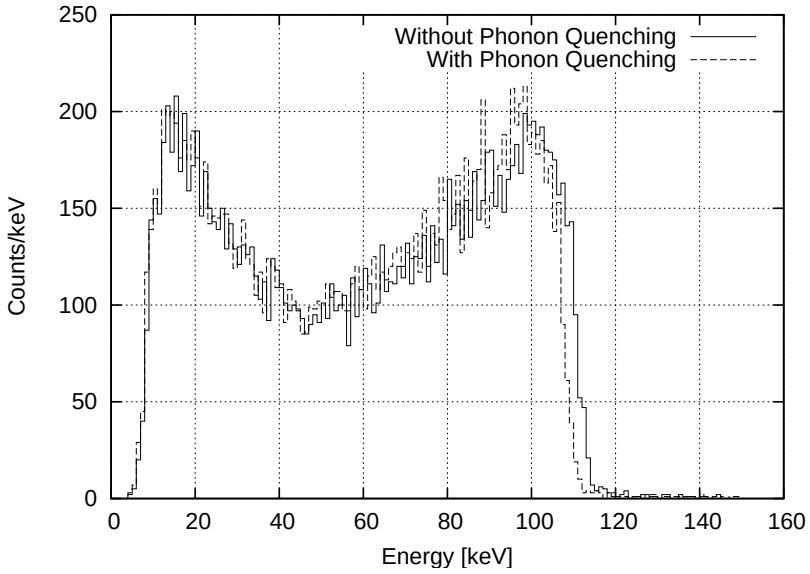

Figure 7.7: Spectrum of the nuclear recoils with and without inclusion of phonon quenching. When phonon quenching is taken into account the end point of the spectrum is shifted to lower energies and matches better the maximum energy of the ^{206}Pb recoil (103 keV).

the maximum recoil energy (103 keV) than half the resolution (in FWHM) of the detector in this energy range, i.e. 2.2 keV. For the case without phonon quenching, i.e. the energy calibration of the electron recoils is used also for nuclear recoils, this point is found to be at (110 ± 0.5) keV (the error is estimated to be half an energy bin). For the case with phonon quenching the point is at (107 ± 1) keV (combined error for the binning and the error of C_p), which is closer to the maximum recoil energy, but still too large. Possible reasons for this are:

- The light detector is not linear. Higher energies are underestimated, and thus a light yield too small for the electron recoils is determined, leading to too small a phonon quenching for nuclear recoils.

- The resolution of the light channel is not negligible. The demonstrated method for obtaining the light output relies on the assumption that the width of the electron recoil band is dominated by the crystal. When the resolution of the light detector is not good enough, the electron recoil band is more smeared out in the light channel, leading to a smaller tilt of the lines in the band, which will also result in a light yield too small for the electron recoils.

- For electron recoils there is also a third channel, providing another branch for the energy loss. In this case, the phonon and light channel would not account for the full amount of energy for electron recoils, while for nuclear recoils still almost the complete energy would be seen in the phonon signal. This third channel could be explained by excited states in the crystal with lifetimes much longer than the time window of the recorded pulses (several ms).

Light Output for Recoiling Nuclei

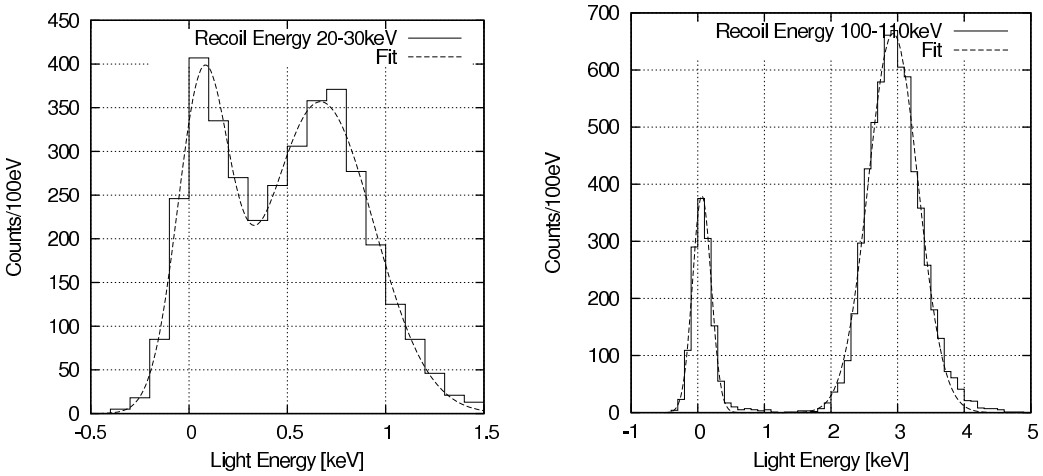

Figure 7.8: Obtaining the light output: The data is distributed in energy bins of 10 keV width. For each bin the histogram of the light output is fitted with two Gaussians, one for the nuclear and one for the electron recoils. This way the light output of the two event classes can also be obtained below the separation threshold (left plot).

In order to obtain the light signal of the nuclear recoils, the light output of all events from 10–110 keV is histogrammed in 10 keV bins and fitted with two Gaussians, one for the electron and one for the nuclear recoils. This way the light yield for the nuclear recoils can also be determined for energies below the separation threshold, where an event-by-event discrimination is no longer possible (see Fig. 7.8).

The results of this analysis (Fig. 7.9) were unexpected: The light output decreases with rising energy. This is in contradiction to the simple assumption that ^{206}Pb is the only nucleus hitting the crystal, as in this case one would expect a monotonously rising light curve.

This effect can be seen even more clearly in the quenching factors of the nuclear recoil band obtained for each energy bin (see Fig. 7.10). The

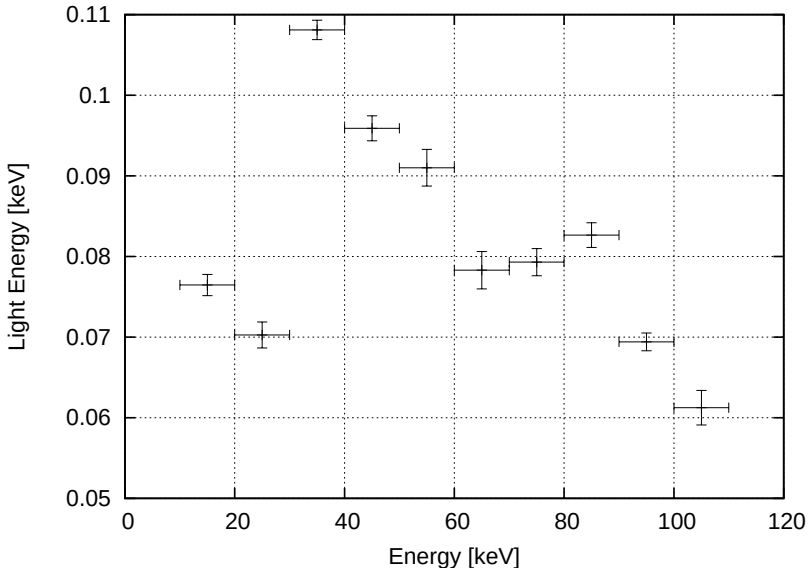

Figure 7.9: Light output for the recoiling nuclei events as obtained from the Gaussian fits. The error bars on the y-axis indicate the statistical error from the fits, the error bars on the x-axis merely show the binning.

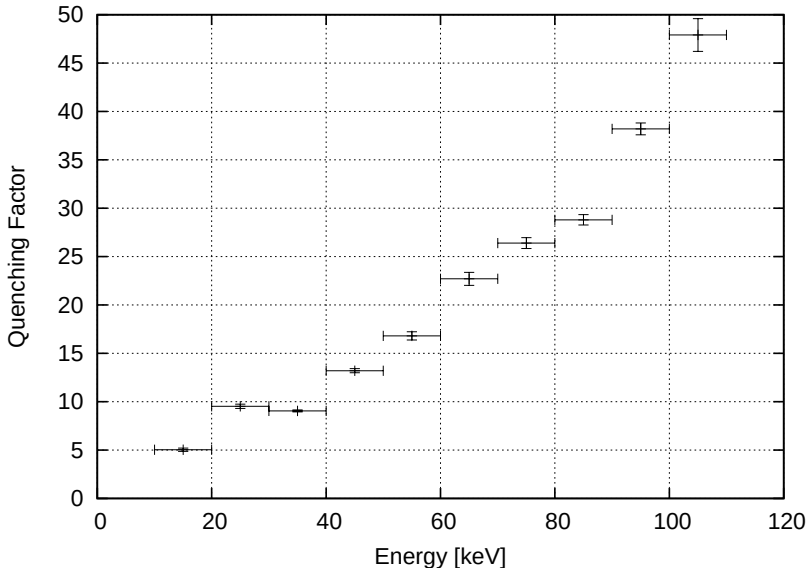

Figure 7.10: Quenching factors for the recoiling nuclei events, obtained for each 10 keV bin from the ratio of the light output for electron and nuclear recoils.

quenching factor for each energy bin is calculated as the ratio of the light energy of the electron recoil band to the light energy of the nuclear recoil band. While for small energies very small quenching factors are obtained, the value in the last bin (100–110 keV) is 47.9 ± 1.7. This is in agreement with the quenching factor for ^{206}Pb obtained from CRESST data [53]. To solve this puzzle Monte Carlo simulations were performed.

7.1.4 Monte Carlo Simulations

For the Monte Carlo simulations SRIM-2003 [104] was used. SRIM is a tool to simulate the stopping range of ions in a given material. It features a full damage calculation including the emission of particles from the target material due to scattering of the projectile. Normally the tool is used to calculate the stopping and damage caused by ions shot from outside into the target, but the starting point and direction of the initial ion can be chosen freely and can also be located underneath the surface of the target material.

The target material chosen for the first simulations was polyethylene, as its composition is simple and should be close enough to the composition of the polymeric foil to yield reasonable results. The depth profile of the initial ^{210}Po isotopes in the material was generated by using SRIM to calculate the implantation of ^{214}Pb and then ^{210}Pb from a set of 10000 ^{218}Po decays on the surface where the direction of the recoiling nucleus is evenly distributed on the half sphere towards the target. The beta decays of ^{214}Pb and ^{214}Bi are skipped in the simulation as here the recoil on the nucleus is negligible. For the subsequent ^{214}Po decay the direction is 4π distributed. This should result in a realistic distribution of ^{210}Po in the material.

For each ^{210}Po decay the full damage including emitted particles is calculated for the ^{206}Pb nucleus as well as for the alpha particle. The initial direction for the nucleus is random, the alpha is sent off antipodally. Fig. 7.11 shows an example for a track of a ^{206}Pb nucleus starting at a certain depth in the source heading towards the surface. Along the track secondary particles that may also leave the source are produced. The calculation for the lead nuclei and the alphas is performed independently. At the end, the data of particles emitted from the source together with the energies that they carry are merged.

The results of these simulations show that for events, where less than 30 keV are emitted from the source, most of the energy is not carried away by the lead recoil, but rather by carbon and hydrogen (Fig. 7.12). In fact, there is a significant number of events, where the lead does not leave the source at all, and only the carbon and hydrogen atoms that have been scattered from the lead do so.

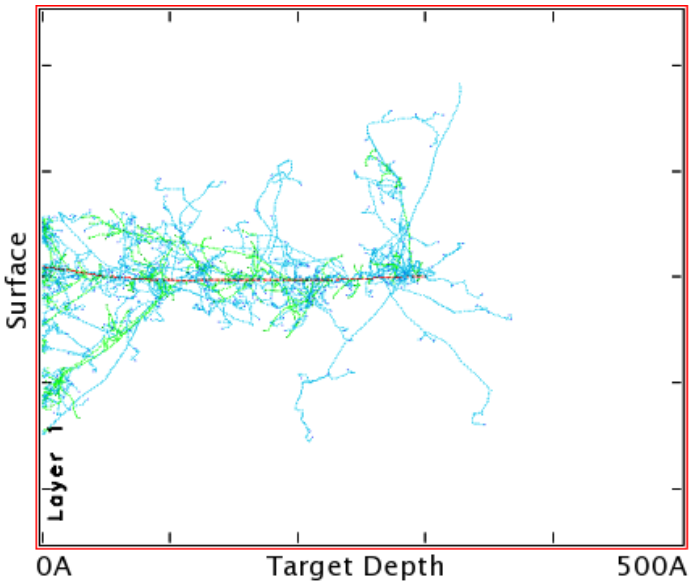

Figure 7.11: Example for a simulated propagation track of a ^{206}Pb nucleus in SRIM-2003. Along the track secondary particles are kicked out of their positions and may also leave the source.

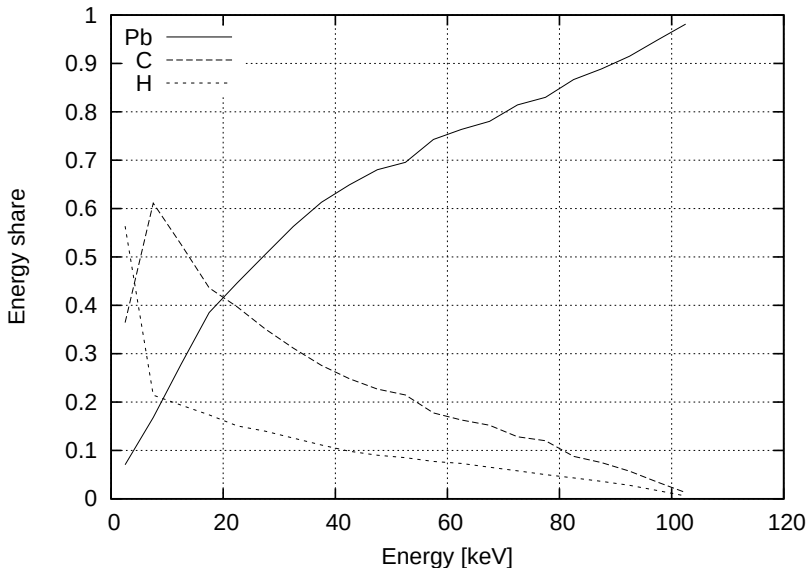

Figure 7.12: Energy share carried by the particles involved in the simulation in dependence of the total energy emitted by the source.

To estimate the light output it is simply assumed that every particle leaving the source deposits its energy in the $CaWO_4$ crystal independent of the angle of emission. For each simulated event the expected total light output is calculated by summing up the energies of all emitted particles reduced by the respective quenching factor for the particle:

$$E_{\text{light}} = \sum_{i=\text{H,He,C,Pb}} \frac{E_i}{Q_i} \tag{7.3}$$

The quenching factors Q_i are taken from a measurement performed with a time-of-flight spectrometer at the Max-Planck-Institut of Physics in Munich [58]. In (7.3) the quenching factors used are $Q_{\text{H}} = 2.2$, $Q_{\text{He}} = 5.7$, $Q_{\text{C}} = 9.7$ and $Q_{\text{Pb}} = 49$, the value for carbon being interpolated between hydrogen and oxygen. This yields a result which is in agreement with the results of the measurement, showing a decreasing light output for higher energies up to 103 keV, as soon as the contributions of C and H becomes less important (Fig. 7.13).

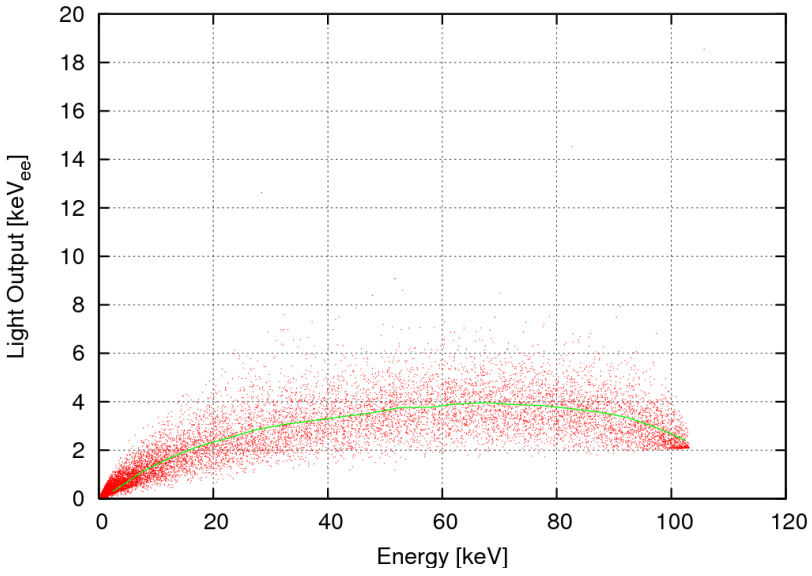

Figure 7.13: Light output calculated for the simulated events in the case that all particles leaving the source hit the $CaWO_4$ crystal.

7.1.5 Outlook: Radon Activated Reflector

The measurements so far combined with the results of the Monte Carlo simulations have demonstrated that for recoiling nuclei from surface alpha decays

the low energy part of the spectrum, particularly the revelant region below 40 keV, is dominated by secondary particles. As those particles are typically lighter than lead, they produce more scintillation light in the crystal. Thus a certain part of this background might not fall below the tungsten threshold in the light yield.

However, the results of the measurement cannot directly be transferred to the situation in the CRESST experiment. Especially the spectrum of the nuclei resulting from naturally implanted ^{210}Po may be different from the source produced chemically. Also the materials involved, and thus the composition of the secondary particles, are different. Future experiments have thus to deal with enriched radon induced radioactivity on the materials that face the $CaWO_4$ crystals in the CRESST experiment. This is mainly the reflective foil.

The next step would thus consist in activating the reflective foil used in the experiment with radon daughters in order to characterize the spectrum of the recoils as it would occur in the real experiment. Also the scintillation properties and veto efficiency of the foil should be determined.

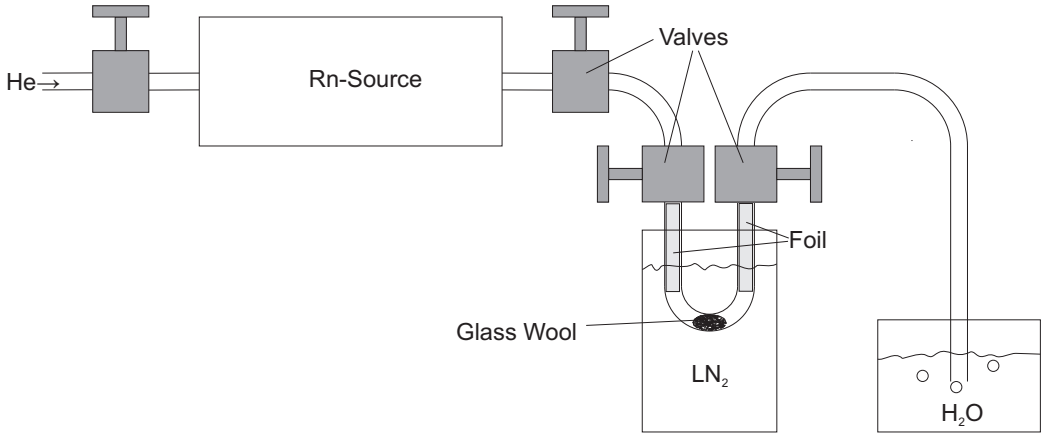

Figure 7.14: Proposed setup for the deposition of radon daughters onto the reflector foil of the CRESST experiment.

Fig. 7.14 shows a possible setup for the deposition of radon daughters onto the reflector foils. The central part would be a cold trap where radon gas taken from a radon emanation source is frozen. In the cold trap are two pieces of the reflector foil. As the foil scintillates only on one side, the orientation of the two pieces should be such, that for one preferably the scintillating and for the other the non-scintillating side is exposed to the radon gas. The radon gas from the source could be flushed through the system using He gas.

The non-scintillating foil should be able to deliver more realistic data for

the properties of the ^{210}Po background in the experiment since the implantation profile of the ^{210}Po should be similar to a natural contamination. By comparing the data from the scintillating and the non-scintillating foil the veto efficiency could be determined. And furthermore the light output of the scintillating foil, and possibly even the scintillation time constants could be determined in such an experiment.

7.2 Transport Mechanism for Calibration Sources in CRESST

7.2.1 Setup

The detector modules in the CRESST experiment are calibrated using low energetic gamma sources, typically ^{57}Co, providing gamma lines at 122.1 and 136.5 keV. The calibration sources have to be introduced into the inner lead and copper shields of the experiment (for an image of the CRESST shielding see Fig. 2.3 and Fig. 2.4 in chapter 2), preferably without opening it. Prior to the upgrade of CRESST, the cold box could only host two detector modules, for these a single position for the calibration source was sufficient. The source was introduced using a copper rod that could be fed through the bottom of the inner shield. After the upgrade the cold box can now support 33 detector modules which, however, cannot all be reached from a single position of the ^{57}Co source. Thus a possibility to calibrate the detectors from several positions inside the inner shield is required.

A mechanism for this purpose was developed by W. Rau and H. Hess and was installed in the CRESST setup at the LNGS as part of this work. The source is introduced into the inner shield through a polyethylene tube that is fed through the lead and copper shields and embraces the cold box. The calibration source is transported through the tube in a small capsule attached to a drawstring. See Fig. 7.15 for a photograph of the tube around the cold box. The tube is mounted with pipe clamps in the inner copper shield and completely surrounds the cold box. In order to be able to open the inner shield without having to remove the tube, an open path around the cryostat is chosen, which automatically opens and releases the cold box, when the shield is removed.

The path along the tube leads through several narrow curvatures. Thus, the rope with the transport capsule cannot be moved easily. Therefore a drawstring with small plastic balls is used as rope. This can be blown through the tube with pressurized air. Fig. 7.16 shows a photograph of the pressurized air system that can be attached to the transport tube. The air can

Figure 7.15: The tube with the drawstring embracing the cold box containing the CRESST detectors. Inset: Close-up view of the tube with the drawstring and the capsule bearing the calibration source.

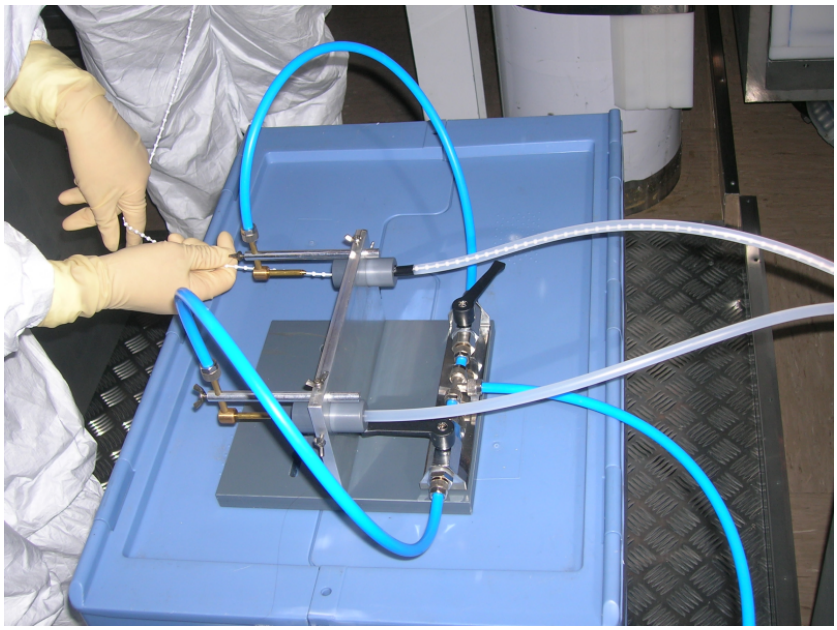

Figure 7.16: The pressurized air system connected to the transport tube.

be blown into either end of the tube via nozzles depending on the desired direction of the source motion.

Isotope/Chain	**Activity Limit** [mBq/kg]
^{226}Ra	< 157
^{228}Th	< 43
^{228}Ac	< 103
^{40}K	< 466

Table 7.1: Limits for the activity of the drawstring measured in a germanium detector by H. Simgen (MPI, Heidelberg).

When not needed the pressurized air system is detached from the tube. The drawstring was monitored concerning its radiactivity and no significant contamination was found (see Table 7.1), so that it can remain in the tube after removing the source from the capsule. However, if desired, the drawstring can also be removed from the tube and the tube can be attached to the nitrogen flushing system of the radon box to avoid radon contamination in the inner shield via the tube.

7.2.2 First Calibration Measurements

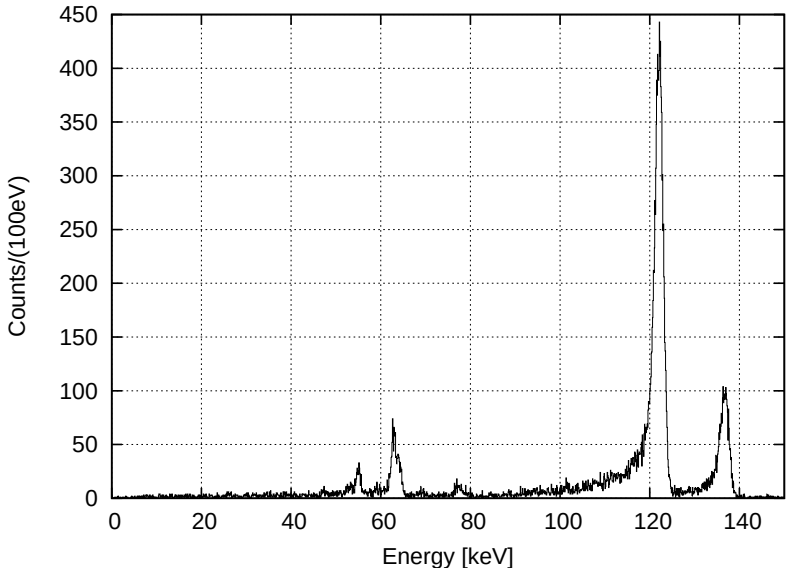

Figure 7.17: Spectrum of the phonon signal in the detector "Verena" obtained with a ^{57}Co source introduced into the inner shield using the new transport mechanism.

The calibration source is a small ^{57}Co source with an initial activity of 70 kBq. Due to the short halflife of ^{57}Co (276 days) this activity was reduced to about 30 kBq by the time of the first calibration measurements (Jan 2007). Fig. 7.17 shows the energy spectrum seen in the phonon detector "Verena" during a first calibration run using the new transport system. The motion of the source in the tube causes a small disturbance in the detector stabilization, so that it takes a couple of minutes until the measurement can be resumed after positioning the source.

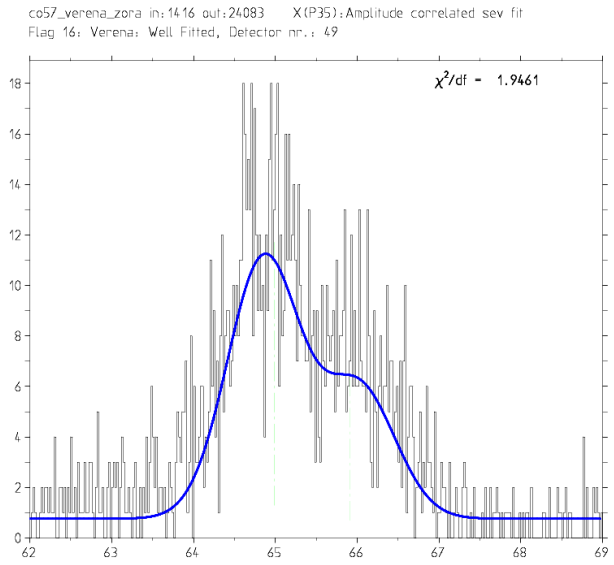

Figure 7.18: The tungsten K_α escape lines as observed in the $CaWO_4$ detector "Verena", the resolution of $\sim$ 1 keV (FWHM) at $\sim$ 63 keV allows to observe the substructure of the $K_{\alpha 1}$ and $K_{\alpha 2}$ lines.

The low background level of the experiment allows also weak lines in the calibration spectrum, like the tungsten escape peaks from the 136 keV line, to be observed. The detector resolution was determined to be $\sim$ 1 keV at 63 keV, this allows a partial separation of the $K_{\alpha 1}$ and $K_{\alpha 2}$ W-escape peaks of the 122 keV line (see Fig. 7.18).

As shown in section 7.1.3 a dependency of the light yield on the phonon signal is observed as a tilt of the calibration lines in the phonon-light plot. Again, the light output of the crystal can be determined from the tilt of the 122 keV line. Fig. 7.19 shows the calculated energy fraction emitted as scintillation light for the calibration data. In this case, an average of $\sim$ 4.5% is converted into light with electron recoil events.

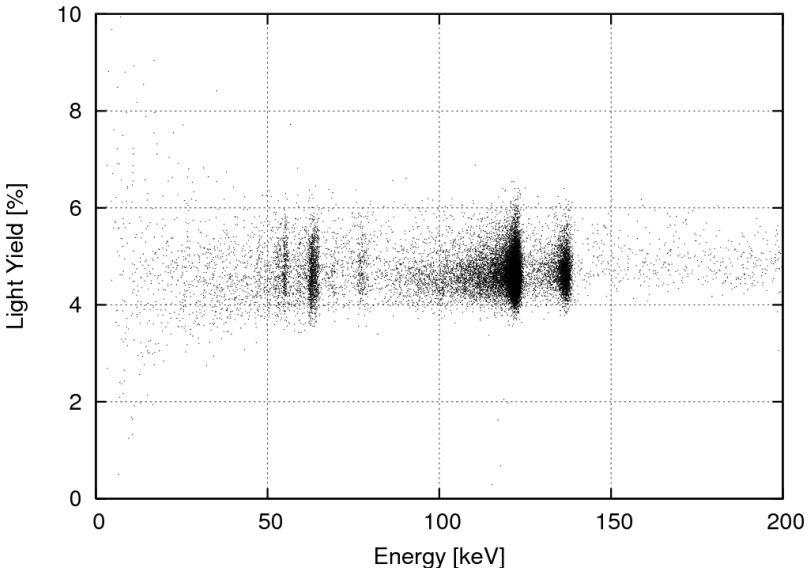

Figure 7.19: Absolute light yield for the events recorded with the ^{57}Co source.

Chapter 8

Summary and Outlook

The CRESST experiment aims at the direct detection of non-baryonic dark matter particles via coherent scattering off nuclei in scintillating $CaWO_4$ crystals. The simultaneous measurement of the heat and the scintillation light allows a discrimination of the background from betas and gammas due to the higher light output of electron recoils. As the light output of the nuclear recoils depends on the recoiling nucleus, a partial discrimination of the neutron background (mainly oxygen recoils) from the anticipated WIMP signal (tungsten recoils) is also possible. It is thus important to understand the quenching of the scintillation light of all event classes. The quenching factors for the nuclear recoils are being measured in a cryogenic neutron scattering experiment at the accelerator laboratory in Garching (see chapters 2 and 6.2). In this work detectors for these calibration measurements were developed. Further contributions to the background calibration of the CRESST experiment were made.

A phonon detector with a small cylindrical $CaWO_4$ crystal with 20 mm diameter and 5 mm height for neutron calibration measurements was successfully developed and tested (see chapter 6.2). The detector showed good performance at low energies with a threshold of 250 eV and a resolution of 340 eV at 5.9 keV. A dynamic range of at least 1.4 MeV was reached in the test measurement. Optimized settings in the data acquisition system, e.g. longer time windows for the recorded pulses, should make it possible to reach even higher energies. The detector was successfully installed in the cryogenic neutron scattering facility at the Maier-Leibnitz accelerator laboratory in Garching together with a light detector also produced in this work. Since the contribution of multiple scattered neutrons is small, the determination of the quenching factors of the constituent elements of the crystal has been made possible. First measurements with a monoenergetic neutron beam were performed and showed good results (see [63] and [97]).

For the upcoming large-scale ($\sim$ 1 ton) cryogenic dark matter searches, like EURECA, a large number of detectors will be needed. Thus, it is desirable to fabricate many detectors on a short time scale and in a highly reproducible way. To reach this goal the composite detector design is an option to be investigated. Here, the structure of the TES is produced on a small crystal which is then glued onto the actual large absorber crystal. In the present work a composite detector with a cylindrical $CaWO_4$ crystal (20 mm diameter, 20 mm height) as absorber was produced and tested (see chapter 6.1). An Ir/Au TES was fabricated on a small silicon substrate and then glued onto the $CaWO_4$ crystal. While the performance of this particular detector was not satisfactory, the results showed an interesting prospect for future detector designs. There is a strong indication that the pulses seen in the TES on the silicon substrate contained components due to the scintillation light and due to the heat signal from the crystal at the same time. If one succeeds to separate the energy information of the two contributions via pulse shape analysis, it is possible to measure both signals with only one detector channel. This would also enormously simplify the data-acquisition system.

A potentially harmful background for the CRESST dark matter search are recoiling nuclei from surface alpha decays originating from ^{210}Po contamination on the surfaces in the proximity of the target crystal. Measurements for the characterization of this kind of background were performed in this work using a chemically produced source, where ^{210}Po activity is deposited onto a polished silver disc (see chapter 7.1). The results of these measurements combined with Monte Carlo simulations show, that for lower energies, corresponding to alpha decays beneath the surface, the energy deposition into the target crystal occurs mainly via secondary particles from the surface material. Future experiments are proposed for a further characterization of the background under conditions that are closer to those in the actual experiment. This involves the activation of the reflective foil with ^{210}Po activity using ^{222}Rn gas.

The light emission of the crystals for electron recoils was determined to be in the range of 2.8% (see section 7.1.3) to 4.5% (see chapter 7.2), the spread of the values can be due to systematics caused by the use of different light detectors or be indeed due to the different light yields of the crystals. The fraction of the total energy eventually detected as light in the light detector was determined to be in the range of 0.7% to 1.9% (see chapter 6.3). Thus, only about 25–30% of the emitted light is detected in the light detector. The reason for this low light detection in the CRESST experiment is not clear. Additional experiments have to be carried out with the goal to improve the light collection considerably. From pulse shape analysis of the

light detector the scintillation decay time constants of the $CaWO_4$ crystals were obtained. For electron recoils two decay times of $\tau_1 \sim 0.3$–$0.4\,\mathrm{ms}$ and $\tau_2 \sim 2\,\mathrm{ms}$ were found, where about 80% of the energy is emitted with the faster decay time. For nuclear recoils there is an indication, that the slower decay time is strongly suppressed, if not completely absent (see chapter 6.3). However, the data used for comparing electron and nuclear recoils were not good enough to allow an unambiguous statement. Data of better quality and higher statistics containing both event classes are needed. The measurements at the neutron scattering facility can be expected to reach this goal.

The detectors used for the calibration measurements use phonon collectors (see section 3.2) consisting of Ir/Au/Al multilayers. A limiting factor in the design of the phonon collectors is the quasiparticle diffusion length. In this work this length was measured for the multilayer system used in the phonon collectors. The result yielded a diffusion length of $l_D \sim 0.7\,\mathrm{mm}$ (see chapter 5.7). This rather large value indicates a high quality of the produced films, and is well above the typical structure size of the phonon collectors ($0.25\,\mathrm{mm}$). Thus, such collectors should be very efficient and are expected to drastically increase the sensitivity of the detectors for the CRESST and EURECA experiments.

Appendix A

Some Calculations

A.1 Quasiparticle Diffusion

The diffusion and decay of quasiparticles is described by the differential equation

$$\frac{\partial n}{\partial t} - D\frac{\partial^2 n}{\partial x^2} + \gamma_D n = 0 \tag{A.1}$$

x	...	Location
t	...	Time
$n(x,t)$	...	Quasiparticle density
D	...	Diffusion constant
$\gamma_D = \tau_D^{-1}$	...	Decay constant

This equation has to be solved for the boundary conditions

$$n(x=0,t) = 0 \tag{A.2}$$

$$\frac{\partial}{\partial x} n(x=L,t) = 0 \tag{A.3}$$

where (A.2) describes the boundary condition at the collecting end for perfect quasiparticle collection and (A.3) the condition at the reflecting end.

The ansatz for solving (A.1) is the separation of the local and time component:

$$n(x,t) = X(x) \cdot T(t) \tag{A.4}$$

An elementary solution of the local function has the form

$$\tilde{X} = c_1 \cos ax + c_2 \sin ax \tag{A.5}$$

From (A.2) one obtains $c_1 = 0$ and from (A.3) $a = (2k+1)\pi/(2L)$. Thus the general solution for X is

$$X_k = c_k \sin(2k+1)\tfrac{\pi x}{2L} \qquad k = 0, 1, 2 \ldots \tag{A.6}$$

A special solution is obtained by expanding the initial distribution into the series (A.6). If one looks at direct hits (e.g. from an X-ray source) this can be written as

$$X(x, t = 0) = N_0 \delta(x - x_0) \tag{A.7}$$

This is only defined for $x \in [0; L]$, for the expansion it has to be extended over the whole space by mirroring. This involves a sign change for the points defined by the boundary condition (A.2); the sign is kept for points defined by the boundary condition (A.3). The result is a $4L$ periodic function. For the coefficients c_k one then easily obtains

$$c_k = \frac{2N_0}{L} \sin\left((2k+1)\frac{x_0\pi}{2L}\right) \tag{A.8}$$

and thus

$$X_k(x, t = 0) = \frac{2N_0}{L} \sin\left((2k+1)\frac{x_0\pi}{2L}\right) \sin\left((2k+1)\frac{x\pi}{2L}\right) \tag{A.9}$$

For the time dependence the equation

$$\frac{\dot{T}_k}{T_k} = D\frac{X_k''}{X_k} - \gamma_D \tag{A.10}$$

which is derived from (A.1) has to be solved.

With

$$X_k'' = -\frac{2N_0}{L}(2k+1)^2 \frac{\pi^2}{2L^2} \sin\left((2k+1)\frac{x_0\pi}{2L}\right) \sin\left((2k+1)\frac{x\pi}{2L}\right) \tag{A.11}$$

one obtains

$$\frac{\dot{T}_k}{T_k} = -\left(D(2k+1)^2 \frac{\pi^2}{2L^2} + \gamma_D\right) \tag{A.12}$$

which is solved by

$$T_k(t) = \mathrm{e}^{-\left(D(2k+1)^2 \frac{\pi^2}{2L^2} + \gamma_D\right)t} \tag{A.13}$$

So in total the quasiparticle density in the film at position x at the time t is

$$n(x,t) = \frac{2N_0}{L} \sum_{k=0}^{\infty} \mathrm{e}^{-\left(D(2k+1)^2 \frac{\pi^2}{2L^2} + \gamma_D\right)t} \sin\left((2k+1)\frac{x_0\pi}{2L}\right) \sin\left((2k+1)\frac{x\pi}{2L}\right) \tag{A.14}$$

The energy collected in the sensor is the integral of the current of quasiparticles over the collecting edge at $x = 0$ over all times:

$$N = D \int_0^\infty \frac{\partial n}{\partial x}(x = 0, t)dt \tag{A.15}$$

With

$$\frac{\partial n}{\partial x}(x = 0, t) = \frac{N_0 \pi}{L^2} \sum_{k=0}^{\infty} (2k + 1) \mathrm{e}^{-\left(D(2k+1)^2 \frac{\pi^2}{2L^2} + \gamma_D\right)t} \sin\left((2k + 1)\frac{x_0 \pi}{2L}\right) \tag{A.16}$$

this yields after exercising the integral

$$N = D \frac{N_0 \pi}{L^2} \sum_{k=0}^{\infty} \frac{(2k + 1)\frac{\pi}{2L}}{D(2k + 1)^2 \frac{\pi^2}{4L^2} + \gamma_D} \sin\left((2k + 1)\frac{x_0 \pi}{2L}\right) \tag{A.17}$$

which is the sinus expansion of

$$N = N_0 \frac{\cosh\left(\alpha\left(1 - \frac{x_0}{L}\right)\right)}{\cosh \alpha} \tag{A.18}$$

with $\alpha = L/\sqrt{D\tau_D} = \sqrt{2}L/l_D$, where l_D is the "diffusion length", the characteristic length for the quasiparticle diffusion and decay in the strip. This is valid if all quasiparticles are excited at the same place x_0, for example by an absorbed X-ray. For a phonon collector the excitation on the other hand is evenly distributed over the whole length. In this case the initial distribution which has to be expanded according to (A.6) is

$$n(x, t = 0) = \frac{N_0}{L} \theta(x)\theta(l - x) \tag{A.19}$$

This again has to be extended to the whole space with the above mentioned method. The coefficients in (A.6) then become

$$c_k = \frac{N_0}{L^2} \frac{4L}{(2k + 1)\pi} \tag{A.20}$$

and thus the local and time components yield

$$X_k = \frac{4N_0}{(2k + 1)\pi L} \sin\left((2k + 1)\frac{\pi x}{2L}\right) \tag{A.21}$$

$$T_k = \mathrm{e}^{-\left(D(2k+1)^2 \frac{\pi^2}{4L^2} + \gamma_D\right)t} \tag{A.22}$$

The quasiparticle density in the strip then is

$$n(x,t) = \sum_{k=0}^{\infty} \frac{4N_0}{(2k+1)\pi L} \mathrm{e}^{-\left(D(2k+1)^2 \frac{\pi^2}{4L^2} + \gamma_D\right)t} \sin\left((2k+1)\frac{\pi x}{2L}\right) \tag{A.23}$$

from which the current into the sensor can be obtained:

$$D\frac{\partial n}{\partial x}(x=0,t) = D\sum_{k=0}^{\infty} \frac{2N_0}{L^2} \mathrm{e}^{-\left(D(2k+1)^2 \frac{\pi^2}{4L^2} + \gamma_D\right)t} \tag{A.24}$$

This is the time dependent current into the sensor if all quasiparticles are excited at the same time. For a more realistic description this expression has to be convoluted with the function describing the phonon current into the collector.

The total amount of quasiparticles collected in the sensor is calculated from (A.24):

$$\begin{aligned} N &= \int_0^{\infty} D\sum_{k=0}^{\infty} \frac{2N_0}{L^2} \mathrm{e}^{-\left(D(2k+1)^2 \frac{\pi^2}{4L^2} + \gamma_D\right)t} dt \\ &= 2N_0 \sum_{k=0}^{\infty} \frac{4}{\pi^2} \frac{1}{(2k+1)^2 + \alpha^2 \frac{4}{\pi^2}} \end{aligned} \tag{A.25}$$

which involves an expansion of tanh. This yields a collection effiency for a collector strip of length L expressed with the diffusion length l_D

$$\frac{N}{N_0} = \frac{l_D}{\sqrt{2}L} \tanh\left(\frac{\sqrt{2}L}{l_D}\right) \tag{A.26}$$

A.2 Mean Free Path of Neutrons in $CaWO_4$

The mean free path of neutrons in a material can be calculated from the total cross section for neutron interaction and the material's density. The total neutron interaction cross sections are available online at the *National Nuclear Data Center* [105] as datafiles per isotope. The cross section is dependend on the neutron energy. As the detector discussed in section 6.2 is employed at the neutron scattering facility, the nominal energy of the neutron beam there is used, i.e. 11 MeV. At this energy the cross sections for the natural isotopes of Ca, W and O are used to calculate the average cross section for each element honoring the natural abundances of the isotopes. This way values of 2.46 barn for calcium, 5.15 barn for tungsten and 1.51 barn for

oxygen are obtained. This results in a total cross section σ of 13.65 barn for one unit cell of $CaWO_4$.

The specific gravity of $CaWO_4$ is typically in the range between 5.9 and 6.1 g/cm^3, for the following calculations a value of 6.0 g/cm^3 is used. The mass of a unit cell is 290 amu, i.e. $4.82 \cdot 10^{-22}$ g. Thus the density of unit cells per volume n is $1.24 \cdot 10^{22}\,cm^{-3}$. From this and the total neutron interaction cross section σ the mean free path l_n for 11 MeV neutrons can be calculated as

$$l_n = \frac{1}{n\sigma} = 5.9\,\text{cm} \tag{A.27}$$

Bibliography

[1] F. Zwicky. *On the Masses of Nebulae and of Clusters of Nebulae*. Astroph. J., **86** (1937) 217.

[2] J. A. Tyson et al. *Detailed Mass Map of CL 0024+1654 from Strong Lensing*. Astroph. J. Lett., **498** (1998) L107. `arXiv:astro-ph/9801193`.

[3] D. Clowe et al. *A Direct Empirical Proof of the Existence of Dark Matter*. Astroph. J. Lett., **648** (2006) L109. `arXiv:astro-ph/0608407`.

[4] K. G. Begeman et al. *Extended rotation curves of spiral galaxies - Dark haloes and modified dynamics*. Mon. Not. R. Astron. Soc., **249** (1991) 523.

[5] M. Milgrom. *A modification of the Newtonian dynamics as a possible alternative to the hidden mass hypothesis*. Astroph. J., **270** (1983) 365.

[6] C. L. Bennett et al. *First-Year Wilkinson Microwave Anisotropy Probe (WMAP) Observations: Preliminary Maps and Basic Results*. Astroph. J. Suppl. S., **148** (2003) 1. `arXiv:astro-ph/0302207`.

[7] D. N. Spergel et al. *Three-Year Wilkinson Microwave Anisotropy Probe (WMAP) Observations: Implications for Cosmology*. Astroph. J. Suppl. S., **170** (2007) 377. `arXiv:astro-ph/0603449`.

[8] A. B. McDonald et al. *Direct Evidence for Neutrino Flavor Transformation from Neutral-Current Interactions in SNO*. In V. Elias et al., editors, *Theoretical Physics: MRST 2002*, volume 646 of *American Institute of Physics Conference Series*, pages 43–58, December 2002.

[9] L. Bergström and A. Goobar. *Cosmology and Particle Astrophysics*. Springer-Verlag Berlin Heidelberg New York, 2nd edition, 2003.

[10] C. Weinheimer. *Review of direct neutrino mass measurements*. In N. J. C. Spooner and V. Kudryavtsev, editors, *Identification of Dark Matter*, page 543, 2003.

[11] S. Dodelson and L. M. Widrow. *Sterile neutrinos as dark matter*. Phys. Rev. Lett., **72** (1994) 17.

[12] X. Shi and G. M. Fuller. *New Dark Matter Candidate: Nonthermal Sterile Neutrinos.* Phys. Rev. Lett., **82** (1999) 2832.

[13] L. J. Rosenberg. *Searches for invisible axions.* Phys. Rep., **325** (2000) 1.

[14] G. Bertone et al. *Particle dark matter: evidence, candidates and constraints.* Phys. Rep., **405** (2005) 279. `arXiv:hep-ph/0404175`.

[15] G. Jungman et al. *Supersymmetric dark matter.* Phys. Rep., **267** (1996) 195. `arXiv:hep-ph/9506380`.

[16] R. Trotta et al. *Prospects for direct dark matter detection in the constrained MSSM.* New Astron. Rev., **51** (2007) 316. `arXiv:astro-ph/0609126`.

[17] T. Falk et al. *Heavy sneutrinos as dark matter.* Phys. Lett. B, **339** (1994) 248. `arXiv:hep-ph/9409270`.

[18] J. L. Feng et al. *Superweakly Interacting Massive Particles.* Phys. Rev. Lett., **91** (2003) 011302. `arXiv:hep-ph/0302215`.

[19] J. F. Navarro et al. *The Structure of Cold Dark Matter Halos.* Astroph. J., **462** (1996) 563. `arXiv:astro-ph/9508025`.

[20] L. Bergström et al. *Observability of gamma rays from dark matter neutralino annihilations in the Milky Way halo.* Astropart. Phys., **9** (1998) 137. `arXiv:astro-ph/9712318`.

[21] J. D. Lewin and P. F. Smith. *Review of mathematics, numerical factors, and corrections for dark matter experiments based on elastic nuclear recoil.* Astropart. Phys., **6** (1996) 87.

[22] R. H. Helm. *Inelastic and Elastic Scattering of 187-Mev Electrons from Selected Even-Even Nuclei.* Phys. Rev., **104** (1956) 1466.

[23] E. V. Bugaev et al. *Atmospheric muon flux at sea level, underground, and underwater.* Phys. Rev. D, **58** (1998) 054001.

[24] J. Gascon. *Direct search for WIMP dark matter.* Available Online. `arXiv:astro-ph/0504241`.

[25] P. Meunier et al. *Discrimination between nuclear recoils and electron recoils by simultaneous detection of phonons and scintillation light.* Appl. Phys. Lett., **75** (1999) 1335. `arXiv:physics/9906017`.

[26] S. Yellin. *Finding an upper limit in the presence of an unknown background.* Phys. Rev. D, **66** (2002) 032005. `arXiv:physics/0203002`.

[27] D. S. Akerib et al. *Exclusion limits on the WIMP-nucleon cross section from the first run of the Cryogenic Dark Matter Search in the Soudan Underground Laboratory.* Phys. Rev. D, **72** (2005) 052009.

[28] J. Hellmig et al. *The CDMS II Z-sensitive ionization and phonon germanium detector*. Nucl. Instr. and Meth. A, **444** (2000) 308.

[29] D. S. Akerib et al. *Limits on Spin-Independent Interactions of Weakly Interacting Massive Particles with Nucleons from the Two-Tower Run of the Cryogenic Dark Matter Search*. Phys. Rev. Lett., **96** (2006) 011302.

[30] Z. Ahmed et al. *A Search for WIMPs with the First Five-Tower Data from CDMS*. Available Online. `arXiv:0802.3530`.

[31] R. W. Schnee et al. *The SuperCDMS experiment*. In H. V. Klapdor-Kleingrothaus and R. Arnowitt, editors, *Dark matter in astro- and particle physics*, page 259, 2005.

[32] V. Sanglard et al. *Final results of the EDELWEISS-I dark matter search with cryogenic heat-and-ionization Ge detectors*. Phys. Rev. D, **71** (2005) 122002. `arXiv:astro-ph/0503265`.

[33] O. Martineau et al. *Calibration of the EDELWEISS cryogenic heat-and-ionization germanium detectors for dark matter search*. Nucl. Instr. and Meth. A, **530** (2004) 426. `arXiv:astro-ph/0310657`.

[34] A. de Bellefon et al. *Dark matter search with a low temperature sapphire bolometer*. Astropart. Phys., **6** (1996) 35.

[35] V. Sanglard and for the EDELWEISS collaboration. *EDELWEISS-II : Status and future*. Available Online. `arXiv:astro-ph/0612207`.

[36] S. Marnieros et al. *Identification of near surface events using athermal phonon signals in low temperature Ge bolometers for the EDELWEISS experiment*. Nucl. Instr. and Meth. A, **520** (2004) 185.

[37] H. Kraus et al. *EURECA – the European future of cryogenic dark matter searches*. J. Phys. Conf. S., **39** (2006) 139.

[38] R. Bernabei et al. *Particle dark matter: From DAMA/NaI to DAMA/LIBRA*. Phys. Atom. Nucl., **69** (2006) 2056.

[39] R. Bernabei et al. *Dark Matter search*. Nuovo Cimento Rivista Serie, **26** (2003) 1. `arXiv:astro-ph/0307403`.

[40] N. W. Evans et al. *Triaxial haloes and particle dark matter detection*. Mon. Not. R. Astron. Soc., **318** (2000) 1131. `arXiv:astro-ph/0008156`.

[41] R. Bernabei et al. *Search for WIMP annual modulation signature: results from DAMA/NaI-3 and DAMA/NaI-4 and the global combined analysis*. Phys. Lett. B, **480** (2000) 23.

[42] R. Brunetti et al. *WARP liquid argon detector for dark matter survey.* New Astron. Rev., **49** (2005) 265. `arXiv:astro-ph/0405342`.

[43] G. J. Alner et al. *First limits on nuclear recoil events from the ZEPLIN I galactic dark matter detector.* Astropart. Phys., **23** (2005) 444.

[44] E. Aprile et al. *The XENON dark matter search experiment.* New Astron. Rev., **49** (2005) 289. `arXiv:astro-ph/0407575`.

[45] A. I. Bolozdynya. *Two-phase emission detectors and their applications.* Nucl. Instr. and Meth. A, **422** (1999) 314.

[46] J. Angle et al. *First Results from the XENON10 Dark Matter Experiment at the Gran Sasso National Laboratory.* Available Online. `arXiv:0706.0039`.

[47] L. M. Krauss et al. *Solar System constraints and signatures for dark-matter candidates.* Phys. Rev. D, **33** (1986) 2079.

[48] W. H. Press and D. N. Spergel. *Capture by the sun of a galactic population of weakly interacting, massive particles.* Astroph. J., **296** (1985) 679.

[49] S. Fukuda et al. *The Super-Kamiokande detector.* Nucl. Instr. and Meth. A, **501** (2003) 418.

[50] Y. Fukuda et al. *Measurement of the Flux and Zenith-Angle Distribution of Upward Throughgoing Muons by Super-Kamiokande.* Phys. Rev. Lett., **82** (1999) 2644.

[51] S. Desai et al. *Search for dark matter WIMPs using upward through-going muons in Super-Kamiokande.* Phys. Rev. D, **70** (2004) 083523. `arXiv:hep-ex/0404025`.

[52] G. Angloher et al. *Limits on WIMP dark matter using sapphire cryogenic detectors.* Astropart. Phys., **18** (2002) 43.

[53] G. Angloher et al. *Limits on WIMP dark matter using scintillating CaWO4 cryogenic detectors with active background suppression.* Astropart. Phys., **23** (2005) 325. `arXiv:astro-ph/0408006`.

[54] S. Henry et al. *Multichannel SQUID readout for CRESST II.* Nucl. Instr. and Meth. A, **520** (2004) 588.

[55] H. Wulandari. *Study On Neutron-Induced Background in the Dark Matter Experiment CRESST.* PhD thesis, Technische Universität München, July 2003.

[56] H. Wulandari et al. *Neutron Background Studies for the CRESST Dark Matter Experiment.* Available Online. `arXiv:hep-ex/0401032`.

[57] J. Åström et al. *Fracture processes observed with a cryogenic detector.* Phys. Lett. A, **356** (2006) 262. arXiv:physics/0504151.

[58] J. Ninković et al. *New technique for the measurement of the scintillation efficiency of nuclear recoils.* Nucl. Instr. and Meth. A, **564** (2006) 567. arXiv:astro-ph/0604094.

[59] I. Bavykina et al. *Interpretation of Light-Quenching Factor Measurements.* Available Online. arXiv:0707.0766.

[60] T. Jagemann et al. *Measurement of nuclear recoil quenching factors in $CaWO_4$.* Astropart. Phys., **26** (2006) 269.

[61] T. Jagemann et al. *Neutron scattering facility for the measurement of nuclear recoil quenching factors.* Nucl. Instr. and Meth. A, **551** (2005) 245.

[62] T. Jagemann et al. *Measurement of the scintillation light quenching at room temperature of sodium recoils in NaI(Tl) and hydrogen recoils in NE 213 by the scattering of neutrons.* Nucl. Instr. and Meth. A, **564** (2006) 549.

[63] C. Coppi. *In Preparation.* PhD thesis, Technische Universität München, 2008.

[64] C. Coppi et al. *Quenching factor measurement for $CaWO_4$ by neutron scattering.* Nucl. Instr. and Meth. A, **559** (2006) 396.

[65] M. Stark. *Detektoren mit effizienter und schneller Phononensammlung für das CRESST Experiment.* PhD thesis, Technische Universität München, 2005.

[66] W. Rau et al. *Results and status of the CRESST experiment.* J. Phys. Conf. S., **39** (2006) 75.

[67] W. Seidel. *The CRESST experiment.* In *The tenth international conference on Topics in Astroparticle and Underground Physics (TAUP2007)*, 2007.

[68] C. Cozzini et al. *Detection of the natural α decay of tungsten.* Phys. Rev. C, **70** (2004) 064606. arXiv:nucl-ex/0408006.

[69] F. A. Danevich et al. *α activity of natural tungsten isotopes.* Phys. Rev. C, **67** (2003) 014310.

[70] F. Pröbst et al. *Model for cryogenic particle detectors with superconducting phase transition thermometers.* J. Low Temp. Phys., **100** (1995) 69.

[71] P. C. F. di Stefano et al. *Textured silicon calorimetric light detector.* J. Appl. Phys., **94** (2003) 6887. arXiv:physics/0307042.

[72] T. Lachenmaier. *Messungen mit undergrundarmen Tieftemperaturdetektoren zum hocheffizienten Nachweis des ^{71}Ge Zerfalls.* PhD thesis, Technische Universität München, July 2005.

[73] S. Roth. *Sputtered Tungsten Thin Films and Composite Detectors for the Application in the Dark Matter Experiments CRESST and EURECA.* Diploma thesis, Technische Universität München, September 2007.

[74] K. D. Irwin. *An application of electrothermal feedback for high resolution cryogenic particle detection.* Appl. Phys. Lett., **66** (1995) 1998.

[75] J. Schnagl. *Entwicklung von Lichtdetektoren mit Phonondetektoren für das CRESST Experiment.* PhD thesis, Technische Universität München, May 2001.

[76] K. D. Irwin et al. *Thermal-response time of superconducting transition-edge microcalorimeters.* J. Appl. Phys., **83** (1998) 3978.

[77] K. D. Irwin et al. *A quasiparticle-trap-assisted transition-edge sensor for phonon-mediated particle detection.* Rev. Sci. Instrum., **66** (1995) 5322.

[78] H. Kraus. *Quasiteilchen-Einfang in supraleitenden Tunneldioden – Ein neues Detektorkonzept.* PhD thesis, Technische Universität München, Dezember 1989.

[79] H. Kraus et al. *Quasiparticle trapping in a superconductive detector system exhibiting high energy and position resolution.* Phys. Lett. B, **231** (1989) 195.

[80] J. Jochum. *Supraleitende Tunneldioden als Detektoren für Neutrino- und Astrophysik.* PhD thesis, Technische Universität München, July 1994.

[81] F. Pobell. *Matter and Methods at Low Temperatures.* Springer-Verlag Berlin Heidelberg New York, 2nd edition, 1996.

[82] C. Isaila. *In Preparation.* PhD thesis, Technische Universität München, 2008.

[83] J. Höhne. *Strahlungsnachweis mit supraleitenden Iridium Gold Phasenübergangsthermometern.* PhD thesis, Technische Universität München, 1998.

[84] U. Nagel et al. *Proximity effect in iridium-gold bilayers.* J. Appl. Phys., **76** (1994) 4262.

[85] `http://www.microresist.de/`.

[86] C. Hollerith et al. *Energy dispersive X-ray spectroscopy with microcalorimeters.* Nucl. Instr. and Meth. A, **520** (2004) 606.

[87] J. J. Hauser et al. *Superconductivity in Cu and Pt by Means of Superimposed Films with Lead.* Phys. Rev., **136** (1964) A637.

[88] D. U. Gubser and R. J. Soulen. *Thermodynamic properties of superconducting iridium.* J. Low Temp. Phys., **13** (1973) 211.

[89] N. R. Werthamer. *Theory of the Superconducting Transition Temperature and Energy Gap Function of Superposed Metal Films.* Phys. Rev., **132** (1963) 2440.

[90] C. V. Thompson. *Grain Growth in Thin Films.* Annual Review of Material Science, **20** (1990) 245.

[91] J. Ninković. *Investigation of $CaWO_4$ Crystals for Simultaneous Phonon-Light Detection in the CRESST Dark Matter Search.* PhD thesis, Technische Universität München, 2005.

[92] J.-C. Lanfranchi. *Development of a New Composite Cryogenic Detection Concept for a Radiochemical Solar Neutrino Experiment.* PhD thesis, Technische Universität München, 2005.

[93] K. E. Gray et al. *Measurements of the Lifetime of Excitations in Superconducting Aluminium.* Philos. Mag., **20** (1969) 273.

[94] P. W. Epperlein and W. Eisenmenger. *Measurements of effective quasiparticle recombination times and of densities of electronic states at the Fermi level in superconducting Al- and Pb-films.* Phys. Kondens. Mater., **32** (1979) 167.

[95] M. Loidl. *Diffusion und Einfang von Quasiteilchen – Konzepte für Kryodetektoren.* PhD thesis, Ludwigs-Maximilians-Universität München, 1999.

[96] J.-C. Lanfranchi et al. *Development of a cryogenic detection concept for GNO.* Nucl. Instr. and Meth. A, **520** (2004) 135.

[97] C. Ciemniak. *In Preparation.* PhD thesis, Technische Universität München, 2009.

[98] P. N. Luke. *Voltage-assisted calorimetric ionization detector.* J. Appl. Phys., **64** (1988) 6858.

[99] S. Scholl. *In Preparation.* PhD thesis, Universität Tübingen, 2008.

[100] T. Saab et al. *Design of QET phonon sensors for the CDMS ZIP detectors.* Nucl. Instr. and Meth. A, **444** (2000) 300.

[101] V. B. Mikhailik et al. *Scintillation studies of $CaWO_4$ in the millikelvin temperature range.* Phys. Rev. B, **75** (2007) 184308.

[102] G. Blasse and G. Bokkers. *Low-temperature decay-time measurements on the luminescence of calcium tungstate ($CaWO_4$).* J. Solid State Chem. F., **49** (1983) 126.

[103] W. W. Flynn. *The determination of low levels of polonium-210 in environmental materials.* Anal. Chim. Acta, **43** (1968) 221.

[104] J. F. Ziegler. *SRIM-2003.* Nucl. Instr. and Meth. B, **219-220** (2004) 1027.

[105] `http://www.nndc.bnl.gov/sigma`.